A Study of the $\omega\pi^0$ Enhancement Photoproduced in the Energy Range 20 to 70 GeV.

by

Colin Neil Paterson

Submitted in Partial Fulfilment of the Work Required for the Degree of Doctor of Philosophy from the Faculty of Science of the University of Glasgow

Department of Natural Philosophy

University of Glasgow

June 1984

Acknowledgments

Firstly I would like to thank all the members of the Omega Photon Collaboration for their work in preparing and running the experiment and processing the data and in particular I wish to thank the members of the $\omega\pi^0$ analysis team.

Thanks go to my supervisor, Dr. Peter Bussey, and to Dr. Ian Skillicorn, for their continued help and encouragement throughout the period of my research, and for their patience during the later stages of my work.

I would also like to thank Dr. David Frame, Dr. Stan Thompson, Dr. Douglas M^{c}Fadzean and Dr. Ian Wilkie for many helpful and enjoyable discussions both about and around the subject of High Energy Physics.

I am grateful to the Science and Engineering Research Council for their financial support during the three years of my work, and to both CERN and RAL for the provision of facilities to run and analyse the experiment.

Finally, I would like to thank both my parents and Francesca for the help and encouragement they gave, especially during the closing stages of my work.

Contents

Abstract

This Thesis presents a description of the photoproduction experiment WA57, and an analysis of the data from that experiment from the reaction $\gamma p \rightarrow \omega \pi^0 p$.

The experiment was performed by the the E-Gamma Collaboration at CERN using the Omega Prime Spectrometer and the Tagged Photon beam in the West Experimental Area in CERN.

The aim of the experiment WA57 was to clarify the status of the enhancement at a mass of 1.25 GeV seen in the reation $\gamma p \rightarrow \omega \pi^0 p$. This enhancement has been suggested as a candidate for the first radial recurrence of the ρ-meson, but may also have been produced by the B(1235) meson.

A detailed spin-parity analysis was performed on the $\omega\pi^0$ data from the experiment and the results are as follows : ---

1) There is little or no 0^- contribution to the enhancement

2) The 1^- component is approximately SCHC across the whole mass range studied, i.e. from 0.9 GeV to 1.8 GeV

3) When the 1^- component is constrained to be SCHC, the dominant contribution to the enhancement has spin-parity 1^+. This 1^+ signal peaks at an $\omega\pi^0$ mass of ~1.25 GeV, with a width of ~200 MeV; the D/S ratio in the peak region is ~0.4.

The 1^+ signal seen in the enhancement is consistent with being the B(1235) meson, and as the 1^- signal shows no resonant structure, the data do not need a $\rho'(1250)$.

In conclusion then, the enhancement has been shown to be dominantly a 1^+ signal, consistent with the B(1235) meson, with a 20% 1^- SCHC background which exhibits no resonance structure. The t dependance seen in the data suggests a diffractive production for the enhancement.

Chapter 1

PHOTOPRODUCTION AND VECTOR MESONS.

1.1 INTRODUCTION.

For many years after the photon had been proposed as the quantum of the electromagnetic field, the idea of a structureless photon was used with great success in atomic physics. The accuracy with which various phenomena such as the intensities of spectral lines and the photoelectric effect could be predicted, gave no indication that there may be some 'internal structure' to the photon. With the discovery of the process,

$$\gamma \rightarrow e^+e^- \qquad \ldots\ldots (1.1)$$

in the presence of a nuclear Coulomb field, came the first indication that there is some structure associated with the quantum of the electromagnetic field, for although not usually interpreted in this way, pair creation can be seen as evidence that the photon has a large e^+e^- component in its structure. The discovery of the other strong contributions to the photon's structure had to await the advent of high energy photon beams. With these beams, it was experimentally observed that the photon - nucleon interaction showed a number of similarities to the hadron - nucleon interaction. The total γN cross-section for instance, was found to be similar in energy dependance to the average of the π^+N and π^-N cross-sections, although of the order of 200 times smaller in size. These similarities were understood as

arising from the existence of a hadronic component in the photon's structure which manifests itself in the photoproduction of hadronic final states. In these processes, the photon is seen as undergoing a transition to a virtual hadronic state which subsequently scatters elastically from the target nucleon to become real.

As will be seen, the interpretation of photoproduction in terms of some structure internal to the photon provides only a partial description of what occurs. In any complete treatment of the process, it is probably impossible to divorce thoughts on the photon's structure from considerations of the structure of the target nucleon; the success with which this can be done depends heavily on the energy range being investigated.

In this chapter, we will briefly present some of the main ideas involved in the development of the theory of photoproduction and of vector mesons, along with, where appropriate, a review of the experimental evidence which led to these ideas. In Section 1.2, we introduce the Vector Dominance Model, whilst in Section 1.3 we discuss the application of Regge Theory to photoproduction. Section 1.4 introduces the parton model interpretation of vector mesons and finally, in Section 1.5, we briefly present the experimental evidence concerning the high mass vector meson states.

1.2 VECTOR MESONS AND THE VECTOR DOMINANCE MODEL

The hadronic states which might contribute to the structure of the photon have restrictions placed on them by the requirement that they have the same quantum numbers as the photon, i.e. $J^{PC} = 1^{--}$, with Q = B = S = 0, and I = 0,1. These are in fact the quantum numbers of the neutral, non-strange vector mesons, and in this section, we briefly outline the developments leading to the discovery of these states, their photoproduction, and a description, the Vector Dominance Model (VDM), of the hadronic interaction of the photon in terms of these states.

In the late 1950s, the first suggestions that a number of vector mesons may be required arose in connection with difficulties associated with the nucleon electromagnetic form factors. The extended charge structure of the proton, which had been observed in electron scattering experiments, was interpreted as a 'cloud' of positive pions, enveloping a nucleon core. This led, via symmetry considerations, to the expectation that some such structure i.e. a negative pion 'cloud', existed around the neutron. This structure was not however observed experimentally, and an alternative approach to the observed anomalies was sought. A mechanism proposed by Nambu[1-1], attempted to resolve these difficulties. In this model, the electron - nucleon scattering process was thought to proceed via the exchange of an isoscalar state with spin 1, enhancing the effects of the pion cloud in the proton case, whilst cancelling out the effects in the neutron case. The experimental evidence available on eN scattering was detailed enough to allow Frazer and Fulco[1-2] to predict some of the properties of this state, viz. that is was in fact an isovector $J = 1$ $\pi\pi$ resonance with a mass of approximately 550 MeV. In the same year, 1960, Sakurai[1-3], working with the general gauge field theory of Yang and Mills, predicted the existence of a family of such vector mesons.

The first experimental evidence for the predicted $\pi\pi$ resonance, dubbed the 'ρ' meson, came in 1960 from the πN interactions

$$\pi^- p \longrightarrow \pi^- \pi^0 p$$

$$\pi^- p \longrightarrow \pi^- \pi^+ n \qquad \ldots\ldots (1.2)$$

studied by Erwin at al.[1-4], where the ρ was observed in both charged and neutral channels. A few months later the first of the isoscalar vector mesons predicted by Sakurai, the 'ω' meson, was discovered by Maglic et al.[1-5], in the neutral three pion combinations resulting from the reaction

$$\bar{p} p \longrightarrow \pi^+ \pi^- \pi^+ \pi^- \pi^0 \qquad \ldots\ldots (1.3)$$

Then in 1962, shortly after the discovery of the ω meson, the second isoscalar meson predicted by Sakurai, named the 'φ' meson, was seen in an experiment by Bertanza et al.[1-6], as a two kaon resonance in the reactions

$$K^- p \longrightarrow \Lambda K^0 \bar{K}^0$$

$$K^- p \longrightarrow \Lambda K^- K^+ \qquad \ldots\ldots (1.4)$$

A photoproduction experiment, carried out by Macleod et al.[1-7] in 1961 provided the first evidence for the photoproduction of ρ mesons. Experimental evidence for the photoproduction of the ω and φ mesons did not however become available for some years, and it was not until the late 1960s that it was shown that these states could be photoproduced.

In the early 1960s then, there were three non-strange mesons, as predicted by Sakurai, an isovector and two isoscalars. In

1961 it was suggested by Gell-Mann and Zacharaisen[1-8] that the two vector mesons known at the time, the ρ and the ω, coupled to the same current as the electromagnetic field, and that this could lead to a direct photon - vector meson coupling. This idea, that the photon could couple directly to hadronic states was extended to include the φ meson, and the postulate that the photon's hadronic interactions are mediated by the ρ,ω and φ mesons, forms the core of the Vector Dominance Model of high energy photon - nucleon interactions.

Within the framework of VDM, the photon, in its hadronic interactions, acts as a superposition of the virtual vector meson states, i.e. ρ,ω and φ. The electromagnetic current, j^{em}_{μ}, is related to the fields ρ_i, ω_i, ϕ_i, of the vector mesons, via the Field Current Identity (FCI) ;--

$$J^{em}_{\mu} = \frac{m_\rho^2}{f_\rho}\rho_i + \frac{m_\omega^2}{f_\omega}\omega_i + \frac{m_\phi^2}{f_\phi}\phi_i \qquad \ldots\ldots (1.5)$$

where m_ρ etc. are the vector meson masses, and the constants, f_ρ, etc. are proportional to the direct photon - vector meson coupling.

In 1964, using a coupling scheme which is equivalent to VDM, Berman and Drell[1-9] showed, in a comparison of various models for vector meson photoproduction, that the process should be diffractive, sharply peaked in the forward direction and with a cross-section roughly independent of energy at high energies. In the following year, the diffractive nature of the γN cross-section was confirmed experimentally by Lanzarotti et al.[1-10]. In 1966, Ross and Stodolsky[1-11] and Freund[1-12] used VDM to establish a connection between the forward cross-sections for the processes of vector meson photoproduction and vector meson - nucleon scattering, viz.

$$\left(\frac{d\sigma}{dt}\right)^{t=0}_{\gamma p \to v p} = \frac{e^2}{f_v^2}\left(\frac{d\sigma}{dt}\right)^{t=0}_{v p \to v p} \qquad \ldots\ldots (1.6)$$

Using the Optical Theorem, this leads to the following equation,

$$\left(\frac{d\sigma}{dt}\right)^{t=0}_{\gamma p \to v p} = \frac{\alpha}{16\pi} \cdot \frac{4\pi}{f_v^2}(1+\beta^2)\,\sigma^2_{tot}(vN) \qquad \ldots\ldots (1.7)$$

where β is the ratio of the real to imaginary parts of the vN scattering amplitude, and $\sigma_{tot}(vN)$ is the total cross-section for vector meson - nucleon scattering. Thus a knowledge of $\sigma_{tot}(vN)$, obtained from experiments on the coherent production of vector mesons from nuclei, makes it possible to calculate the coupling parameters, f_ρ, etc.. This is important due to the fact that reactions such as $e^+e^- \to \pi^+\pi^-$, which are mediated by a virtual photon, allow the calculation of the f_ρ parameters, starting from premises other than VDM. The values for the f_ρ coupling parameters calculated from the e^+e^- annihilation experiments are in good agreement with those calculated from VDM, suggesting that the same process i.e. direct photon - vector meson coupling, occurs in both cases.

Other tests of VDM are a) its predictions in comparing the scattering amplitudes for the processes i) $\gamma p \to \gamma p$, i.e. Compton scattering, and ii) $\gamma p \to v p$, vector meson photoproduction. b) its ability to explain the value of the total γN cross-section. In both these tests, VDM, in the form described above, is not completely successful, the experimentally observed total γN cross-section for instance being about 20% higher than the VDM prediction. In 1969, in an inelastic electron scattering experiment, futher difficulties for VDM emerged

when it was found that the inelastic eN scattering cross-section was surprisingly large, too large to be accounted for within the framework of VDM as it then was. Here we have the first indications that our attempts to treat the photon's structure as something distinct from the structure of the target nucleon and the dynamics of the process, are too simple, and need to be refined.

In the same year, e^+e^- colliding beam experiments showed that the hadronic structure of the photon was more complicated than a superposition of the three low mass vector mesons, with the discovery of the $\rho'(1600)$ and its confirmation as a vector meson. With the discovery of this high mass state, and the continuum of hadronic states suggested by the e^+e^- experiments, the predictive power of the FCI diminished, although attempts were made by Gribov[1-13], and Brodsky[1-14], amongst others, to develop more general models along the same lines as VDM, these Generalised Vector Dominance Models (GVDM) incorporating further terms for the high mass states.

In conclusion then, models which treat the photon's hadronic interactions as occuring through the mediation of a number of virtual vector mesons, are able to explain some aspects of photoproduction. However, at high energies, in experiments in which virtual photons are involved, the structure of the target nucleon makes its presence felt via the direct coupling of the photon to the internal components of the nucleon. The need, at these energies, to introduce higher mass states, and possibly a continuum, as part of the photon's 'internal' structure, make a GVDM approach to the interpretation of the photon's hadronic interactions less attractive.

1.3 VECTOR MESONS AND REGGE THEORY

After entering the realm of hadronic physics via the photon's direct coupling to the vector mesons, the photoproduction process becomes another example of a high energy two body scattering reaction. In this case, the virtual vector meson scatters either elastically or inelastically from the proton to become real, and the usual framework within which such reactions are described is Regge Theory and its extensions. This section is devoted to a brief description of this theory and its relevance to the process of high energy diffractive scattering.

High energy hadron-hadron scattering is interpreted as taking place via the exchange in the t-channel of a virtual elementary particle which effectively transfers the quantum numbers of its real counterpart. This picture, the One Particle Exchange Model, was successful in explaining some, though not all, of the features of high energy scattering processes. One of the main failures of the model was its prediction of a reaction amplitude which contained a factor of s^j, where s is the centre of mass energy, and j is the spin of the exchanged particle. At high energies and with high spins, this amplitude, and hence the cross section rises steeply with energy, contrary to experimental evidence ; indeed as s is increased, it is found that the cross-section for high energy scattering processes becomes almost constant. The work done by Regge in non-relativistic potential theory, and applied to the high energy regime by Chew, allows a solution to this problem.

In Regge Theory, the partial wave amplitude T, is expressed as an analytic function of a complex variable α, which is interpreted as a complex angular momentum, and the centre of mass energy, s. This function $T(\alpha,s)$ is constructed in such a way that for

the situations in which α is 'almost' real, i.e. when $Im(\alpha) << 1.0$, and $Re(\alpha) = l$, where l is an integer, the amplitude corresponds to the usual $T_l(s)$ scattering amplitude for the partial wave of angular momentum l. In these situations, it can be shown that the simple poles of the function $T(\alpha,s)$, called 'Regge poles', correspond to s-channel resonances. With increasing s, the position of each pole in the complex α plane may change, its path being described as a 'Regge trajectory', and for some of these trajectories, (the shape of the trajectory being governed by the details of the scattering potential) a series of resonances can be predicted, each with the same quantum numbers apart from the spin. In 1960, Chew and Frautschi showed that the hadrons can be collected into such groups, lending further weight to the ideas contained in Regge Theory. They also showed that if the squares of the masses of the particles on a particular trajectory were plotted against the spin of the particle, the resulting plot showed that the Regge trajectories were almost straight lines. This relation between the hadrons on a trajectory is not a consequence of Regge Theory, but there are now some parton models which predict just such a quadratic dependance for the mass versus spin between hadrons with the same quantum numbers. The Regge Theory approach to high energy interactions, i.e. those in which the centre of mass energy is of the order of 5 GeV or more, involves the t-channel exchange of Regge trajectories, whilst the dominant process at low energies is the formation of s-channel resonances. These two regimes, and their particular ways of looking at the underlying dynamics, were connected by Veneziano via the concept of 'duality'. In 1968, Veneziano[1-15] showed that the scattering amplitude could be expressed as a summation over poles in either the s-channel or the t-channel, the two descriptions being in some ways equivalent. A consequence of this

expansion of the amplitude was that each pole appeared to have associated with it a family of 'daughter' trajectories, each daughter having a spin which differed from that of the 'parent' trajectory by a negative integer. This in turn led to the prediction of higher mass states which had not at that time been seen experimentally. The relation between the mass of the parent, m_p and that of the daughters, m_d, is given by

$$m_d^2 = m_\rho^2 + n/\alpha \qquad \ldots\ldots (1.8)$$

where α is the Chew-Frautschi slope of the trajectory (which is approximately 1.0). This leads to the prediction of daughters at masses of approximately 1.25 GeV, 1.65 GeV, etc., for the ρ trajectory, and these states could be identified as ρ' recurrences, differing from the $\rho(770)$ only in the mass of the state.

Diffractive high energy scattering is characterised by being peripheral, i.e. predominantly with a low four-momentum transfer squared to the target with a cross section which is roughly independent of energy and with an exchange in the t-channel which is equivalent to the exchange of the quantum numbers of the vacuum. The exchanged 'state' in this case, called the Pomeron (after its originator, Pomeranchuk), does not correspond to any physically realised particle ; despite this, the Regge theory description is a usefull tool in describing high energy diffractive scattering processes, of which photoproduction can be considered a part.

1.4 THE QUARK-PARTON MODEL AND VECTOR MESONS

Although Regge Theory is successful in describing some aspects of the data for high energy diffractive scattering, and does to some extent provide a framework for the classification of hadronic states, the basis for such a classification is unclear as there is no evident underlying dynamical structure. An alternative scheme for classifying the hadrons and for describing their interactions is provided by the Quark-Parton Model, proposed independently by Gell-Mann[1-16] and Ne'eman[1-17]. This section will briefly describe how the vector mesons which form the core of any description of the photon's hadronic interactions, are accomodated into this model.

Within the group theoretical framework of the Quark Model, the mesons arise as representations of the group formed by the direct product of the basis group with its conjugate. In a 3 Quark Model, i.e. in which the three basis states are the quarks u, d and s, the representations found in Nature are the octet and the singlet, i.e. $3 \otimes 3 = 8 \oplus 1$, which together combine to form the low mass meson nonets. The mesons are usually classed as a nonet rather than a separate octet and singlet because it seems that the singlet and the 8th component of the octet mix to form the physically observed meson states. The baryons are incorporated into the Parton Models as representations of the group formed by the direct product $3 \otimes 3 \otimes 3$, and indeed no other representations seem to be found in nature.

The classification scheme illustrated above is very successful in grouping the hadrons, both baryons and mesons, into multiplets, but the basis states, the quarks, have not as yet been seen free in Nature. Deep inelastic scattering experiments in which leptons are scattered from protons, have yielded evidence for some pointlike

structure within the protons[1-18]. The evidence for the number of scattering centres suggests that there are three, and there is evidence that these scattering centres are spin 1/2 fermions. By identifying these nucleon constituents with the group theoretical basis of the Parton Model, the quarks, the known hadrons can all be interpreted as either bound states of a quark antiquark pair (the mesons) or as a bound state of three quarks (the baryons). The spin of the quarks allows the pseudo-scalar and vector mesons to be distinguished. The former correspond to the case where the quark spins (the quarks being in a relative s-wave), are antiparallel, whilst in the vector meson states, the quark spins are parallel. All the low mass mesons can be interpreted in such a scheme where there are 3 basis states, as described above, corresponding to u d and s quarks. With the discovery of the J/Ψ, a fourth, c or charmed quark was found to be necessary ; recently a fifth quark, the b or bottom quark, has been found, and a sixth, t or top quark is also being suggested.

The dynamics of the quark-antiquark system are governed by some potential, and within this potential, the possibility of there being radially excited states exists. This is how the higher mass vector mesons are interpreted, and if the form of the potential is known, the mass of these states can be predicted, or alternatively, a knowledge of the mass of the higher mass mesons will yield some indications as to the form of the quark-antiquark potential. Much work has been done on fitting the known mesons into such potential models, with some success. De Rujula, Georgi and Glashow[1-19] have used a linear confining potential to predict hadronic masses close to those observed, whilst Gunion and Willey[1-20] have used such a potential model to study the possibility of there being radial occurrences of the low mass vector mesons, the ρ ω and ϕ. The mass scale for these models, whether a

simple harmonic oscillator or a complicated logarithmic plus linear potential is used, is set by the mass spacing between the ground state and the first excited state. The identification of these first radial occurences provides a simple way in which the theory can be tested by experiment. In particular, the first radial occurence of the ρ is important, as there are conflicting theoretical views about whether it should be at a mass of of 1.25 GeV, or a mass of 1.6 GeV. The work done by Gunion and Willey suggests that the first radial occurence of the ρ should not be identified as the ρ'(1600), as this leads to an inaccurate representaion of the data, while the work done by De Rujula et al. has been extended by Barbieri et al.[1-21] and this too suggests the existence of a ρ' state at a mass of approximately 1.25 GeV. Using a harmonic oscillator potential Graham and O'Donnell[1-22] have been able to predict hadronic masses quite accurately, and in this work, the ρ'(1600) emerges as the candidate for the first recurrence of the ρ-meson. Bradley[1-23] working with a long range linear confining potential and a short range one-gluon exchange potential predicts a series of ρ' states at 1.25, 1.57 and 1.77 GeV; he also predicts a family of ω' states with similar masses to the ρ's. A candidate for the 1.6 GeV state already exists in the well established ρ'(1600), but there is some evidence for a ρ'(1250), although the evidence is not strong. The ρ'(1600) was first seen in a photoproduction experiment in 1969, as an enhancement in both the 2 charged π and the 4 charged π final states. It has since been seen in e^+e^- annihilation experiments, and also in the final state $\pi^+\pi^-\pi^0\pi^0$. A number of spin parity analyses have been done on the ρ'(1600), and it is well established as a vector meson, with $J^{PC} = 1^{--}$ The contender for the low mass state, at 1.25 GeV has been seen in a number of photoproduction experiments, in the channel $\gamma p \rightarrow \omega\pi^0$, and some evidence also exists from e^+e^- experiments for an

enhancement at this mass. In each case however, the statistics collected have not been enough to do a complete spin parity analysis of the $\omega\pi^0$ final state, and the possibility remains that the observed enhancement is due to the B(1235), which has $J^P = 1^+$.

The existance of radial occurrences of the ρ's low mass companions, the ω and ϕ, are also expected, and there is some evidence that these have been seen, both from photoproduction experiments, and from e^+e^- annihilation experiments. As yet, none of the evidence is very strong, but there is the suggestion that there are high mass companions to the $\rho'(1600)$, corresponding to the ω' and the ϕ', but the experimental situation is complicated due to the possibility that these states are very broad, and overlap considerably. The experiment WA4[1-24,1-25,1-26] has reported evidence for both ω' and ϕ' states. There is further evidence for the existence of an ω' state from e^+e^- annihilation experiments done by the DCI/DM1 group[1-27] The main objective of the CERN experiment WA57 was to determine the spin and parity of the 1.25 GeV enhancement seen in the reaction $\gamma p \rightarrow \omega\pi^0 p$ and to identify it either with the B(1235) meson, or with a possible radial recurrence of the ρ-meson. The work presented in this Thesis is a double-moments spin-parity analysis of the data from the reaction $\gamma p \rightarrow \omega\pi^0 p$, from WA57.

References

1-1 Nambu
Phys. Rev. Vol. 106 (1366) 1957

1-2 Fraser and Fulco
Phys. Rev. Vol. 117 (1609) 1960
Phys. Rev. Lett. Vol. 2 (365) 1959

1-3 Sakurai
Ann. Phys. Vol. 11 (1) 1960

1-4 Erwin et al.
Phys. Rev. Lett. Vol. 6 (628) 1961

1-5 Maglic et al.
Phys. Rev. Lett. Vol. 7 (178) 1961

1-6 Bertanza et al.
Phys. Rev. Lett. Vol. 9 (180) 1962

1-7 MacLeod et al.
Phys. Rev. Lett. Vol. 7 (383) 1961

1-8 Gell-Mann and Zacharaiesen
Phys. Rev. Vol. 124 (953) 1961

1-9 Berman and Drell
Phys. Rev. Vol. 133 (791) 1964B

1-10 Lanzarotti et al.
Phys. Rev. Vol. 166 (1365) 1968

1-11 Ross and Stodolsky
Phys. Rev. Vol. 149 (1172) 1966A
Phys. Rev. Lett. Vol. 17 (563) 1699B

1-12 Freund
Nuov. Cim. Vol. A44 (411) 1966

1-13 Gribov
Sov. Jour. Phys. JETP. Vol. 30 (709) 1970

1-14 Brodsky and Pumplin
Phys. Rev. Vol. 182 (1794) 1969

1-15 Veneziano
Nuovo Cimento Vol. 57A (190) 1968

1-16 Gell-Mann
Phys. Lett. Vol. 8 (214) 1964

1-17 Ne'emen
Nuc. Phys. Vol. 26 (222) 1961

1-18 Nachtmann
1977 Int. Symp. on Lepton and Photon
Interactions at High Energies

1-19 De Rujula et al.
Phys. Rev. Vol. D12 (147) 1975

1-20 Gunion and Willey
Phys. Rev. Vol. D12 (174) 1975

1-21 Barbieri et al.
Nuc. Phys. B Vol. 105 (125) 1976

1-22 Graham and O'Donnell
Phys. Rev. Vol. D19 (284) 1979

1-23 Bradley
Journal of Phys. Vol. G4 (1517) 1978

1-24 Aston et al.
Nuc. Phys. B Vol. 174 (269) 1980

1-25 Aston et al.
Nuc. Phys. B Vol. 174 (269) 1980

1-26 Aston et al.
Phys. Lett. B Vol. 92 (219) 1980

1-27 Delcourt et al.
1981 Int. Symp. on Lepton and Photon Phys.

Chapter II

THE PHOTON BEAM

2.1 INTRODUCTION

The experiment WA57 used a high energy tagged photon beam, with photons in the energy range 20 to 70 GeV, derived from the bremsstrahlung of an electron beam, to study the photoproduction of vector meson states. The energy resolution of the tagging system allowed the determination of the energy of the radiated photon to an accuracy of approximately 200 MeV, whilst its normal spatial resolution was sufficient to allow the calculation of the photon polarisation. The method used to produce the photon beam, i.e. coherent bremsstrahlung from a silicon crystal, yielded a useful degree of linear polarisation ; the maximum polarisation produced was approximately 60% whilst the mean photon polarisation was approximately 30%. This polarisation was calculated on an event by event basis, and could be used in analyses to determine the naturality of the exchange in photoproduction processes.

The purpose of this chapter is to describe the production and characteristics of the tagged photon beam, including the polarisation. A more complete description of the E-Gamma Collaboration tagging system can be found in Aston et al. [2-1]

2.2 DERIVATION OF THE ELECTRON BEAM

The first stage in the formation of the electron beam involved the extraction of 240 GeV protons from the SPS and the transport of these protons into the West Experimental Area. In the West Area, the proton beam was split into three to serve three fixed targets, T1, T2 and T3. The target T3 consisted of 40 cm. of beryllium, and it was from this target that the electron beam E1A was derived.

Charged products from the proton interactions in the beryllium target were swept out of the beam by a dipole magnet immediately downstream of it, whilst photons from the decay of neutral pions hit a secondary target of approximately half of a radiation length of lead; this target was immediately downstream of the dipole magnet. The positrons from the pairs produced in the lead were swept from the beamline, leaving the electrons to form the E1A beam. The electrons were then led into the photon tagging system via a series of bending magnets and collimators which selected the required electron momentum of 81 GeV, with a $\Delta p/p$ of approximately 2%. Figure 2.1 shows the formation of the E1A beamline, and Table 2.1 shows the beamline characteristics.

The beam was focussed on the centre of the hydrogen target in the Omega-Prime Spectrometer, and the beamline optics were monitored online during data-taking using the programme BMPHAS, which ran on one of the user computers stationed at the Omega-Prime Spectrometer. The layout of the West Area beamlines is shown in Figure 2.2.

2.3 THE TAGGING SYSTEM

The physical principles of the tagging system were simple, invoking nothing more than the conservation of energy and momentum at the tagging target. The procedure involved measuring the primary electron momentum, (in regions 'A_t' and 'B_t'), and the scattered electron momentum, (in region 'C_t'), the difference giving the momentum of the radiated photon. A plan of the tagging system regions A_t and B_t is given in Figure 2.3. Thus, a description of the tagging system falls naturally into three parts, regions A_t and B_t ; the tagging target ; region C_t.

Tagging system regions A_t and B_t each contained 16 multi-wire proportional chambers with 1 mm. wire spacing and two scintillator hodoscopes. The wire chambers were used in determining the incident electron trajectory, whilst the scintillator detectors were used to reduce ambiguities in the cases where two electrons entered the tagging system at the same time, by measuring their time of flight through the system. After it had passed through region A_t, the electron underwent a horizontal bend of approximately 68 mrad. which deflected it into region B_t, where once again, its direction was determined. A knowledge of the bending field and the angle through which the electron was deflected then allowed the calculation of the electron momentum. After regions A_t and B_t, a further deflection of approximately 10 mrad. brought the electron onto the tagging target, this last deflection serving to clean the beam of any electrons which had radiated in the material in regions A_t and B_t, as well as removing the associated unpolarised photons from the photon beam.

The tagging target itself was a monolithic silicon crystal, 2.2 mm. thick and 75 mm. in diameter. The crystal was mounted on a

goniometer which allowed the crystal to be precisely orientated in space. Coherent bremsstrahlung from a set of crystal planes results in a linearly polarised photon; the degree of polarisation depends crucially on the angle of incidence of the electron on the planes, and thus accurate determination of the orientation of the planes in space is neccessary for the understanding of the polarised beam. The polarised beam is discussed more fully by Bussey at al. [2-2]

Immediately after the tagging target, the scattered electrons were deflected into region C_t, the unscattered electrons being directed onto a beam dump. Region C_t was equipped with multi-wire proportional chambers, scintillator hodoscopes, and an array of lead glass blocks; the plan of region C_t is shown in Figure 2.4. The wire chambers were used in determining the scattered electron momentum whilst one of the hodoscopes was used to define a time origin for the triggers formed on the experiment.

2.4 CHARACTERISTICS OF THE TAGGED PHOTON BEAM

As can be seen from the preceeding section, an accurate determination of the photon momentum is dependent upon there being sufficient information available from all three of the tagging system regions, A_t, B_t and C_t. In the cases where some of the information was missing, there existed methods for approximating the missing information and thus calculating the photon momentum, although the accuracy of the determination was decreased. The quality of the momentum determination was flagged on the final event record, there being four different cases. An explanation of each of these categories is given in Table 2.2, and

the photon energy spectrum for each is shown in Figure 2.5. The data from which these figures are taken were a selection of the events coming from the unbiased pairs trigger which was set up to provide a means of monitoring the beam. The data from this trigger consisted, at the level of approximately 98%, of electromagnetic pairs. It can be seen that the photon energy spectrum for the first and best measured of the classes of tag is not the $1/E_\gamma$ spectrum, that would be expected for an unpolarised bremsstrahlung spectrum, the deviations from this being caused in part by the coherent production mechanism.

In bremsstrahlung from an amorphous radiator, each photon is itself polarised, but the photon beam as a whole will exhibit no net polarisation due to the random alignment of the plane of polarisation of the individual photons. The process of coherent bremsstrahlung from a set of crystal planes however imposes a definite direction on the polarisation plane of the photon, due to the kinematics of the process. In coherent bremsstrahlung, the electron effectively radiates from a set of crystal planes, rather than a single atom, and thus the direction in space of the photon's polarisation plane can be determined by identifying the orientation of the crystal planes from which the electron radiated. The radiated spectrum then consists of two parts, a contribution originating from this coherent process, which is plane polarised, and a contribution from the incoherent process, which is unpolarised. The relative magnitude of these two contributions is dependent upon the incident electron energy and angle. The polarisation for the process is then proportional to the ratio of the coherent part to the total, for each value of the electron energy and angle of incidence. The details of the coherent bremsstrahlung process can be found in Diambrini [2-3] and Timm [2-4]. The probability that the photon will be linearly polarised in this plane can be calculated if E_0,

the incident electron energy, k the energy of the radiated photon, and θ_s, the 'sensitive angle', between the incident electron direction and the radiating planes, are all known.

The energies E_o and k are calculated event by event as explained in the previous section, the direction of the incident electron being determined from the region B_t track information. For the calculation of the polarisation for each photon, all that remains to be measured is the value of θ_s ; the method used to do this is outlined below.

The silicon crystal was mounted on a goniometer which was driven by stepping motors so that the degree of 'tilt' and 'turn' of the crystal in space could be controlled, one discrete step being equivalent to a rotation of 10 μrad.. By plotting the angles of tilt and turn against the intensity of low energy bremsstrahlung photons, the crystal orientations which correspond to a maximum of this intensity could be identified. When the crystal was in an orientation such that the the intensity of the low energy photons was at a maximum, the incident electrons were travelling parallel to the crystal planes, and thus the direction of the crystal planes in space could be found, knowing the direction of the incident electron.

Having determined the orientation of the crystal planes, θ_o, the angle between an 'on axis' electron and the radiating plane, could be chosen so as to maximise the degree of linear polarisation for photons in a particular range of energies. The conflicting aims of producing highly polarised photons, requiring a setting of θ_o at which the intensity of low energy photons was enhanced, and of producing as many high energy photons as possible, entailing a value of θ_o which would produce smaller values for the photon polarisation, were reconciled by choosing a setting for θ_o which would produce an

enhancement in the photon energy spectrum that peaked at approximately 30 GeV.

At the time of the data-taking, this was accomplished by offsetting the crystal by the required value of θ_0, using the goniometer, but this could be done only to a limited degree of precision. The precise value of θ_0 for each of the goniometer settings used (there were four different periods of running conditions of the crystal orientation), was found offline. This was done by studying a subset of events in which the radiating electron had undergone double bremsstrahlung in the crystal, producing a second radiated photon of a fairly low energy. The kinematics of the process are such that the second bremsstrahlung photon travels parallel to the crystal axes. This second photon was detected and the energy measured, and by plotting the probability of detecting a second bremsstrahlung photon as a function of the electron angle, the crystal orientation could be determined from the position of the peak probability. Once the θ_0 position had been found for each period (θ_0 was of the order of 0.5 mrad.), it was incorporated into the polarisation calculation. This calculation was implemented as an interpolation between values stored in a look-up table, this table itself being generated from a theoretical calculation of the coherent bremsstrahlung process. The photon energy spectrum and the corresponding polarisation spectrum for each of the four periods of data-taking are shown in Figures 2.6 and 2.7.

2.5 THE TAG TRIGGERS

We now describe the requirements which had to be fulfilled before a cleanly tagged photon was signalled as entering the Omega-Prime Spectrometer.

Within the tagging system itself there were a number of veto counters which served to veto the tag under certain circumstances. The Radiation Vetoes, lead - scintillator sandwiches, were used to veto events in which the electron had radiated in region B_t. Downstream of the tagging target and upstream of the Omega-Prime spectrometer, there were various veto counters which were used to veto events in which the photon produced on the tagging target had converted somewhere between the tagging target and the aperture of the Omega-Prime magnet. Events in which the electron had undergone double bremsstrahlung in the tagging target were vetoed by a Beam Veto counter, placed in the beamline approximately 10 m. behind the Omega-Prime target. The threshold of this counter was set in such a way that below a certain photon energy, the signal was recorded for use as a correction offline to the tag, and the event was not vetoed.

The Quick Tag trigger, QT, was formed by asking for a signal in both the region C_t hodoscopes and for a beam gate signal, this latter being the signal issued from the SPS during its spill. This trigger, the QT, in conjunction with signals derived from the Omega-Prime spectrometer, was used to form the Loose Trigger, the LT. The final tag trigger, the Real Tag trigger, RT, was formed from the LT, a signal from the region C_t lead glass array, and the requirement that none of the tagging system vetoes had counted. The RT was then incorporated into the event triggers formed at the Intermediate Loose Trigger, the ILT, stage.

References

2-1 D. Aston et al.

Nucl. Inst. & Methods Vol. 197 (278) 1982

2-2 P. Bussey et al.

Nuc. Inst. & Methods Vol. 211 (301) 1983

in Physics Research

2-3 G. Diambrini-Palazzi

Rev. Mod. Phys. Vol. 40 (611) 1968

2-4 U. Timm

Fortschr. Phys. Vol. 17 (767) 1696

Figures And Tables for Chapter 2

Table 2.1 : Parameters for the E1A beam

Parameter	Value
Maximum momentum	80 GeV
Production angle	0^{0}
Angular Acceptance	x' ±1.2 mrad.
	y' ±2.8 mrad.
	$\Delta\Omega$ 10.5 μstr.
Momentum acceptance	±2% $\Delta p/p$
Dispersion at first slit	15.5 mm./%
Beam length	218 m.
Intrinsic Momentum	
resolution	0.1%
Dispersion at 3rd	
horizontal focus	7.1 mm./%
Magnification at Omega	
(horizontal)	1.30
(vertical)	1.67
Beam spill length	2.0 sec.
Proton/pulse on T3	2.0×10^{12}
Electrons/pulse on	
tagging target	1.5×10^{7}
Tagging target length	
(radiation lengths)	5%
Double bremsstrahlung rate	
by tagging target	18%

Table 2.2 : Tag Quality Flag for the Beam

TAG-FLAG = 0 : Single unambiguous track found in regions A_t and B_t of tagging system OR 'C_t-rescue' failures ie. region C_t package cannot work out a scattered electron momentum even by using HC1/HC2/LG crudely. In this case beam momentum set to 0.0

1 : Scattered electron track out of range of polynomial which is used to determine it's momentum

2 : Bad match between regions B_t and C_t

3 : Ambiguity in region A_t/B_t - primary electron momentum set to 80 GeV./c

4 : Scattered electron momentum determined by C_t-rescue (uses HC1/HC2/LG to give a crude momentum)

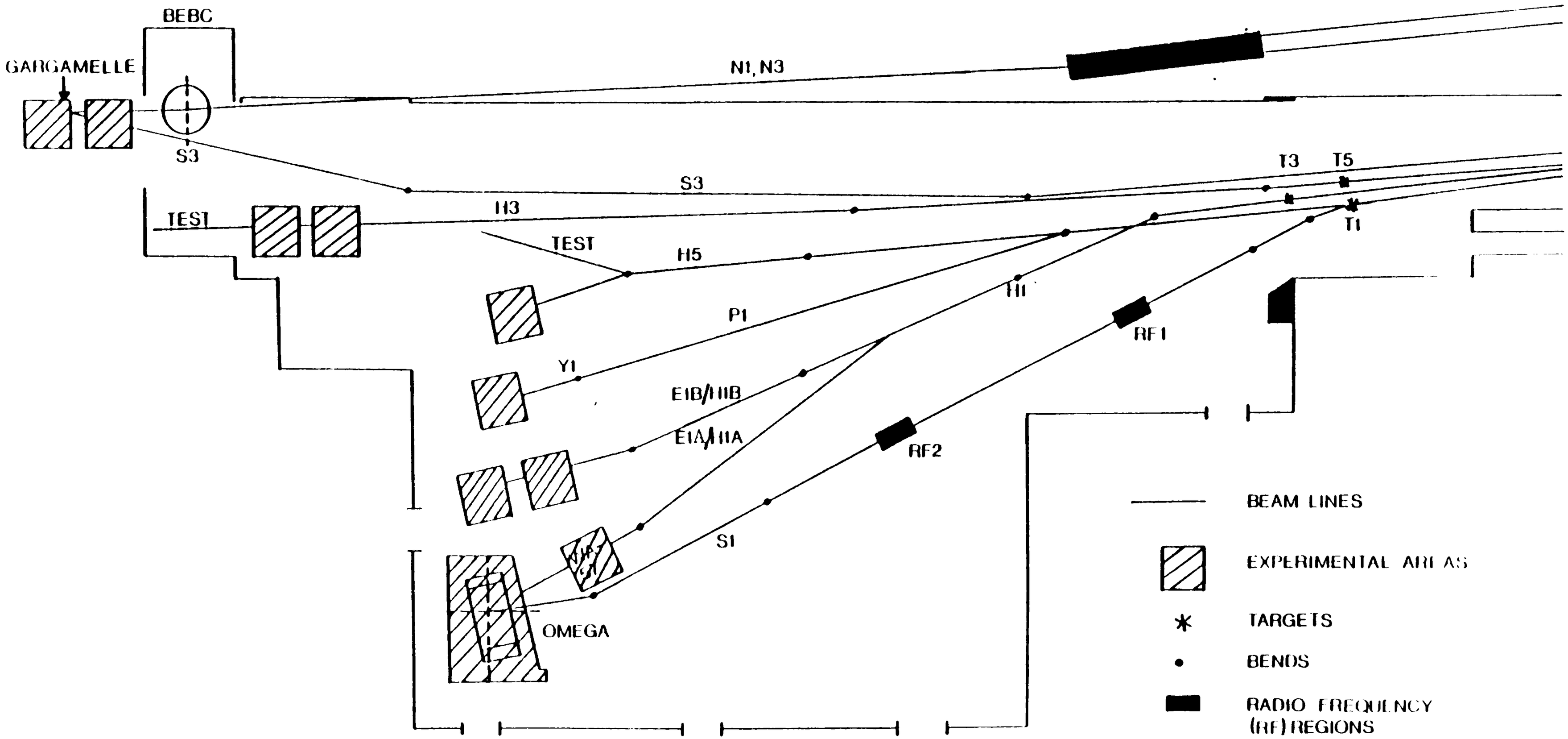
BEBC
GARGAMELLE
N1, N3
S3
T3
T5
S3
TEST
H3
T1
TEST
H5
H1
P1
RF1
Y1
E1B/H1B
E1A/H1A
RF2
S1
OMEGA
BEAM LINES
EXPERIMENTAL AREAS
TARGETS
BENDS
RADIO FREQUENCY (RF) REGIONS

Figure 2.1

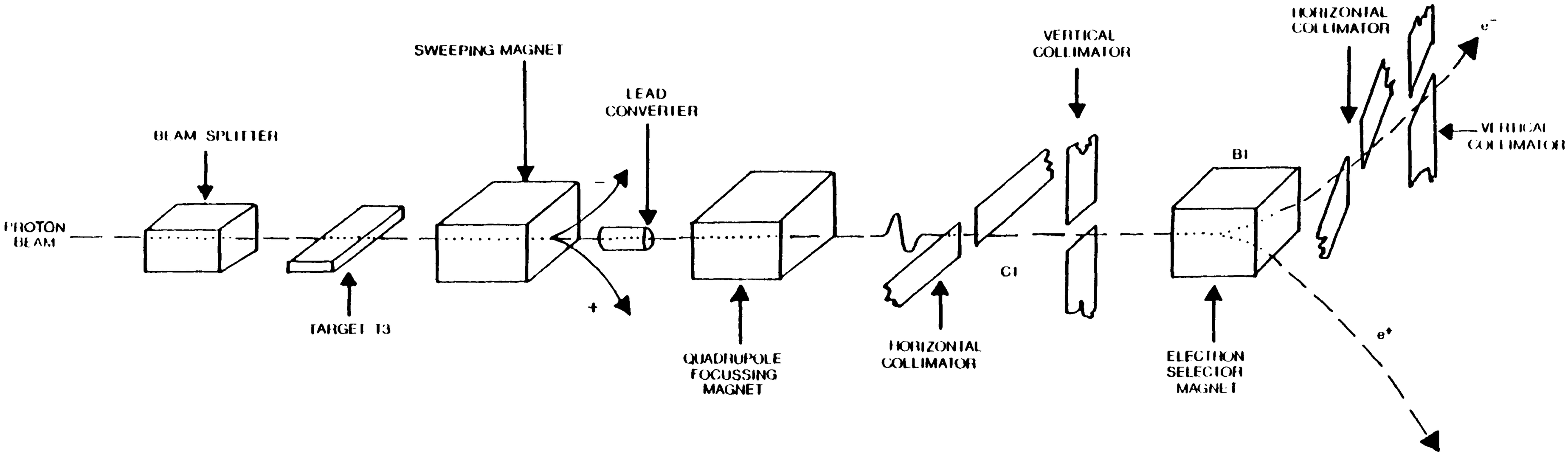
SWEEPING MAGNET
LEAD
CONVERTER
VERTICAL
COLLIMATOR
HORIZONTAL
COLLIMATOR
e⁻
BEAM SPLITTER
B1
VERTICAL
COLLIMATOR
PROTON
BEAM
C1
TARGET T3
QUADRUPOLE
FOCUSSING
MAGNET
HORIZONTAL
COLLIMATOR
ELECTRON
SELECTOR
MAGNET
e⁺

Figure 2.2

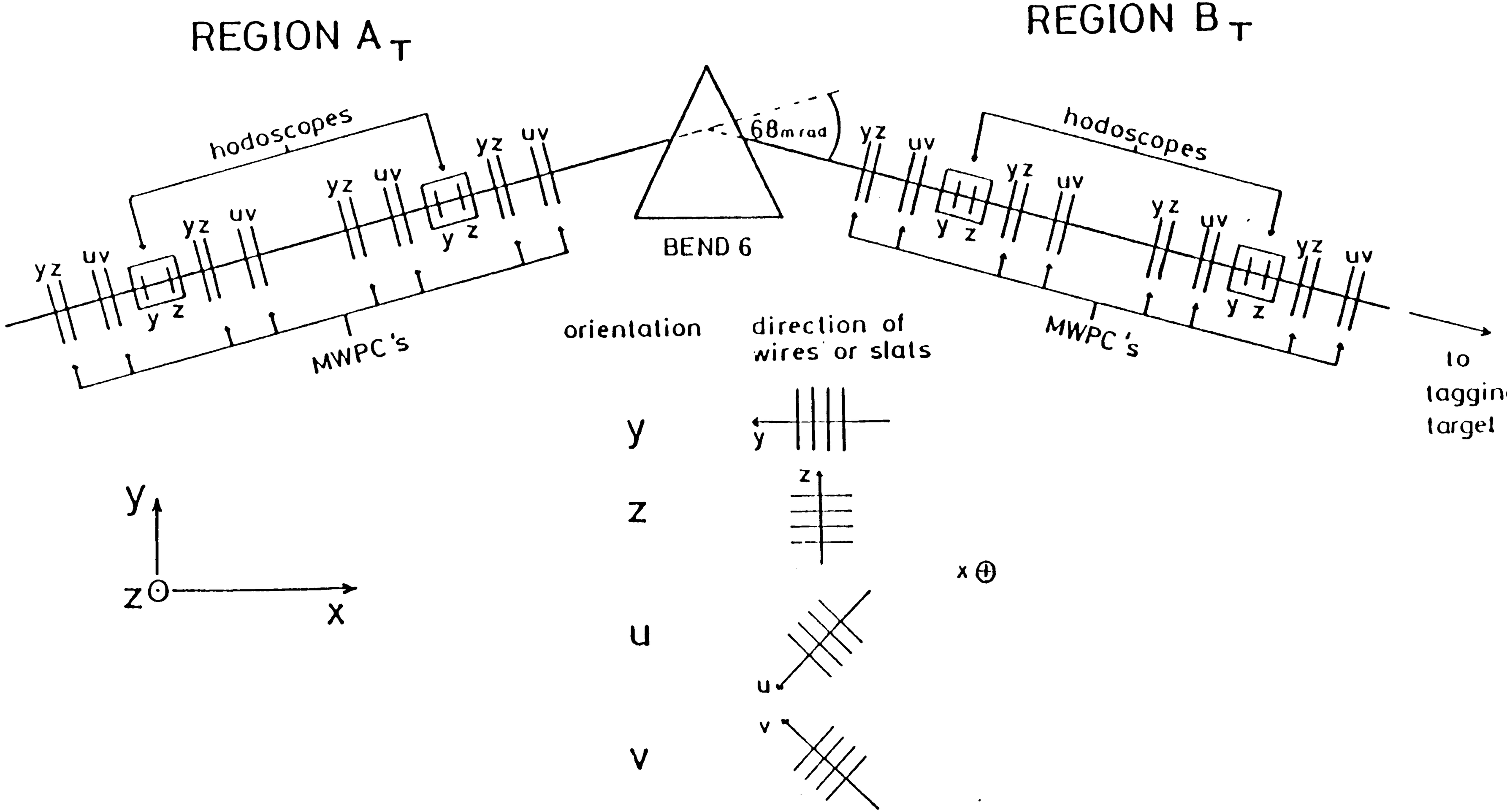
REGION A T
REGION B T
hodoscopes
hodoscopes
yz
uv
68 m rad
BEND 6
MWPC's
MWPC's
orientation
direction of wires or slats
to tagging target
y
z
u
v
x ⊕

Figure 2.3

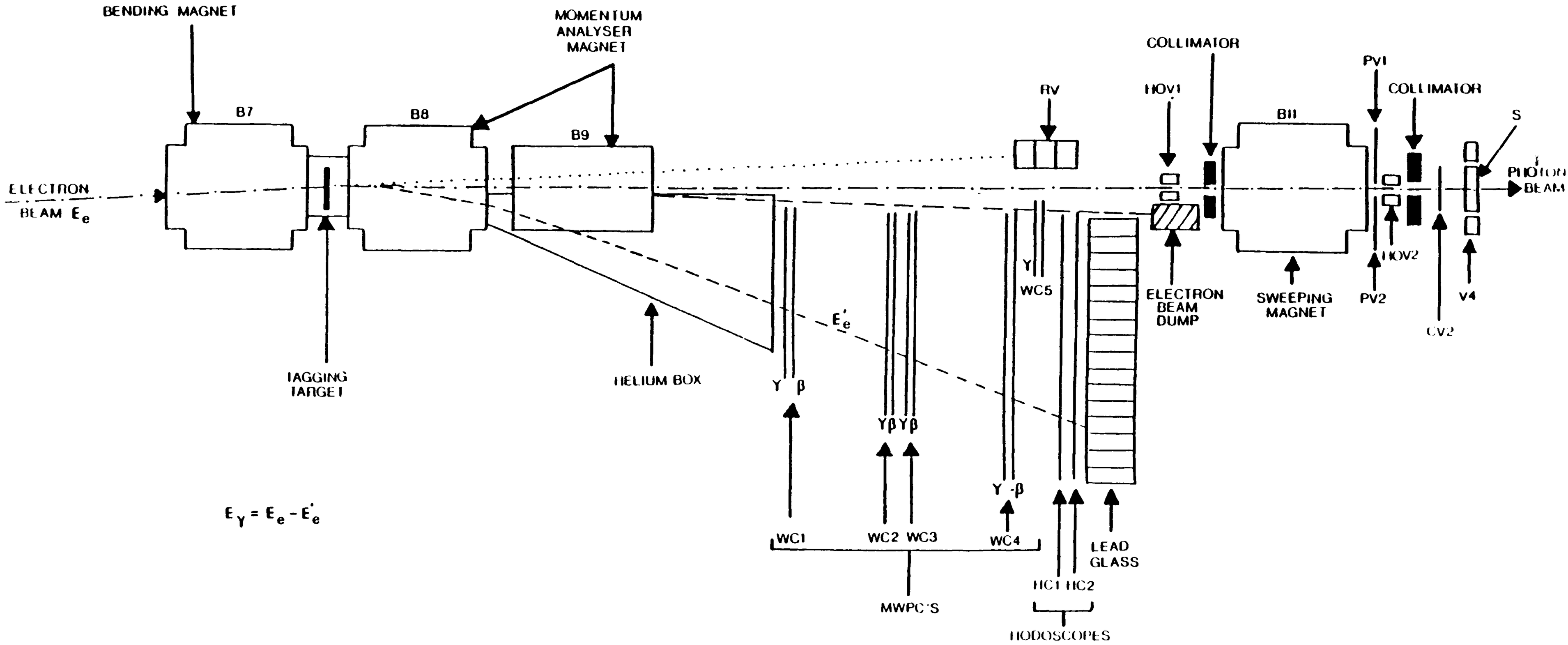
BENDING MAGNET
MOMENTUM ANALYSER MAGNET
B7
B8
B9
RV
COLLIMATOR
HOV1
PV1
COLLIMATOR
B11
S
ELECTRON BEAM E_e
PHOTON BEAM
Y
WC5
ELECTRON BEAM DUMP
SWEEPING MAGNET
HOV2
PV2
V4
CV2
TAGGING TARGET
HELIUM BOX
E'_e
Y β
Yβ Yβ
Y -β
WC1
WC2 WC3
WC4
LEAD GLASS
HC1 HC2
MWPC'S
HODOSCOPES
$E_\gamma = E_e - E'_e$

Figure 2.4

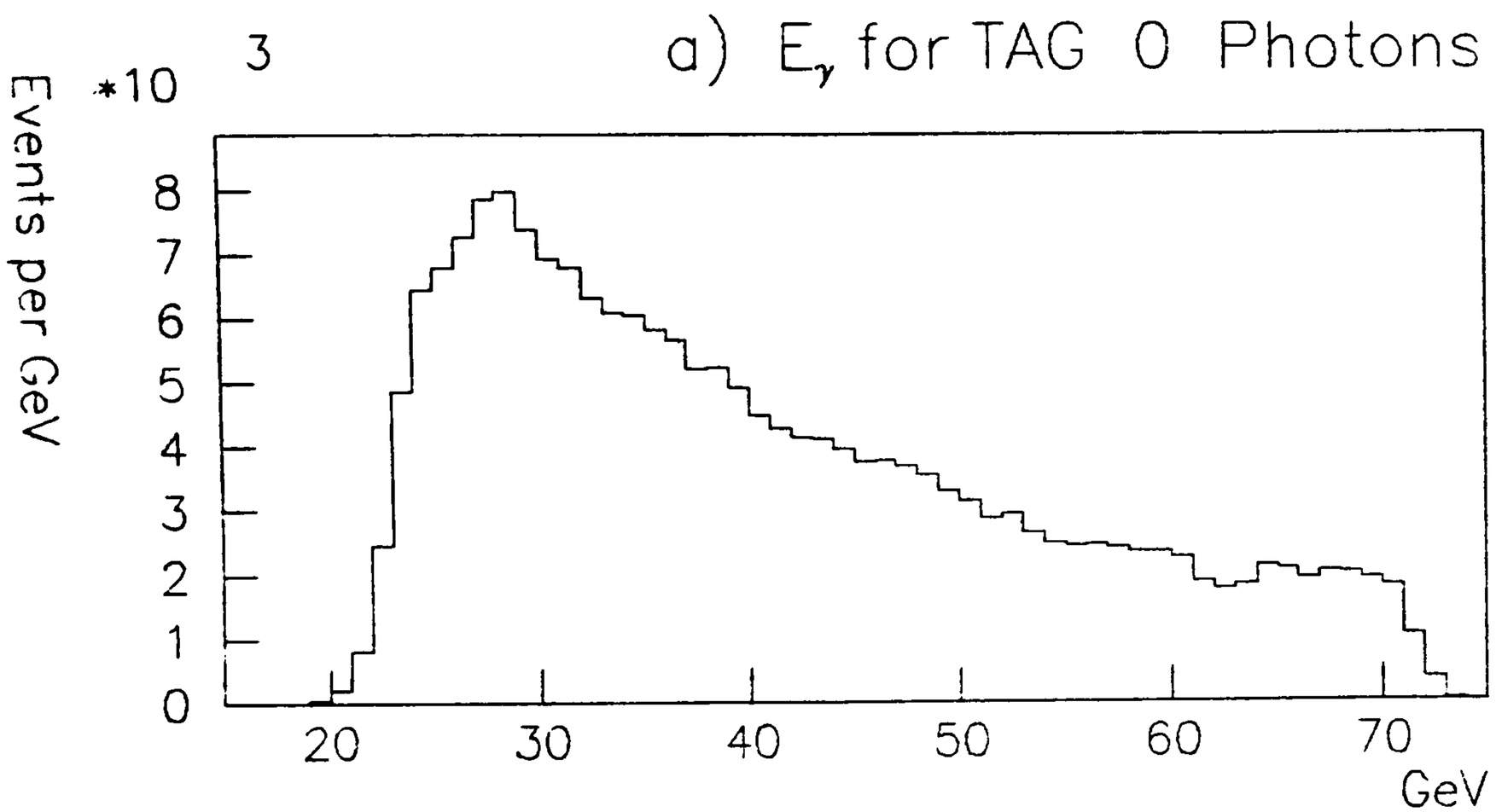
a) E_γ for TAG 0 Photons
3
*10
Events per GeV
0
1
2
3
4
5
6
7
8
20
30
40
50
60
70
GeV

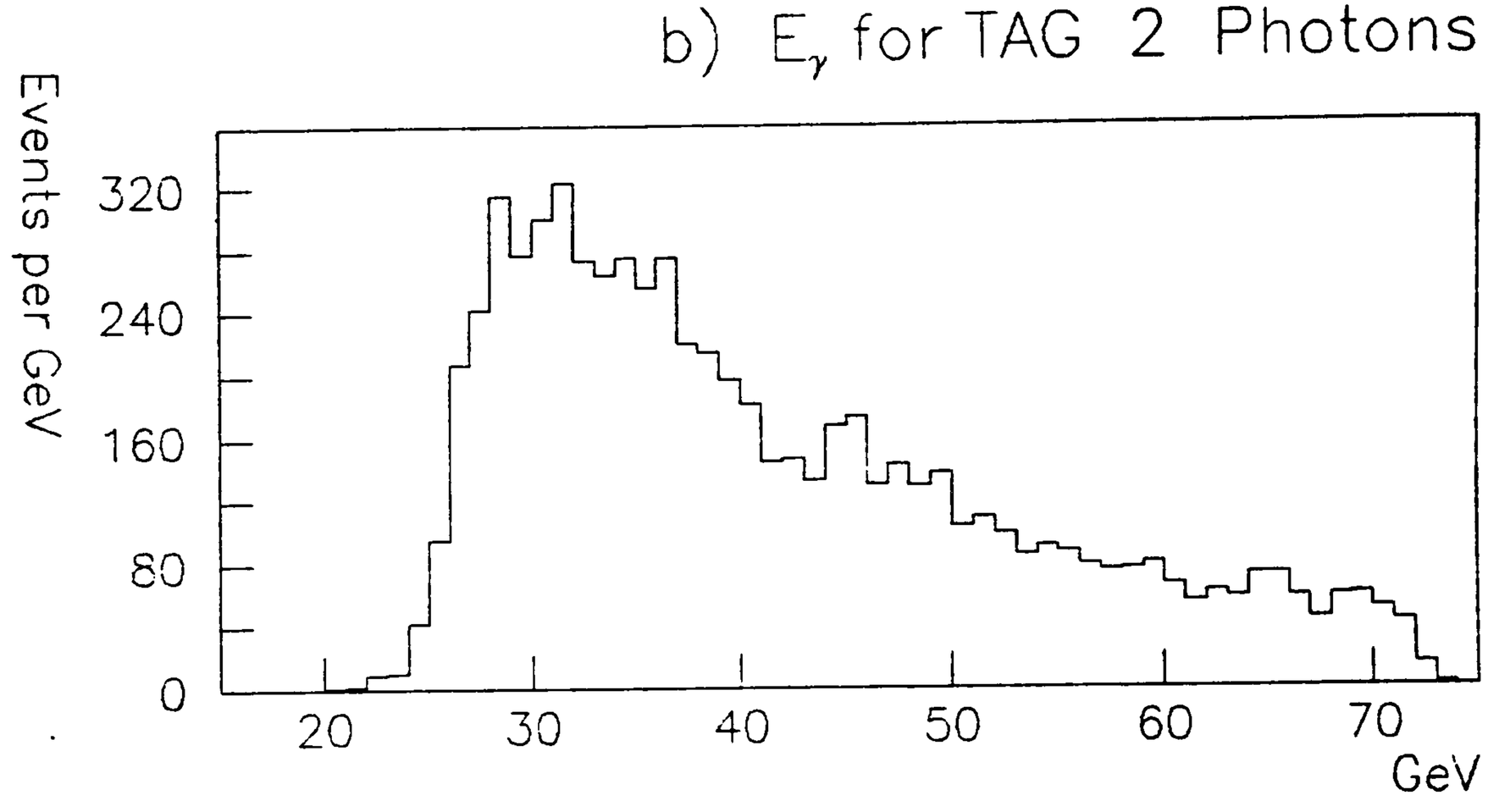
b) E_γ for TAG 2 Photons
Events per GeV
0
80
160
240
320
20
30
40
50
60
70
GeV

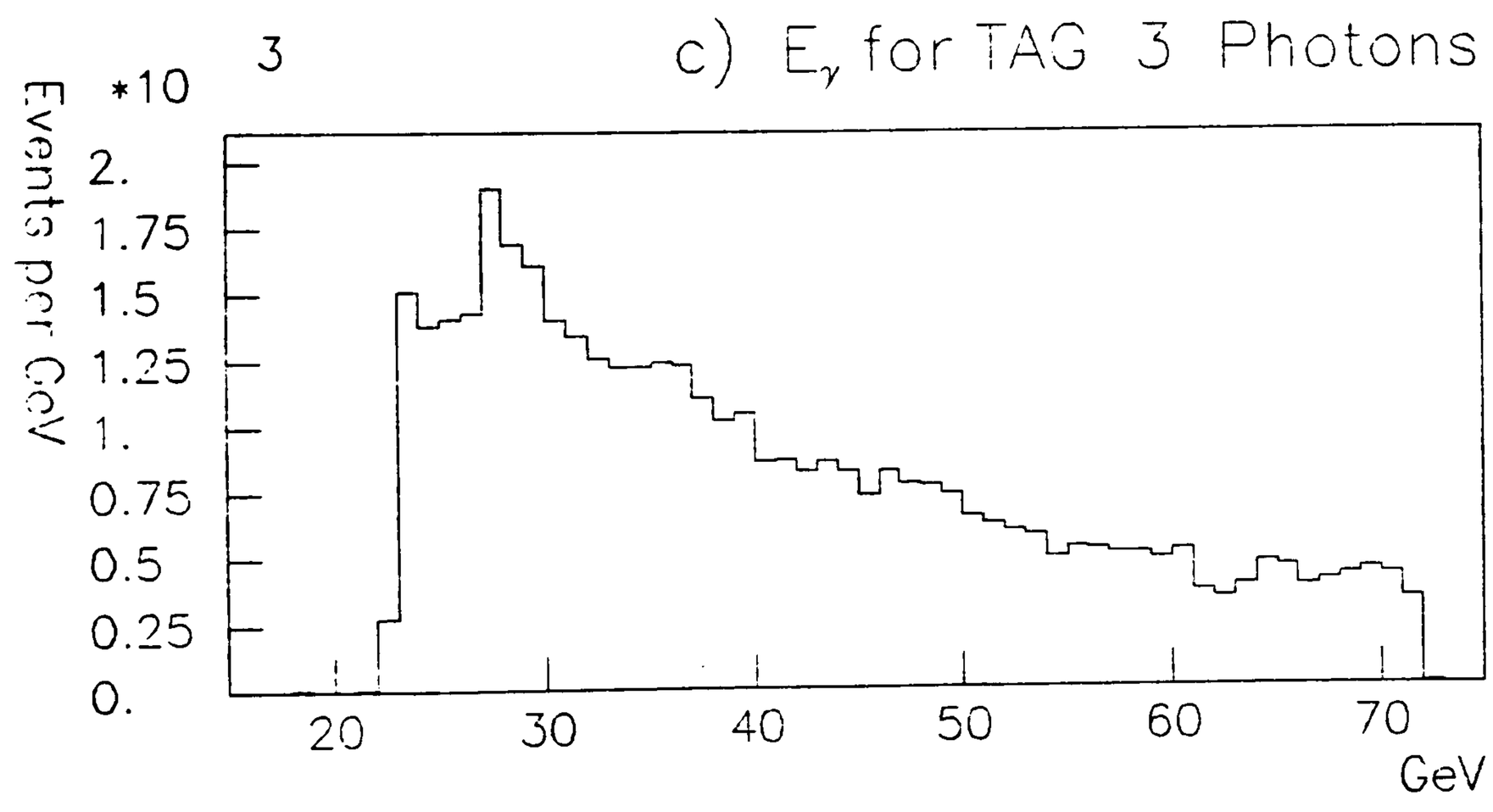
c) E_γ for TAG 3 Photons
3
*10
Events per GeV
0.
0.25
0.5
0.75
1.
1.25
1.5
1.75
2.
20
30
40
50
60
70
GeV

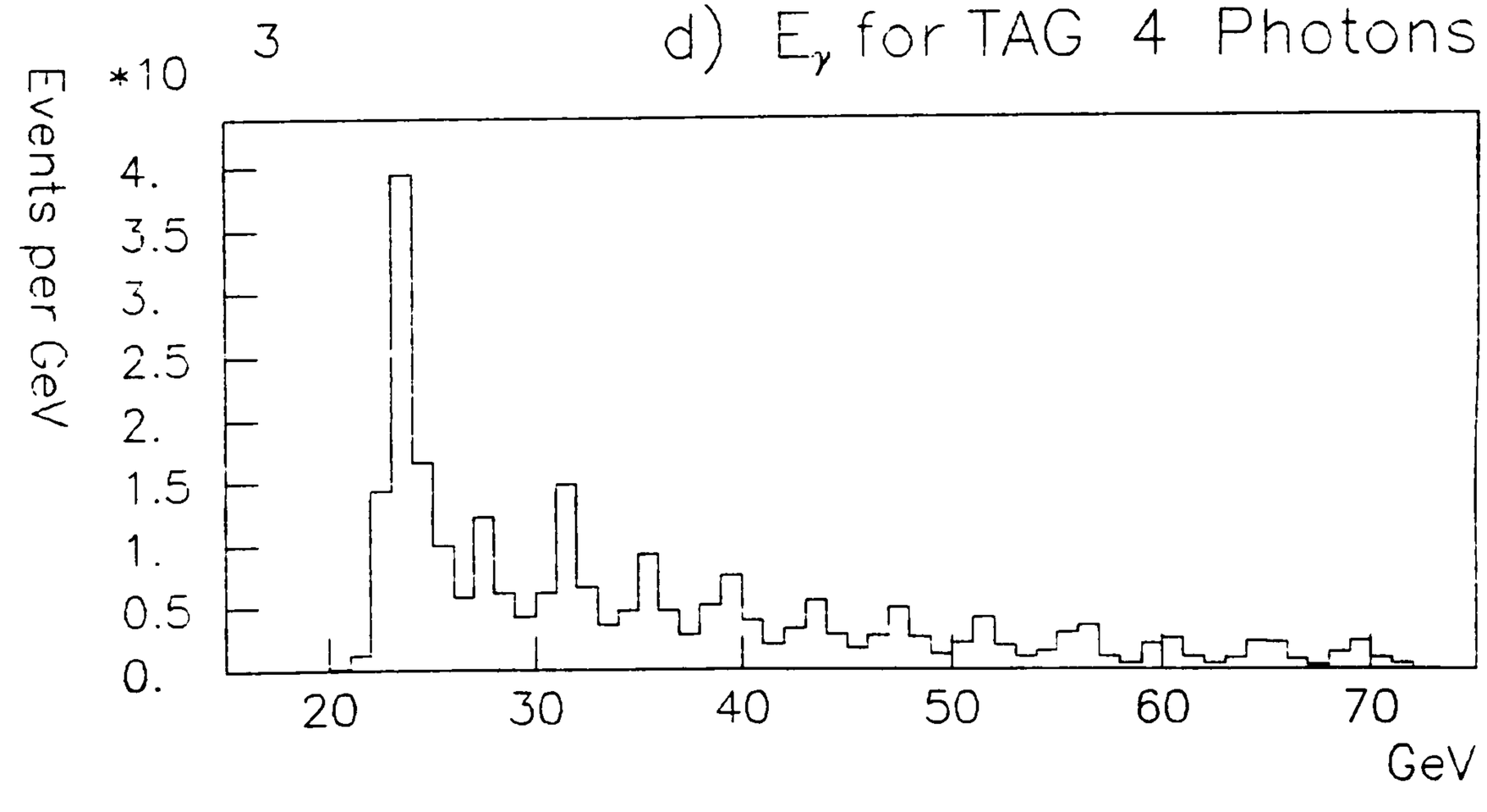
d) E_γ for TAG 4 Photons
3
*10
Events per GeV
0.
0.5
1.
1.5
2.
2.5
3.
3.5
4.
20
30
40
50
60
70
GeV

Figure 2.5

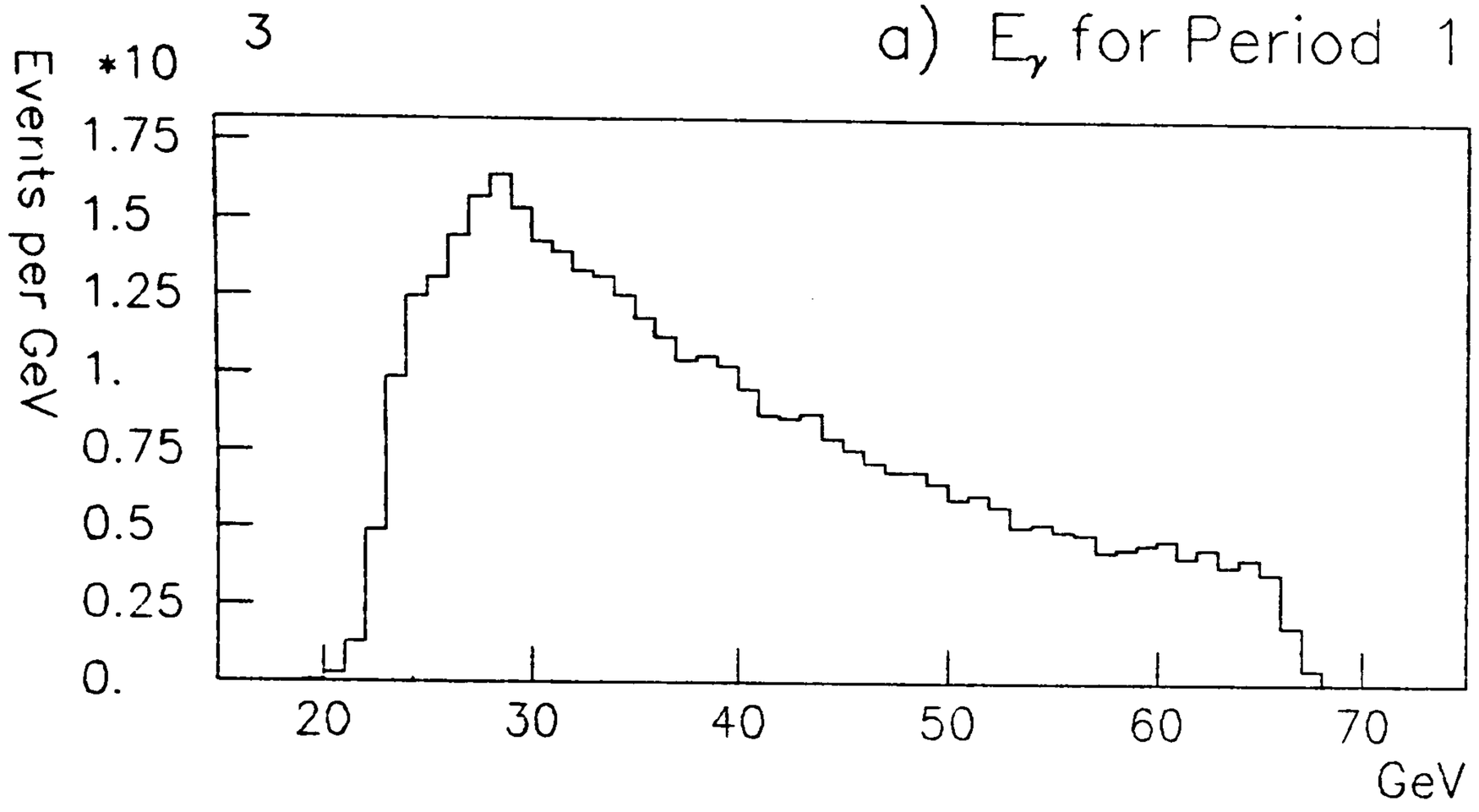
a) E_γ for Period 1
3
*10
Events per GeV
1.75
1.5
1.25
1.
0.75
0.5
0.25
0.
20
30
40
50
60
70
GeV

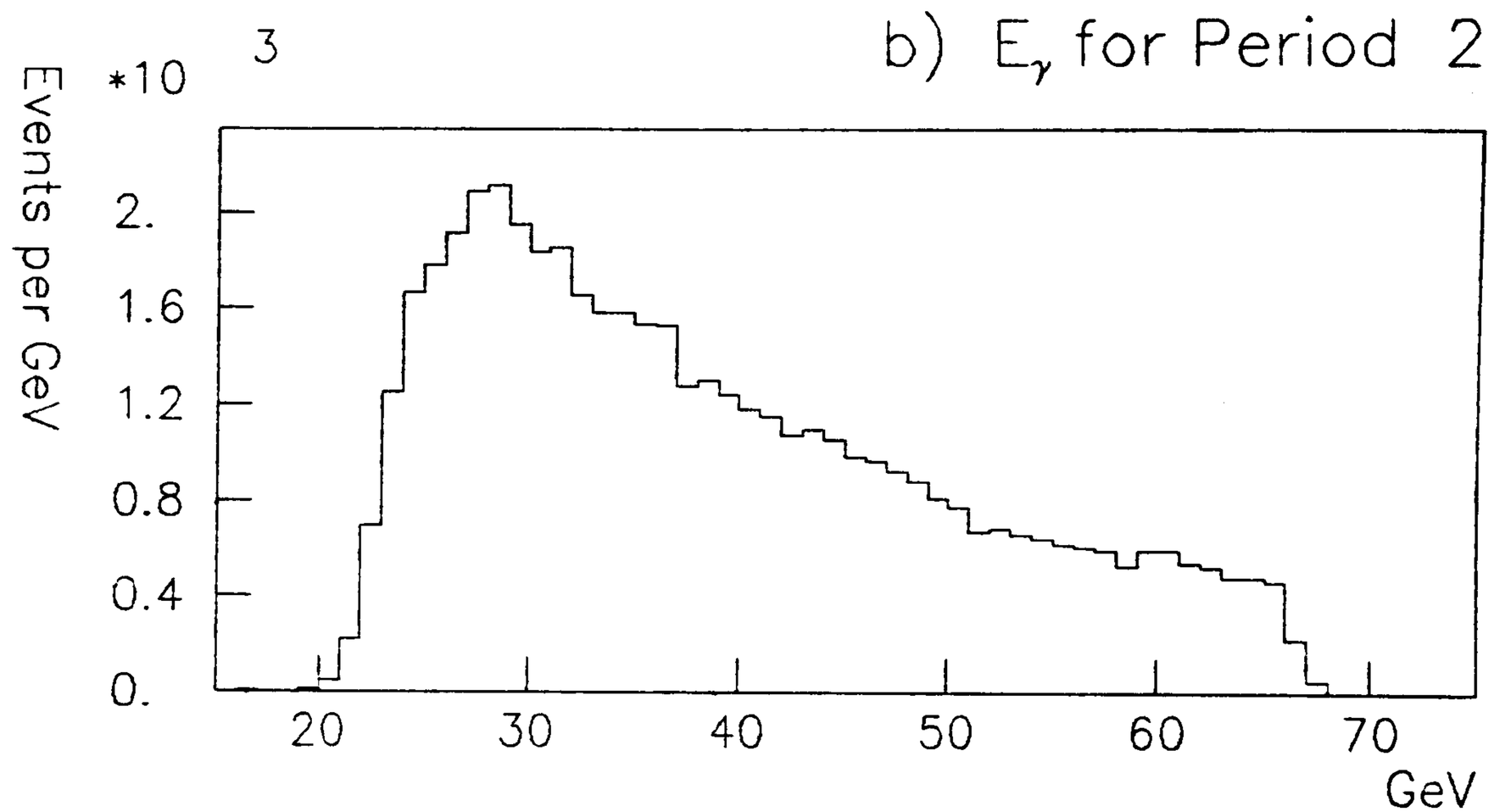
b) E_γ for Period 2
3
*10
Events per GeV
2.
1.6
1.2
0.8
0.4
0.
20
30
40
50
60
70
GeV

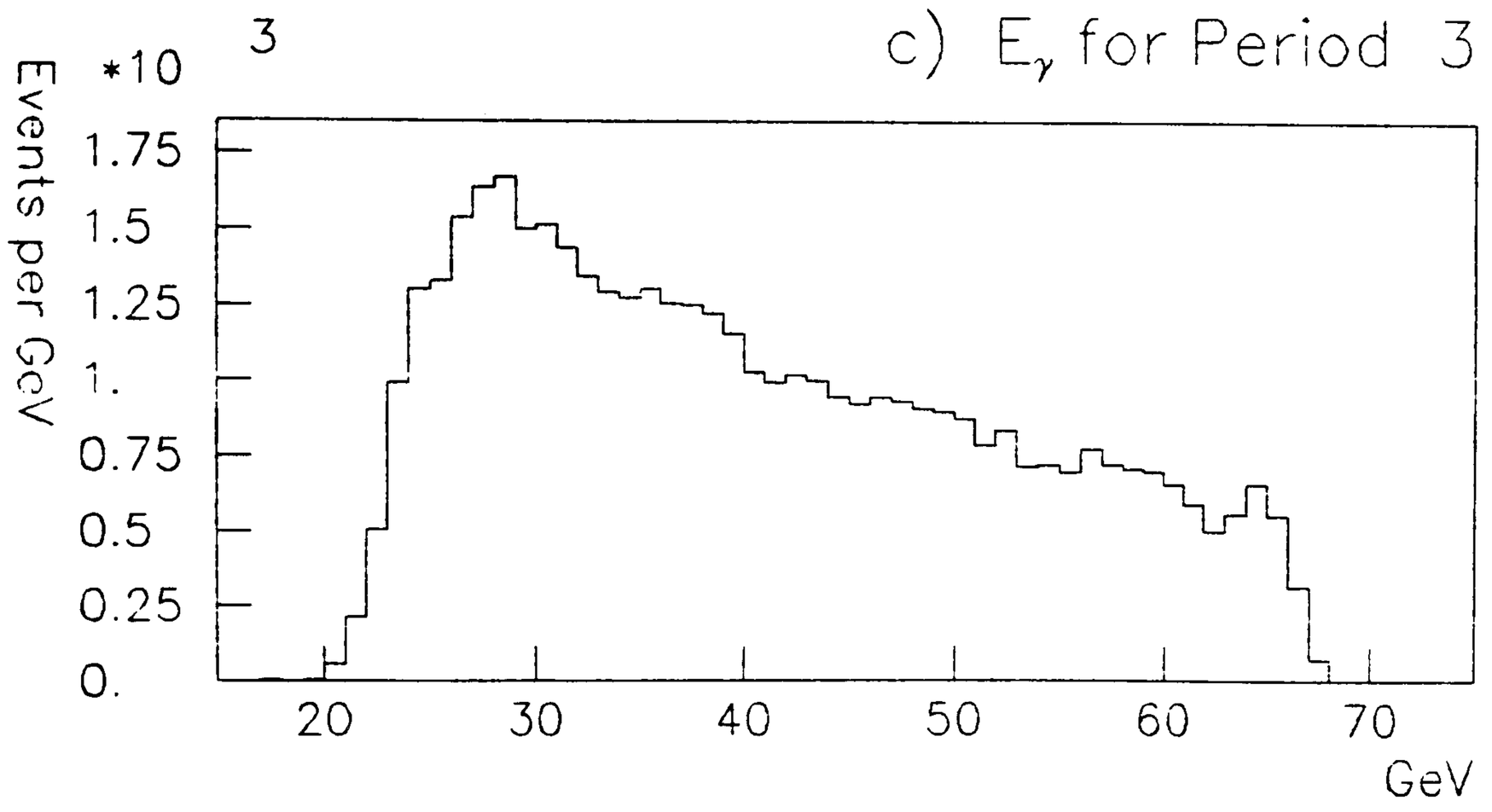
c) E_γ for Period 3
3
*10
Events per GeV
1.75
1.5
1.25
1.
0.75
0.5
0.25
0.
20
30
40
50
60
70
GeV

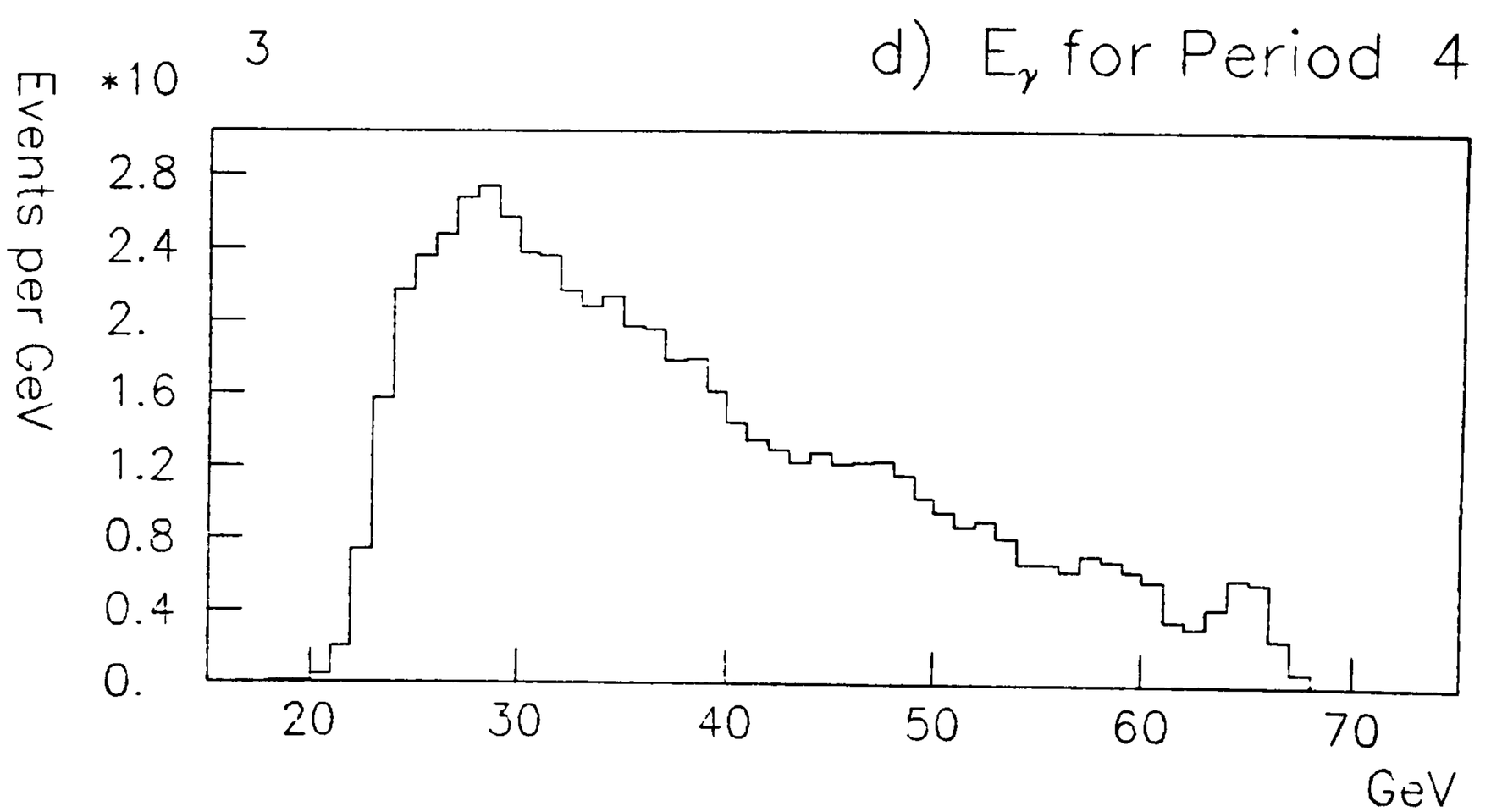
d) E_γ for Period 4
3
*10
Events per GeV
2.8
2.4
2.
1.6
1.2
0.8
0.4
0.
20
30
40
50
60
70
GeV

Figure 2.6

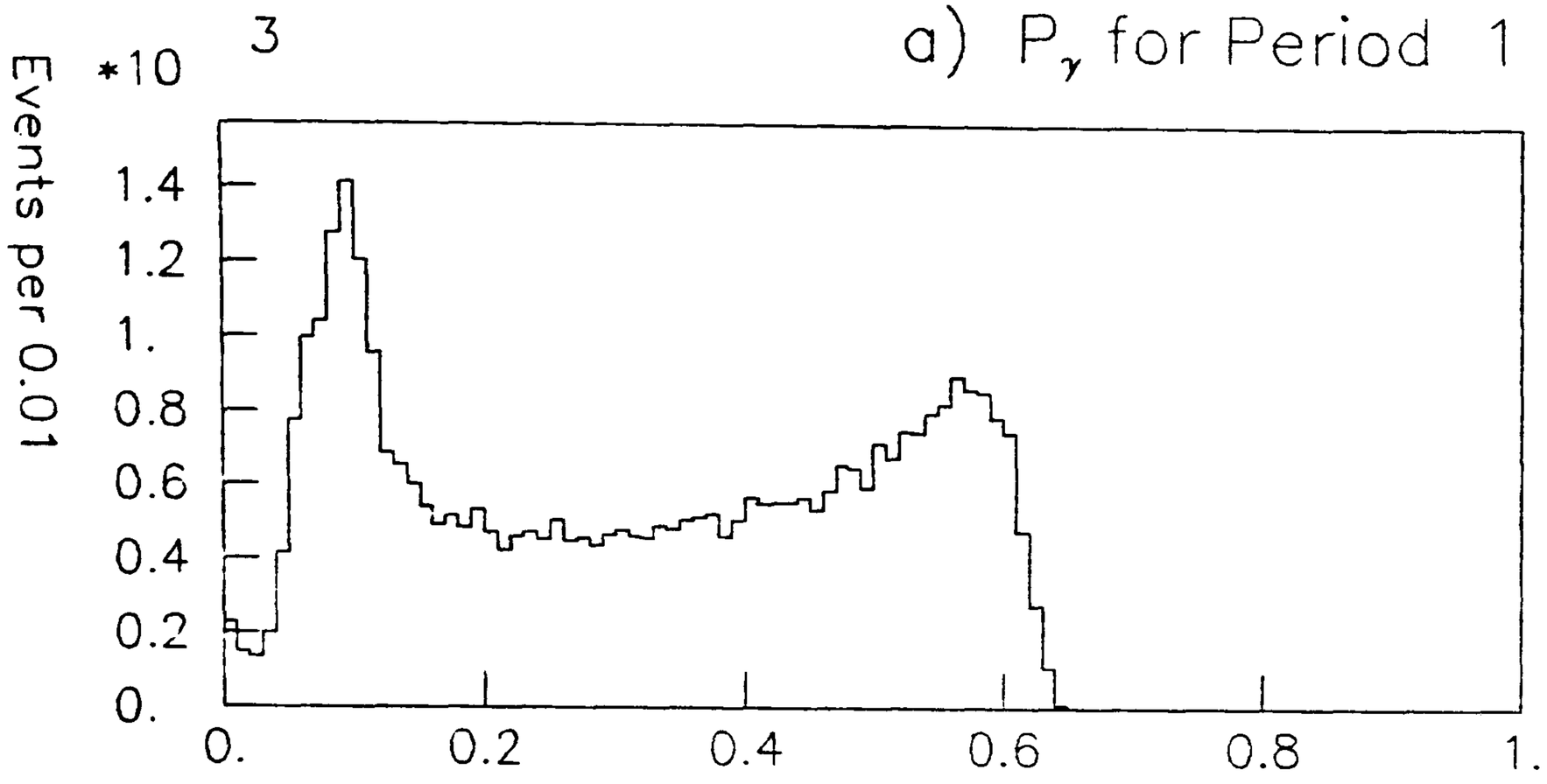
a) P_γ for Period 1
3
*10
Events per 0.01
1.4
1.2
1.
0.8
0.6
0.4
0.2
0.
0.
0.2
0.4
0.6
0.8
1.

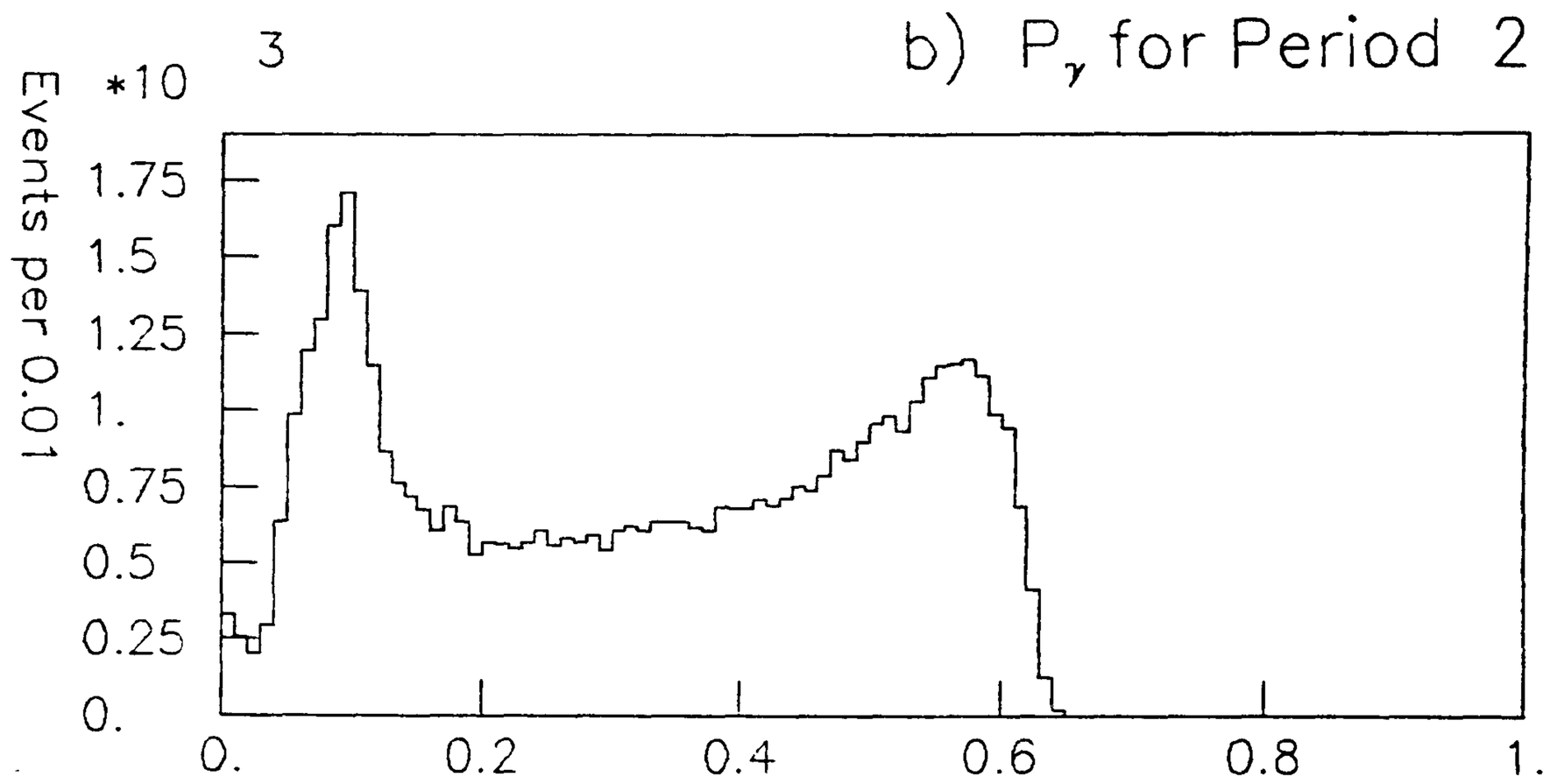
b) P_γ for Period 2
3
*10
Events per 0.01
1.75
1.5
1.25
1.
0.75
0.5
0.25
0.
0.
0.2
0.4
0.6
0.8
1.

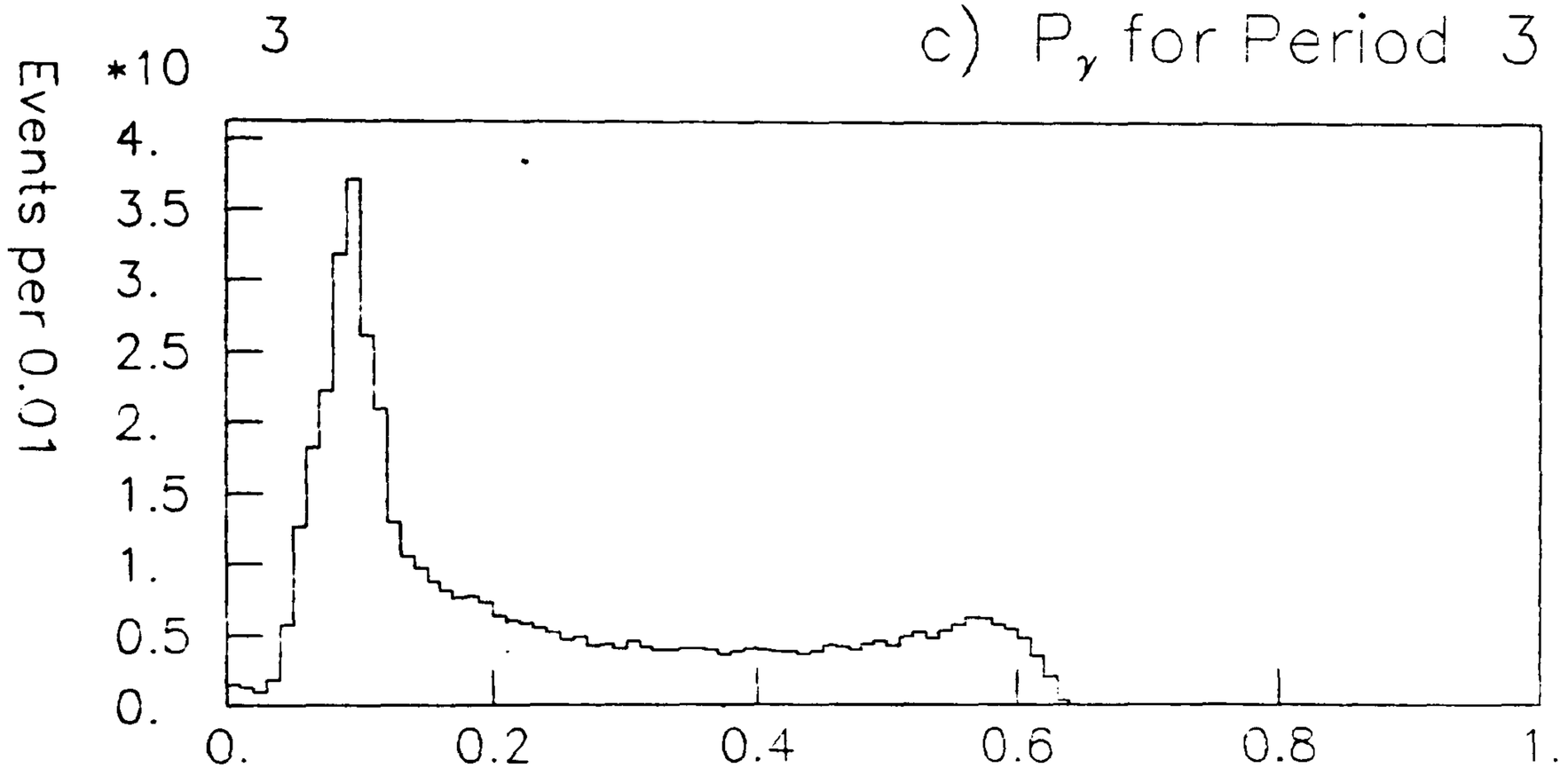
c) P_γ for Period 3
3
*10
Events per 0.01
4.
3.5
3.
2.5
2.
1.5
1.
0.5
0.
0.
0.2
0.4
0.6
0.8
1.

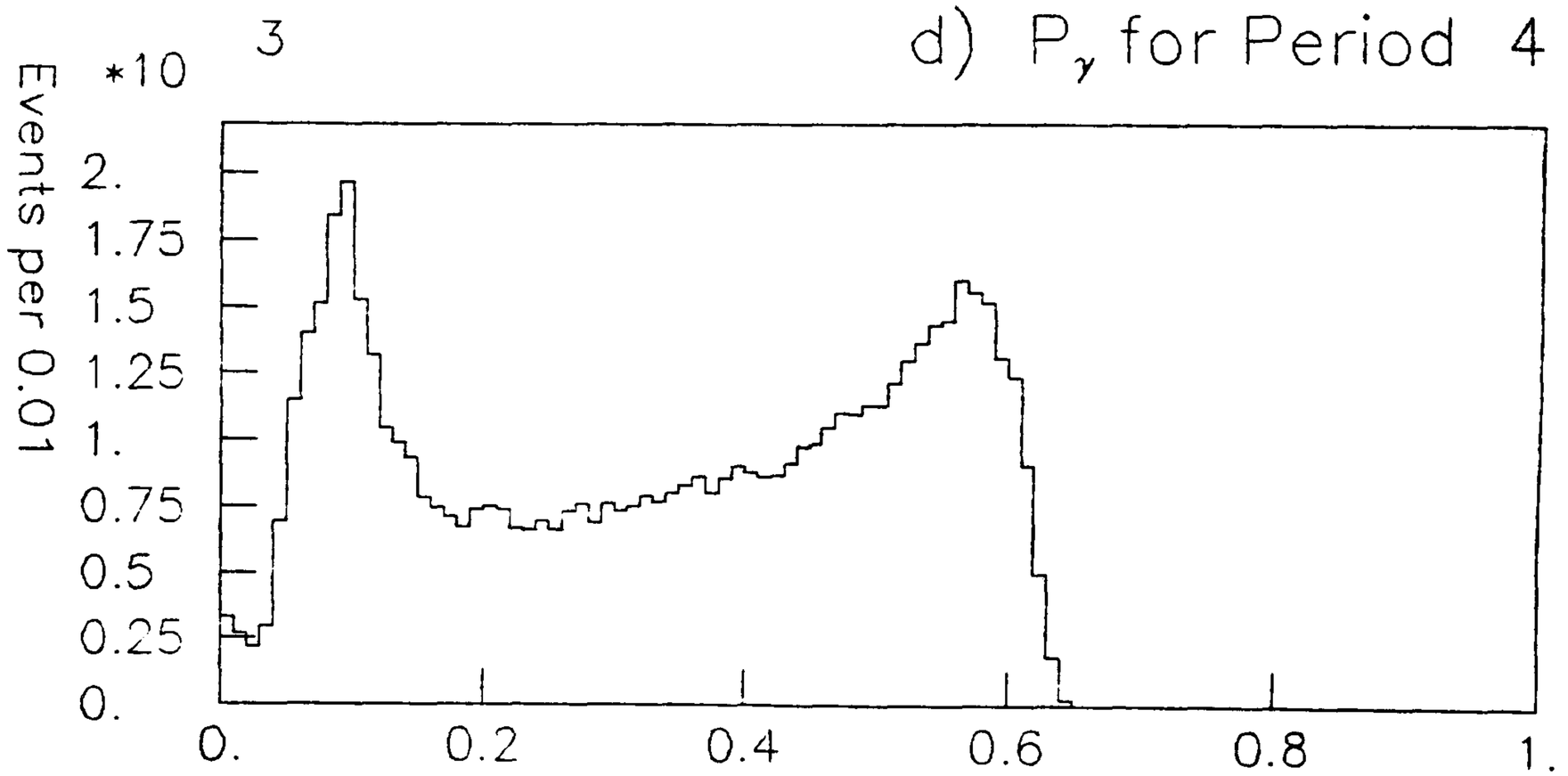
d) P_γ for Period 4
3
*10
Events per 0.01
2.
1.75
1.5
1.25
1.
0.75
0.5
0.25
0.
0.
0.2
0.4
0.6
0.8
1.

Figure 2.7

Chapter III

THE OMEGA-PRIME SPECTROMETER

3.1 INTRODUCTION

Tagged photons entered the liquid hydrogen target which was situated inside the magnetic field of the Omega-Prime spectrometer. The Omega magnet itself consists of two superconducting coils of radius 1.5 m., held 2 m. apart by four iron columns; for WA57 data-taking, the peak field of approximately 1.8 Tesla was used.

The Omega-Prime spectrometer was equipped with three sets of Multiwire Proportional Chambers (MWPCs), which together with other, user specific detectors, formed the event detection system. For WA57, the other detectors employed included Drift Chamber modules (DCs), scintillator hodoscopes, high-precision MWPCs, and for photon detection, a lead-glass and scintillator array. Charged particle identification was by means of an atmospheric pressure gas filled Cerenkov detector.

The purpose of this chapter is to describe in more detail the detectors used, the triggers formed during data-taking and the data aquisition system. The spectrometer, together with the other detectors used in WA57, is shown on Figure 3.1. The coordinate system referred to as the 'Omega' system is also shown in this figure.

3.2 THE TARGET REGION

The incoming tagged photons entered the Omega-Prime spectrometer at an angle of 44.5 mrad. to the Omega x-axis, this rotation of the beamline being due to the fact that the spectrometer was designed as a multi-user facility, and thus had another beamline entering it. The liquid hydrogen target, a cylindrical vessel 67 cm. in length with a radius of 2.5 cm., was rotated by the 44.5 mrad., so that the beam entered the target along the axis.

Surrounding the target and coaxial with it, was the Barrel Counter, (BC). This counter was constructed from 24 equal width slats of plastic scintillator, arranged in a cylinder of radius 8 cm., which ran the whole length of the target. Information from the BC was used offline to help in the identification of recoil protons from events within the target.

Covering the downstream end of the target was a disk of scintillator, the End Cap (EC), and a signal from this was incorporated in all the event triggers formed in the experiment as the first indication that a photon had interacted in the target.

On each side of the target there was a group of MWPCs, the region C chambers. There were five chambers on each side, aligned perpendicular to the Omega x-axis. Each chamber had 2 planes of 256 sense wires, these wires being spaced 2 mm. apart. The wires were orientated either vertically, (a 'Y' plane), or at +10.4° to the vertical, (a 'U' plane), or at -10.4° to the vertical, (a 'V' plane). Each chamber had a Y plane of wires, and the U and V planes alternated from chamber to chamber along the target.

3.3 REGIONS A AND B

Downstream of the target was a group of 6 MWPCs, the region B chambers, which, like those in region C, had two planes of sense wires per chamber, and again as in region C, the planes in each chamber were oriented either U-Y, or V-Y, alternating from chamber to chamber. In these chambers, each plane had 760 wires with a 2 mm. wire spacing.

Between the target and the region B chambers there was a high-precision MWPC, the HPC1. This chamber had two wire planes, one parallel to the Omega z-axis, a Y plane, and the other parallel to the Omega y-axis, a Z plane. Both planes had 160 wires with a wire spacing of 0.5 mm., giving the detector a sensitive area of approximately 64 cm.^{2}. .

The third set of standard Omega-Prime MWPCs was downstream of the region B chambers. There were five of these chambers, the region A chambers, and each chamber had three planes of sense wires, orientated U,V,Y, with 760 wires per plane and a wire spacing of 2 mm.. The A1Y plane was used in several of the main triggers formed for providing multiplicity information, whilst A3Z (an additional trigger plane), was similarly used in some of the secondary triggers formed.

An additional chamber, the Beusch Chamber, was positioned dowstream of the A chambers. This MWPC had two planes of sense wires, a Y plane with 736 wires, and a Z plane with 480 wires, the wire spacing in each plane being 2 mm..

3.4 THE FRINGE FIELD AND DOWNSTREAM DETECTORS

In the fringe field of the Omega magnet, there were two drift chamber modules. Each module had 4 wire planes with orientations Y,U,Y',V, the Y' plane being a Y plane which was offset from the first Y plane by half the wire spacing. There were 64 sense wires per plane, with a spacing of 5 cm., the chamber dimensions being 3 m. in y and 1.5 m. in z. The positional accuracy with which a track passing through the chambers could be found was approximately 0.2 mm., and this made them ideally suited for forming a 'lever arm' to be used in the track finding and fitting program TRIDENT. (See Chapter 4.)

Behind the Drift Chambers was the Bonn Hodoscope which was constructed from 18 vertical slats of scintillator, each of width 18 cm. and height 3 m.. For each slat, a signal from each end was fed into a mixer/timer with an 8 ns. gate, and this time gate had the effect of restricting the active length of the slats to approximately 1.6 m.. Multiplicity information from this hodoscope was used in the formation of some of the event triggers.

The Cerenkov detector used for charged particle identification was an atmospheric pressure threshold detector filled with CO_2. It had 32 cells which were divided into two sets of 16 by a reflecting membrane placed horizontally across the detector at z = 3 cm., just above the beam height. Every cell had a width of 14 cm. and a height of 1.5 m.. Under normal running conditions, the π,K,p thresholds were 5.5, 17.0 and 32.0 GeV/c respectively.

At the rear of the Cerenkov detector was the Back Hodoscope, a detector which was constructed from 36 vertical slats of scintillator, arranged in two sets of 18. Each slat was 27 cm. wide and had a 9 cm. overlap, thus forming an effective array of 72 slats. Multiplicity information from this detector was used in trigger formation.

3.5 THE PHOTON DETECTOR AND ELECTROMAGNETIC VETO

The photon detector consisted of three distinct parts, each one with its own specific purpose, and this section describes in some detail each part and its role in the detection and identification of photons.

The first part of the detector, the Sampler, was constructed from 42 horizontal lead-glass blocks, each 145 cm. long, 14 cm. high, and 10 cm. deep. The 10 cm. of lead glass presented by this element of the detector to an incident photon was approximately 3 radiation lengths, and thus the Sampler served to initiate electromagnetic showers. The energy deposited in the Sampler by a photon (or electron) induced shower was recorded to be used in calculating the energy of the incident photon (or electron).

The second element was an array of scintillator 'fingers', and this was used to detect the position of the showers induced in the Sampler, as they passed through the detector. This detector, Penelope, was itself in two parts, the first consisting of two half planes with vertical fingers, one above and one below the median plane; the second consisted of two half planes with horizontal fingers. In the first part, each half plane had 192 scintillator fingers, whilst in the second, each half plane had 204 fingers. Each finger was 1 cm. high, 1.5 cm. deep along the beam direction, and 150 cm. long, these dimensions allowing the determination of the position of a shower with an accuracy of approximately 2 mm..

The third and final section of the photon detector was an array of 344 lead glass blocks, the (Omega Lead Glass Array, OLGA),

each block being 50 cm. deep, with a square cross-section of 14 cm.. The 50 cm. of lead glass represented about 20 radiation lengths, and so this element acted as a total absorption counter, measuring the energy of the shower and hence that of the incident photon or electron. A hadron incident upon the calorimeter deposited a small amount of energy, and any hadron showers were eliminated from the photon/π^o reconstruction at a later stage in the analysis by matching the impacts with identified hadronic tracks.

Signals from the photon detector were used in the formation of the main event triggers in the experiment ; the actual trigger conditions are described in the next section.

An important part of all the triggers formed (other than some monitor triggers), was the electromagnetic veto, designed to veto the copiously produced electromagnetic pairs. This veto was formed from signals from a number of separate components. In front of the median plane of blocks in OLGA were the OLAP counters, two horizontal strips of scintillator which were positioned so as to overlap one another in the middle region of the median plane row. Each of these counters, one to the left and one to the right of the beam hole, extending the height of an OLGA block, was used in conjunction with the lead glass blocks behind it to form a signal which would veto the event. On either side of the lead glass array were two scintillator counters, the EVA detectors, which were "ORED" with the OLAPS to form the full electromagnetic veto.

3.6 THE EVENT TRIGGERS

In the course of an event occurring in the Omega-Prime spectrometer, information from the various parts of the detector system became available at different times, depending upon the characteristics of the detector. In order to use what information was available as soon as possible, the event triggers were built up in successive stages, each stage developing from those before, as more information became available. The purpose of this section is to describe the way in which the final event triggers were constructed from the various signals originating in the Omega-Prime detector system. The trigger logic development is shown in Figure 3.2 and Table 3.1.

The first stage in the formation of the trigger was the requirement that there was a Clean Gamma (CG) leaving the tagging system. The information for this came from the various scintillation vetoes in the tagging system, downstream of the tagging target, which were designed to veto the event if the radiated photon interacted in the region between the tagging target and the Omega hydrogen target. The SYSREADY signal, indicating that the Omega data aquisition system was ready to record another event, was also incorporated at this stage.

The next information incorporated into the trigger was related to the tagged photon, and its interaction in the hydrogen target. A signal from the scintillators in region C_t of the tagging system was taken to indicate that there was a tagged photon entering the hydrogen target, whilst a signal from the End Cap scintillator at the end of the target was taken as an indication that the tagged photon had interacted in the hydrogen. At this stage of formation, the trigger was termed the Loose Trigger (LT).

The LT was then combined with information from the Beam-Veto (BV) and from the Bonn Hodoscope (BH), to form four triggers which were termed the Intermediate Loose Triggers (ILTS) ; these differed from one another in the way in which the BV and BH information was incorporated ; this is shown in Table 3.1 and Figure 3.2. By this time, the information from the lead-glass in the tagging system was available, and this was incorporated into a Trigger Tightener (TT), which served to indicate a well tagged photon. The TT was then combined with each of the ILTS. At this point in the trigger formation, the four triggers were essentially the same, but the next stage involved the inclusion of some of the multiplicity information from the detectors downstream of Omega and from the Omega wire chambers, which resulted in distinct event triggers.

Charged track multiplicity information from both of the scintillator detectors, the Bonn and the Back Hodoscopes was included at this stage, as was the multiplicity information from the A1Y trigger plane and the Beusch chamber. The signals from the electromagentic veto were then included, and finally the signals from the photon detector and the Cerenkov were combined to form the User Final Triggers (UFT). There were ten UFTs formed, some of them for monitoring purposes, and they are detailed in Table 3.2.

There has been some evidence from a previous photoproduction experiment at Omega, WA4, that there is some p_t-limited "jet like" structure in the final state in the reaction $\gamma p \rightarrow \pi^+\pi^-\pi^+\pi^-\pi^+\pi^- p$ and trigger 1, the "jet trigger", was designed to continue the study of these high energy, high multiplicity events. Trigger 3, the 'ρ trigger' was used to trigger on di-pion pairs, the major contribution to this data sample being ρ mesons apart from a residuum of electromagnetic pairs. The beam monitor trigger, trigger 8,

was used as a check on the characteristics of the beam as already explained in Chapter 2. This triggered on electromagnetic pairs which in turn could be used to reconstruct the beam. The main experimental trigger was trigger 5, the 'OLGA trigger', which was designed to collect data from the channel $\gamma p \rightarrow \omega \pi^0 p$; this trigger is described in more detail below. Associated with this were two monitor triggers, triggers 4 and 10. These were used as checks on various parts of the trigger 5 logic, to try and ensure the minimum bias. The remaining triggers were associated with the K-Matrix, a two step coincidence trigger, set up specifically to trigger on kaons. Statistics for the total data-taking for each trigger are shown in Table 3.3.

As mentioned above, trigger 5, the OLGA trigger, was the one from which the data for the analysis presented in this Thesis were taken. This trigger consisted of two main parts; the actual photon trigger and a charged particle multiplicity requirement. The A1Y plane was used as the trigger plane to provide information on the charged track multiplicity in the event, and for trigger 5, the requirement was that there were either 2 or 5 charged tracks in the event. The photon trigger was designed to trigger on a certain minimum photon energy being deposited in the calorimeter, this minimum being set by the thresholds on the calorimeter electronics. The minumum was decided upon by running a Monte-Carlo on a $\omega \pi^0$ model and examining the energy spectrum of the photons hitting the photon detector ; from this, the minimum was set to be 2 GeV. Further to this minimum energy requirement however, there was the requirement that the energy was deposited by a single photon. This latter condition was imposed by forming the sum of the energies deposited in adjacent pairs of half columns of OLGA blocks, and then testing on these sums for the minimum. The reason for forming the sums in this way was that there

existed the possibility that a photon hitting an OLGA block near the edge would leak energy into an adjacent block, thus distributing the energy over a column of blocks. No leakage was possible across the median plane and so each half, top and bottom, of the lead-glass array could be treated separately.

3.7 THE DATA AQUISITION SYSTEM

The data aquisition system for the Omega-Prime Spectrometer consisted of a central processor, (the Data Aquisition Computer or DAC), which was equipped with tape drives, and a number of auxilliary computers which were used for monitoring the detector system during data-taking. There were three of these auxilliary computers (all the computers were PDP-11s); one, U0 was used to monitor the performance of the Omega detector system itself, whilst the other two, U1 and U2, were used to monitor user specific detectors, such as the Tagging system and the photon detector. After an event in the Omega Spectrometer, the DAC read the Omega data block, followed by data from the user computers; then, continuing outside of the beam spill, it wrote the events from its event buffer onto a 1600 b.p.i. tape unit.

A number of monitoring programmes were run on-line during data-taking to look at the beam, the photon detector and other detectors downstream of the Omega Spectrometer. Programmes were also run off-line on the CERN IBM 370/168 system to give a more detailed picture of the detector performance and to check the on-line programmes.

Figures And Tables for Chapter 3

Symbol	Description
A	BONNHOD OR
B	BONNHOD ≥ 2
C	BONNHOD FAST -OR
D	A1Y $2_{\wedge}3$
E	BONNHOD $2_{\wedge}3$
F	BACKHOD LEFT $1_{\wedge}2$
G	BACKHOD RIGHT $1_{\wedge}2$
H	BACK WINGS VETO
I	A1Y 2 → 5
J	BACKHOD ≥ 1
K	BEUSCH Y ≥ 1
L	A1Y 3 → 8
M	A3Z 3 → 10
N	A1Y 6 → 11
O	A1Y 1 → 3
P	TOTAL ČERENKOV VETO
Q	Σ OLGA.LT
R	K-MATRIX ≥ 1
S	HIGH E_{γ}

Table 3.1

Bit No.	Trigger	Trigger Word (octal)	Description
1	$S6/3_D$	00001	$\overline{ILT3.TT.A1Y\ 6 \rightarrow 11.A3Z\ 3 \rightarrow 10}$ $\overline{EMVETO}.HIE_\gamma$
2	$S6/1_B$	00002	ILT1.TT.BONNHOD 2$\wedge$3.A1Y 2$\wedge$3. Beusch Y 2$\wedge$3.$\overline{BACKHOD(1\wedge2)_{LEFT}}$. $BACKHOD(1\wedge2)_{RIGHT}$.$\overline{EMVETO}$.C VETO
3	$S6/1_C$	00004	ILT1.TT.BONNHOD 2$\wedge$3.A1Y 2$\wedge$3. Beusch Y 2$\wedge$3. $\overline{BACKHOD(1\wedge2)_{LEFT}}$. $BACKHOD(1\wedge2)_{RIGHT}$.$\overline{EMVETO}$
4	$S6/2_A$	00010	ILT2.TT.A1Y 2 $\rightarrow$ 5.$\overline{EMVETO}$.Scaled by 2^7
5	$S6/2_B$	00020	ILT2.TT.A1Y 2 $\rightarrow$ 5.$\overline{EMVETO}$.OLGA
6	$S6/3_A$	00040	ILT3.TT.A1Y $\overline{3 \rightarrow 8}$.Beusch Y $\geq$ 1. BACKHOD $\geq$ 1.$\overline{EMVETO}$.Scaled by 2^6
7	$S6/3_B$	00100	ILT3.TT.A1Y $\overline{3 \rightarrow 8}$.Beusch Y $\geq$ 1. BACKHOD $\geq$ 1.$\overline{EMVETO}$.KMAT $\geq$ 1.
8	S6/4	00200	ILT4.TT.A1Y 1$\wedge$2$\wedge$3.Scaled by 2^7
9	$S6/3_C$	00400	ILT3.TT.A1Y 3 $\rightarrow$ 8.Beusch Y $\geq$ 1. BACKHOD $\geq$ 1.Beusch Z or A3Z guillotine.KMAT $\geq$ 1.
10	$S6/2_C$	01000	ILT2.TT.A1Y 2 - 5.Beusch Z or A3Z guillotine.scaled by 2^5.OLGA.
11	-	02000	A3Z guillotine
12	-	04000	Σ OLGA.LT
13	-	10000	KMAT $\geq$ 1
14	-	20000	Σ OLGA.LT.BACKHOD VETO
15	-	40000	Beusch Z guillotine

Table 3.2

Definition	Number	%
Total number of triggers	12 573 570	100.0%
Number of calibration triggers	637 202	5.1%
Number of amorphous data triggers	169 434	1.3%
Number of setting up triggers	1 953 487	15.5%
Real triggers (Percentage of Real triggers)	9 813 477	73.0%
Trigger bit 1	707 893	7.2%
Trigger bit 2	104 143	1.7%
Trigger bit 3	1 149 311	11.7%
Trigger bit 4	474 832	4.8%
Trigger bit 5	5 398 924	55.0%
Trigger bit 6	129 654	1.3%
Trigger bit 7	1 681 474	17 1%
Trigger bit 8	401 631	4.1%
Trigger bit 9	2 295 121	23.4%
Trigger bit 10	188 949	1.9%

Table 3.3

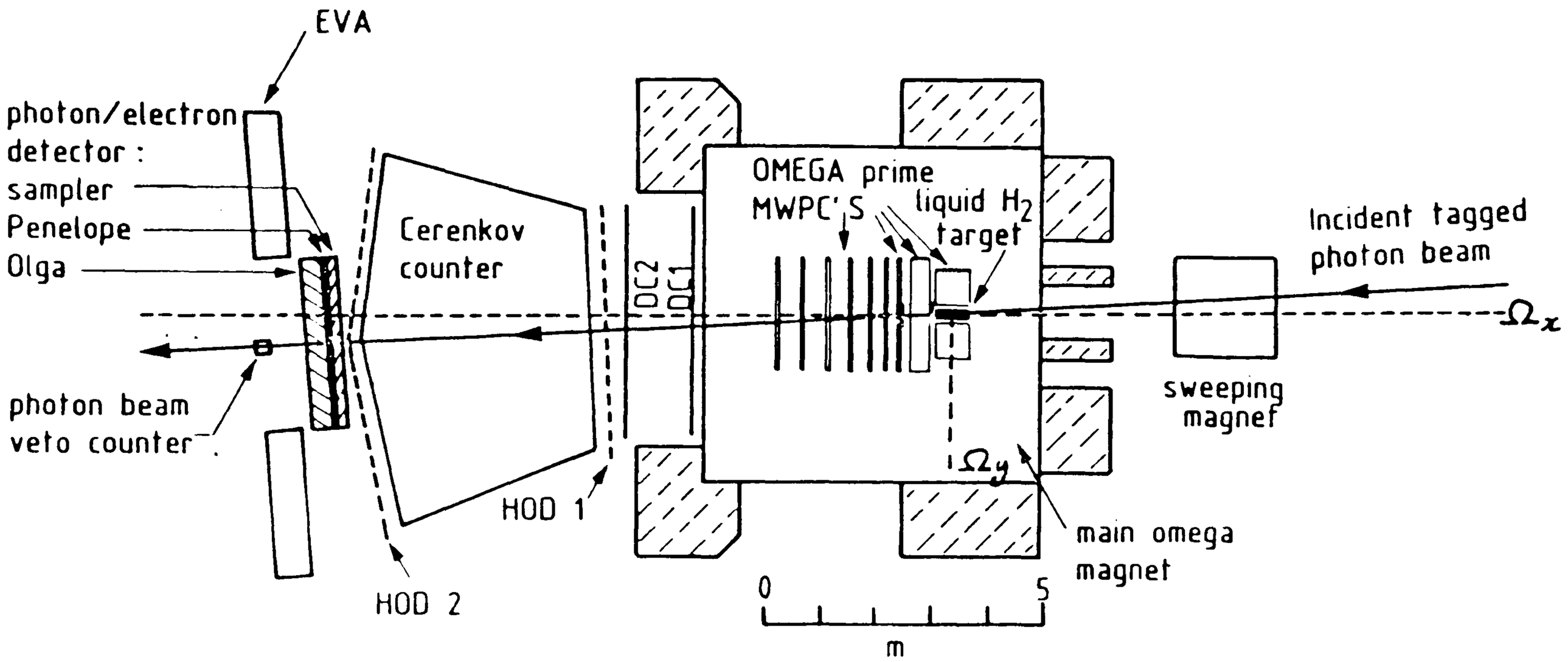
EVA
photon/electron
detector :
sampler
Penelope
Olga
Cerenkov
counter
DC2
DC1
OMEGA prime
MWPC'S
liquid H_2
target
Incident tagged
photon beam
Ω_x
sweeping
magnef
photon beam
veto counter
HOD 1
HOD 2
Ω_y
main omega
magnet
0
5
m

Figure 3.1

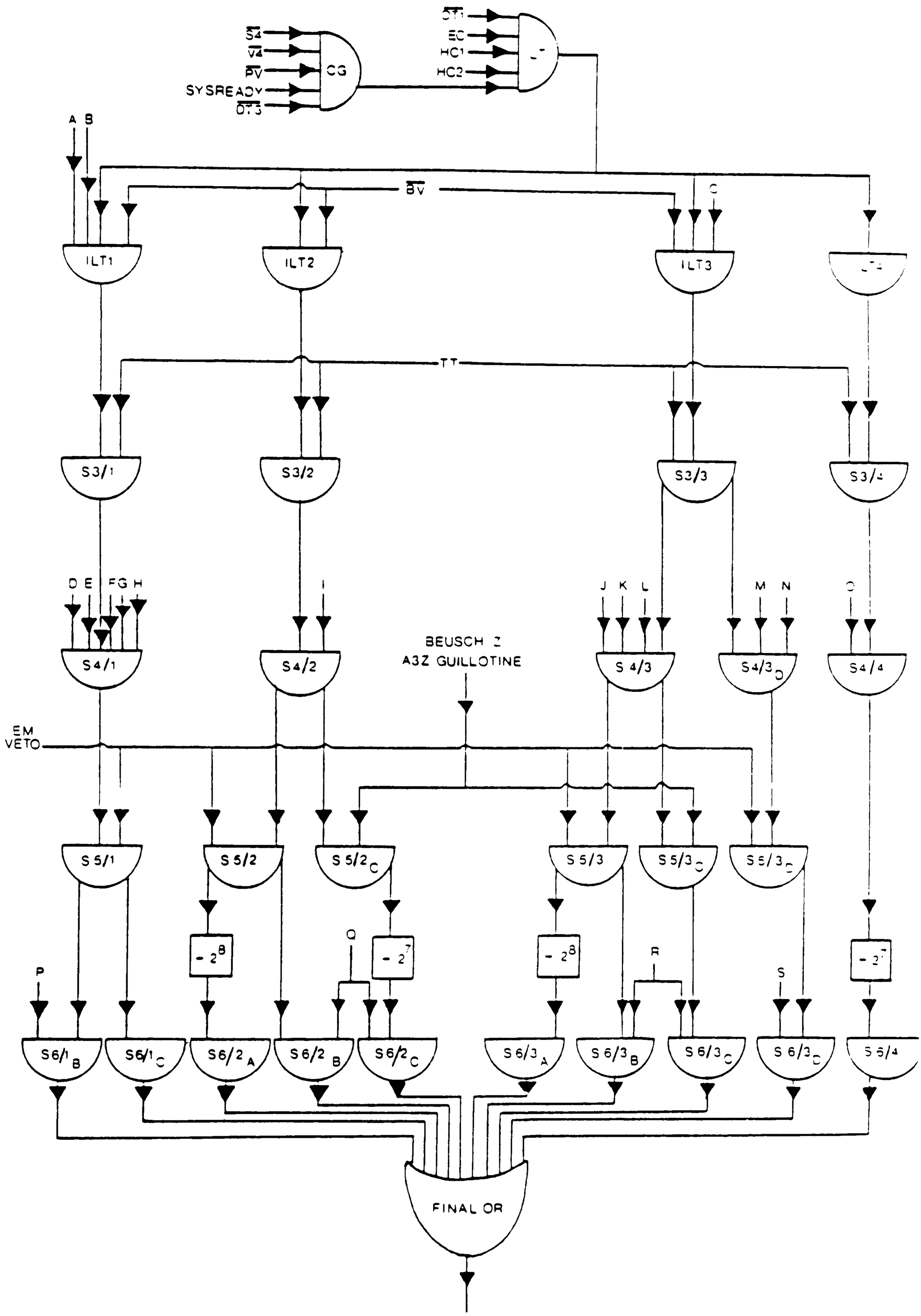
S4
V4
PV
SYSREADY
DT3
CG
DT1
EC
HC1
HC2
A B
BV
C
ILT1
ILT2
ILT3
TT
S3/1
S3/2
S3/3
S3/4
D E F G H
I
J K L
M N
O
S4/1
S4/2
S4/3
S4/3D
S4/4
BEUSCH 2
A3Z GUILLOTINE
EM
VETO
S 5/1
S 5/2
S 5/2C
S 5/3
S 5/3C
S 5/3D
Q
R
S
P
S6/1B
S6/1C
S6/2A
S6/2B
S6/2C
S6/3A
S6/3B
S6/3C
S6/3D
S6/4
FINAL OR

Figure 3.2

Chapter IV

THE DATA PROCESSING AND REDUCTION

4.1 INTRODUCTION

In a modern electronic counter experiment the quantity of data which it is possible to record is usually large. There were almost 10 million events recorded during WA57 data-taking, and such a data sample requires a fast and efficient method of processing and data reduction. The data taken during WA57 were processed through a series of large and sophisticated computer programmes, and this Chapter will briefly outline the various steps through which the data passed on their way to the final Data Summary Tapes (DSTs). The real data case will be described first, followed by a description of the simulation software.

There were approximately 400 data tapes written from the DAC during data taking, and these were subsequently copied onto high density tapes, reducing the number of tapes to about 100. It was on these high density tapes that the first of the data processing programmes, TRIDENT, was run.

4.2 TRIDENT

The bulk of the spatial information for each event came from the Omega Prime Spectrometer wire chambers, and the purpose of TRIDENT[4-1] was to use this information to find and fit tracks in space, computing their momentum, then combine the tracks to form an event vertex. TRIDENT processing therefore falls into three sections a) track identification, b) track fitting and c) vertex fitting.

The steps which TRIDENT takes during the track finding process are as follow. Firstly, the digitisings in the Drift Chambers (DCs) are taken, and formed into track segments. The high accuracy with which these digitisings can be related to space points then allows the various track segments to be tested in order to ensure that they might have originated in the Omega hydrogen target. If they pass this test, they are then extrapolated back in to the region A chambers, then into the B chambers, and finally into the C chambers. A straight line projection is used in the x-z plane whilst a cubic spline is used in the x-y plane, and digitisings in the three regions are assigned to the track element if they are within some predetermined distance from the extrapolated track. The digitisings which are not associated with tracks which have been extrapolated from the DCs are then formed into track segments which are matched to form tracks.

Having found a set of tracks, TRIDENT then fits each of these to a quintic spline, using the full Omega magnetic field, thus determining the track parameters.

The final stage in the TRIDENT processing of an event is the reconstruction of the event vertex. To do this, the tracks are taken in pairs, approximated to circles in the bending plane, and the intersection points of these pairs of tracks are used to form a set of primary two-track vertices. This set of vertices is then examined, and

the vertices are merged to form multi-track vertices, depending upon their distance apart. A χ^2 is formed for the vertex hypothesis, and if the χ^2 probability is too low, the track contributing most to the χ^2 is removed and the process repeated. This fitting procedure continues until an acceptable fit is produced, and at this stage, any remaining two-track vertices are tested for compatibility with being a V^0. These V^0. vertices can come from the decay of K^0's or Λ's, or from a photon converting to an e^+e^- pair inside the Omega field. If there is any ambiguity at this stage as to whether or not such a vertex should be included in the main event vertex, TRIDENT constructs two hypotheses, one with the 'V^0.' vertex included in the main vertex, and the other with the two-track vertex maintained as a separate vertex.

After this process has finished, any remaining tracks which have been assigned neither to the main vertex nor to a V^0. are classified as 'extra-tracks' and recorded. The information output by TRIDENT consists of the fitted event parameters i.e. the fitted vertex position and the momentum, dip and azimuth of each track, and an additional electronics block. This block of data contains information recorded from the other detectors used during data-taking, such as the photon detector and the Cerenkov detector, and it is this information, along with the TRIDENT fitted event, which JULIET uses to form π^0s and to identify the charged tracks as π's, K's or baryons.

4.3 JULIET

The programme JULIET[4-2] is itself a collection of packages, each with its own role in the full reconstruction of the events. Each of these packages will be described below. JULIET reads the TRIDENT output tapes and rearranges the information into a more easily accessible form. The first stage in the JULIET processing is the reconstruction of the beam which is done by PHOTAG.

4.3.1 PHOTAG

As explained in Chapter 2, the calculation of the beam momentum requires a knowledge of the incident electron momentum and the scattered electron momentum, the difference giving the momentum of the radiated photon. These momenta were calculated in PHOTAG using information from the tagging system wire chambers in A_t, B_t, and C_t, along with the lead-glass information from region C_t. Depending upon the availability of the information, the photon's polarisation was also calculated in PHOTAG. More details of this calculation can be found in Chapter 2 and the references in Chapter 2.

4.3.2 CERENK

The package CERENK used the track momenta fitted by TRIDENT and the information from the CO_2 gas Cerenkov detector to identify the charged tracks. Because of a known inefficiency in the Cerenkov, due to inactive regions and a non-uniformity of the light collection across the active region, each track, once identified, was also assigned a probability that the identification was correct, this probability being made available for use on the DSTs. For the analysis presented in this Thesis the Cerenkov information was not used.

4.3.3 VZERO

The V^o. vertices found by TRIDENT were analysed by the package VZERO, which, using the Cerenkov information for the tracks attached to the V^o., identified the decaying particles as K's, Λ's, or as converted photons. The momentum 4-vector of the V^o was then calculated, and from that point on in the processing, these reconstructed V^os were treated as detected particles.

4.3.4 RECPRO

The function of RECPRO was to identify and reconstruct the recoil protons from the hydrogen target. Using information from the Barrel Counter and from region C, the recoil protons were identifed as being the slowest positive tracks in an event (with momentum less than 1.4 GeV), and they were required to be at a large angle to the direction of motion of the incoming beam. Only those tracks which made an angle between 0.5 rad. and $\pi/2$ rad. were accepted as recoil proton candidates. The tracks which succesfully filled these criteria were corrected for energy-loss and scattering in the target and flagged as recoil protons.

4.3.5 SNARK

As the main physics channel in which the experiment was interested involved two π^0's in the final state, the detection of the photons from the π^0 decay and the reconstruction of the π^0's themselves was one of the most important aspects of the data processing. Inside JULIET, this task was accomplished by SNARK. The first step in the reconstruction of the π^0's was the identification of photon candidates, which made use of the positional information from the photon detector. Impacts on the detector were classified as "clusters", often comprising of signals from more than one of the lead-glass blocks, and then, depending upon the positional information available, SNARK attempted to resolve impacts close together by splitting the clusters. After deciding upon a set of clusters, SNARK assigns each of them an energy and flags each with a quality flag which indicates any ambiguity that might be present in the identification. These photon candidates are then taken two at a time and fitted to the π^0 mass, using the calculated momenta and positions of impact. All combinations which had a χ^2 probability of greater than 3% were then accepted as π^0 candidates and their 4-momentum recorded.

The output from JULIET then consisted of fully identified and fitted events, and these were written onto the DSTs, to be used in physics analysis.

4.4 MULTIPI0

As mentioned above, the channels of most interest in WA57 were those in which there were a number of π^0's in the final state, and hence the reconstruction of these π^0's was of great importance for the experiment. The programme MULTIPI0[4-3] was written in order to provide an alternative π^0 reconstruction to that offered by SNARK. As input, MULTIPI0 used the DSTs written by JULIET, which had on them all of the information relating to the photon candidates as found by SNARK. MULTIPI0 took this information and after reclassifying the photons on the basis of how well they had been measured, it formed π^0 candidates from γ-γ pair, much as was done in SNARK. After finding a set of π^0's, MULTIPI0 then took the largest subset of these candidates and performed a global fit to the γ-γ pairs. If this fit was poor, one of the pairs was rejected and the fit repeated on the smaller subsets of candidates. This process was repeated until a fit which satisfied all the criteria was found, at which point, MULTIPI0 designated the members of the set to be π^0's and moved on to perform a similar selection of η candidates. The output from MULTIPI0 was a DST, similar to the one produced by JULIET, the only difference being in the π^0 which were present, and in the inclusion of any η's found by the selection.

4.5 GEORGE

The programme GEORGE[4-4] consisted of a set of routines which formed a framework within which physics analysis programmes could be built. GEORGE provided a standard I/O routine for reading the DSTs produced either by JULIET or by MULTIPIO, and a collection of routines which could be used to calculate the kinematical variables of interest in an event.

4.6 SIMULATION

With a complicated piece of equipment such as the Omega-Prime spectrometer, it is vital that the performance of the detector during data-taking is understood. To this end, a Monte-Carlo Simulation of the experiment was set up, and the purpose of this section is to describe the simulation software. The first step in this chain of simulation programmes is an event generator of some kind which will produce particle 4-momenta according to some physics model. The one used in the work detailed in this Thesis was SAGE[4-5], the output from which consisted of event track parameters in the Omega-Prime coordinate system which could be used as input to the next step of the simulation process. In this next step two approaches are common. In the first, as full as possible a model of the detector system is constructed and after events have been passed through this model, the output is made to conform as closely as possible to the output format of the real data coming from the real detector. This output can then be processed as the real data is, through the production chain of TRIDENT, JULIET, MULTIPIO, and GEORGE, to produce a data sample which can be compared with a data sample from a known and understood physics channel. The objection to this approach is that it is costly in computing time and can be rather inefficient, the simulation of the event output

from the real detector being a very complicated business. In situations in which these complications are not crucial, a second, more approximate approach to the event simulation is used. These two approaches are illustrated by the two programmes GEANT and MAP which are described below.

4.6.1 GEANT

The programme GEANT[4-6] is a general detector simulation programme which can be set up to simulate a given detector. The details neccessary to define the detector are the positions of the various detector elements and the composition of these elements. The interface between the programme GEANT and the Omega-Prime spectrometer was the programme OMGEANT, which contained tables of wire chamber positions and dimensions etc..

The input to GEANT were event records, such as those generated by SAGE, which included particle momenta, masses and charges, and the GEANT processing of each of these events was in three steps. The first step consisted of tracking the particles through the spectrometer, applying as it does so, corrections for energy-loss and multiple scattering in the material of the detector elements. During this tracking, the position of the trajectory at various points, defined by the user, is recorded. The second step in the processing is then to define hits on the physical detector elements for each of these tracks. This requires a knowledge of the construction of each detector element, wire spacings etc.. The third step in the processing then invloves converting these hits to digitisings. At this stage a simulation of the noise or inefficiency in any of the detector elements can be introduced, as can the inability of some elements to resolve hits which are close together, which results in clusters of hits. With these digitisings then,

GEANT has all the neccessary information to ouput a data block which is similar in construction to the data read from the detector during data-taking, and which can be used as input to TRIDENT.

4.6.2 MAP

The whole processing of an event by GEANT is relatively slow as it forms digitisings in the wire chambers, allowing for clustering and noise etc.; it can be of the order of 1 second per event, and for large amounts of data, this is unacceptable. In order to surmount this problem, a less general programme is neccessary, and MAP[4-7] was written for this purpose.

Once again, the input to the programme MAP was a set of event records as generated by SAGE, and once again, the MAP processing of these events involved tracking them through the Omega field. MAP contained information on the positions of the apertures of various detector elements, and as it tracked each particle through the detector system, it checked that certain user definable trigger criteria were satisfied. The charged particle acceptance was completed in MAP by the inclusion of the package CERENK from JULIET, and the simulation of the Cerenkov detector. One of the main areas into which effort was put in WA57 was the simulation of the photon detector, as this was critical to the main physics channel of the experiment. This simulation involved the detailed modelling of the electromagnetic showers caused in the photon detector by incident photons, and their subsequent recording by the separate detector elements. With this model, MAP then wrote a data block which was used as input to SNARK. SNARK then analysed it as it did the real data, and reconstructed photons and π^0's from the event. The output from MAP was written in such a way as to resemble a DST event record, this output then being used as input to a GEORGE analysis programme.

References

4-1 TRIDENT Users Manual

J.-C. Lassalle et al.

CERN/DD/EE/79-2.

4-2 JULIET Users Manual

G. Lafferty

Internal E-Gamma Note

4-3 MULTIPIO Manual

D. Barberis

Internal E-Gamma Note

4-4 GEORGE/JULIET Users Manual

C. Raine and M. Storr

Internal E-Gamma Note

4-5 SAGE Reference Manual

J. Friedman

SLAC Computational Group Technical Memo 145

4-6 GEANT Reference Manual

R. Brun et al

CERN/DD/EE/78-2

4-7 MAP Reference Manual

A. Waite

Internal E-Gamma Note

Chapter V

THE CHANNEL $\gamma P \rightarrow \omega\pi^0 P$

5.1 INTRODUCTION

An enhancement at a mass of 1.25 GeV has been seen in a number of photoproduction experiments in the reaction

$$\gamma p \longrightarrow \pi^+\pi^-\pi^0\pi^0 p \qquad \ldots\ (5.1)$$

This enhancement has been proposed as a possible radial recurrence of the $\rho(770)$, but as yet, no definitive spin-parity analysis has been possible due to the limited statistics available, and there remains the strong possibility that the enhancement seen is due to the B(1235) meson which has spin-parity 1^+.

In 1970 in SLAC, Anderson et al.[5-1] reported on the photoproduction of a broad state with a mass of 1.24 GeV and a width of 100 MeV, and identified it with the B(1235) meson. Four years later, again in SLAC, Ballam et al.[5-2], observed an enhancement of the same mass with a width of 200 MeV, and showed that $\omega\pi^0$ was likely to be the main decay mode. They also observed that the production was consistent with being a s-channel helicity conserving process (SCHC), as is found in the production of the $\rho(770)$, and suggested that the enhancement might be due to a vector meson, although the decay correlations which they studied were not sufficient to allow a spin-parity determination. In 1979, a photoproduction experiment done by Barber et al.[5-3] at Daresbury, saw evidence for a state at a mass of 1.29 GeV, with a width of about 300 MeV, decaying into $\omega\pi^0$. The

spin-parity analysis done on this data yielded a predominantly 1^- component in the enhancement and although the situation was complicated by the presence of a large $\omega\Delta$ background, this state was tentatively identified with a possible $^3S_1$ radial excitation of the $\rho(770)$. At CERN in 1980, the experiment WA4 reported evidence for a state at a mass of 1.25 GeV with a width of 300 MeV, which decayed via $\omega\pi^0$, (Aston et al.[5-4]). They showed that the production was diffractive with an energy independant cross-section and that with the assumption of SCHC, the enhancement could not be attributed totally to the 1^+ B meson.

There is very little evidence from e^+e^- colliding beam experiments for the existance of such a state, although there have been some indications that it may be present[5-5].

The aim of the present experiment was to study the $\omega\pi^0$ enhancement with the intention of performing a spin-parity analysis which would be able to distinguish between the 1^+ B(1235) meson and a possible radial occurrence of the $\rho(770)$. A preliminary analysis of a section of this data has already been published, Atkinson at al.[5-6], and the present analysis is a continuation of that work. The purpose of this chapter is to present the data from the channel (5.1), and describe in detail the spin-parity analysis performed on it. The data selection will be discussed first, followed by a presentaion of the main features of the data. The model independant spin-parity analysis will then be described and this is followed by a discussion of the results obtained from a number of fits to the acceptance-corrected double moments.

5.2 DATA SELECTION

The purpose of the selections imposed on the data was to obtain a sample of well understood and well measured events which it was possible to simulate. The various event selection criteria are now described in more detail.

5.2.1 Beam Cuts

The energy of the incoming photon was required to have been well measured, this being defined by the class of tag produced by PHOTAG, described in Chapter 2. Photons which were tagged as either class 0 or 2 were accepted for the analysis ; these were the only ones for which a polarisation had been calculated. Although the polarisation did not prove to be useful in the analysis of the channel, it was neccessary to understand the polarisation of the events which were used, in order to avoid possible biases which could have been introduced into the analysis due to the acceptance being dependant upon the plane of the photon's polarisation. The tags rejected by this cut, tags 3 and 4, represented approximately 30% of the data-sample.

5.2.2 Vertex Cuts

The event vertex, as reconstructed by TRIDENT, was required to be within the volume of the liquid hydrogen target. The divergence of the beam, together with interactions before and after the target, resulted in event vertices which were outside the hydrogen, and these were rejected on the grounds that they were not examples of the process which we wanted to analyse. These events were more likely to be examples of photoproduction from complex nuclei, and thus were not comparable with the γp interactions which were of interest. In particular, events with vertices within the End-Cap were excluded.

The exclusion of these events reduced the final data sample by approximately 10%.

5.2.3 Charged Track Cuts

The charged tracks in the final state were required to have either charge balance, or a net charge of +1, in which case the slower of the two positive tracks had to be consistent with being a recoiling proton. The recoil proton identification was done within JULIET, which also classified tracks as π's, K's or baryons, on the basis of the information from the Cerenkov detector. Owing to the width of the momentum distribution of the π's and the existence of a region of inefficiency in the Cerenkov detector, there existed a considerable possibility that a π would fail to give Cerenkov light although it was above threshold and hence was misclassified as either a K or a fast baryon. Because of this possibility, all possible JULIET particle assignments were accepted, the tracks (apart from the recoil proton) being reclassified as π's. Thus the charged particles in the final state were either $\pi^+ \pi^- p$ or $\pi^+ \pi^-$.

5.2.4 Neutral Track Cuts

The number of JULIET reconstructed π^0's in the final state was limited to two, and it was required that all four of the photons from these π^0's had an energy above a certain limit, this limit being set at 250 MeV. This energy cut on the π^0 photon energy was decided upon by studying how the signal to background ratio in the photon-photon effective mass plot varied as the limit was changed. At 250 MeV, there were few π^0's lost from the peak, the loss being of the order of 10%, whilst the background was much reduced. This was taken to indicate that the reconstructed photons with energies of less than 250 MeV were in fact not true photons, but were due either electronic noise in the

photon detector, or to hadronic showers in the lead-glass array. Thus events in which there were any number of these low energy photons were accepted for analysis. Events were rejected if there were one or more high energy photons reconstructed i.e. with an energy of greater than 250 MeV, which had not been paired to a π^0.

5.2.5 Missing Mass Squared Cuts

To ensure that the events in the final sample were well measured, a selection was made on the missing mass from the system recoiling against the proton. This cut was made such that only those events with a missing mass squared of $\pm$ 3.0 GeV^2 about the proton mass squared were accepted for analysis. This cut contained all of the missing mass squared peak, and an estimated background of 20%.

5.3 GENERAL FEATURES OF THE 4-π DATA AND $\omega\pi^0$ SELECTION

The data sample obtained by the criteria outlined above consisted of both the $\omega\pi^0$ enhancement and a large contribution from the decay of the $\rho'(1600)$ which is known to decay via $\rho^{\pm}\pi^{\mp}\pi^0$ to $\pi^+\pi^-\pi^0\pi^0$. The general features of the production of the 4-π system are shown in Figure 5.1. In 5.1a, the photon energy spectrum for the selected 4-π events is shown, dropping away rapidly at high energies, this drop being due to the poor acceptance of the detector system for $2\pi^0$s ; this will be discussed in more detail in a later section. The polarisation spectrum for the analysed events, shown in Figure 5.1b, shows the contribution from each of the orientations of the tagging crystal. The numbers of events from the two orientations can be seen here to be unequal, and it is important for the spin-parity analysis that the net polarisation for the events analysed is 0 ; a weighting technique was used to ensure that this was indeed so in the final sample, this

weighting will be described more fully below. The 4-momentum transfer squared to the proton, shown in Figure 5.1c clearly exhibits a diffractive peak, and fits well to an exponential of the form e^{bt}, with b ~5. In Figure 5.1d, a peak can clearly be seen at the proton mass^2 in the missing mass^2 to $\pi^+\pi^-\pi^0\pi^0$. The effective mass of the 4-π system is shown in Figure 5.2a, and the $\rho'(1600)$ with a width of ~300 MeV can be clearly seen. The $\omega\pi^0$ enhancement can be seen at a mass of approximately 1.25 GeV, with a width of ~150 MeV. The Chew-Low plot in Figure 5.2b shows that the production is peripheral over the whole 4-π mass range. The general features of the 3-π system in the data are shown in Figure 5.3. The 3-π effective mass spectrum is shown in Figures 5.3a and 5.3b and shows a strong ω signal with a width of approximately 35 MeV, sitting on a 20% background. For the selection of the $\omega\pi^0$ signal from the data, a peak-wings background subtraction was employed, which will now be described in detail.

For each event there were two possible ω candidates, i.e. two 3-pion combinations. The effective mass of each of these combinations was formed, and then a "weight" was associated with the combination according to the rules given below. The ω 'peak' region was defined to be a range of effective masses which lay between limits 50 MeV above and below the nominal ω mass of 783 MeV. If either of the two candidates had an effective mass lying within this range, a weight of +1 was associated with it. On either side of this peak region, a 'wing' region was defined. Both these wing regions were 50 MeV wide, and any combination with an effective mass lying in either of the wings was labelled with a weight of -1. The mass regions lying outside both peak and wings were given zero weight, and the events in which both ω candidates fell outside both the peak and the wings were not included in the analysis. Each of the two ω candidates were then

used in the subsequent analysis, being incorporated with the appropriate background subtraction weight. In Figures 5.3c and 5.3d λ, the square of the ω decay matrix element is shown for the peak and the wing regions defined for this background subtraction. λ is defined as :----

$$\lambda = |\rho\pi^+ \times \rho\pi^-|^2 / |\rho\pi^+ \times \rho\pi^-|^2_{max} \quad \ldots\ldots (5.2)$$

For a 1^- ω-meson, the expected distributios rises linearly from 0 across the range 0 to 1, and as can be seen from the distributions in Figures 5.3c and 5.3d, the background subtraction method employed does successfully pick out the ω-meson signal. The two pion mass distributions shown in Figure 5.4 show evidence for the ρ^+ and ρ^- from the decay of the $\rho'(1600)$, whilst there is little evidence for a ρ^0 contribution. The angles used in the description of the sequential decay process $X \rightarrow \omega\pi^0 \rightarrow \pi^+\pi^-\pi^0\pi^0$ are shown in Figure 5.5 for all of the 4-π data i.e. before the $\omega\pi^0$ selection. These angles are defined in a later section describing the spin-parity analysis, but it should be noted here that the $\cos\theta$ distribution is severely affected by acceptance effects.

The 4-π effective mass spectrum resulting from this background subtraction is shown in Figure 5.6a, along with the corresponding four momentum transfer squared to the proton, in Figure 5.6b. As can be seen the $\omega\pi^0$ mass spectrum is predominantly in the peak at a mass on 1.25 GeV, with little or no contribution from the $\rho'(1600)$. The background subtracted 2-π effective mass distributions shown in Figure 5.7 show little evidence for any ρ-meson contamination of the data. In Figure 5.8, the background subtracted decay angles are shown.

5.4 SIMULATION OF THE CHANNEL $\gamma P \rightarrow \omega\pi^0 P$

Before embarking upon a description of the analysis procedure used and the results obtained, a brief outline of of the work done on the simulation of channel (5.1) will be given. The simulation work falls into three stages, a) event generation, b) MAP acceptance processing and c) post-MAP 'tuning'.

5.4.1 Event Generation

Using the programme SAGE [4-4], an $\omega\pi^0$ system was generated and then made to decay into the final state, $\pi^+\pi^-\pi^0\pi^0$. The input that SAGE requires is a specification of the particle types in the decay, the parameters of any resonances, and a beam momentum. For the input beam momentum, the experimental data from Trigger 8 (see section 2.4) was used as this gave as accurate a representation as was possible of the photon energy spectrum, and also allowed each event to be given a polarisation. The actual correlation between photon energy and polarisation was thus built into the simulation. For the acceptance studies the $\omega\pi^0$ system was generated with a Breit-Wigner line shape with a mass and width of 1.25 GeV and 150 MeV respectively. The events were generated such that the parent decay to $\omega\pi^0$ was isotropic whilst the decay of the ω into three pions was according to that of a $J^P = 1^-$ ω. The process was generated with a constant cross-section in energy.

5.4.2 MAP Processing

The sample of generated events described above were then used as input to MAP [4-6], the output from MAP being written in a DST format, suitable for reading by the analysis programmes.

MAP was set up to simulate trigger 5 of the experimental triggers described in Chapter 3, and thus used the A1Y wire plane as a trigger plane.

A preliminary analysis of the ρ-meson data from the experiment has shown that there was a considerable region of inefficiency in this trigger plane during the running of the experiment due to an incorrect voltage being applied to one of the support wires in the chamber. These support wires are included in the chamber in order to mechanically strengthen the design, and when raised to the correct voltage, they should not disturb the functioning of the wire chamber. One of the first indications that there was a problem came from the observation that there was an unexpected asymmetry in the dip distribution of the charged pions at the vertex. For the two pions in the ρ^0 data, this is shown in Figure 5.9a and 5.9b. A clearer illustration of the problem can be seen in the distribution of the projected pion impact points in the z-direction at the A1Y trigger plane. This is shown in Figure 5.9c and the strong depletion at the z-coordinate corresponding to the z-position of the support wire is evident. This is shown again in Figure 5.10 on a much expanded scale, and it can be seen that the inefficiency caused by the support wire is not of a simple shape, but consists of an area of very low efficiency centred at the position of the support wire, at z=1.5 cm. and a broader shallower region lying closer to the median plane of the spectrometer. The problem was further complicated by the fact that the inefficiency changed during the 4 periods of data-taking, as can be seen from Figure 5.11 where the z-impact of the pions is plotted for Periods 2 3 & 4. (The data from Period 1 was very badly affected by the trigger inefficiency). A measure of the total A1Y inefficiency can be found by forming an average over the 4 periods of the z-impact

position and then dividing the positive half of this distribution, i.e. the half with +ve z, by the negative half. With the assumption that the A1Y effect is restricted to the positive part of the distribution, and that other effects such as that due to the electromagnetic veto (which is responsible for the depletion at low |z|) are symmetrical about z=0, the resultant distribution should be a fairly good measure of the inefficiency caused by the support wire. This distribution is shown in Figure 5.12a, and in Figure 5.12b the actual distribution used in MAP for the $\omega\pi^0$ processing is shown. The distribution shown in Figure 5.12b was derived from that in Figure 5.12a by varying the depth and width of the inefficiency to obtain the best agreement between the charged pion dips in the $\omega\pi^0$ data and simulation.

For a data sample in which there were four photons i.e. two π^0's in the final state, MAP processing was fairly slow, and to speed this up, a preliminary filter was put on the data for processing which rejected any events in which one or more of the photons missed the geometrical aperture of the OLGA. This approximation led to no bias in the treatment of the data provided that we analysed only those events with four photons in the final state ; preliminary work showed that $\omega\pi^0$ candidates could be reconstructed from data in which there were three photons in the final state, under certain assumptions about the 'missing' photon, but the mass resolution on these events was such that they could not be usefully included in the spin-parity analysis. In addition to this filter, the data was passed through another filter which ensured that SNARK was able to reconstruct two π^0's from the four input photons after energy resolution 'smearing' etc. had been applied. No check was made however on whether or not SNARK reconstructed the π^0's from the correct γ-γ combinations ; the probability of the wrong combination being formed twice was estimated to be very low.

During the course of MAP processing, both the beam momentum and the momenta of the charged tracks were 'smeared' in an attempt to simulate beam resolution and energy-loss/multiple-scattering for the charged tracks.

5.4.3 Post-MAP Tuning

The output from MAP consisted of a sample of events which had both satisfied the required trigger conditions (i.e. those of trigger 5), and had also been subjected to some form of degradation due to a model experimental resolution, and therefore should have been comparable with the data. When this comparison was made however, it was found that there were discrepancies between the two data sets, some of which could be traced to the physics contained in the input data sample i.e. the mass and width of the Breit-Wigner, and some of which could be traced to the modelling of the performance of the detector during data-taking. The simulation of the photon detector was successful, and comparisons between the real data and the simulated data showed good agreement in this area. In the case of the charged tracks however, the main discrepancy between the two data sets was in the dip distribution of the π's at the vertex. The work done on the ρ-meson data has shown that this distribution is sensitive to the form and depth of the inefficiency which is simulated in the A1Y trigger plane. This work has indicated that the inefficiency has a structure similar to that shown in Fig. 5.12a ; the sharp deep region of inefficiency is thought to be due to a 'trigger' inefficiency, (which is what was parameterised and put into MAP), whilst the broader and shallower inefficiency was thought to be due to a track finding effect in TRIDENT. To obtain a better agreement between the simulated data and the real data, this part of the 'A1Y inefficiency' was parameterised and the simulated data

reweighted to give agreement with the real data. This was done by performing a 2-dimensional fit of the joint π dip distributions (π^+ and π^- dips are strongly correlated), to the real data, each of the simulated dip distributions being reweighted by a Gaussian inefficiency ; the χ^2 minimisation gave the best parameters for the reweighting to be used. Using this reweighting technique, the agreement between the simulated and the real data was improved. A comparison of the simulated and real data is given in Figs. 5.13 to 5.17.

The final, reweighted dip distribution of charged pions at the vertex from the 4-π data is shown in Figure 5.13a and the pion momentum distribution in Figure 5.13b. In both these distributions, there is fairly good agreement between the data (solid lines) and the simulation. Figures 5.14 to 5.16 show a comparison between the data and the simulation with respect to the performance of the photon detector and the reconstruction software. The π^0 energy spectrum is sensitive to the way in which energy is deposited in the lead glass array ; for instance, the photons from a symmetric, 10 GeV π^0 will hit the photon detector with a separation of approximately 14 cm., i.e. the width of an OLGA lead glass block, and the difficulty which the reconstruction software finds in trying to resolve the two photons at this energy leads to a loss of high energy π^0s. The minimum γ-γ separation distribution shown in Figure 5.16b is a particularly sensitive test of how the photon simulation agrees with the data, and as can be seen from the plot, the agreement is good.

Another test which was made on the simulation concerned the way in which a particular physics model was degraded by the acceptance. In Figure 5.17 are shown the results of a comparison between the simulation and the data, in which the angular distribution of the decay 5.3 was generated according to a matrix element which was

derived from the preliminary analysis of the data[5-6]. The agreement between the data and the simulation is once again good.

To ensure that the sample of events which were used in the analysis had no net polarisation, equal amounts of the two types of polarisation had to be added together. This was required because the analysis was concerned only with the unpolarised contribution to the angular distribution, and any residual effects due to the polarisation would have interfered with the interpretation of the results. In practice, each event was given a weight such that the polarisation from one orientation cancelled the polarisation from the other.

The simulated mass distribution for the $\omega\pi^0$ system was reweighted to agree with the data. The overall acceptance for the channel is of the order of 6%, most of the losses being caused by either a photon from a π^0 missing the aperture of the photon detector, or by SNARK failing to reconstruct $2\pi^0$'s in the event.

The above procedure was used to check the acceptance software, checking the whole mass range of interest. For the analysis described below, the mass range 0.9 GeV to 1.8 GeV was divided into 9 mass bins, and a dataset was generated for each of these and subsequently passed through the acceptance programme MAP. Each of these datasets was generated as a very narrow Breit-Wigner centred at the centre of the mass bin, and each bin was then weighted so as to reproduce the overall $\omega\pi^0$ mass distribution seen in the data.

5.5 SPIN-PARITY ANALYSIS

5.5.1 One-Dimensional Angular Distributions

The joint angular decay distribution of the $\omega\pi^0$ system, describing the sequential decay ; ---

$$\gamma p \rightarrow X p$$
$$\hookrightarrow \pi^+\pi^-\pi^0 \qquad \ldots\ldots (5.3)$$

can be described by four angles, two to describe each of the steps in the sequence. For the analysis presented in this Thesis, the helicity formalism is used, and the angles used in this description are described below. For the first set of angles the reference system is taken to be the helicity system of the $\omega\pi^0$ state. In this system the z-axis is defined to be the direction of flight of the $\omega\pi^0$ state in the γp c.m.s., and the y-axis is the normal to the production plane, defined by the cross product of the incoming photon momentum and the outgoing $\omega\pi^0$ momentum, both in the γp c.m.s.. The x-axis is then defined so as to make a right handed system. The polar and azimuthal angles θ and ϕ describe the direction of the ω momentum vector in this reference frame. For the second set of angles, the reference frame is the helicity system of the ω. Here, the z-axis is defined as the direction of flight of the ω in the $\omega\pi^0$ c.m.s., the y-axis is defined by the cross product of the $\omega\pi^0$ momentum and the ω momentum, and once again, the x-axis is defined in order to make a right handed system. The analyser relevant to this step in the decay sequence is the normal to the decay plane of the ω ; the direction of the normal is described by the angle θ_H and ϕ_H.

A first indication of the spin-parity content of the $\omega\pi$ system can be obtained from the distributions of these four angles, and although the interpretation of these distributions is complicated by

acceptance effects, they nevertheless give some important pointers to the spin structure of the system. The possible spin-parity states that can contribute to the $\omega\pi^0$ system of channel 5.1 are limited by angular momentum and parity conservation. For spin 0 and 1 the allowed states are 0^- and both 1^+ and 1^-. Both natural and unnatural parity spin 2 states could contribute, but there is no evidence to suggest their presence in the data and hence they have been excluded from the analysis.

Acceptance calculations have shown that the polar angle θ, used to describe the decay step $X \rightarrow \omega\pi^0$, is very heavily biased by both the geometrical acceptance of the detector and the π^0 reconstruction programme, and so no interpretation of the uncorrected distribution is attempted. The three remaining angles have been shown to be relatively unaffected by acceptance ; it is possible therefore to interpret them directly.

The ϕ distribution shown in Fig. 5.8b displays a $\sin\phi$ component, and as this can only arise from interference effects between the helicity ±1 and the helicity 0 substates of the $\omega\pi$, this rules out a completely SCHC production mechanism, in which the helicity of the photon is conserved at the γ-vector meson vertex.

The $\cos\theta_H$ distribution shows a strong $\sin^2\theta_H$ contribution. This arises from the ω helicity ±1 substates and thus rules out the dominance of 0^- in the $\omega\pi$ system. Either a dominant 1^+ or a dominant 1^- state could produce this effect, given a suitable D/S ratio in the first instance and the presence of a non-SCHC background with ω helicity 0 in the second.

The ϕ_H, with a strong $\cos2\phi_H$ component, indicates either a dominant SCHC 1^- state or a dominantly non-SCHC 1^+ state, i.e. one with $\rho^0_{00} > 0.3$. A 1^+ SCHC state would produce a $\sin2\phi_H$ component and is therefore almost ruled out.

The conclusions that can be drawn from an inspection of the single angle distributions are that a dominant 0^- $\omega\pi^0$ state is excluded, but that at this level of analysis a dominant 1^+ state and a dominant 1^- state cannot be distinguished from one another. To go beyond this, the various correlations that exist between the four decay angles must be incorporated into the analysis ; this is described in the next section.

5.5.2 Double-Moments Analysis

The spin-parity analysis of the $\omega\pi^0$ data presented here follows closely that performed by Chung et al.[5-7] on a closely related channel, $\pi^+p \rightarrow \pi^+\pi^-\pi^0\pi^+p$, in which the B(1235) meson was seen, decaying to $\omega\pi^+$; the purpose of this section is to briefly outline the main steps in this analysis ; a fuller description of the formalism is contained in Appendix A.

As shown by Chung[5-8], the joint angular distribution for the sequential decay of Equ.[n] 5.3, can be written in the helicity formalism as :---

$$I_{ij}(\Omega_1,\Omega_2) = \left(\frac{2J_i+1}{4\pi}\right)^{1/2}\left(\frac{2J_j+1}{4\pi}\right)^{1/2}\frac{3}{4\pi}$$

$$\times \sum_{M'\lambda\lambda'} \rho^{ij}_{M'} F^{i}_{\lambda 0} F^{j*}_{\lambda' 0} |F^{1}_{00}|^2$$

$$\times D^{J_i*}_{M\lambda}(\Omega_1) D^{J_j}_{M'\lambda'}(\Omega_1) D^{1*}_{\lambda 0}(\Omega_2) D^{1}_{\lambda' 0}(\Omega_2) \quad \ldots\ldots (5.4)$$

In this expression, the parent state is assumed to be a mixture of different spin-parity states, labelled by 'i' and 'j', and the symbols have the following meaning : ---

J_i, J_j Spins of the two interfering components of the parent state being considered.

Λ, Λ' Helicity subscripts for the parent state

λ, λ' Helicity subscripts for the ω

F^i_λ Helicity decay amplitudes which express the probability that the parent component with spin J_i will decay to produce an ω with helicity λ.

$\rho^{ij}_{\Lambda\Lambda'}$ The interference spin-density matrix elements.

$D^i_{\Lambda\lambda}$ Elements of the rotation matrix.

The two sets of angles, $\Omega_1=(\cos\theta,\phi)$, and $\Omega_2=(\cos\theta_H,\phi_H)$, which are used to describe the decay are defined in the preceding section. The D-functions are the angular rotation matrix elements defined by Rose[5-9], and by using the properties of these D-functions, the joint angular decay distribution can be written as :---

$$I_{ij} = \sum_{LMlm} \left(\frac{2L+1}{4\pi}\right)\left(\frac{2l+1}{4\pi}\right) H_{ij}(lmLM) \times D^{L*}_{Mm}(\Omega_1)\, D^{l*}_{m0}(\Omega_2) \quad \ldots\ldots (5.5)$$

In this expansion, the coefficients $H_{ij}(lmLM)$ are functions of the helicity decay amplitudes and of the interference spin density matrix elements, with : ----

$$H_{ij}(lmLM) = \left(\frac{2J_i+1}{2J_i+1}\right)^{\frac{1}{2}} \sum_{\Lambda\Lambda'} \rho^{ij}_{\Lambda\Lambda'} \langle J_j \Lambda' L M | J_i \Lambda\rangle \langle l\, 0\, L\, 0 | l\, 0\rangle \times \sum_{\lambda\lambda'} F^i_{\lambda 0} F^j_{\lambda' 0} \langle J_j \lambda' L m | J_i \lambda\rangle \langle l\, \lambda' L m | l\, \lambda\rangle \quad \ldots\ldots (5.6)$$

and consequently are subject to certain symmetry conditions (see Appendix A). These symmetry relations arise from parity conservation

in the production and decay of the $\omega\pi^0$ system and from the form of the spin density matrix. The symmetries can be incorporated into the expression for the angular distribution to give :---

$$I_{ij}(\Omega_1,\Omega_2) = \sum_{LL}\sum_{m\geq 0;M\geq 0}\left(\frac{2L+1}{4\pi}\right)\left(\frac{2l+1}{4\pi}\right)(2-\delta_{m0})(2-\delta_{M0}) \times 2\,Re\{H_{ij}(lmLM)\}\ {}^{ij}E_{LM}^{lm}(\Omega_1,\Omega_2) \quad \ldots\ (5.7)$$

where the angular terms are :---

$${}^{ij}E_{LM}^{lm} = \frac{1}{2}Re\left\{D_{Mm}^{L}(\Omega_1)\,D_{m0}^{l}(\Omega_2) + \eta_i\eta_j(-1)^{L}D_{M-m}^{L}(\Omega_1)\,D_{-m0}^{l}(\Omega_2)\right\} \quad \ldots\ (5.8)$$

As can be seen from this expansion, the coefficients in the full angular distribution can be split into two groups, depending upon whether $\eta_i\eta_j$ is +1 or -1, where η_i is the parity of the state labelled i. In the case where this product is +1, only those interference moments which arise from either pure spin parity states or from states of equal parity can contribute, whilst if $\eta_i\eta_j$ is equal to -1, the interference effects from states of different parities can contribute. These two groups will be refered to as 'even' and 'odd' moments respectively. From Equ^{n}. 5.6, the H's can be expressed as functions of the helicity decay amplitudes and the interference spin density matrix ; these expressions are shown in Table 5.1. The number of terms present in the expansion is related by the possible spin-parity states present. For a mixture of 0^-, 1^+ and 1^-, the 25 double moments shown in Table 5.1 are sufficient to describe all possible interference effects. These 25 expressions can be grouped into even and odd moments as described above, with 14 even moments and 11 odd moments. The angular dependance of these double-moments is shown in Table 5.2. By evaluating a sufficient number of moments of the joint angular decay distribution, we can obtain an overconstrained set of equations with which it is possible to fit the spin

density matrix elements and the helicity decay amplitudes. A number of these fits have been done, under various assumptions about the spin-parity content of the parent state, and the results from these fits will be presented in the next section. The method used to correct the data for acceptance effects follows closely that of Grayer et al.[5-10], and is described in Appendix B. The form of the corrected moment sums as a function of $\omega\pi^0$ mass is shown in Fig. 5.18.

5.6 FITS TO THE EXPERIMENTAL MOMENTS

After using the method described in Appendix B to correct the experimental double moments for the effects of acceptance, the expressions shown in Table 5.1 were used to perform fits to the spin density matrix elements and decay amplitudes.

The data moments and correlation matrix were formed in each of nine mass bins in the $\omega\pi^0$ mass range of 0.9 GeV to 1.8 GeV. The moments and correlation matrix for each bin were then corrected for acceptance, and these corrected moments and error matrix were used in conjuction with the expressions shown in Table 5.1 to form a χ^2 function which was minimised using the programme MINUIT[5-11]. The χ^2 minimisation was done for each bin independantly, and a series of such fits to the data moments were done, differing in the assumed spin-parity composition of the parent $\omega\pi^0$ state.

In the first fit, all three of the possible spin-parity components considered in this analysis were included, thus giving 25 moments sums and 17 free parameters in each mass bin. These 17 parameters were as follows : for the 1^+ state there was a normalisation, N^{1^+}, three spin density matrix elements, ρ^{+}_{00}, ρ^{+}_{10}, ρ^{+}_{11} and the D/S ratio ; for the 1^- state there was simililarly a normalistion N^{1^-} and three spin density matrix elements ρ^{-}_{00}, ρ^{-}_{10} and ρ^{-}_{11}; for the 0^- state

there was a normalisation N^{0^-}. The remaining parameters in the fit were interference density matrix elements, four describing the interference between the 1^+ and 1^- states, ρ^{+-}_{11}, ρ^{+-}_{1-1}, ρ^{+-}_{10}, ρ^{+-}_{01}, and three describing the interference effects between the spin 1 states and the spin 0 state, ρ^{0-}_{01}, ρ^{0+}_{00}, and ρ^{0+}_{01}. These 17 parameters are sufficient to describe fully any parent state which consists only of 1^+, 1^- and 0^- components.

The first set of fits were made with no conditions imposed on these 17 parameters, apart from the trace conditions on the spin density matrix elements and conditions that limited the parameters to physically accessible regions. The results from the first fit are shown in Fig. 5.19. Broadly speaking, the results from this first fit indicate a roughly equal amount of 1^+ and 1^- with a 0^- contribution of approximately one third of the size of either of the spin 1 components. The fit gives a good χ^2 probability in all nine mass bins. In general the fitted parameters are strongly correlated with large errors. The errors quoted in these results are those returned by MINUIT, and correspond to a change of 1 in the χ^2 function.

The 1^+ component peaks at an $\omega\pi^0$ mass of 1.25 GeV and has a spin density matrix which exhibits a non-SCHC production mechanism. The 1^- component is much broader, peaks in the same bin as the 1^+ component and has a spin density matrix which is consistent with SCHC, i.e. $\rho_{00}=0$ within errors, across the whole mass range.

The fit was repeated varying the way in which the χ^2 minimum was approached. Another solution, shown in Fig. 5.20 was found which showed almost identical χ^2 behaviour to the first. In this solution however there was a dominant 1^- signal, though in this case it is not so clearly SCHC. We had then two solutions, equally good, in which the relative amounts of 1^+ and 1^- were significantly different,

whilst the 0^- component was the same in either case. The two solutions differ only slightly in the spin density matrices whilst the interference spin density matrix shows no strong $\omega\pi^0$ mass dependance in either case. The inability of the χ^2 function to distinguish between these solutions may be traced back to the large acceptance effect seen in the $\cos\theta$ distibution, and the consequently large errors on the acceptance-corrected moments involving this angle. The main resolving power comes from the remaining three angles, the Φ and the θ_H and Φ_H. The relative amount of helicity 0 and helicity 1 ω could be due either to a 1^+ state with a certain D/S ratio, or a mixture of an SCHC 1^- state and a 0^- state.

In order to proceed further in the analysis, it was neccessary to introduce some further restriction on the possible spin-parity states present in the parent. In view of the observations made above together with the fact that a 0^- state could not have been diffractively produced, the 0^- intensity was fixed at 0 and the fit was repeated. In this second set of fits then, there were 13 free parameters in each of the mass bins. The results of the second fit, for which only one solution was found, are shown in Fig. 5.21. Once again, the fit gives an acceptable χ^2 probability in all of the nine mass bins, and in this fit the amounts of 1^+ and 1^- are again approximately equal. The 1^- signal is approximately SCHC over the mass range.

A third fit was then performed on the moments whilst constraining the 1^- component to be SCHC across the whole mass range, and the results of this fit are shown in Figures 5.22. The χ^2 probability is once again acceptable in all of the mass bins. The dominant signal is now the 1^+, with approximately 20% of the peak signal being 1^-. The 1^+ signal has a ρ_{00} of ~0.4 in the peak region and a D/S ratio close to that expected for the B(1235). The

interference density matrix elements show no strong dependance upon $\omega\pi^0$ mass.

5.7 CONCLUSIONS

The aim of the experiment WA57 was to clarify the status of the enhancement at a mass of 1.25 GeV seen in the reation $\gamma p \rightarrow \omega\pi^0 p$. This enhancement has been suggested as a candidate for the first radial recurrence of the ρ-meson, but may also have been produced by the B(1235) meson.

A detailed spin-parity analysis was performed on the $\omega\pi^0$ data from the experiment and the results are as follows : ---

1) There is little or no 0^- contribution to the enhancement

2) The 1^- component is approximately SCHC across the whole mass range studied, i.e. from 0.9 GeV to 1.8 GeV

3) When the 1^- component is constrained to be SCHC, the dominant contribution to the enhancement has spin-parity 1^+. This 1^+ signal peaks at an $\omega\pi^0$ mass of ~1.25 GeV, with a width of ~200 MeV; the D/S ratio in the peak region is ~0.4.

The 1^+ signal seen in the enhancement is consistent with being the B(1235) meson, and as the 1^- signal shows no resonant structure, it data do not need a ρ'(1250).

In conclusion then, the enhancement has been shown to be dominantly a 1^+ signal, consistent with the B(1235) meson, with a 20% 1^- SCHC background which exhibits no resonance structure. The t dependance seen in the data suggests a diffractive production for the enhancement.

References

5-1 R. Anderson et al.
Phys. Rev. Vol. D1 (22) 1970

5-2 J. Ballam et al.
Nucl. Phys. Vol. B76 (375) 1974

5-3 D. P. Barber et al.
Zeit. Phys. Vol. C4 (169) 1980

5-4 D. Aston et al.
Phys. Lett. Vol. 92 (211) 1980B

5-5 M. Conversi et al.
Phys. Lett. Vol. 52 (493) 1974B

5-6 M. Atkinson et al.
"Photoproduction of the $\omega\pi^0$ State In The Energy Range 20 - 70 GeV.". Paper contributed to the 1981 Int. Conf. on Lepton/Photon Interactions as High Energy, Bonn, 1981.

5-7 S. U. Chung et al.
Phys. Rev. Vol. D11 (2426) 1975

5-8 S. U. Chung
CERN Yellow Report "Spin Formalisms" CERN 71-8 (1971)

5-9 M. E. Rose
Elementary Theory of Angular Momentum
(Wiley and Sons Inc. New York 1957)

5-10 G. Grayer et al.
Nuc. Phys. B Vol. 75 (189) 1974

5-11 F. James and M. Roos
MINUIT
CERN Computer Centre Programme Library Long Writeup

Figures And Tables for Chapter 5

Table 5.1 : Expressions for the coefficients of the joint angular decay distribution on terms of the interference spin-density matrix and the helicity decay amplitudes

Table 5.2 : Expressions for the double-moments of the joint angular decay distribution in terms of the four decay angles θ, ϕ θ_H and ϕ_H

Figure 5.1 : a) The incident photon energy spectrum for all of the 4-π data from the channel $\gamma p \rightarrow \pi^+\pi^-\pi^0\pi^0 p$
b) The polarisation spectrum for the photons used in the analysis of the 4-π data
c) The four momentum-transfer squared to the proton from the channel $\gamma p \rightarrow \pi^+\pi^-\pi^0\pi^0 p$
d) The missing mass squared to the 4-π system recoiling against the proton (shown before the missing mass squared cut of ±3 GeV. about the proton mass^2 has been made)

Figure 5.2 : a) The effective mass of the 4-π system before $\omega\pi^0$ selectiion
b) The Chew-Low plot for the 4-π data

Figure 5.3 : a) The 3-π effective mass for all the 4-π data
b) The 3-π effective mass in the region of the ω
c) The ω decay matrix element for the ω peak region
d) The 3-π decay matrix element for the two wing regions in the 3-π mass range

Figure 5.4 : a) The $\pi^+\pi^-$ effective mass plot for the 4-π data before $\omega\pi^0$ selection
b) The $\pi^+\pi^0$ effective mass plot for the 4-π data before $\omega\pi^0$ selection
c) The $\pi^-\pi^0$ effective mass plot for the 4-π data before $\omega\pi^0$ selection

Figure 5.5 : a) The cosθ distribution for the whole 4-π data sample
b) The ϕ distribution for the whole 4-π data sample
c) The cosθ_H distribution for the whole 4-π data sample
d) The ϕ_H distribution for the whole 4-π data sample

Figure 5.6 : a) The 4-π effective mass after selection
b) [illegible]ution after selection of $\omega\pi^0$

Figure 5.7 : a) The $\pi^+\pi^-$ effective mass plot after $\omega\pi^0$ selection
b) The $\pi^+\pi^0$ effective mass plot after $\omega\pi^0$ selection
c) The $\pi^-\pi^0$ effective mass plot after $\omega\pi^0$ selection

Figure 5.8 : a) The angle θ after $\omega\pi^0$ selection. This angle is the most heavily biased by the acceptance of the apparatus, particularly the π^0 reconstruction
b) ϕ after $\omega\pi^0$ selection
c) θ_H after $\omega\pi^0$ selection
d) ϕ_H after $\omega\pi^0$ selection

Figure 5.9 : a) The dip distribution at the vertex for the π^+ from the ρ data taken during WA57
b) The dip distribution for the π^- from the ρ data
c) The projected impact postion at the A1Y trigger plane of the charged pions from the ρ data

Figure 5.10 : a) & b) Negative and positive hit distributions projected onto A1Y

Figure 5.11 : Projected z-impact positions at A1Y for 3 of the four periods of data-taking, for ρ data

Figure 5.12 : a) A measure of the inefficiency caused by the support wire calculated from the ρ data
b) The A1Y inefficiency used in MAP for the processing of the $\omega\pi^0$ data

Figure 5.13 : a) A comparison of the final simulation dip distribution of the charged πs with the data. The simulation is plotted with a dashed line.
b) The momentum spectrum of the charged πs, data and simulation

Figure 5.14 a) The π^0 energy spectrum from the data and the simulation.
b) The radial separation of γs on the face of OLGA for the data and the simulation

Figure 5.15 a) & b) Minimum and maximum γ energies in the $\omega\pi^0$ events for both data and simulation

Figure 5.16 a) The number of blocks per cluster as found by SNARK during processing of the data and the simulation. This distribution is very sensitive to the way in which energy is shared between the different elements in the photon detector
b) The minimum radial γ-γ separation on the face of OLGA

Figure 5.17 : A comparison the angle used in the analysis. The data is here compared with the results of a simulation in which the $\omega\pi^0$ decay is generated with a matrix element calculated from a preliminary analysis of the data

Figure 5.18 The 25 double moment sums used in the analysis as a function of the $\omega\pi^0$ effective mass

Figure 5.19A The 1^+, 1^- and 0^- intensites from the first set of fits

to the double-moment sums. The χ^2 probability is good in all of the nine mass bins analysed

5.19B The 1^+ signal matrix elements and D/S ratio from the first fit

5.19C The 1^- signal matrix elements from the first fit

5.19D The $1^+/1^-$ interference matrix elements from the first fit

5.19E The interference matrix elements between the spin 0 state and the two spin 1 states

Figure 5.20A - 5.20E As for 5.19a - 5.19E but for a nearby solution

Figure 5.21A The 1^+ and 1^- intensites resulting from the second fit

5.21B The 1^+ parameters from the second fit

5.21C The 1^- parameters from the second fit

5.21D The $1^+/1^-$ interference matrix elements from the second fit

Figure 5.22A The 1^+ and 1^- intensites from the third fit

5.22B The 1^+ parameters from the third fit

5.22C The $1^+/1^-$ interference from the third fit

Table 5.1

Unpolarized moment sums $NH_S^0(\ell mLM)$

1	$NH_S^+(0000)$	$N^+ + N^- + N^0$
2	$NH_S^+(0020)$	$\frac{1}{5} N^+(3\rho_{00}^+-1)(1-3F_1^2) - \frac{1}{10} N^-(3\rho_{00}^--1)$
3	$NH_S^+(0021)$	$\frac{2\sqrt{3}}{5} N^+\rho_{10}^+(1-3F_1^2) - \frac{\sqrt{3}}{5} N^-\rho_{10}^-$
4	$NH_S^+(0022)$	$-\frac{\sqrt{6}}{5} \rho_{1-1}^+(1-3F_1^2) + \frac{\sqrt{6}}{10} N^-\rho_{1-1}^-$
5	$NH_S^+(2000)$	$\frac{2}{5} N^+(1-3F_1^2) - \frac{N^-}{5} + \frac{2}{5} N^0$
6	$NH_S^+(2020)$	$\frac{N^+}{25} (3\rho_{00}^+-1)(2-3F_1^2) + \frac{N^-}{50} (3\rho_{00}^--1)$
7	$NH_S^+(2021)$	$\frac{2\sqrt{3}}{25} N^+\rho_{10}^+(2-3F_1^2) + \frac{\sqrt{3}}{25} N^-\rho_{10}^-$
8	$NH_S^+(2022)$	$\frac{-\sqrt{6}}{25} N^+\rho_{1-1}^+(2-3F_1^2) - \frac{\sqrt{6}}{50} N^-\rho_{1-1}^-$
9	$NH_S^+(2120)$	$\frac{3N^+}{25} (3\rho_{00}^+-1)F_1F_0$
10	$NH_S^+(2121)$	$\frac{6\sqrt{3}}{25} N^+\rho_{10}^+F_1F_0$
11	$NH_S^+(2122)$	$\frac{-3\sqrt{6}}{25} N^+\rho_{1-1}^+F_1F_0$
12	$NH_S^+(2220)$	$\frac{3}{25} N^+(3\rho_{00}^+-1)F_1^2 - \frac{3N^-}{50} (3\rho_{00}^--1)$
13	$NH_S^+(2221)$	$\frac{6\sqrt{3}}{25} N^+\rho_{10}^+F_1^2 - \frac{3\sqrt{3}}{25} N^-\rho_{10}^-$
14	$NH_S^+(2222)$	$\frac{-3\sqrt{6}}{25} N^+\rho_{1-1}^+F_1^2 + \frac{3\sqrt{6}}{50} N^-\rho_{1-1}^-$
15	$NH_S^+(2111)$	$\frac{\sqrt{3}}{5} (N^0N^-)^{\frac{1}{2}} \rho_{01}^{0-}$
16	$NH_S^-(0010)$	$2\sqrt{2} (N^+N^-)^{\frac{1}{2}} \rho_{11}^{+-}F_1 + \frac{2}{\sqrt{3}} (N^0N^+)^{\frac{1}{2}} \rho_{00}^{0+}F_0$
17	$NH_S^-(0011)$	$-\sqrt{2} (N^+N^-)^{\frac{1}{2}} (\rho_{01}^{+-} + \rho_{10}^{+-})F_1 + \frac{2}{\sqrt{3}} (N^0N^+)^{\frac{1}{2}} \rho_{01}^{0+}F_0$
18	$NH_S^-(2110)$	$\frac{-\sqrt{6}}{5} (N^+N^-)^{\frac{1}{2}} \rho_{11}^{+-}F_0 + \frac{2}{5} (N^0N^+)^{\frac{1}{2}} \rho_{00}^{0+}F_1$
19	$NH_S^-(2111)$	$\frac{1}{5}\sqrt{\frac{3}{2}} (N^+N^-)^{\frac{1}{2}} (\rho_{01}^{+-} + \rho_{10}^{+-})F_0 + \frac{2}{5} (N^0N^+)^{\frac{1}{2}} \rho_{01}^{0+}F_1$
20	$NH_S^-(2121)$	$\frac{3}{25}\sqrt{\frac{3}{2}} (N^+N^-)^{\frac{1}{2}} (\rho_{01}^{+-} - \rho_{10}^{+-})F_0$
21	$NH_S^-(2122)$	$\frac{3\sqrt{3}}{25} (N^+N^-)^{\frac{1}{2}} \rho_{1-1}^{+-}F_0$
22	$NH_S^-(2221)$	$\frac{6}{25}\sqrt{\frac{3}{2}} (N^+N^-)^{\frac{1}{2}} (\rho_{01}^{+-} - \rho_{10}^{+-})F_1$
23	$NH_S^-(2222)$	$\frac{6\sqrt{3}}{25} (N^+N^-)^{\frac{1}{2}} \rho_{1-1}^{+-}F_1$
24	$NH_S^-(2010)$	$\frac{-2\sqrt{2}}{5}(N^+N^-)^{\frac{1}{2}} \rho_{11}^{+-}F_1 + \frac{4}{5\sqrt{3}} (N^0N^+)^{\frac{1}{2}} \rho_{00}^{0+}F_0$
25	$NH_S^-(2011)$	$\frac{\sqrt{2}}{5} (N^+N^-)^{\frac{1}{2}} (\rho_{01}^{+-} + \rho_{10}^{+-})F_1 + \frac{4}{5\sqrt{3}} (N^0N^+)^{\frac{1}{2}} \rho_{01}^{0+}F_0$

Table 5.2

$H^{\pm}_{\ell mLM}(\cos\theta, \phi, \cos\theta_H, \phi_H)$

1	$H^+(0000)$	1
2	$H^+(0020)$	$\frac{1}{2}(3\cos^2\theta-1)$
3	$H^+(0021)$	$-\sqrt{\frac{3}{2}}\sin\theta\cos\theta\cos\phi$
4	$H^+(0022)$	$\sqrt{\frac{6}{4}}\sin^2\theta\cos(2\phi)$
5	$H^+(2000)$	$\frac{1}{2}(3\cos^2\theta_H-1)$
6	$H^+(2020)$	$\frac{1}{4}(3\cos^2\theta_H-1)(3\cos^2\theta-1)$
7	$H^+(2021)$	$-\frac{1}{2}\sqrt{\frac{3}{2}}\sin\theta\cos\theta\cos\phi\,(3\cos^2\theta_H-1)$
8	$H^+(2022)$	$\sqrt{\frac{6}{8}}\sin^2\theta\cos(2\phi)\,(3\cos^2\theta_H-1)$
9	$H^+(2120)$	$-\frac{3}{2}\sin\theta\cos\theta\sin\theta_H\cos\theta_H\cos\phi_H$
10	$H^+(2121)$	$-\frac{1}{4}\sqrt{\frac{3}{2}}\sin\theta_H\cos\theta_H\left\{(1+\cos\theta)(2\cos\theta-1)\cos(\phi+\phi_H)-(1-\cos\theta)(2\cos\theta+1)\cos(\phi_H-\phi)\right\}$
11	$H^+(2122)$	$\frac{1}{4}\sqrt{\frac{3}{2}}\sin\theta\sin\theta_H\cos\theta_H\left\{(1+\cos\theta)\cos(2\phi+\phi_H)-(1-\cos\theta)\cos(2\phi-\phi_H)\right\}$
12	$H^+(2220)$	$\frac{3}{8}\sin^2\theta\sin^2\theta_H\cos(2\phi_H)$
13	$H^+(2221)$	$\frac{1}{4}\sqrt{\frac{3}{8}}\sin\theta\sin^2\theta_H\left\{(1+\cos\theta)\cos(2\phi_H+\phi)-(1-\cos\theta)\cos(2\phi_H-\phi)\right\}$
14	$H^+(2222)$	$\frac{1}{8}\sqrt{\frac{3}{8}}\sin^2\theta_H\left\{(1+\cos\theta)^2\cos(2\phi+2\phi_H)+(1-\cos\theta)^2\cos(2\phi-2\phi_H)\right\}$
15	$H^+(2111)$	$-\frac{1}{4}\sqrt{\frac{3}{2}}\sin\theta_H\cos\theta_H\left\{(1+\cos\theta)\cos(\phi+\phi_H)+(1-\cos\theta)\cos(\phi-\phi_H)\right\}$
16	$H^-(0010)$	$\cos\theta$
17	$H^-(0011)$	$-\sqrt{\frac{1}{2}}\sin\theta\cos\phi$
18	$H^-(2110)$	$-\frac{\sqrt{3}}{2}\sin\theta\sin\theta_H\cos\theta_H\cos\phi_H$
19	$H^-(2111)$	$\frac{1}{4}\sqrt{\frac{3}{2}}\sin\theta_H\cos\theta_H\left\{(1-\cos\theta)\cos(\phi-\phi_H)-(1+\cos\theta)\cos(\phi+\phi_H)\right\}$
20	$H^-(2121)$	$-\frac{1}{4}\sqrt{\frac{3}{2}}\sin\theta_H\cos\theta_H\left\{(1+\cos\theta)(2\cos\theta-1)\cos(\phi+\phi_H)+(1-\cos\theta)(2\cos\theta+1)\cos(\phi-\phi_H)\right\}$
21	$H^-(2122)$	$\frac{1}{4}\sqrt{\frac{3}{2}}\sin\theta\sin\theta_H\cos\theta_H\left\{(1+\cos\theta)\cos(2\phi+\phi_H)+(1-\cos\theta)\cos(2\phi-\phi_H)\right\}$
22	$H^-(2221)$	$\frac{1}{4}\sqrt{\frac{3}{8}}\sin\theta\sin^2\theta_H\left\{(1+\cos\theta)\cos(2\phi_H+\phi)+(1-\cos\theta)\cos(2\phi_H-\phi)\right\}$
23	$H^-(2222)$	$\frac{1}{8}\sqrt{\frac{3}{8}}\sin^2\theta_H\left\{(1+\cos\theta)^2\cos(2\phi+2\phi_H)-(1-\cos\theta)^2\cos(2\phi-2\phi_H)\right\}$
24	$H^-(2010)$	$\frac{1}{2}\cos\theta\,(3\cos^2\theta_H-1)$
25	$H^-(2011)$	$-\frac{1}{2\sqrt{2}}\sin\theta\cos\phi\,(3\cos^2\theta_H-1)$

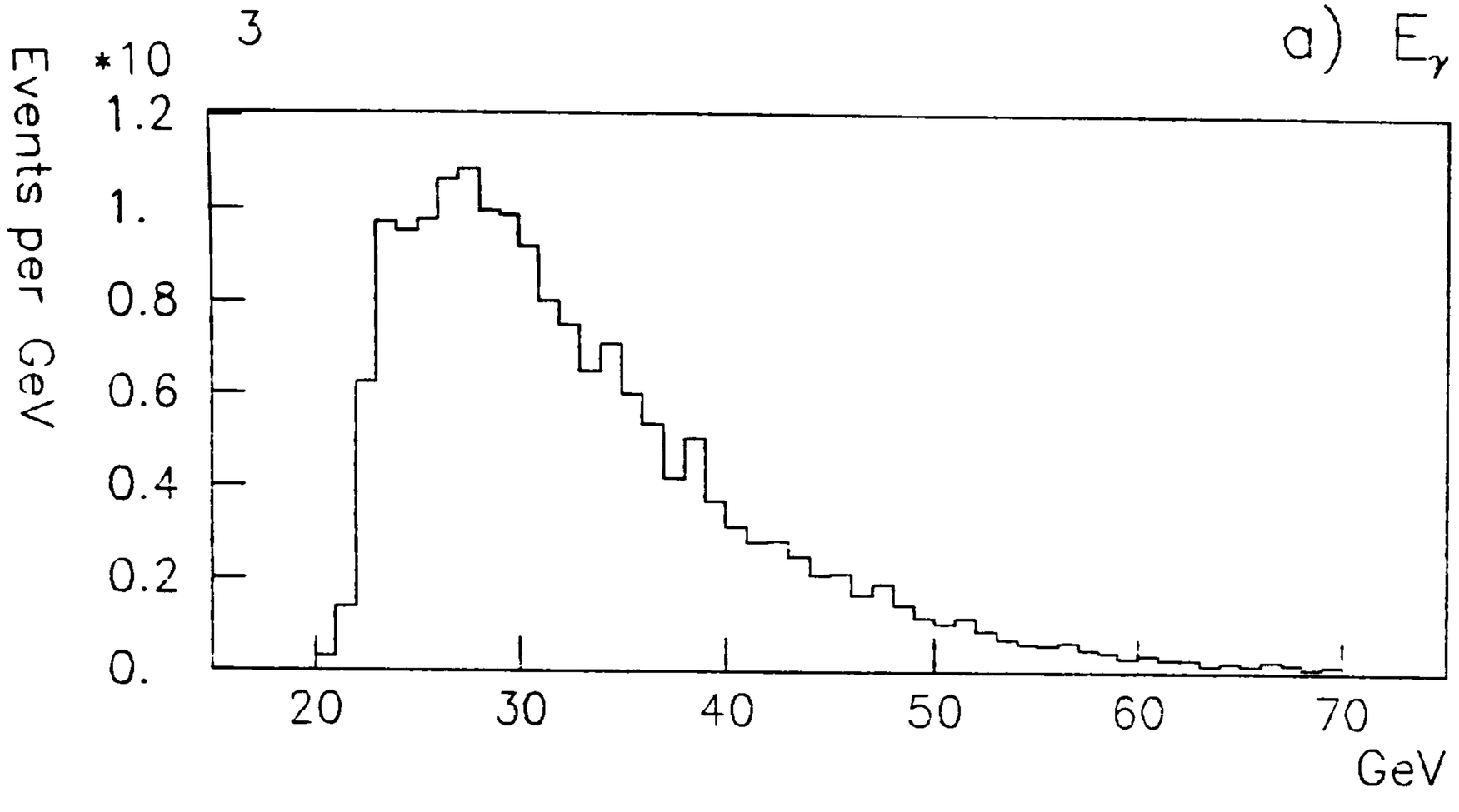
a) E_γ
3
*10
Events per GeV
1.2
1.
0.8
0.6
0.4
0.2
0.
20
30
40
50
60
70
GeV

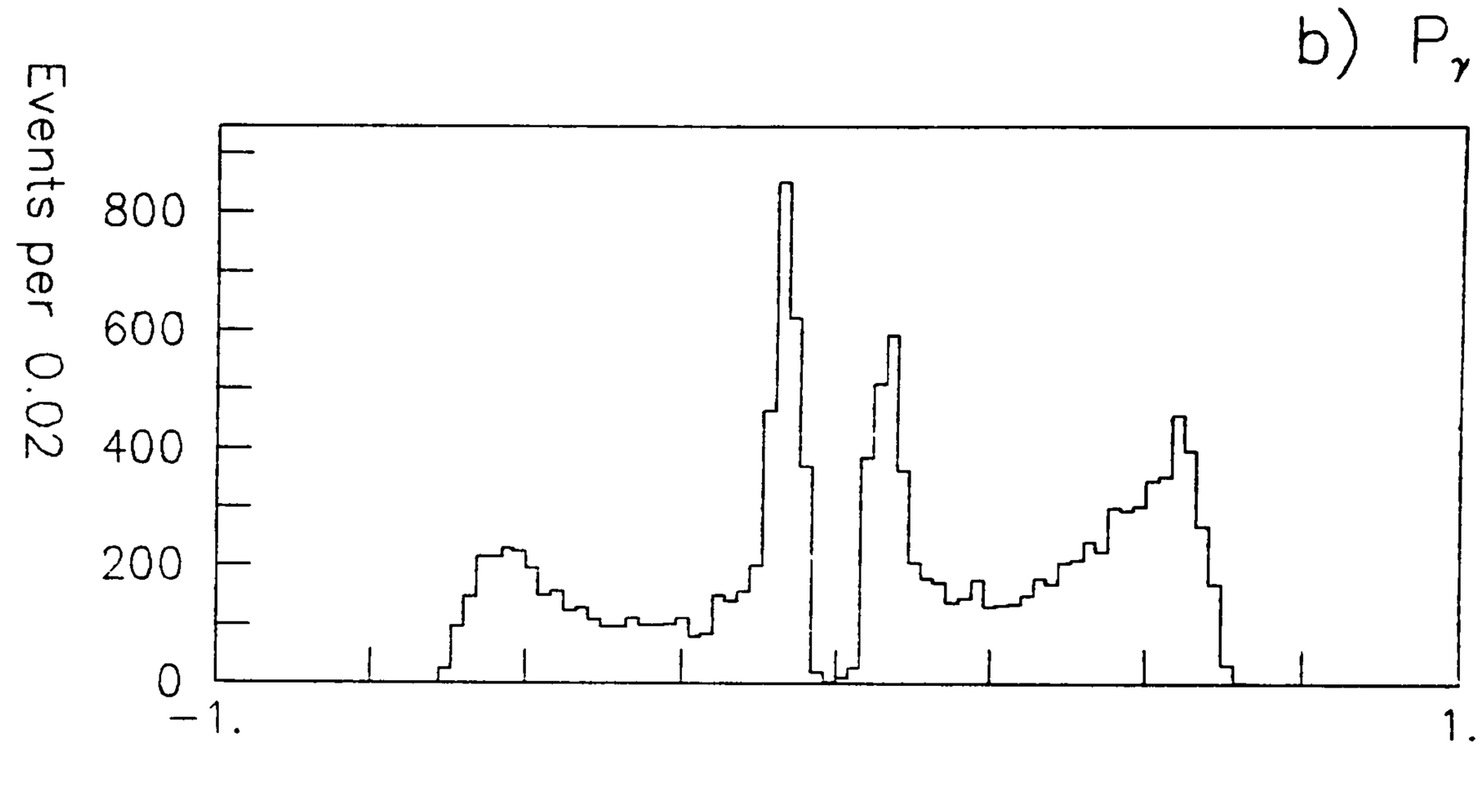
b) P_γ
Events per 0.02
800
600
400
200
0
−1.
1.

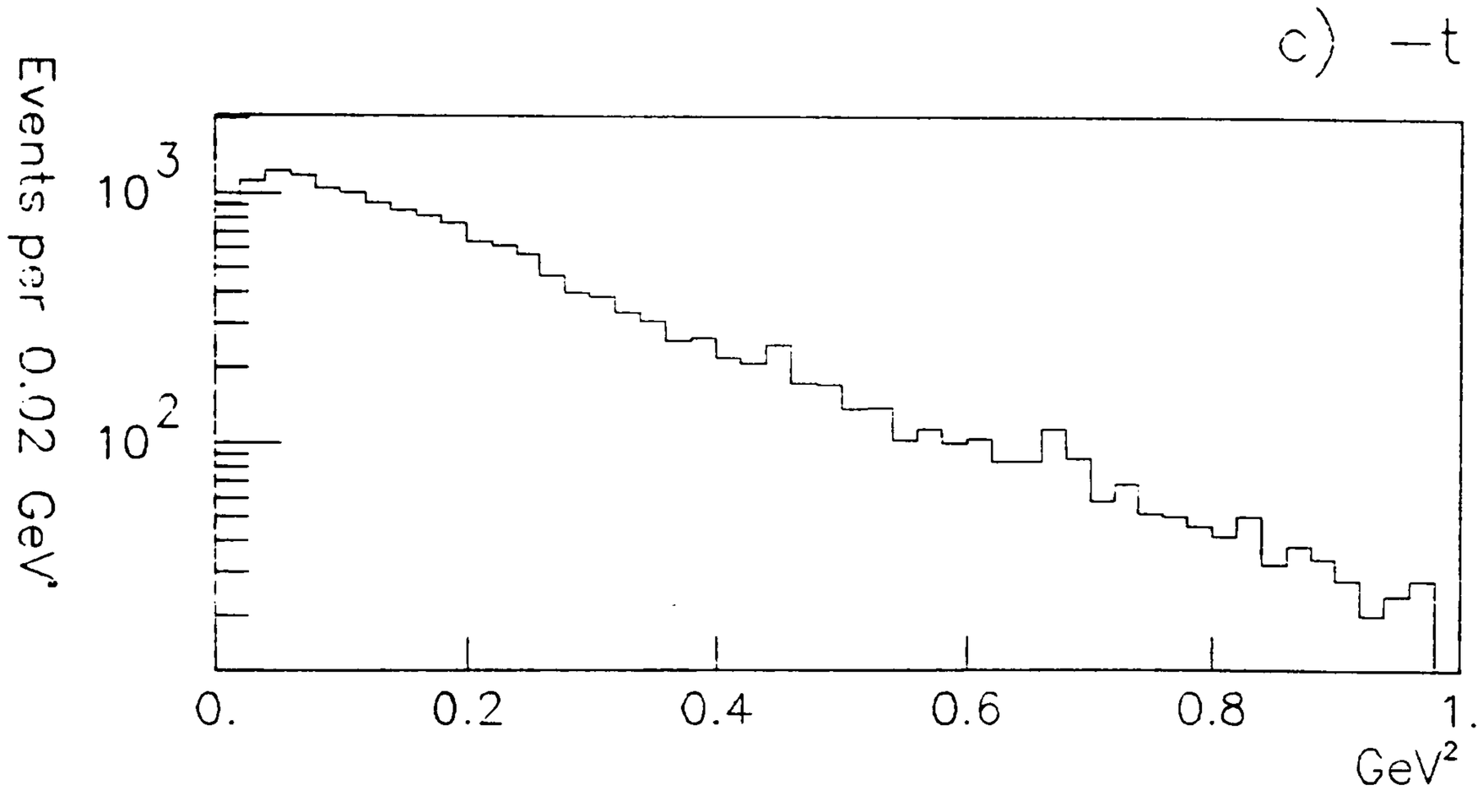
c) −t
Events per 0.02 GeV²
10^3
10^2
0.
0.2
0.4
0.6
0.8
1.
GeV²

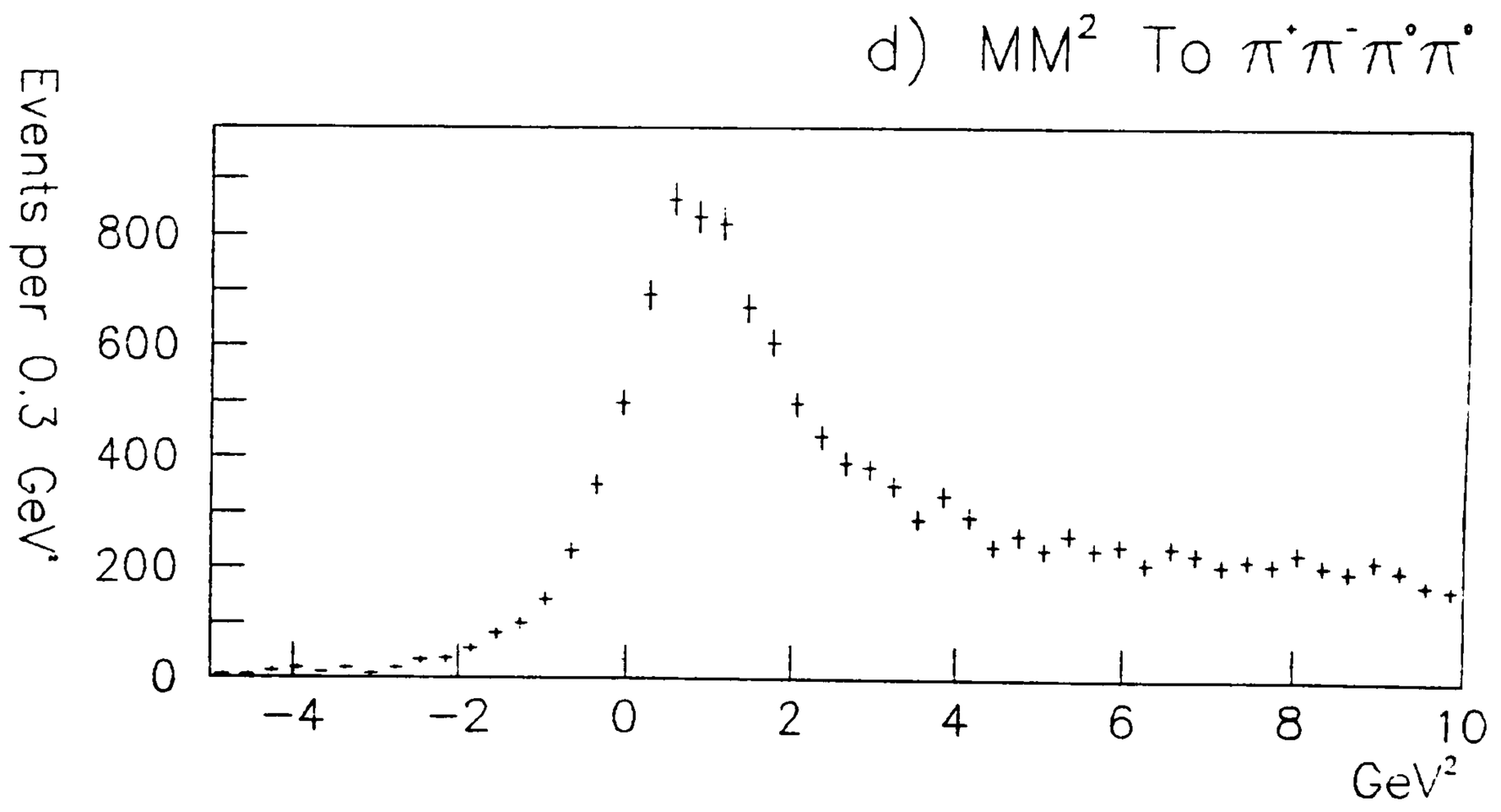
d) MM^2 To $\pi^+\pi^-\pi^0\pi^0$
Events per 0.3 GeV²
800
600
400
200
0
−4
−2
0
2
4
6
8
10
GeV²

Figure 5.1

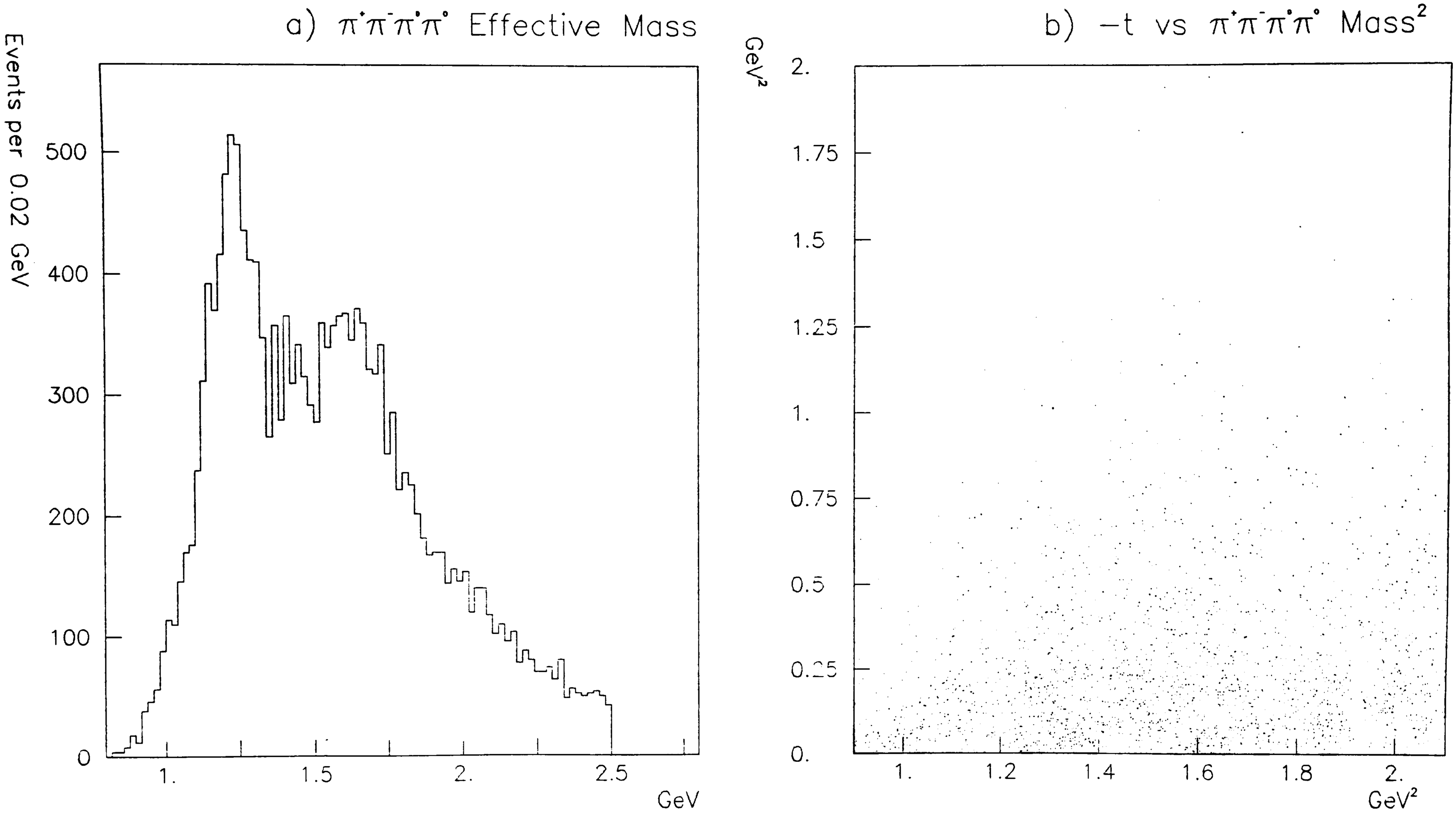
a) $\pi^+\pi^-\pi^+\pi^-$ Effective Mass
Events per 0.02 GeV
500
400
300
200
100
0
1.
1.5
2.
2.5
GeV
b) $-t$ vs $\pi^+\pi^-\pi^+\pi^-$ Mass^2
GeV^2
2.
1.75
1.5
1.25
1.
0.75
0.5
0.25
0.
1.
1.2
1.4
1.6
1.8
2.
GeV^2

Figure 5.2

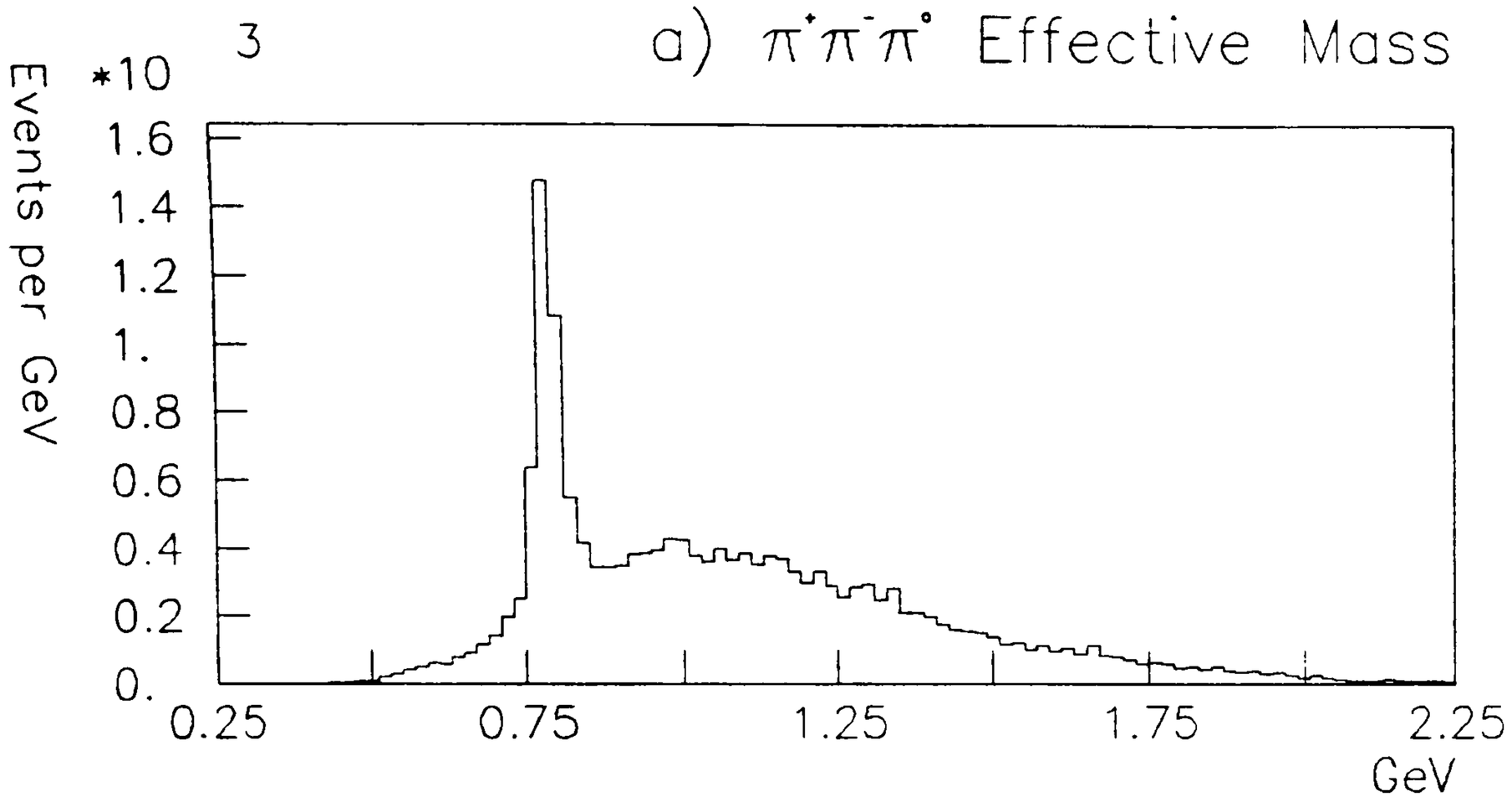
a) $\pi^+\pi^-\pi^\circ$ Effective Mass
3
*10
Events per GeV
1.6
1.4
1.2
1.
0.8
0.6
0.4
0.2
0.
0.25
0.75
1.25
1.75
2.25
GeV

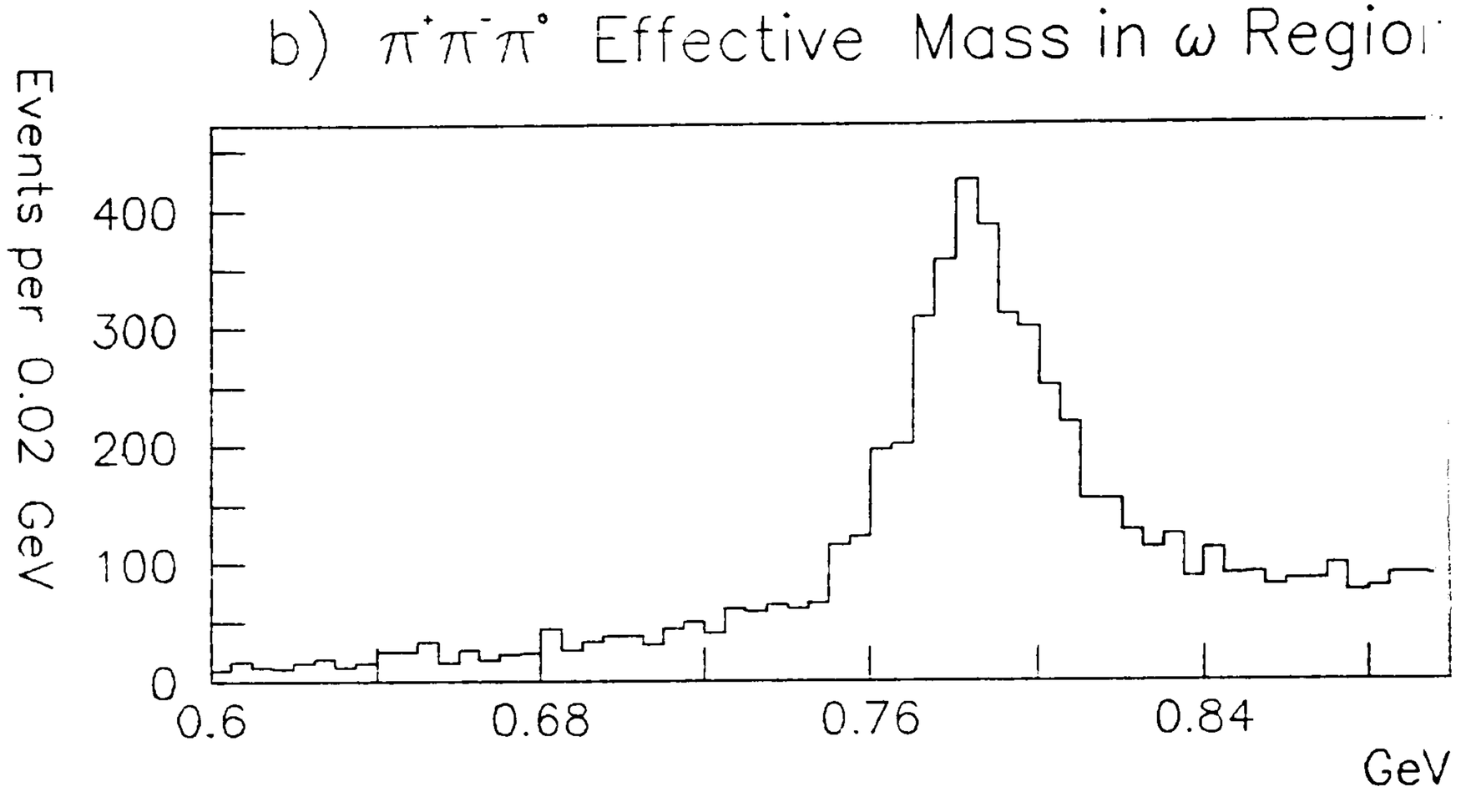
b) $\pi^+\pi^-\pi^\circ$ Effective Mass in ω Regio
Events per 0.02 GeV
400
300
200
100
0
0.6
0.68
0.76
0.84
GeV

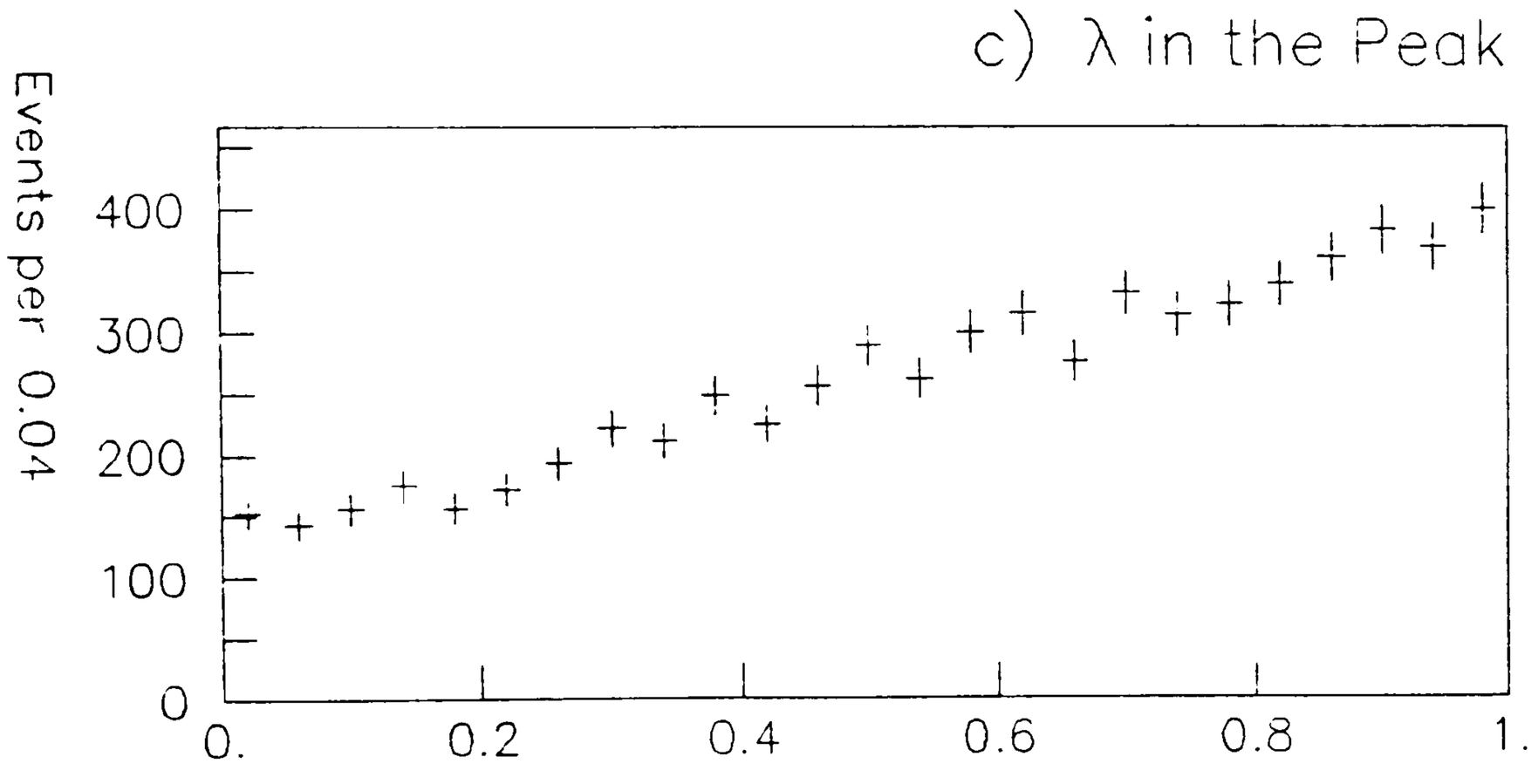
c) λ in the Peak
Events per 0.04
400
300
200
100
0
0.
0.2
0.4
0.6
0.8
1.

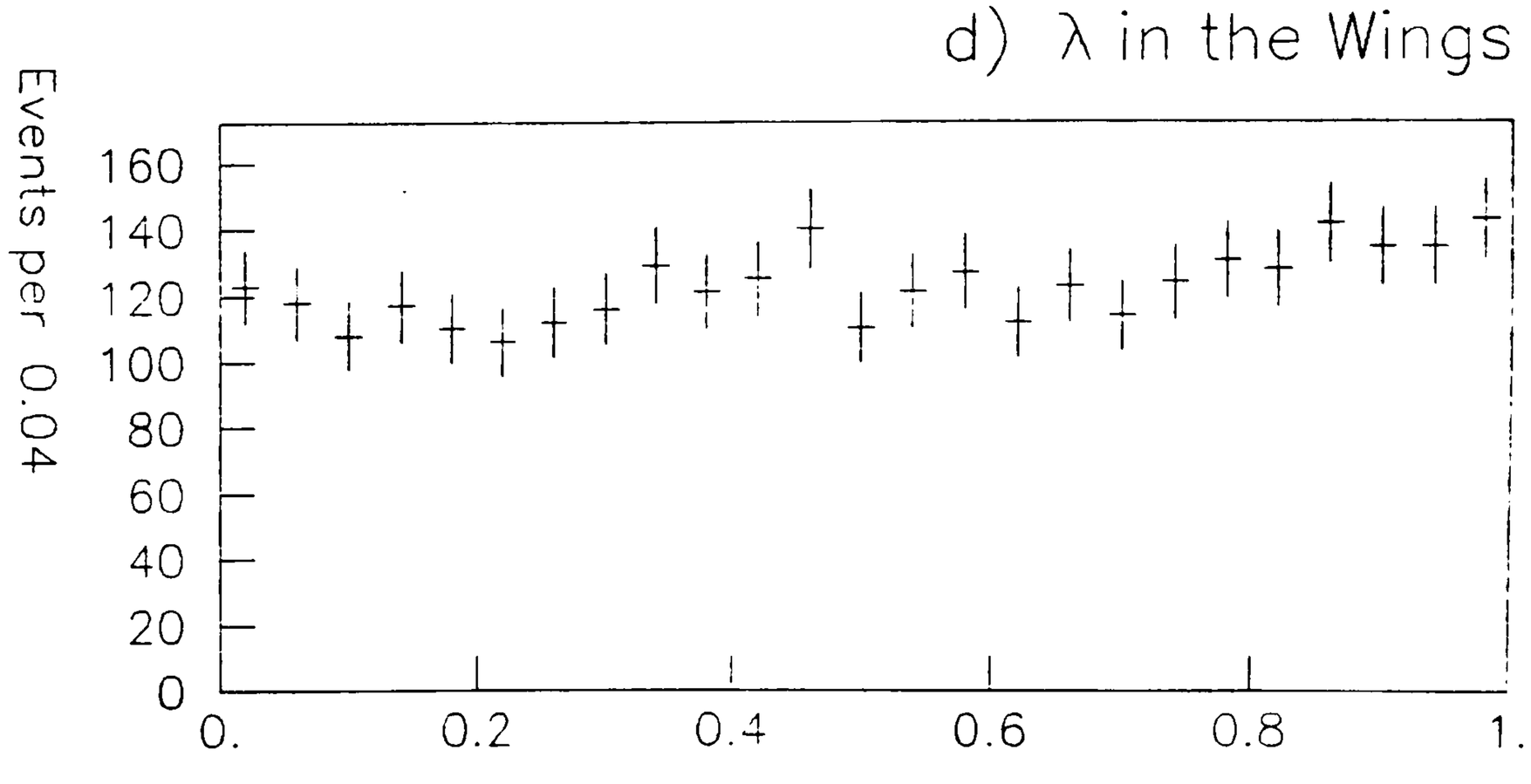
d) λ in the Wings
Events per 0.04
160
140
120
100
80
60
40
20
0
0.
0.2
0.4
0.6
0.8
1.

Figure 5.3

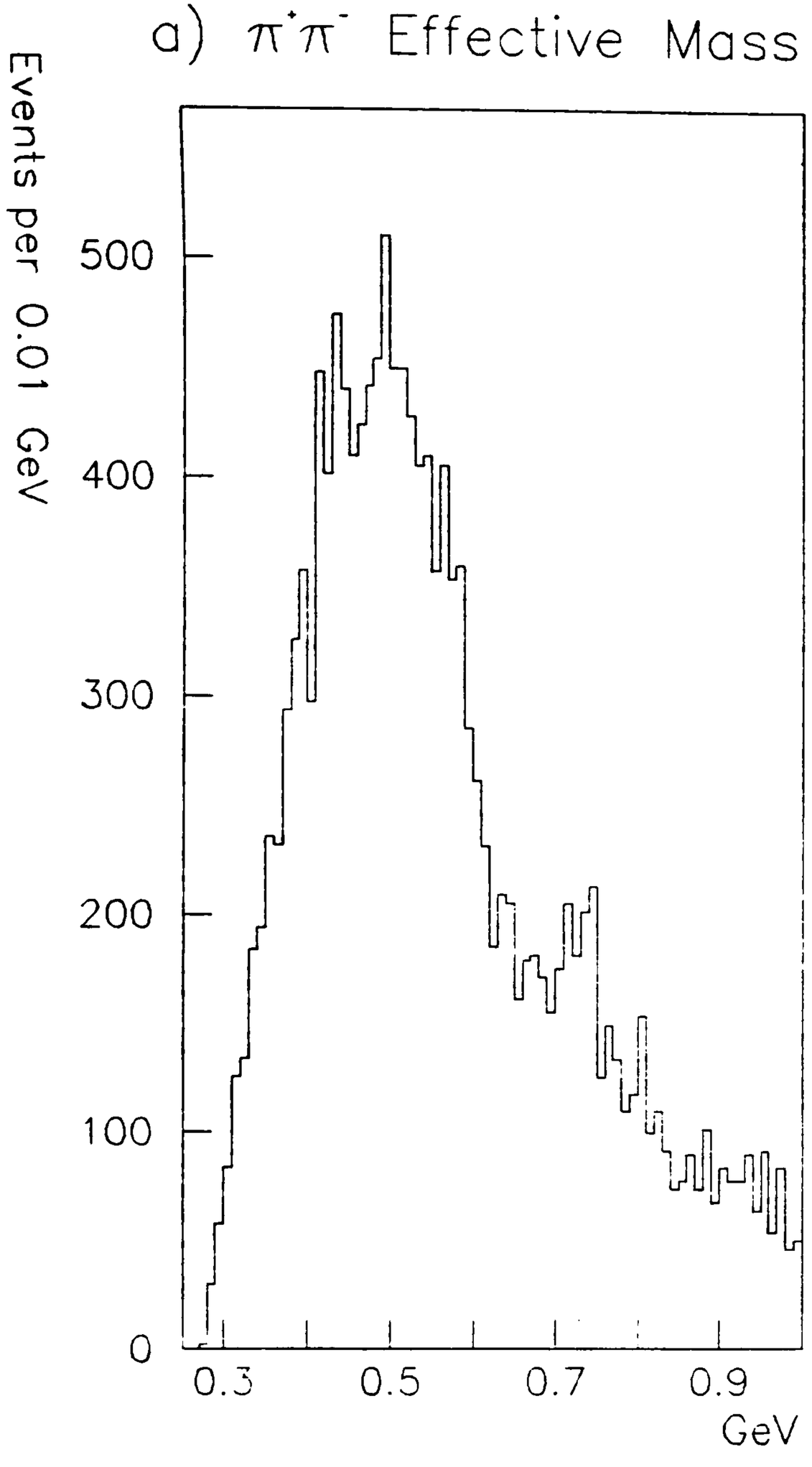
a) $\pi^+\pi^-$ Effective Mass
Events per 0.01 GeV
500
400
300
200
100
0
0.3
0.5
0.7
0.9
GeV

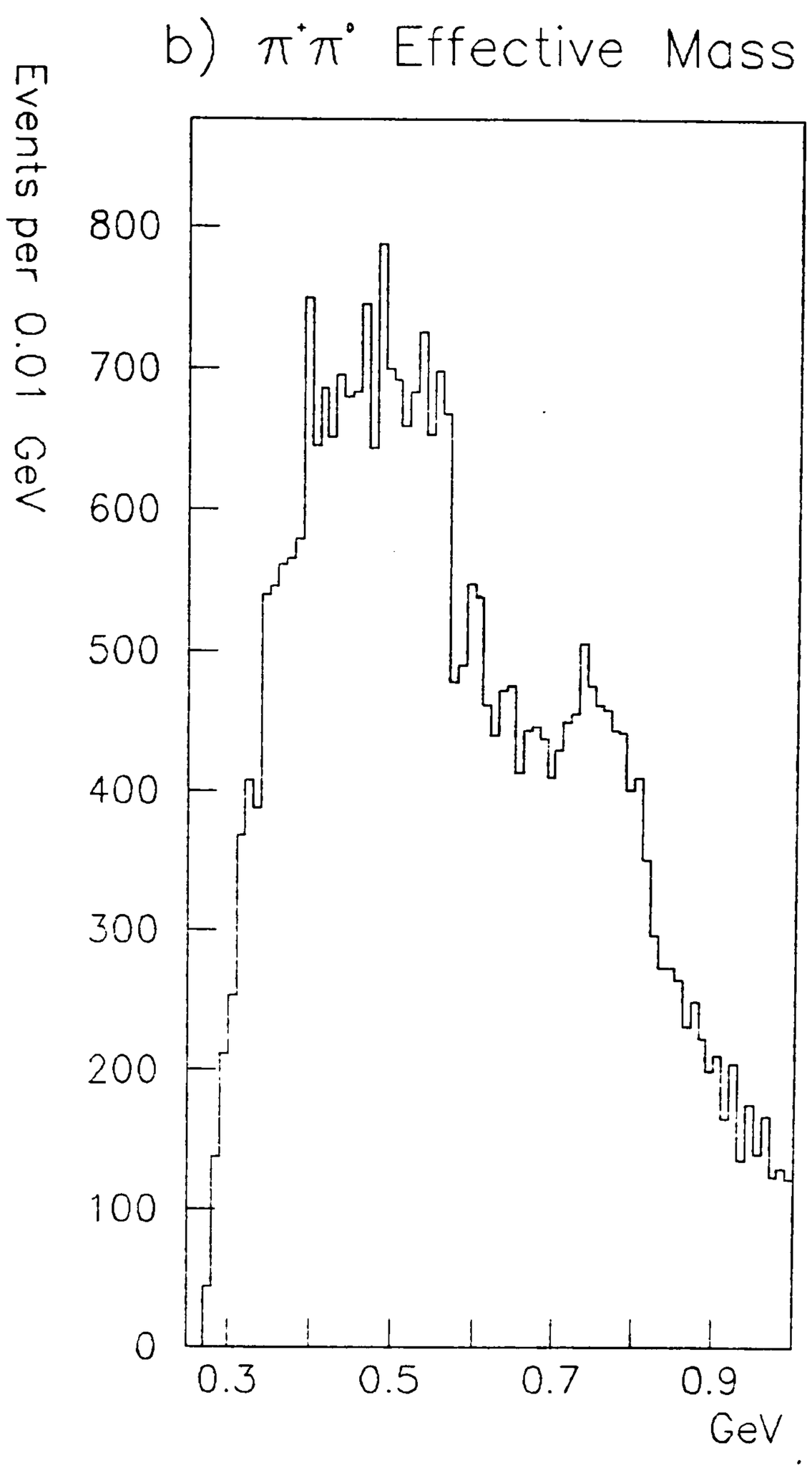
b) $\pi^+\pi^\circ$ Effective Mass
Events per 0.01 GeV
800
700
600
500
400
300
200
100
0
0.3
0.5
0.7
0.9
GeV

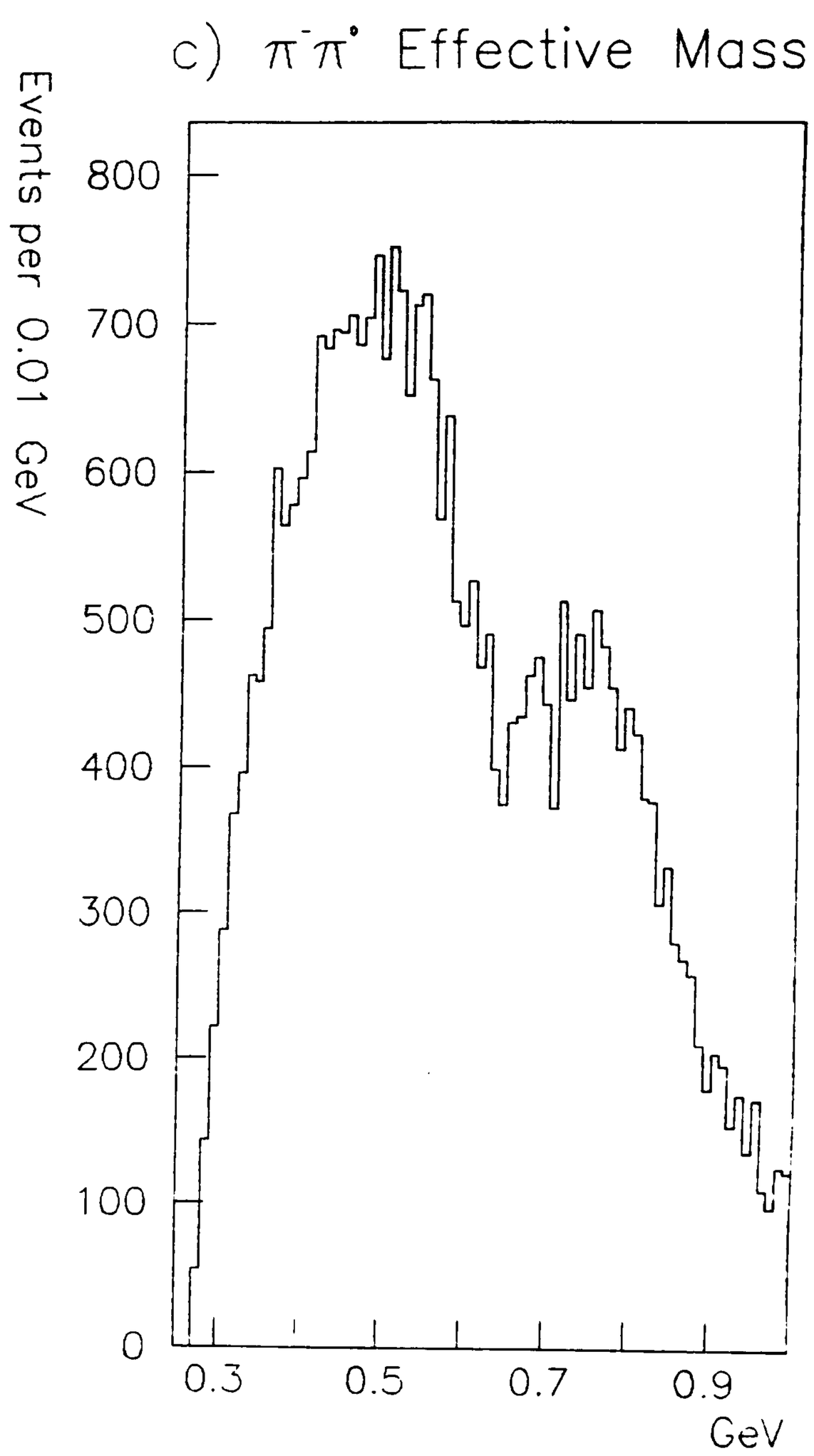
c) $\pi^-\pi^\circ$ Effective Mass
Events per 0.01 GeV
800
700
600
500
400
300
200
100
0
0.3
0.5
0.7
0.9
GeV

Figure 5.4

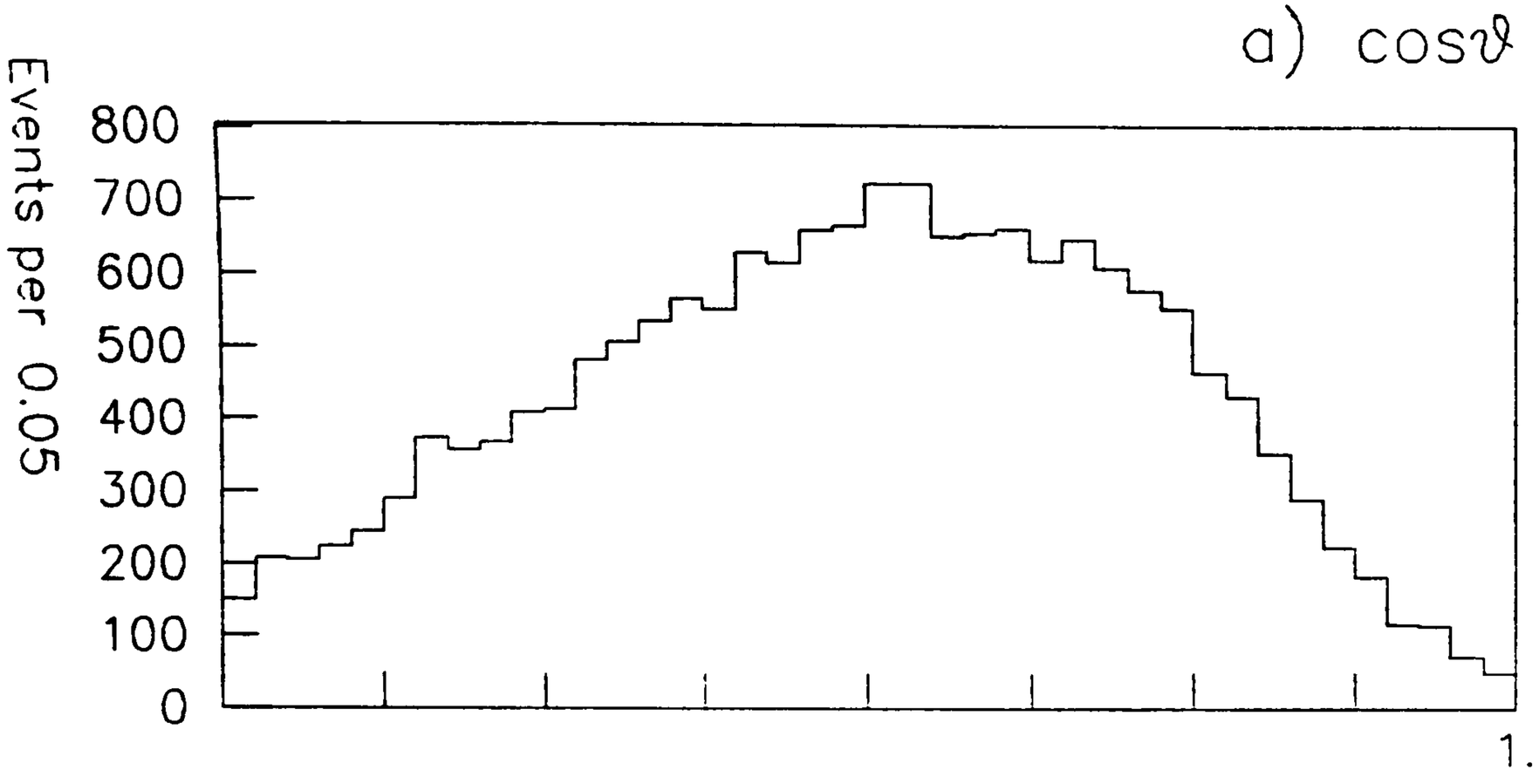
a) cosϑ
Events per 0.05
800
700
600
500
400
300
200
100
0
1.

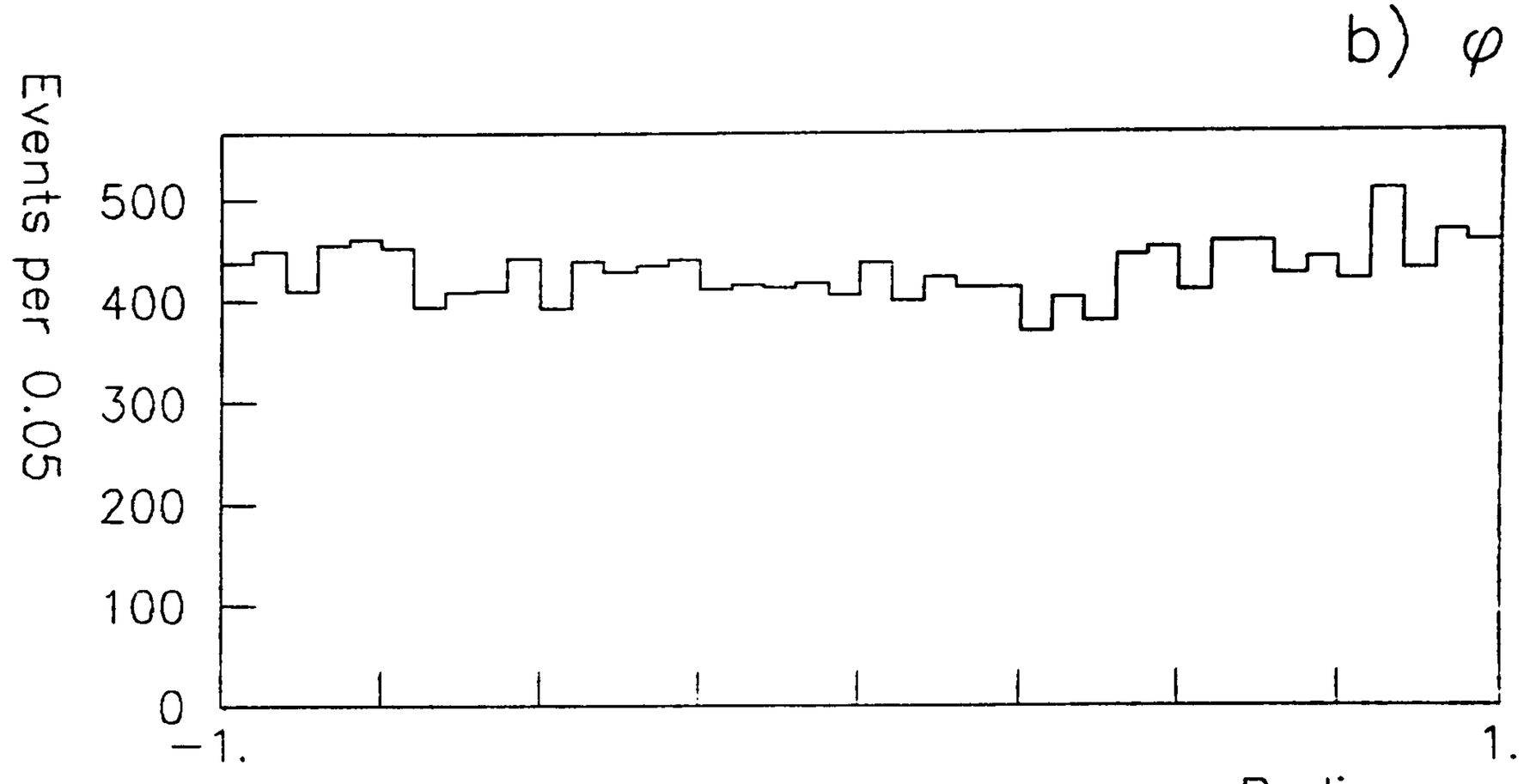
b) φ
Events per 0.05
500
400
300
200
100
0
−1.
1.
Radians*π

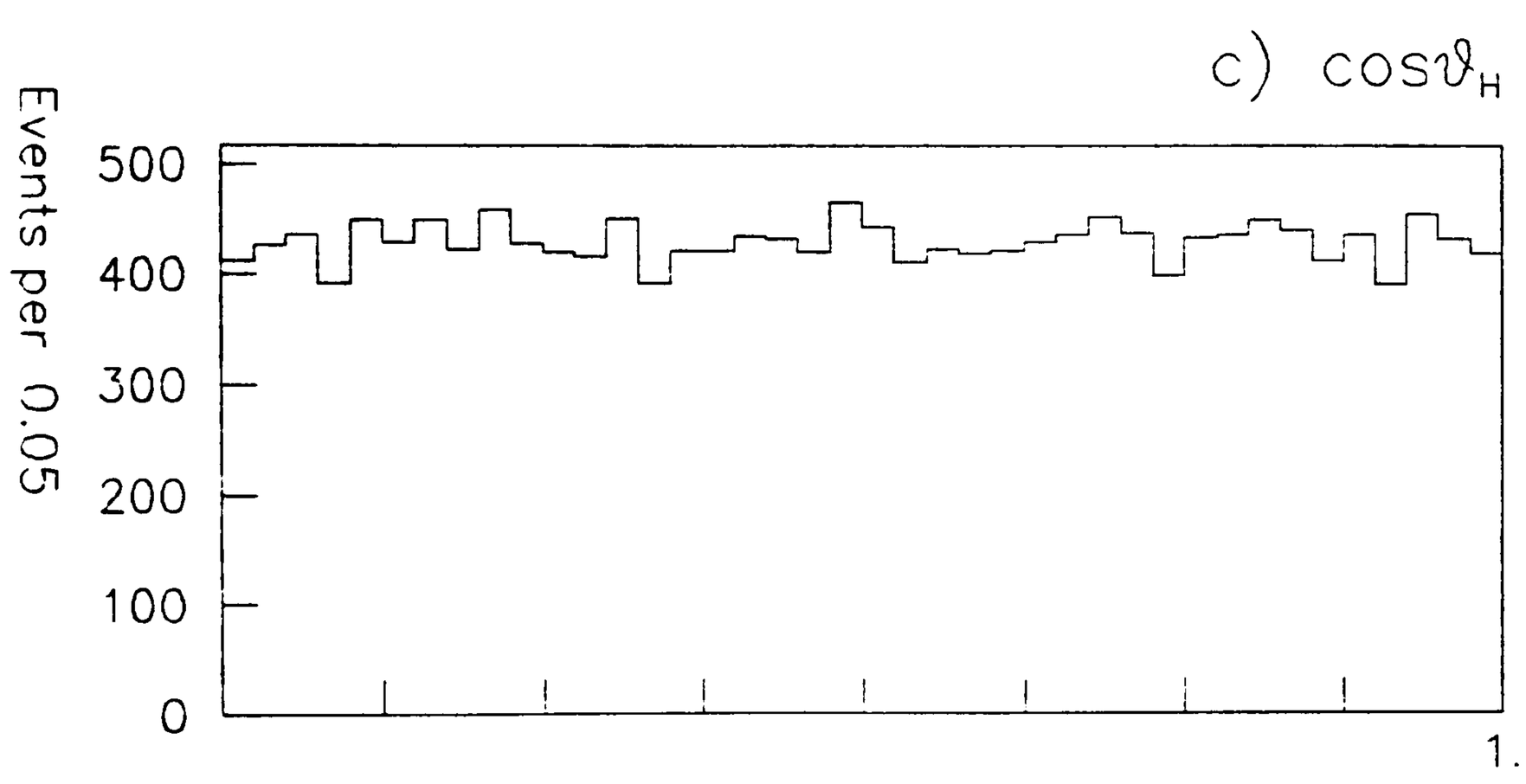
c) cosϑH
Events per 0.05
500
400
300
200
100
0
1.

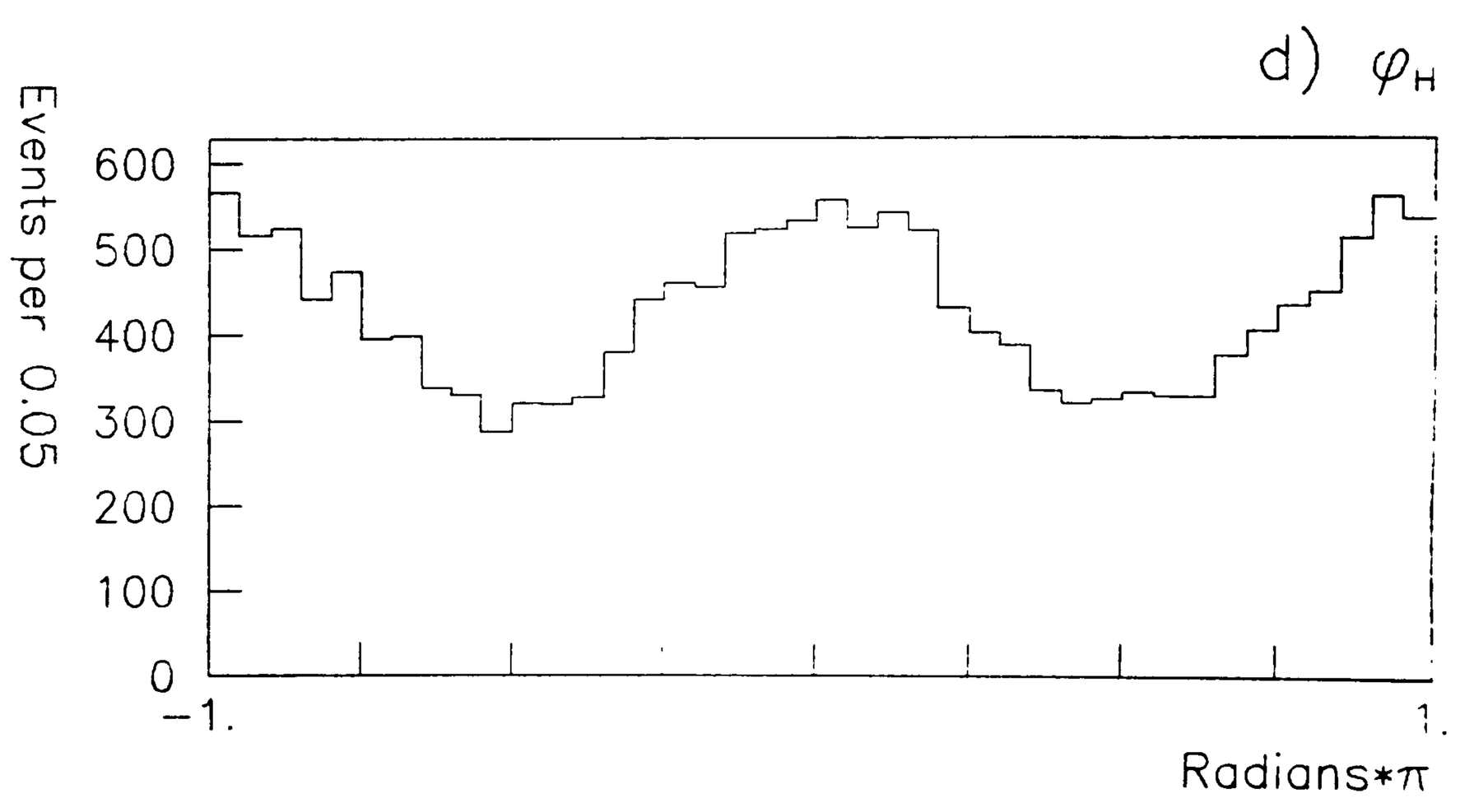
d) φH
Events per 0.05
600
500
400
300
200
100
0
−1.
1.
Radians*π

Figure 5.5

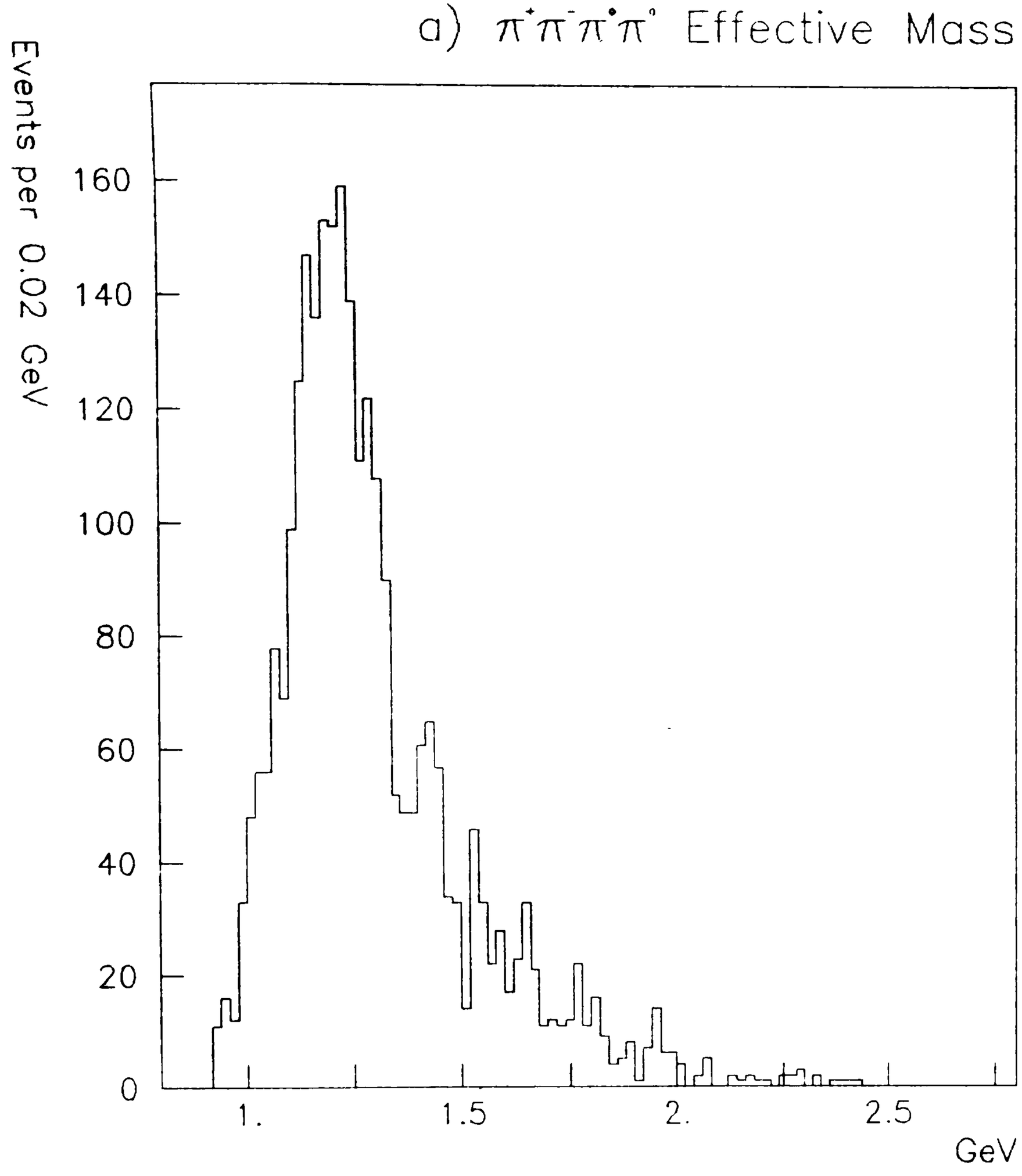
a) $\pi^+\pi^-\pi^+\pi^-$ Effective Mass
Events per 0.02 GeV
160
140
120
100
80
60
40
20
0
1.
1.5
2.
2.5
GeV

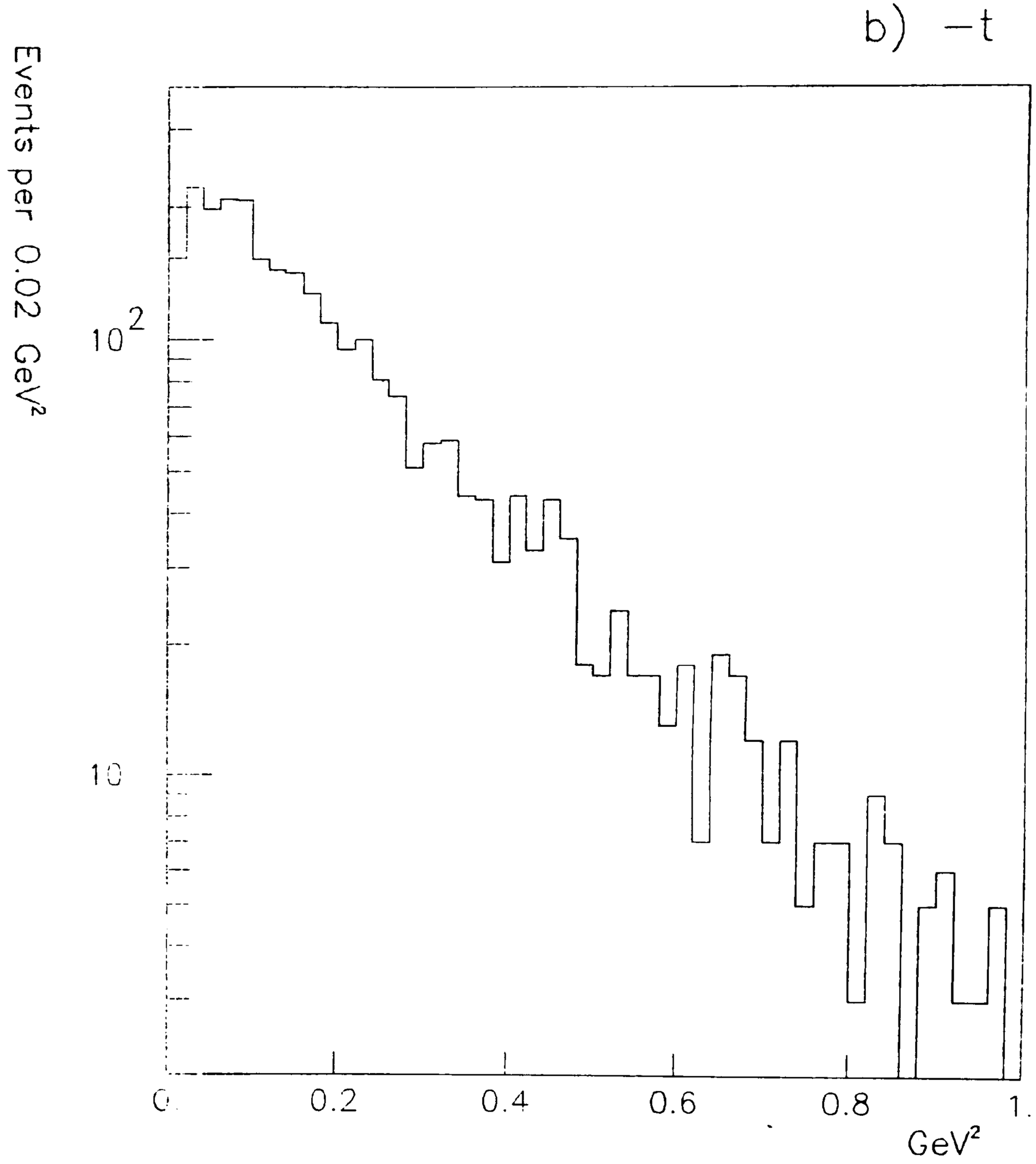
b) $-t$
Events per 0.02 GeV^2
10^2
10
0
0.2
0.4
0.6
0.8
1.
GeV^2

Figure 5.6

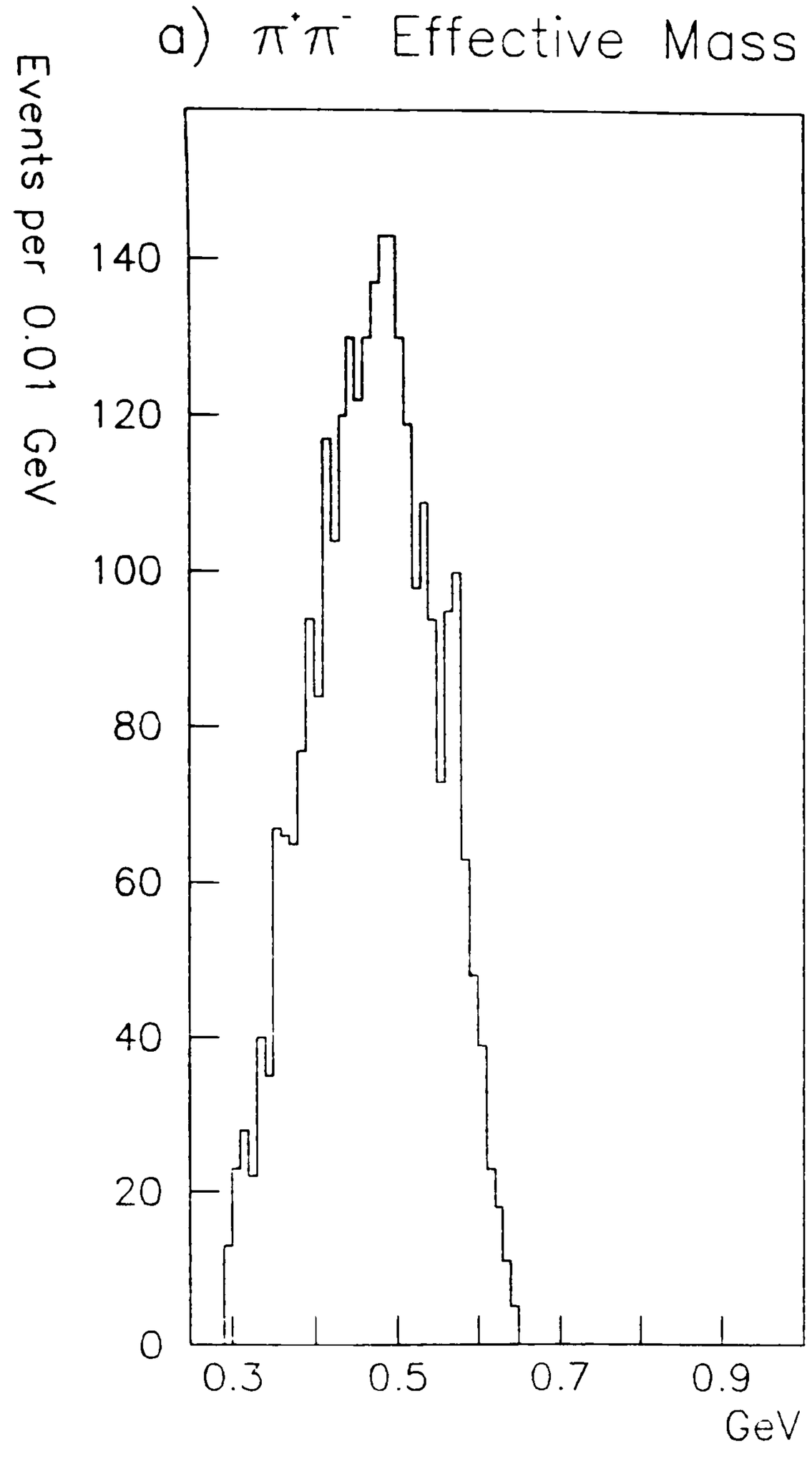
a) $\pi^+\pi^-$ Effective Mass
Events per 0.01 GeV
140
120
100
80
60
40
20
0
0.3
0.5
0.7
0.9
GeV

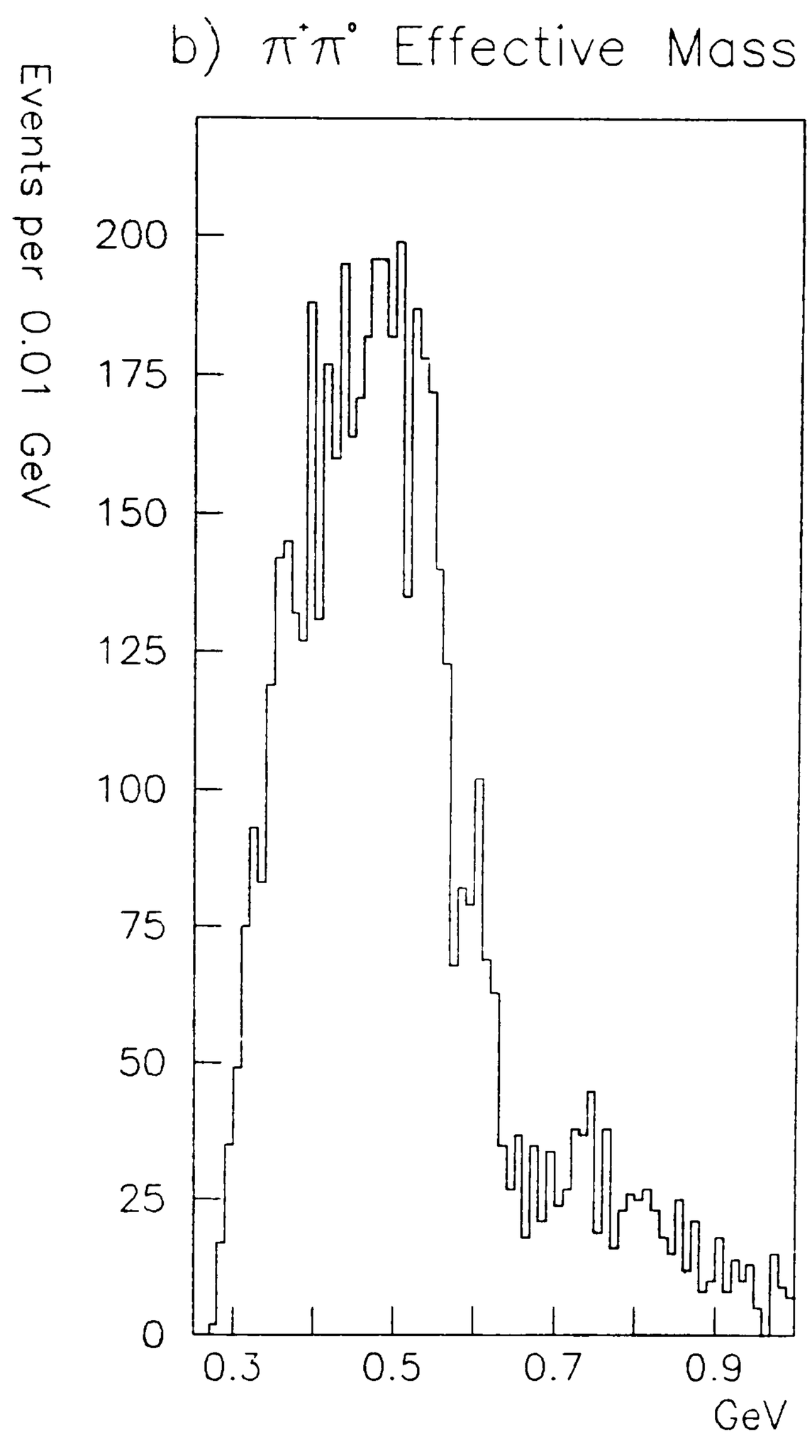
b) $\pi^+\pi^\circ$ Effective Mass
Events per 0.01 GeV
200
175
150
125
100
75
50
25
0
0.3
0.5
0.7
0.9
GeV

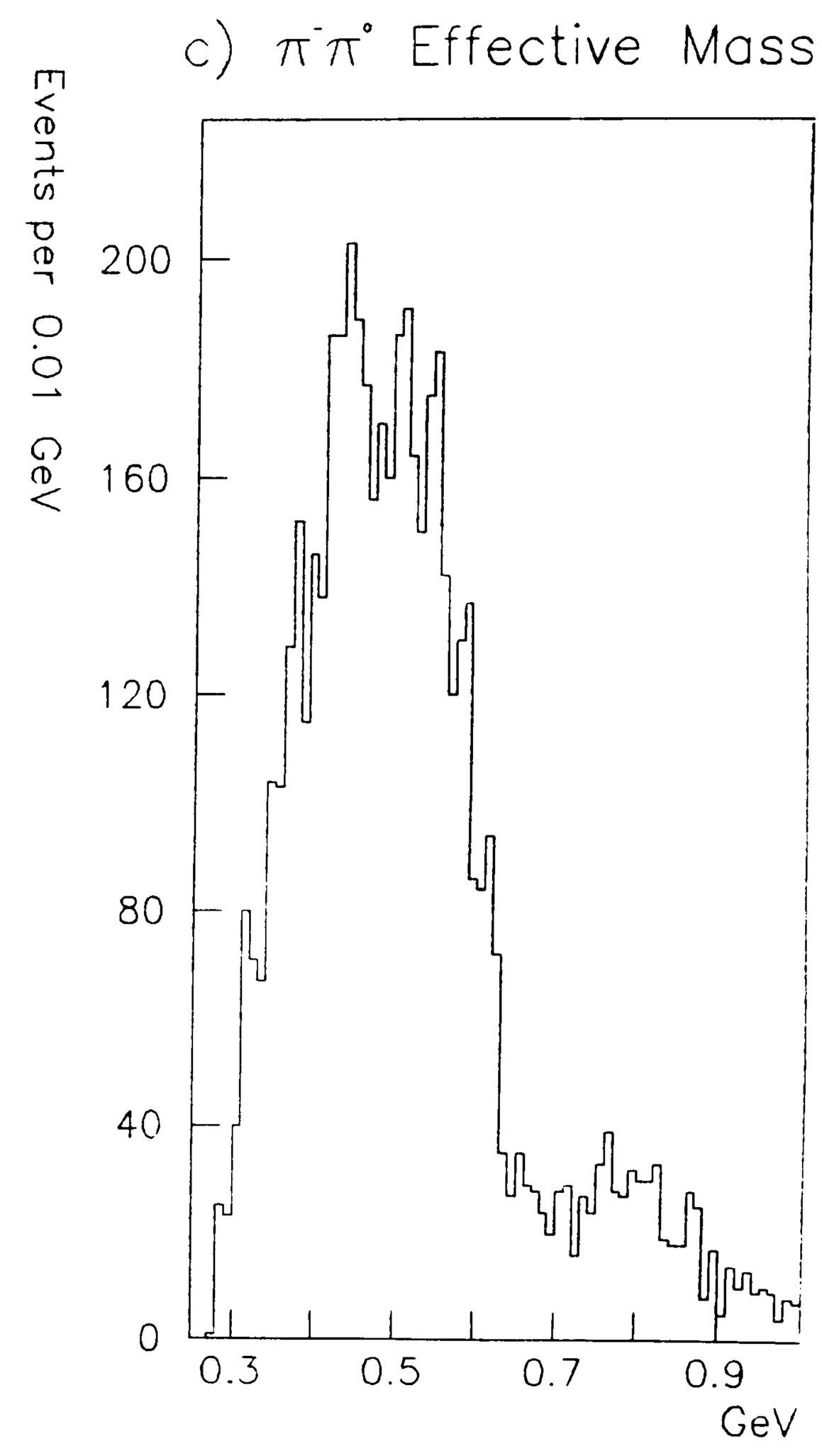
c) $\pi^-\pi^\circ$ Effective Mass
Events per 0.01 GeV
200
160
120
80
40
0
0.3
0.5
0.7
0.9
GeV

Figure 5.7

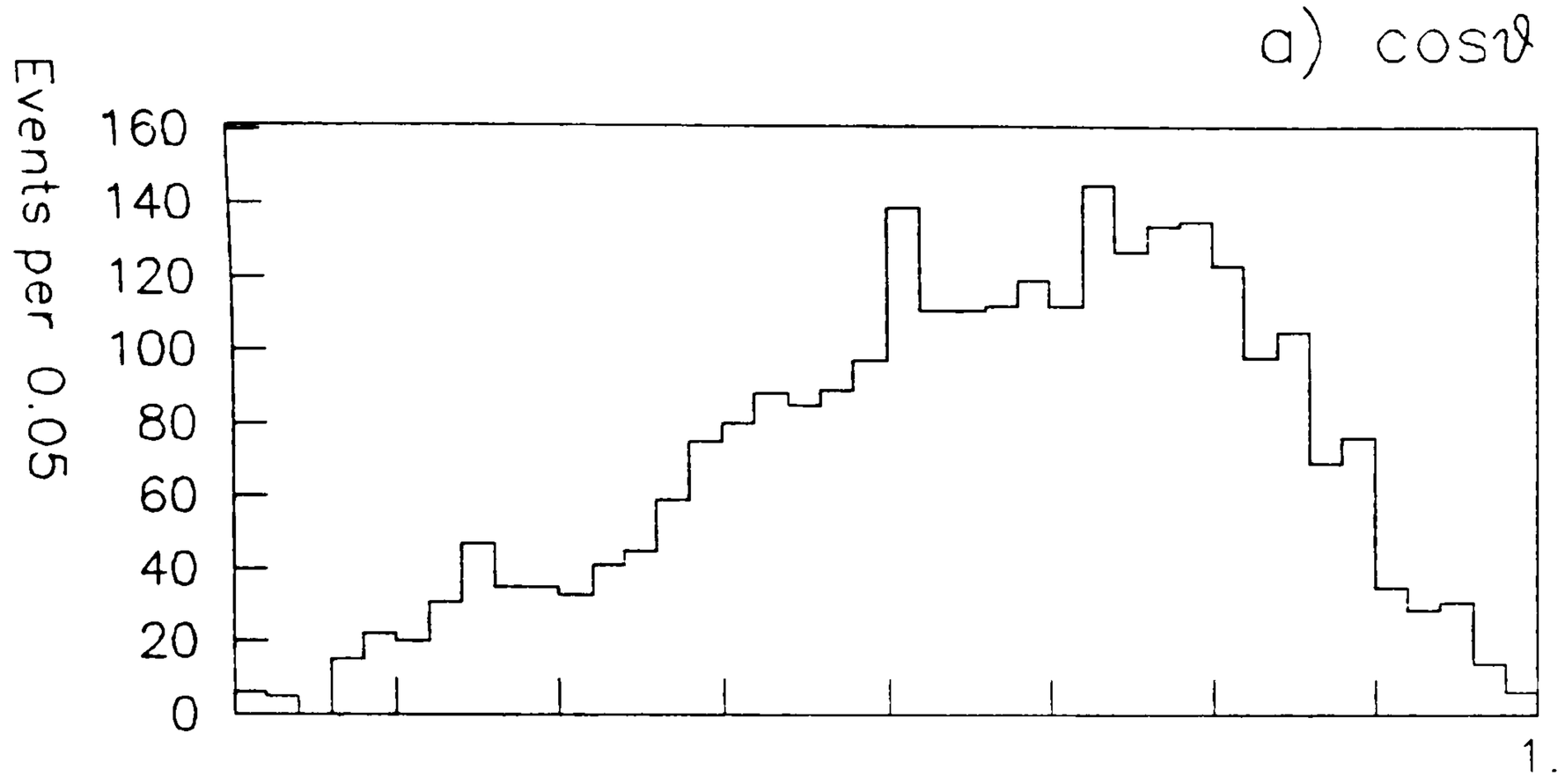
a) cosϑ
Events per 0.05
160
140
120
100
80
60
40
20
0
1.

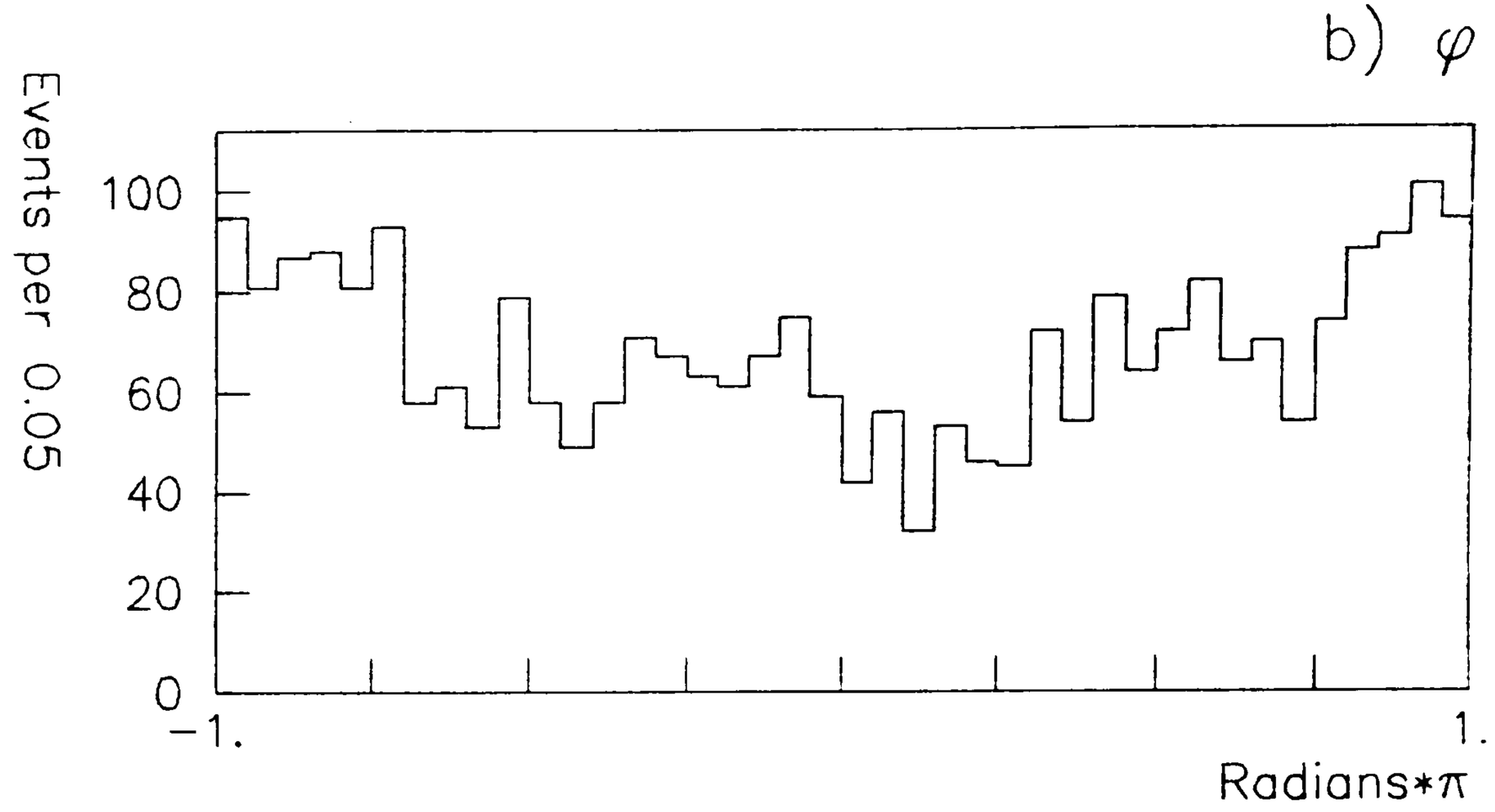
b) φ
Events per 0.05
100
80
60
40
20
0
−1.
1.
Radians*π

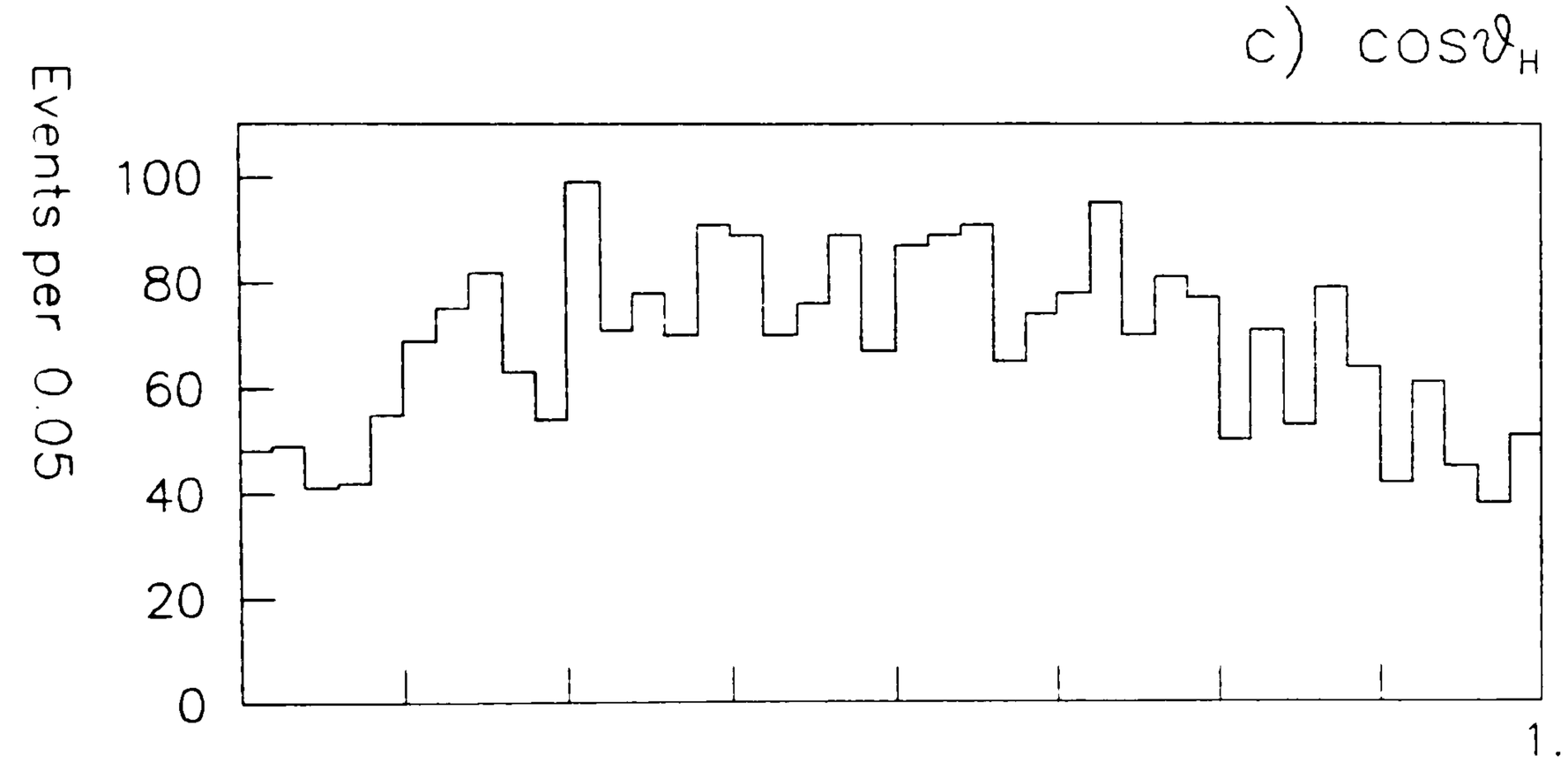
c) cosϑH
Events per 0.05
100
80
60
40
20
0
1.

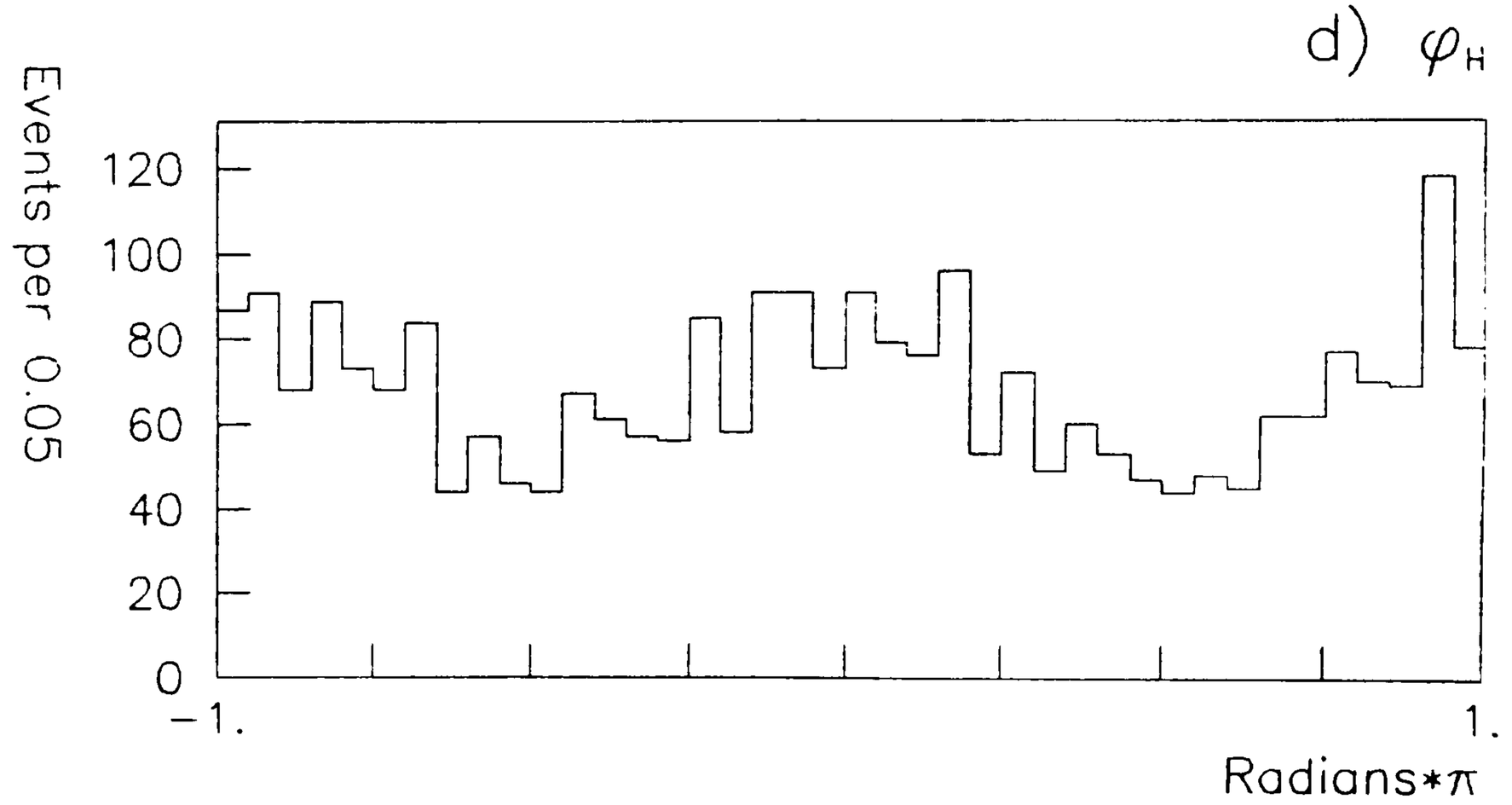
d) φH
Events per 0.05
120
100
80
60
40
20
0
−1.
1.
Radians*π

Figure 5.8

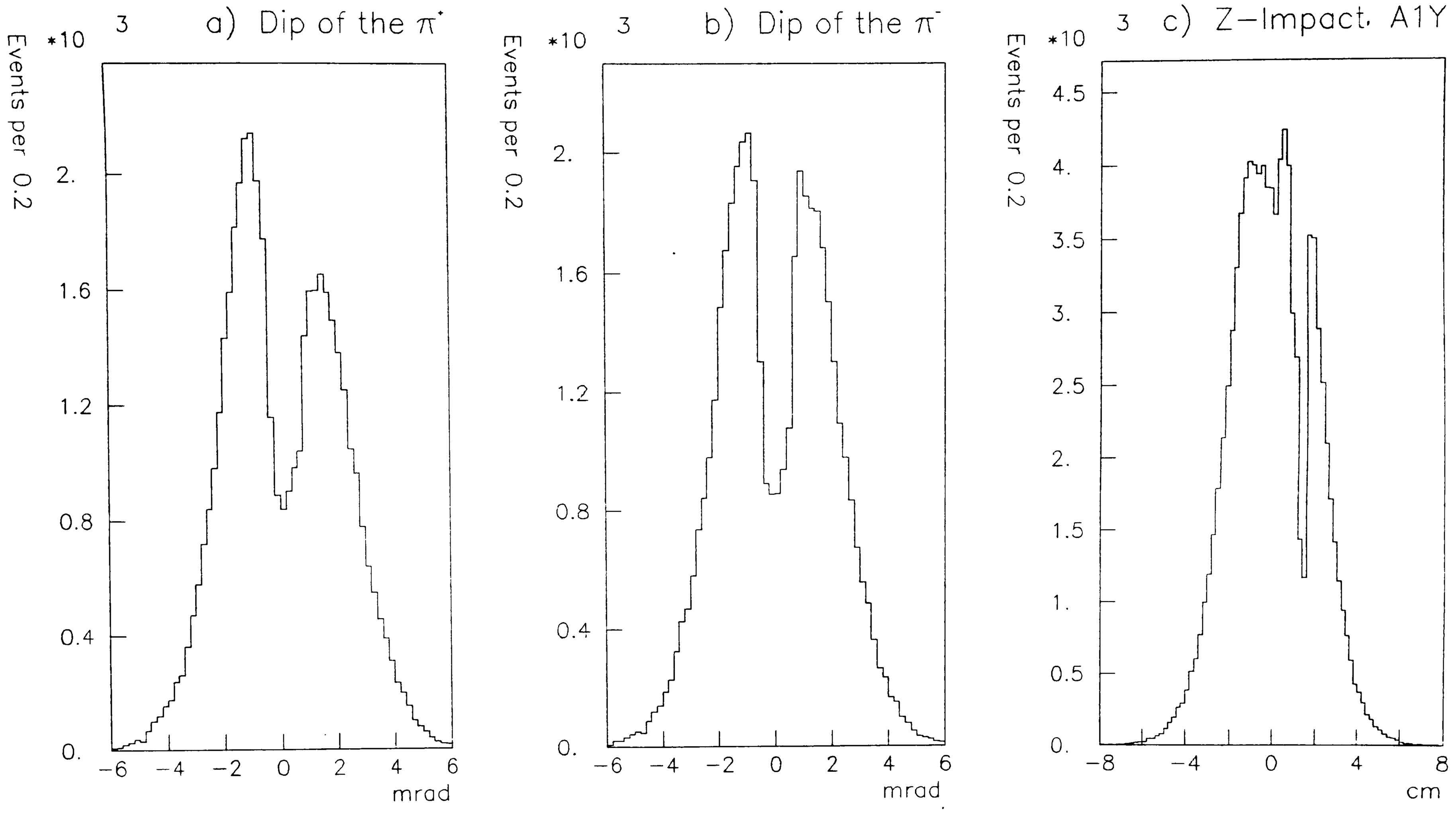

Figure 5.9 (ρ Data)

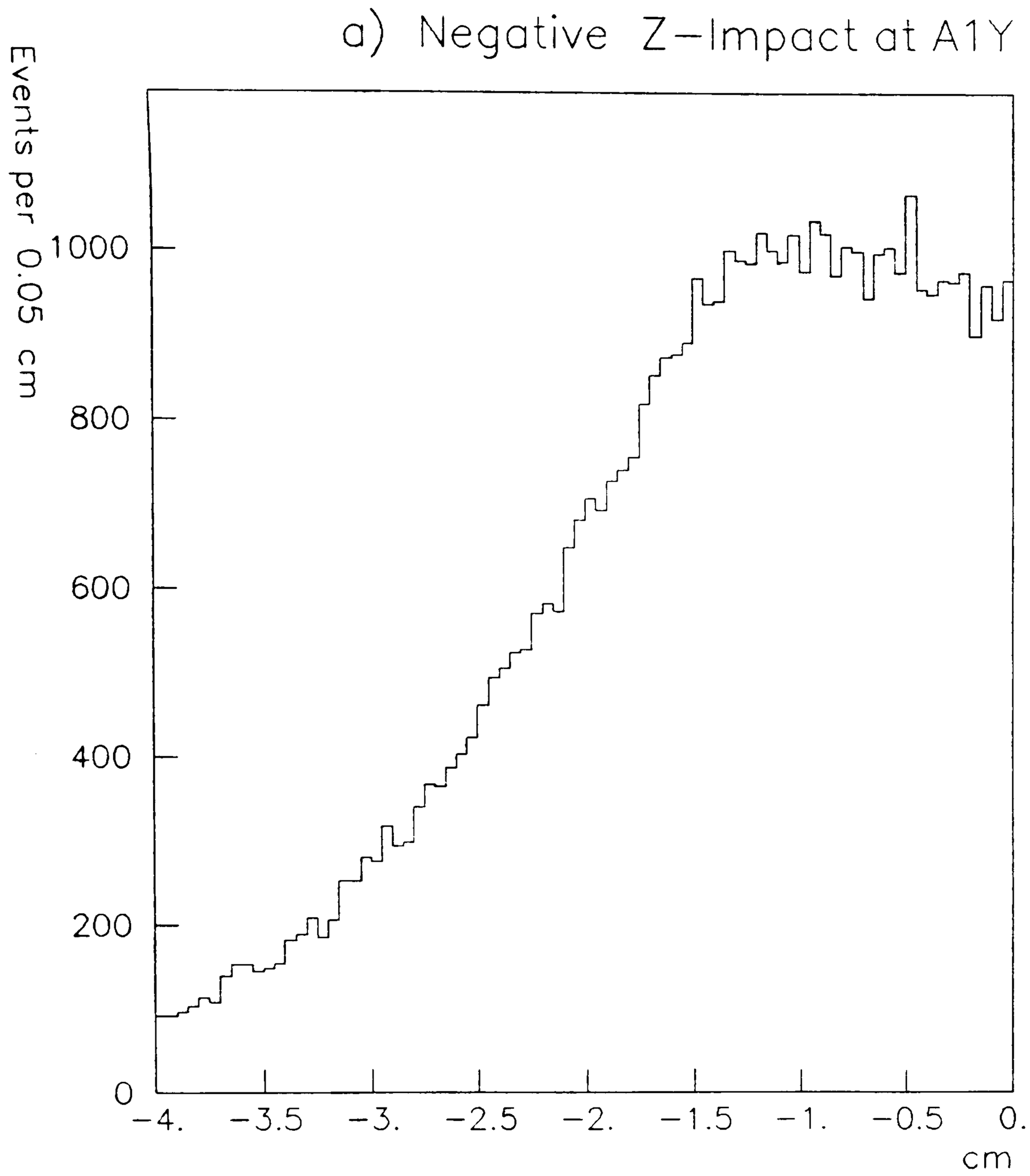

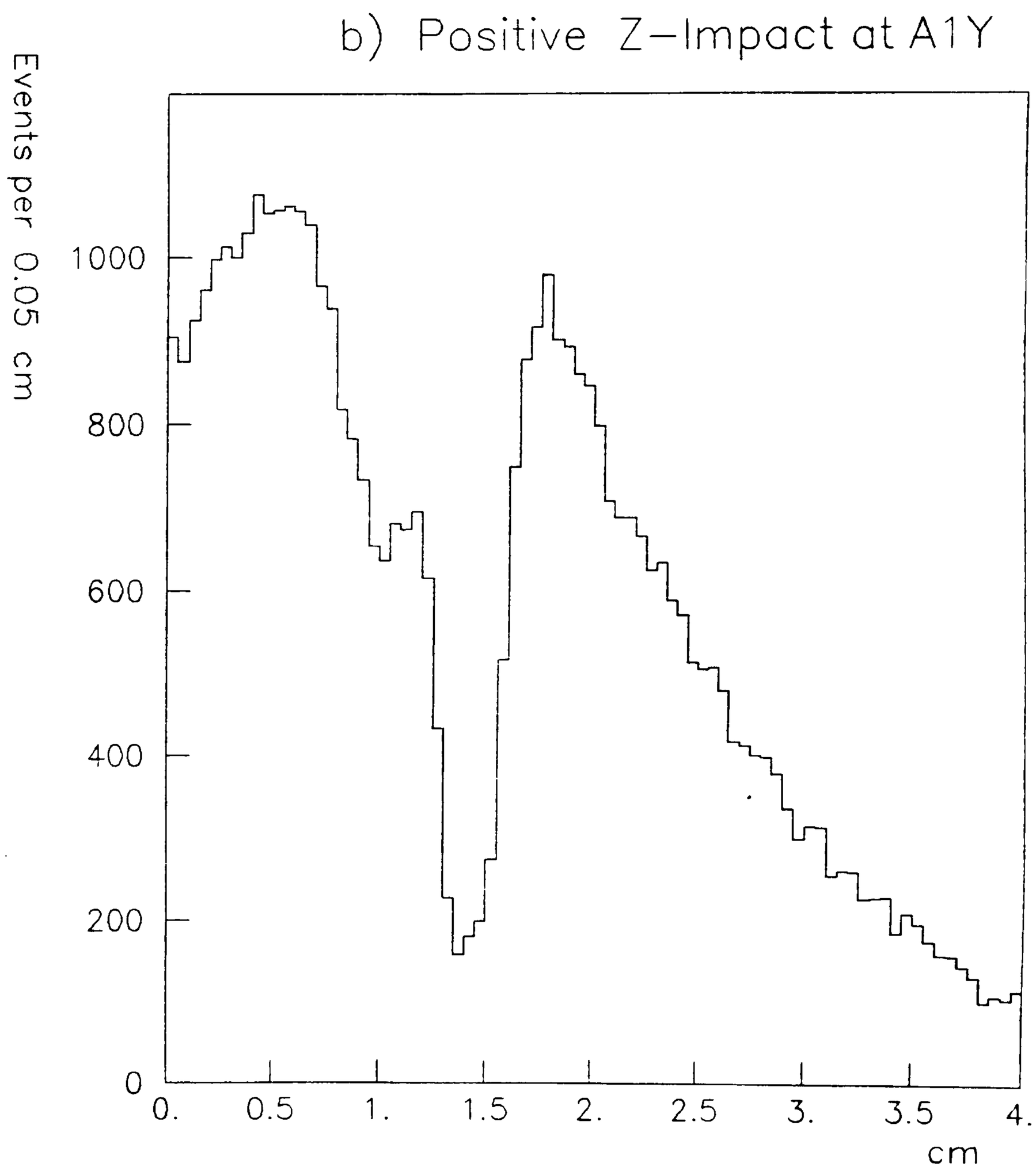

Figure 5.10 (ρ Data)

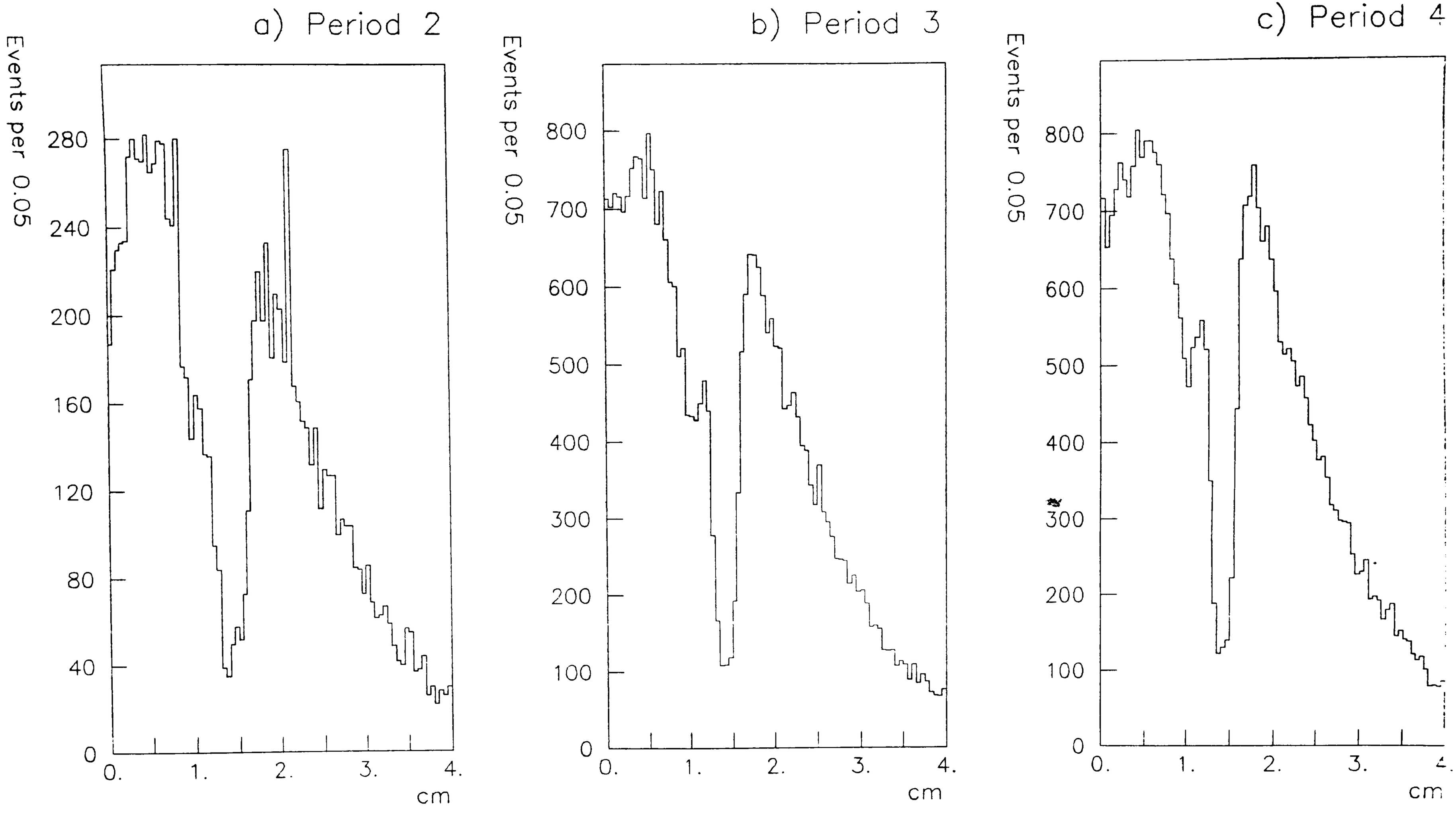

Figure 5.11 (ρ Data)

a) Measure of Inefficiency from ρ Data

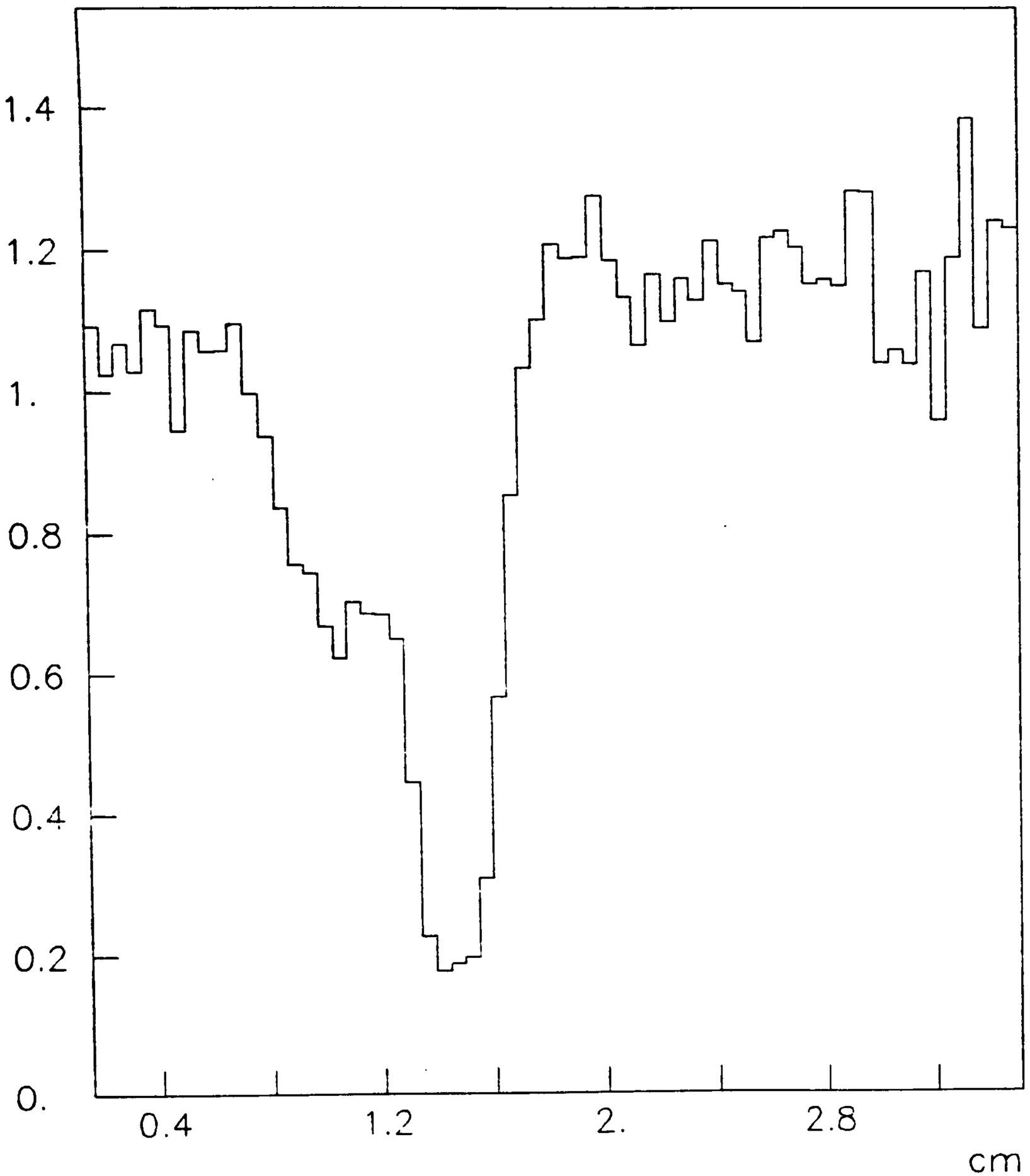

b) Parameterisation Used in MAP

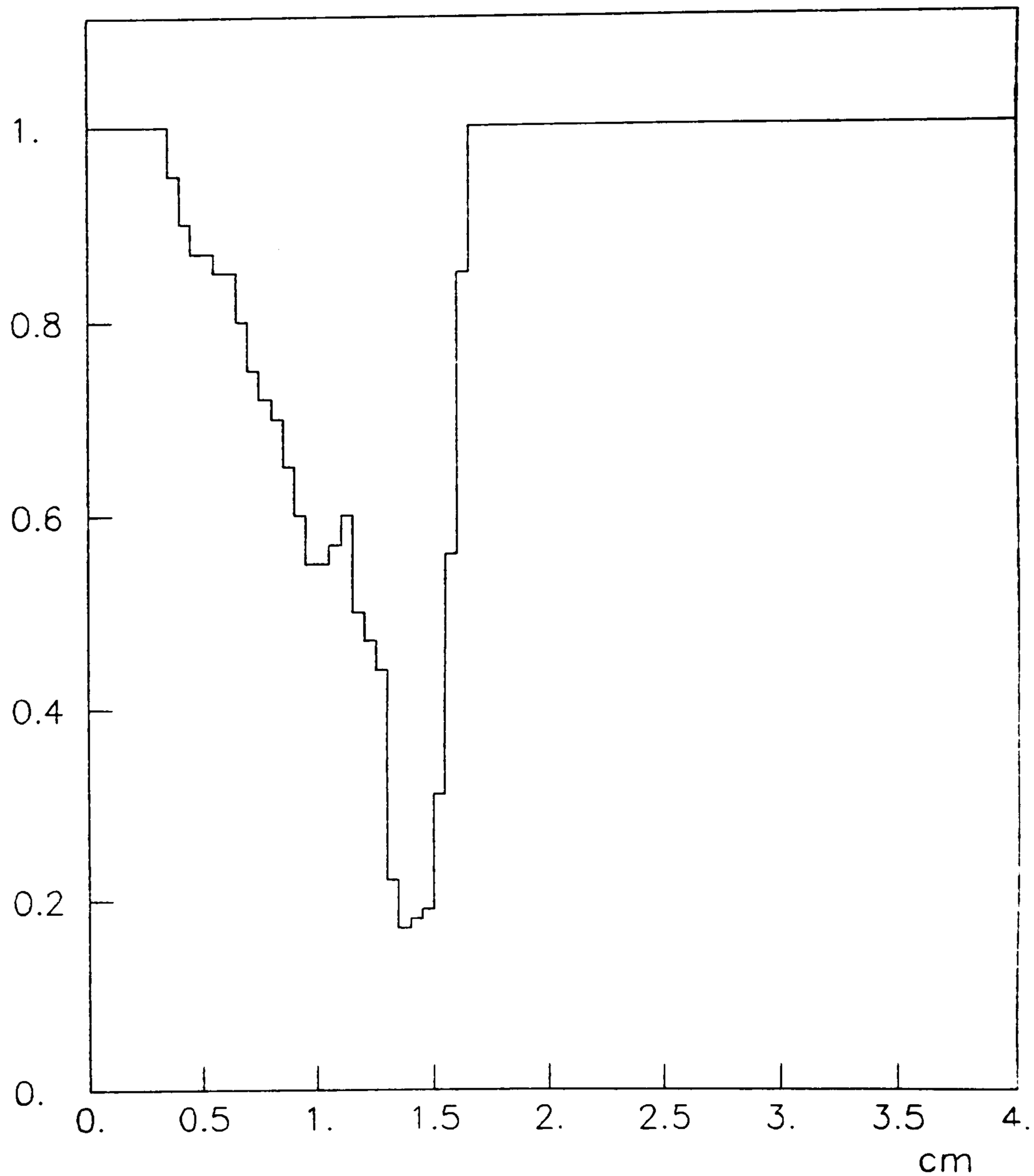

Figure 5.12 (ρ Data)

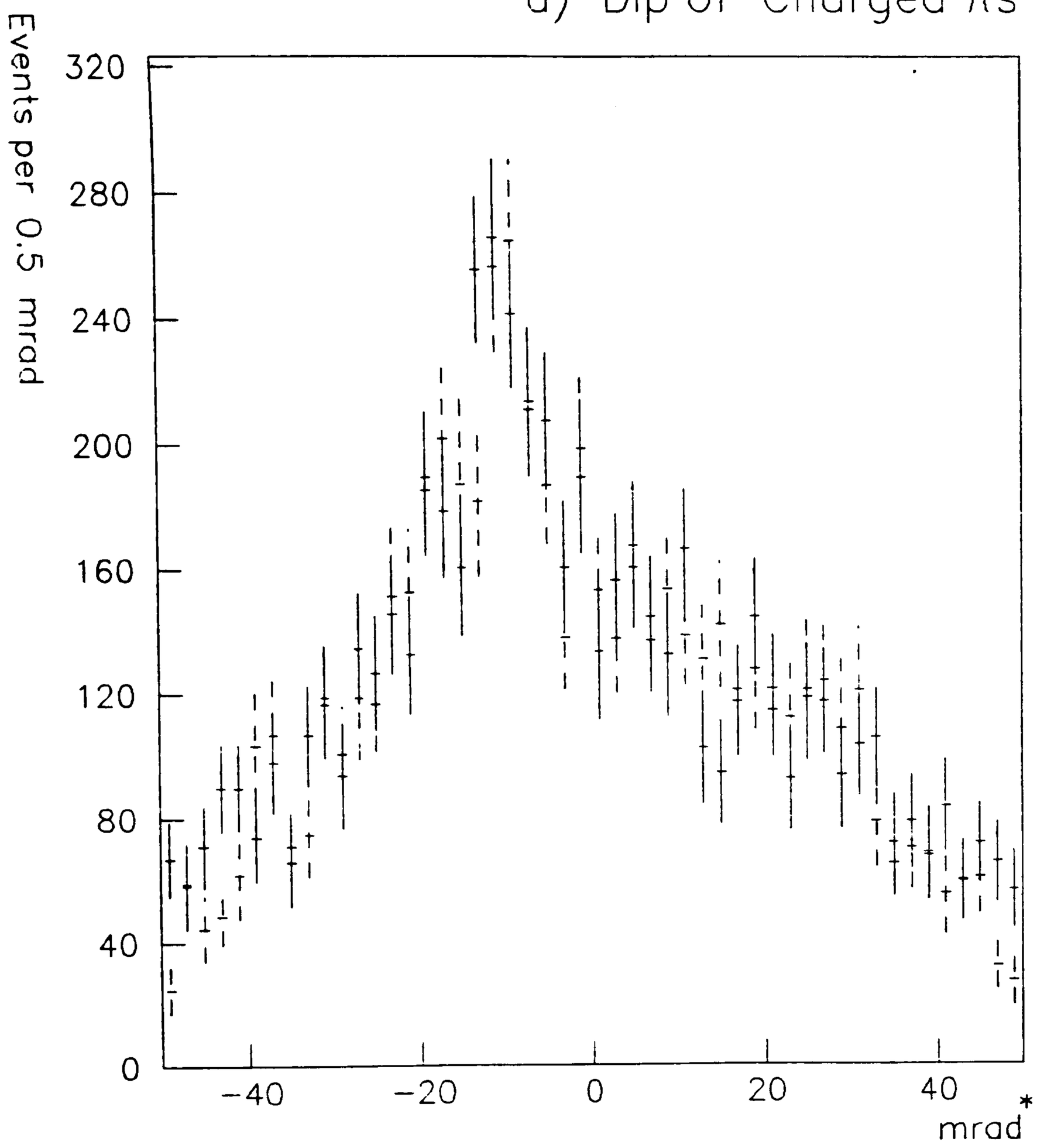
a) Dip of Charged πs
Events per 0.5 mrad
320
280
240
200
160
120
80
40
0
−40
−20
0
20
40
*10 − 3
mrad

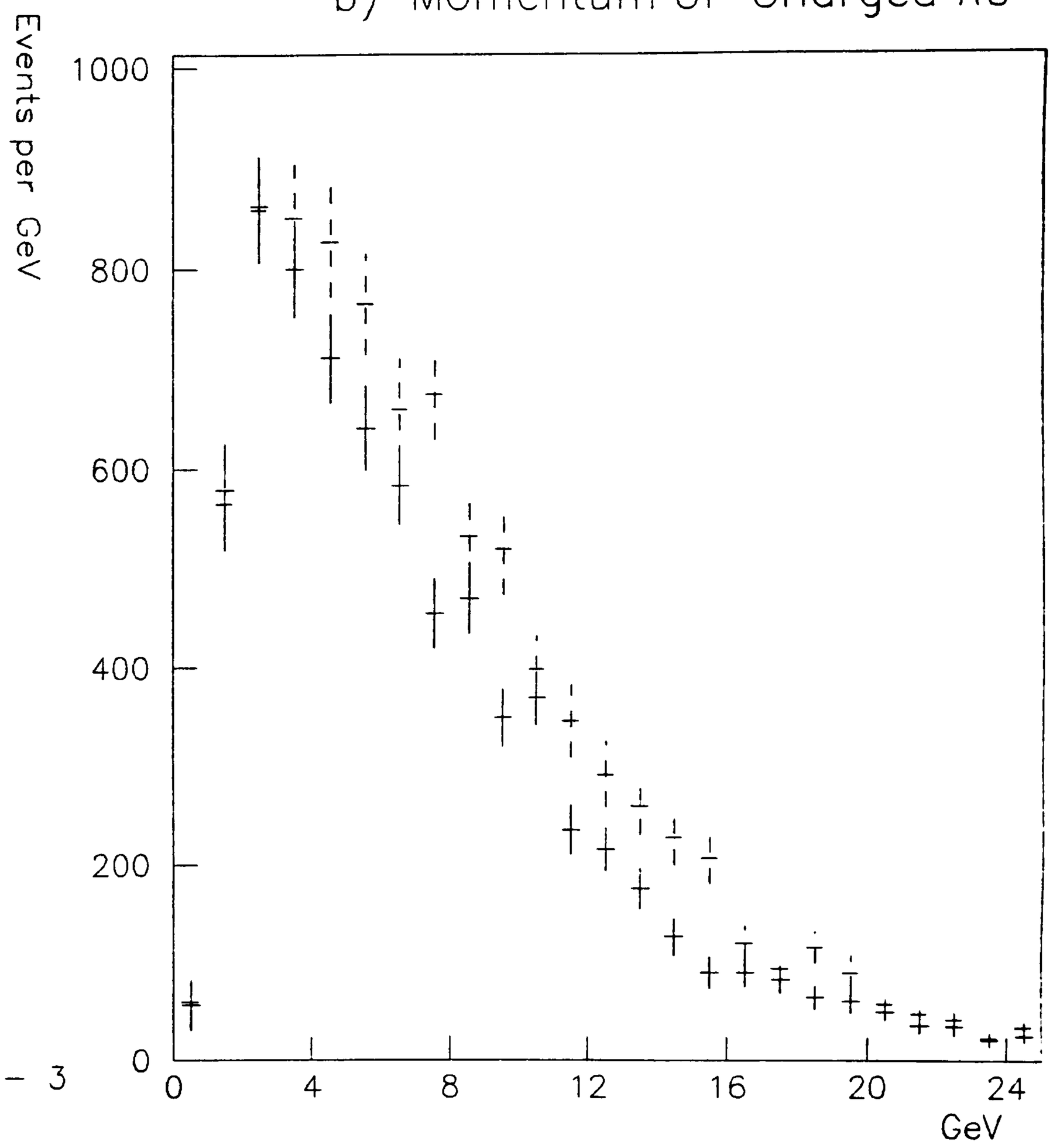
b) Momentum of Charged πs
Events per GeV
1000
800
600
400
200
0
0
4
8
12
16
20
24
GeV

Figure 5.13

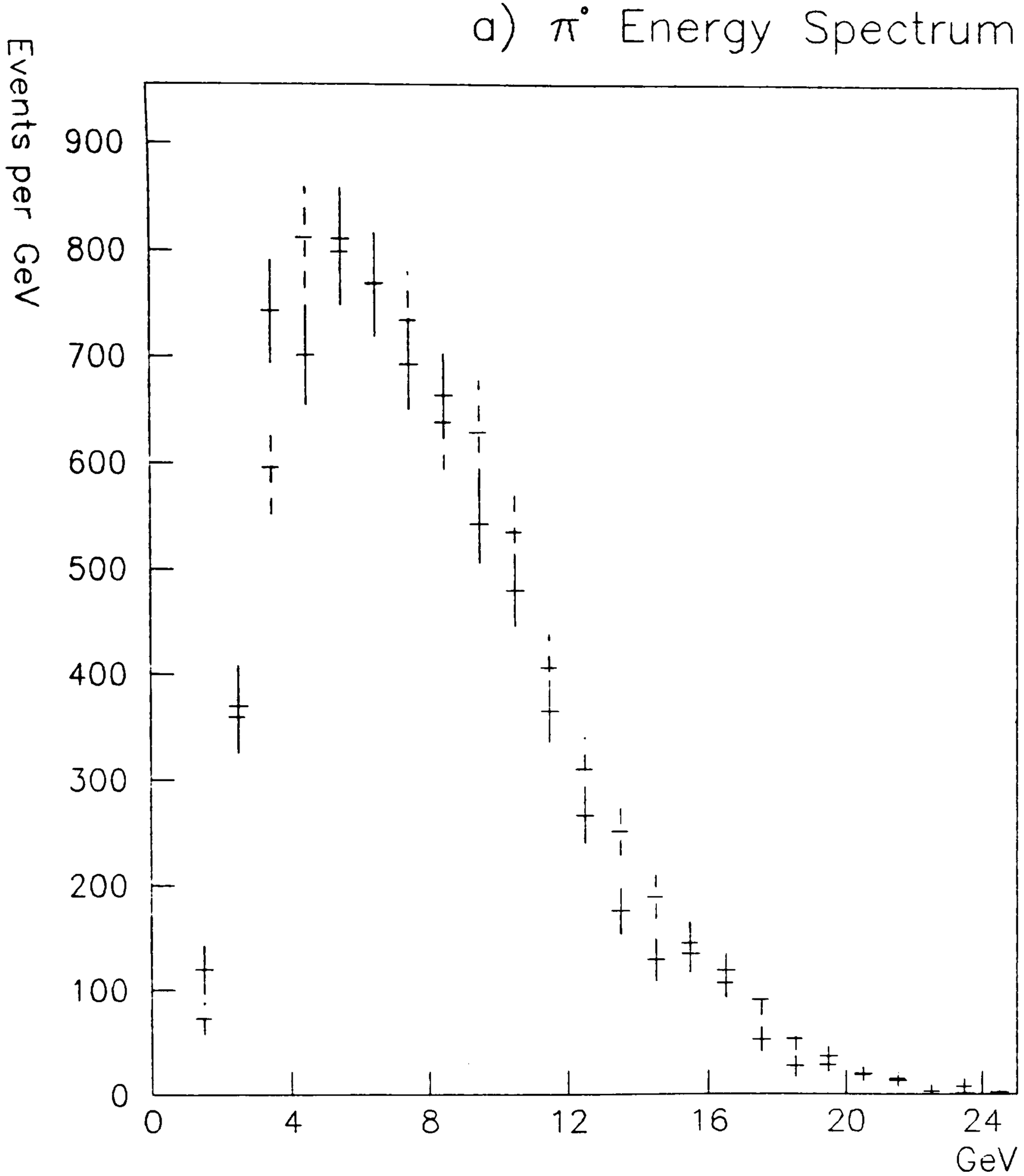
a) π° Energy Spectrum
Events per GeV
900
800
700
600
500
400
300
200
100
0
0
4
8
12
16
20
24
GeV

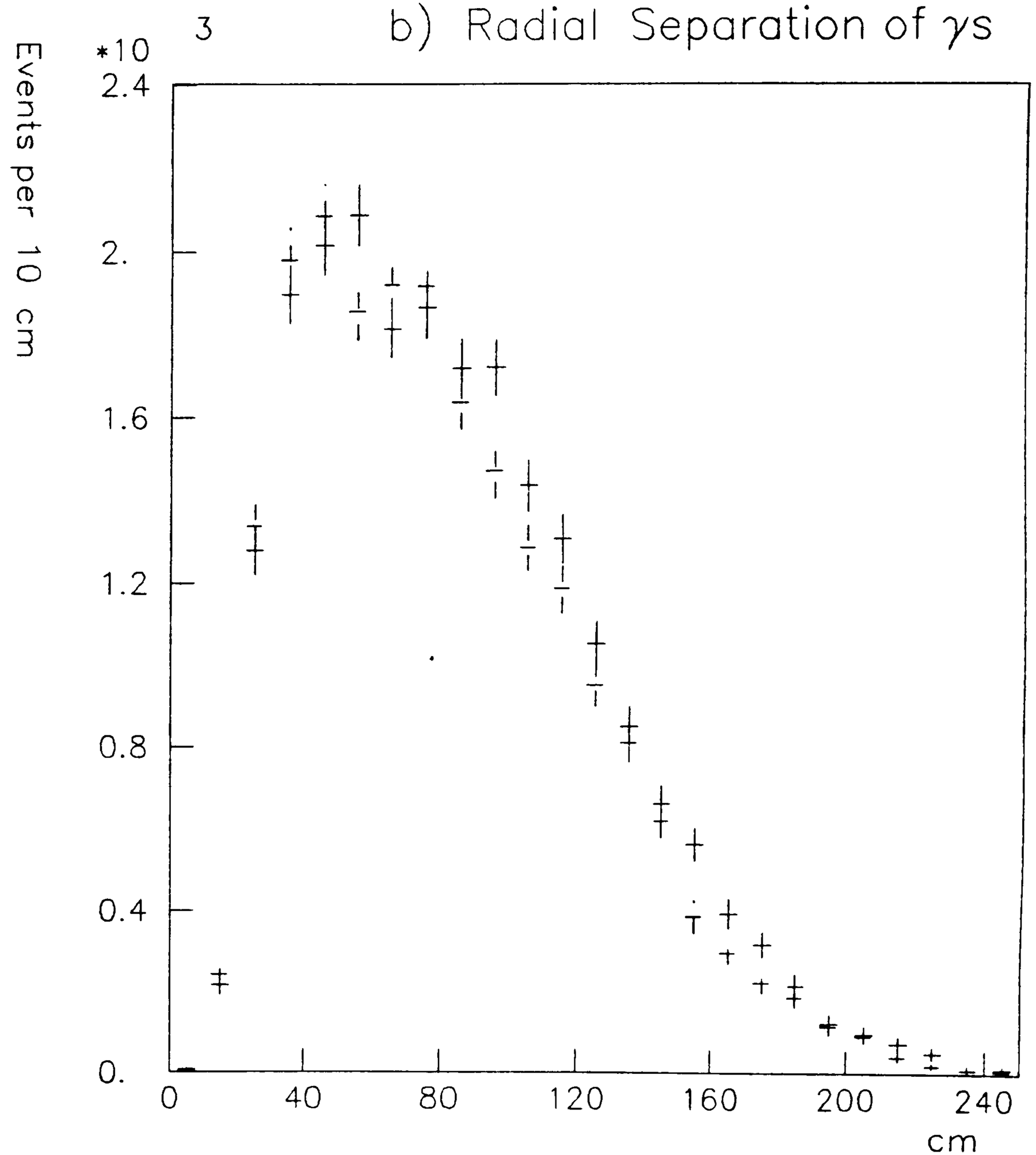
b) Radial Separation of γs
*10 3
Events per 10 cm
2.4
2.
1.6
1.2
0.8
0.4
0.
0
40
80
120
160
200
240
cm

Figure 5.14

a) Minimum γ Energy in Event

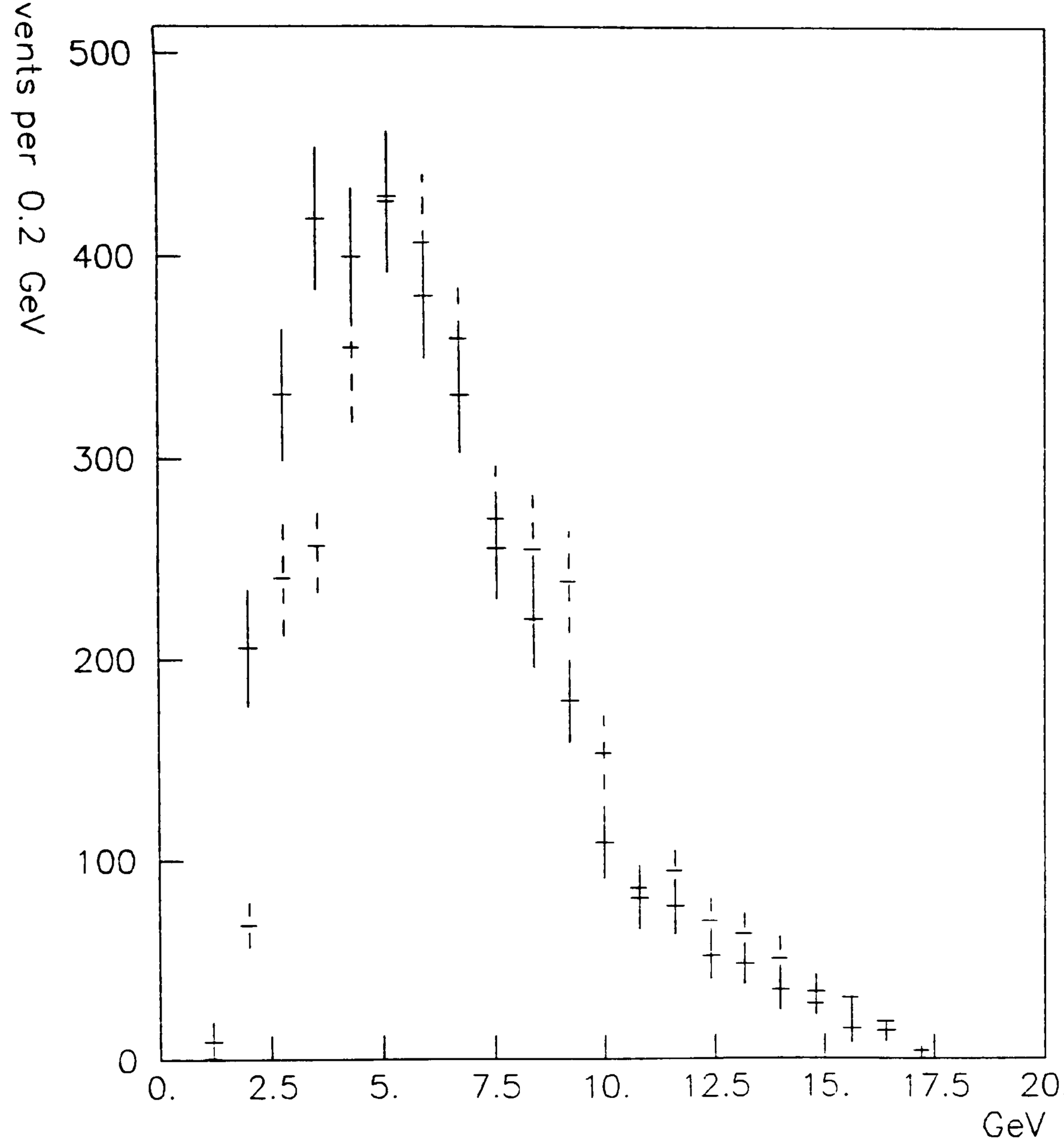

b) Maximum γ Energy in Event

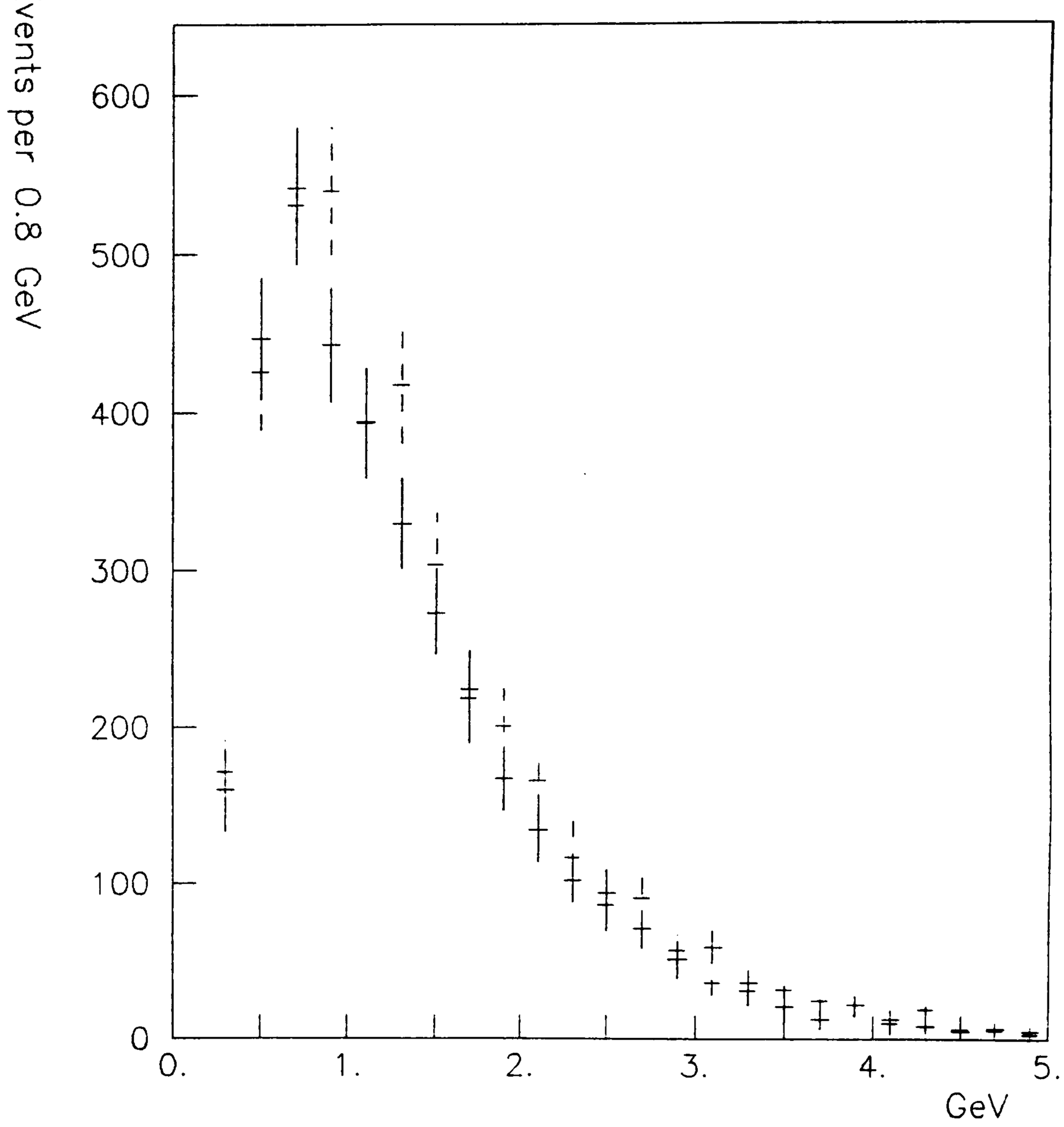

Figure 5.15

a) No. Blocks per Cluster

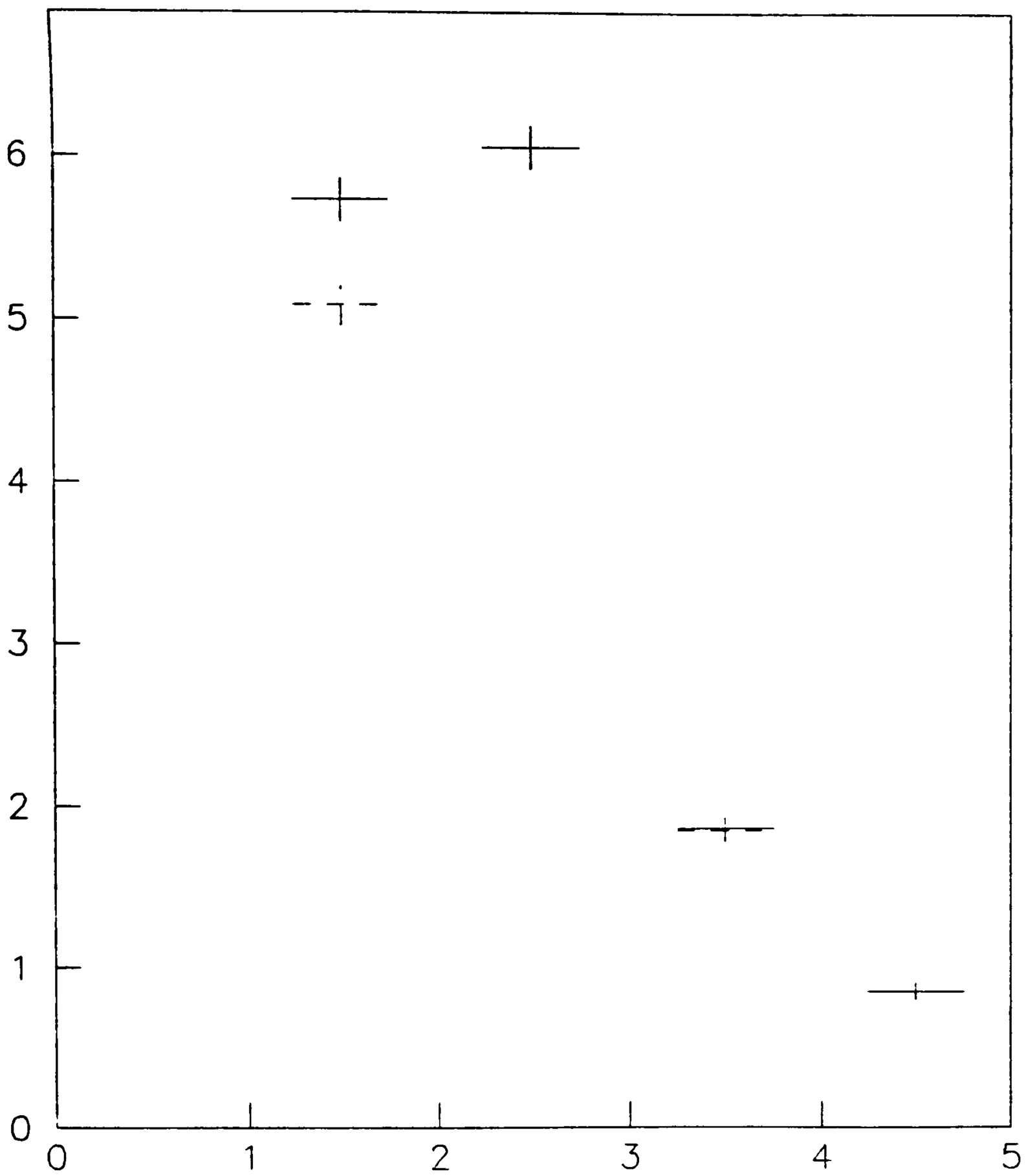

b) Minimum γ-γ Separation

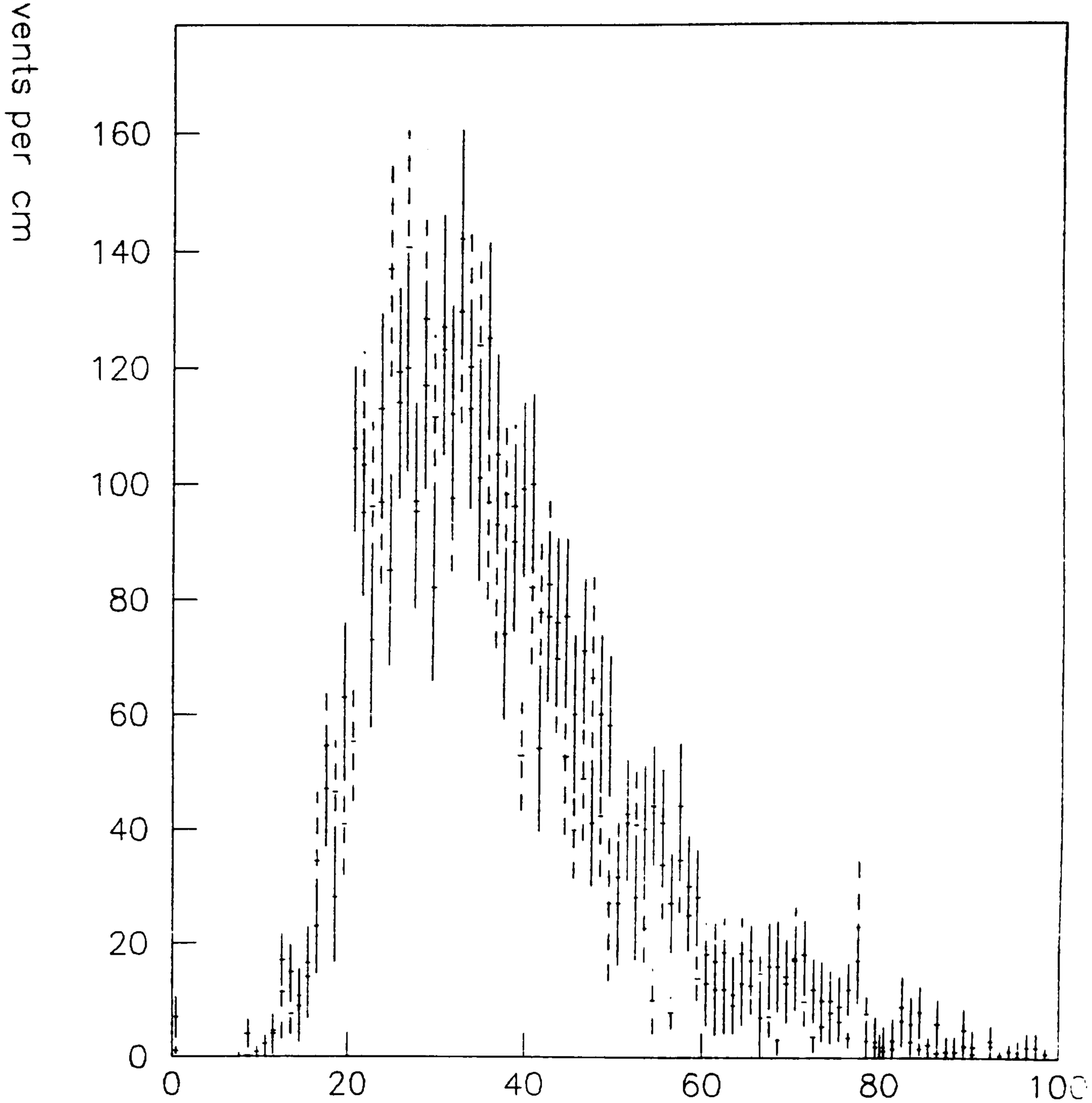

Figure 5.16

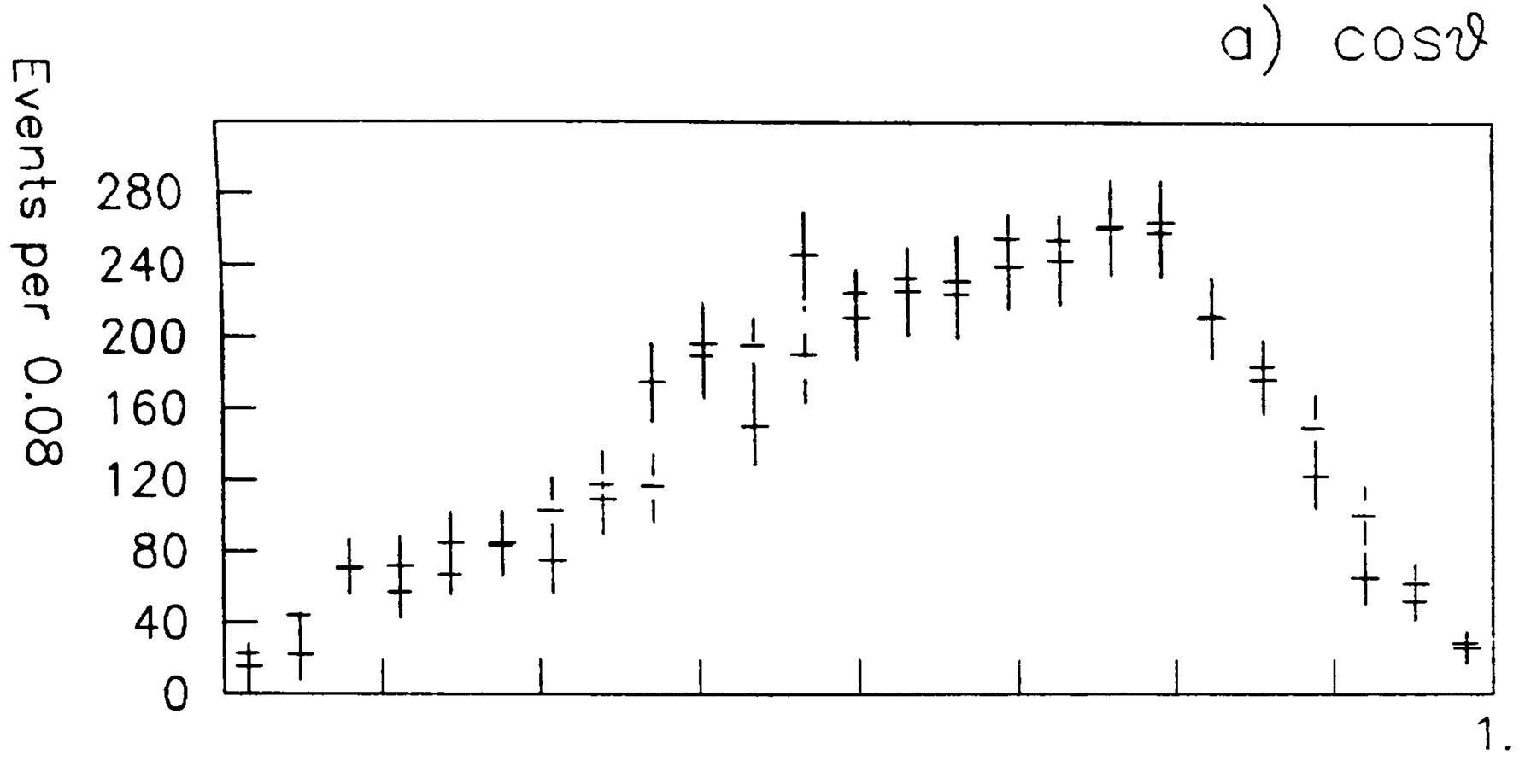
a) cosϑ
Events per 0.08
280
240
200
160
120
80
40
0
1.

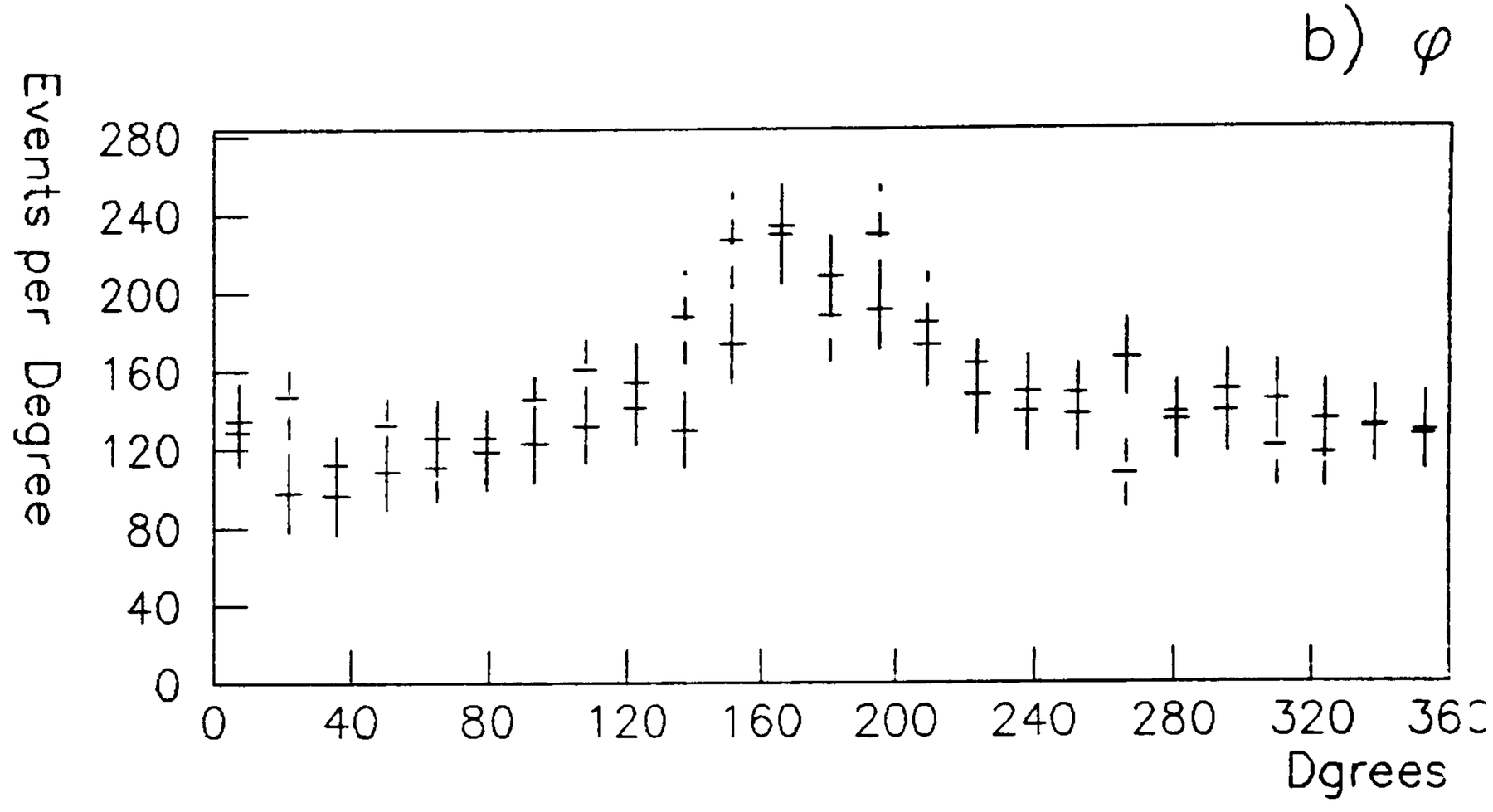
b) φ
Events per Degree
280
240
200
160
120
80
40
0
0
40
80
120
160
200
240
280
320
Dgrees

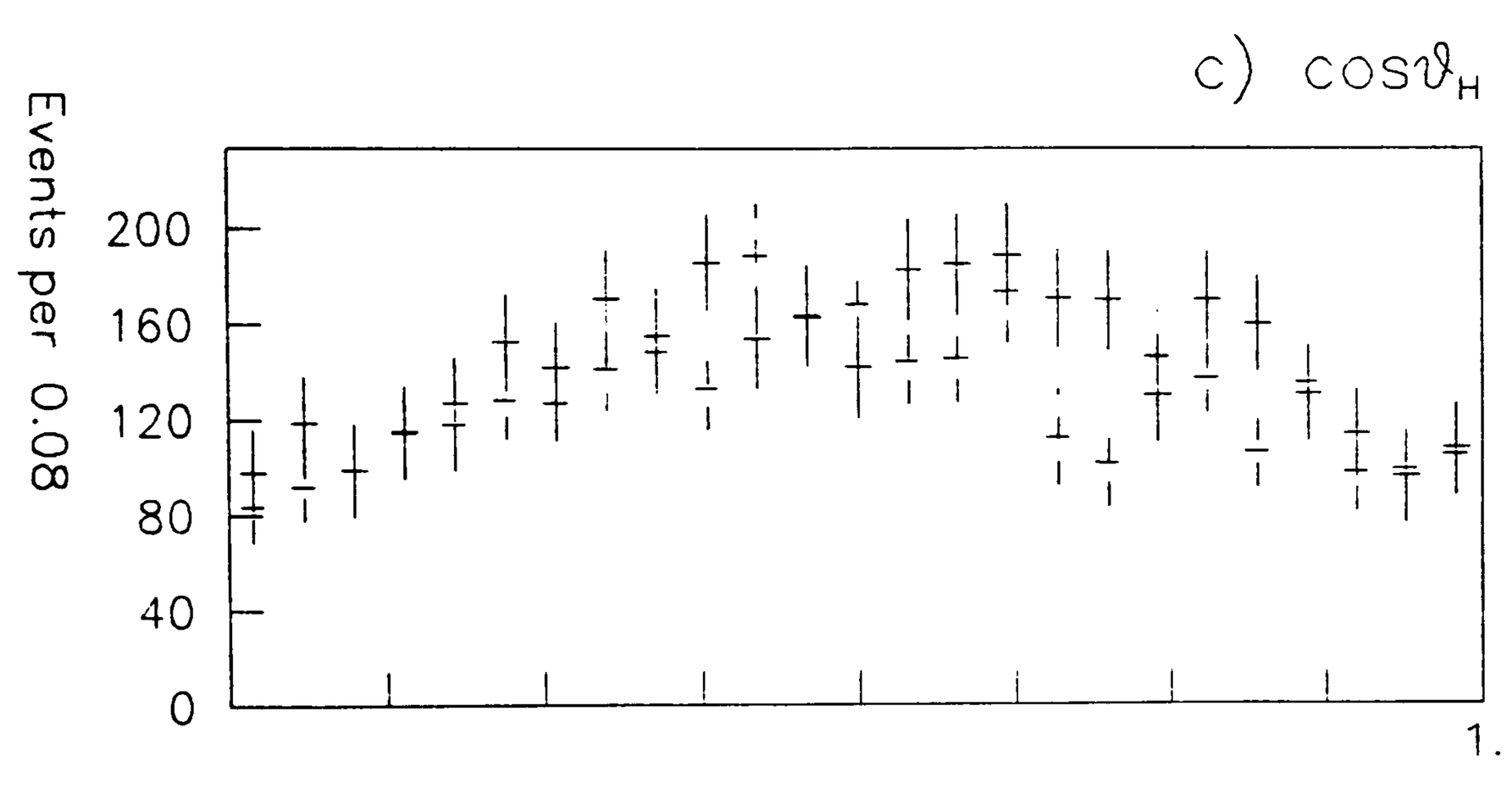
c) cosϑH
Events per 0.08
200
160
120
80
40
0
1.

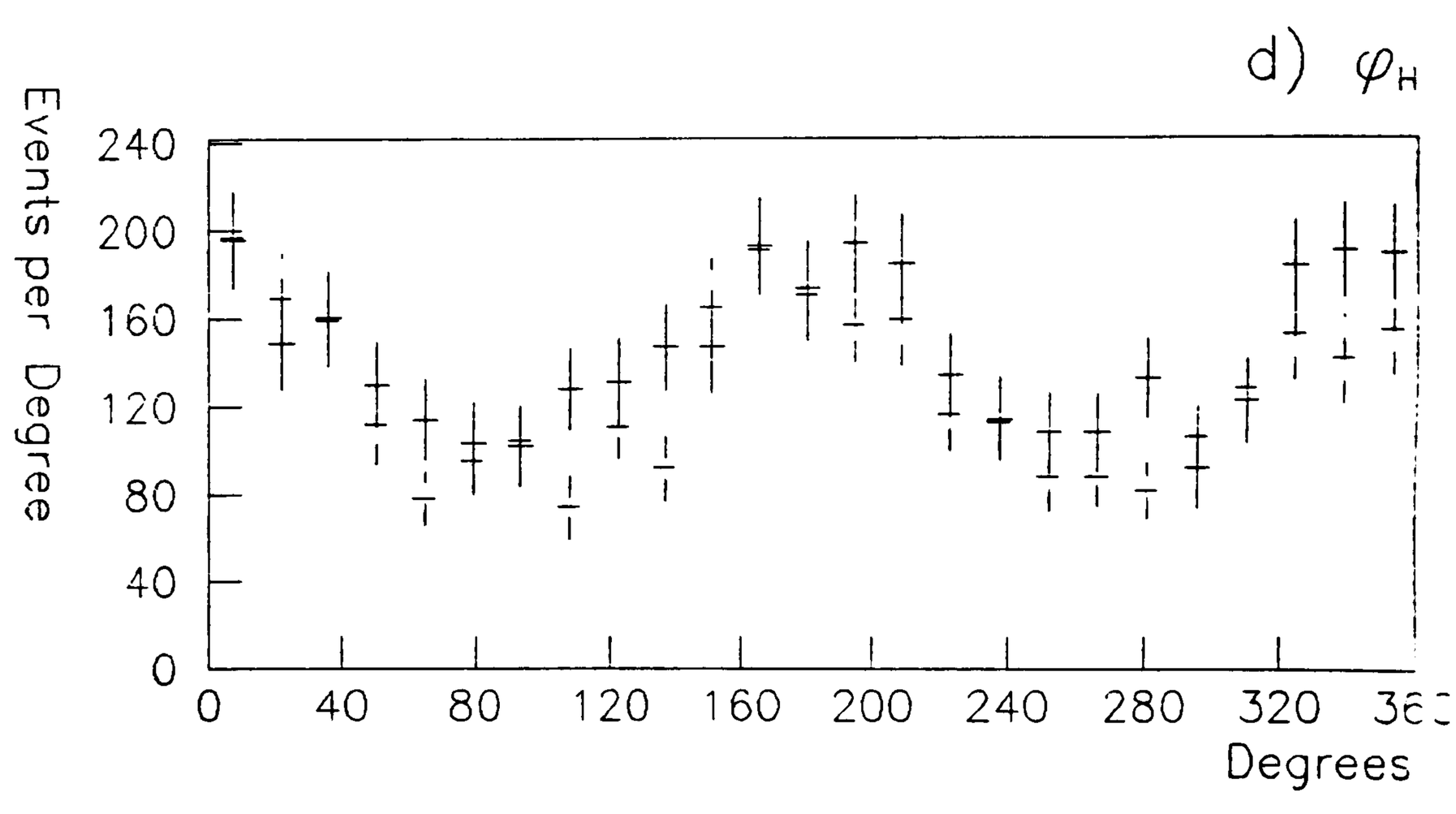
d) φH
Events per Degree
240
200
160
120
80
40
0
0
40
80
120
160
200
240
280
320
Degrees

Figure 5.17

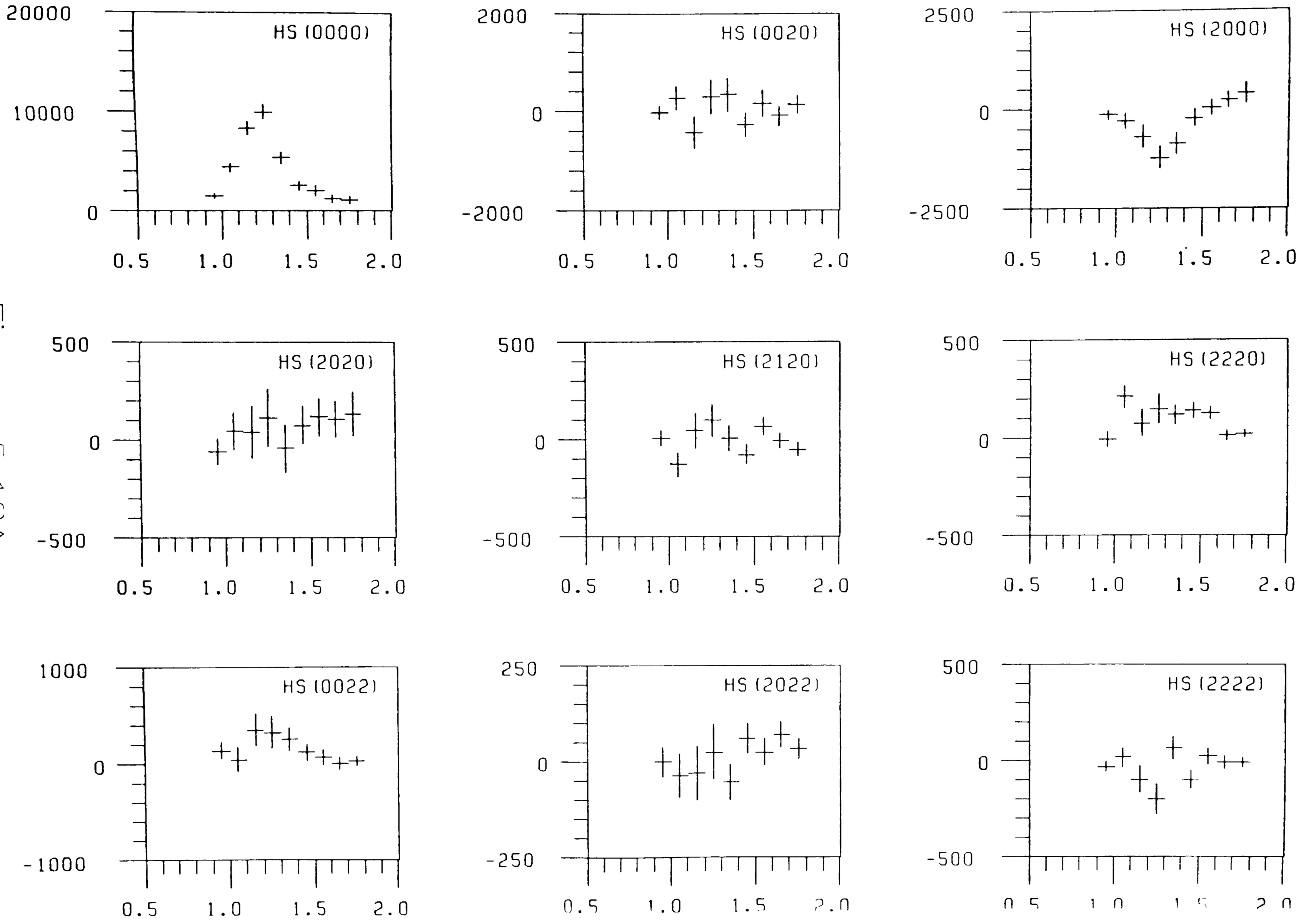
HS (0000)
20000
10000
0
0.5
1.0
1.5
2.0
HS (0020)
2000
0
-2000
HS (2000)
2500
-2500
HS (2020)
500
-500
HS (2120)
HS (2220)
HS (0022)
1000
-1000
HS (2022)
250
-250
HS (2222)

Figure 5.18A

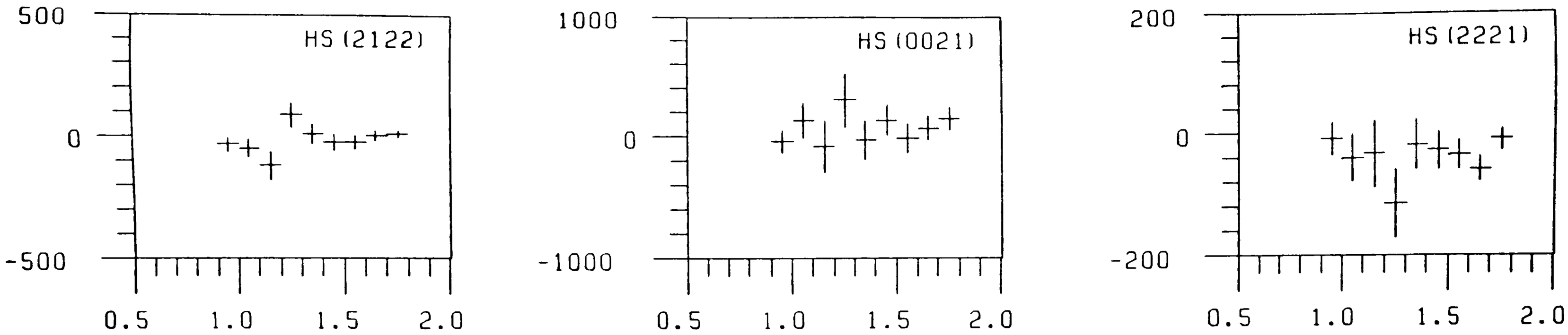
HS (2122)
500
0
-500
0.5
1.0
1.5
2.0
HS (0021)
1000
0
-1000
0.5
1.0
1.5
2.0
HS (2221)
200
0
-200
0.5
1.0
1.5
2.0
HS (2021)
500
0
-500
0.5
1.0
1.5
2.0
HS (2121)
250
0
-250
0.5
1.0
1.5
2.0
HS (2111)
500
0
-500
0.5
1.0
1.5
2.0
HA (0010)
2000
0
-2000
0.5
1.0
1.5
2.0
HA (0011)
2000
0
-2000
0.5
1.0
1.5
2.0
HA (2110)
1000
0
-1000
0.5
1.0
1.5
2.0

Figure 5.188

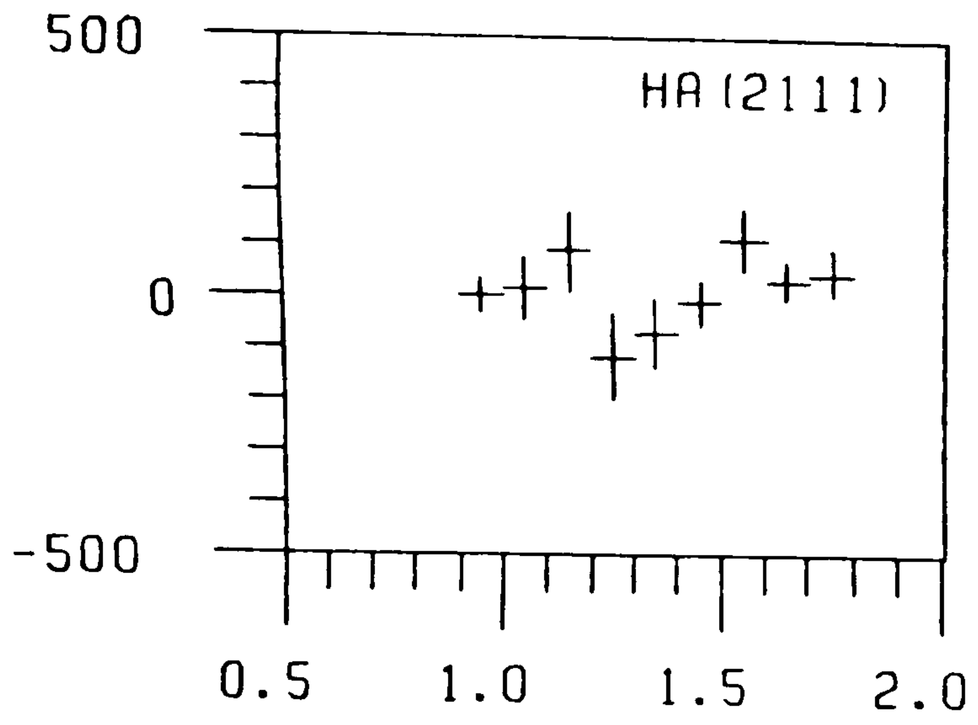
HA(2111)
500
0
-500
0.5
1.0
1.5
2.0

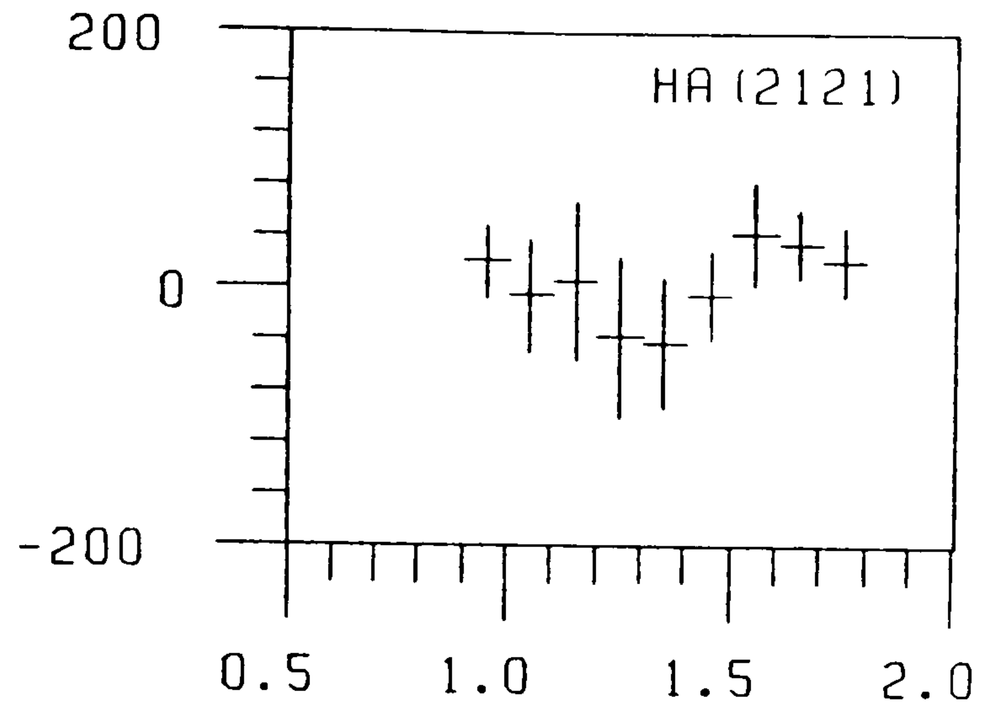
HA(2121)
200
0
-200
0.5
1.0
1.5
2.0

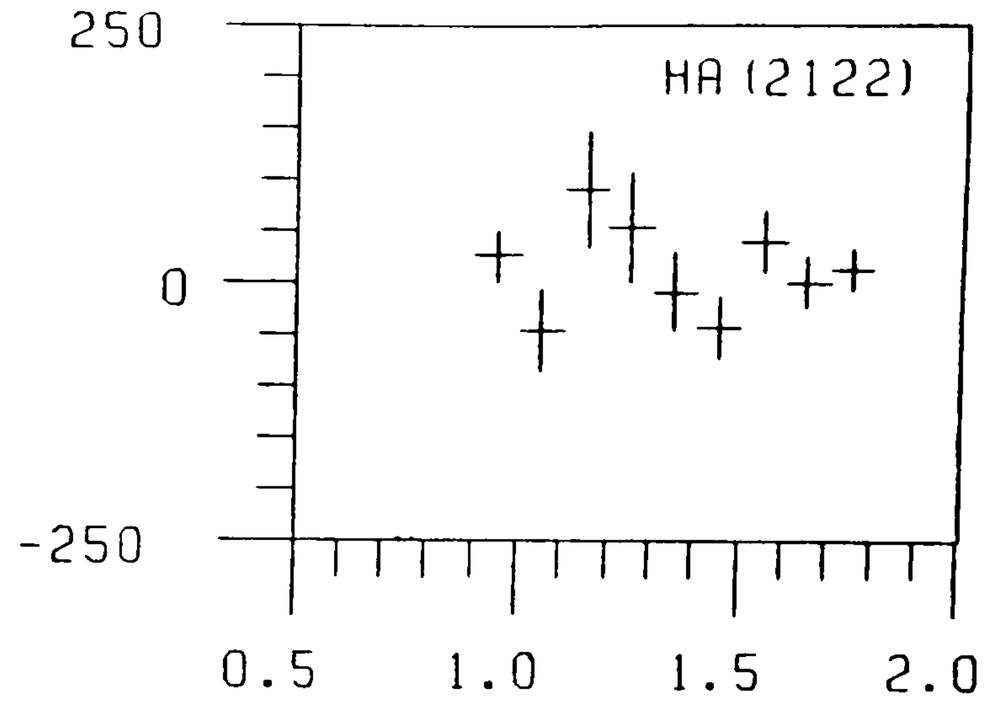
HA(2122)
250
0
-250
0.5
1.0
1.5
2.0

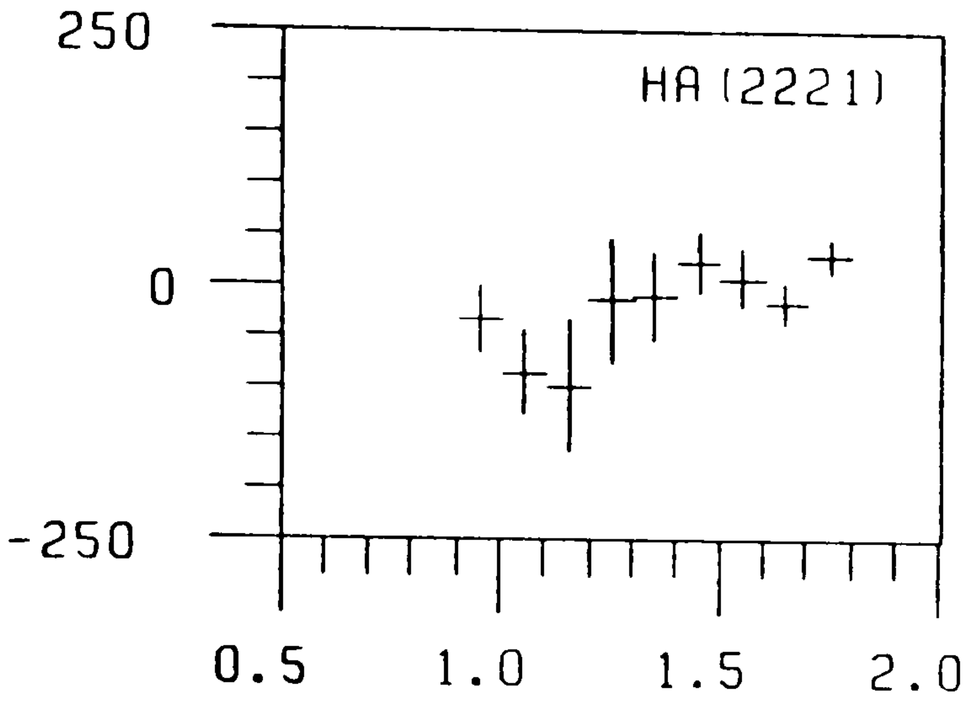
HA(2221)
250
0
-250
0.5
1.0
1.5
2.0

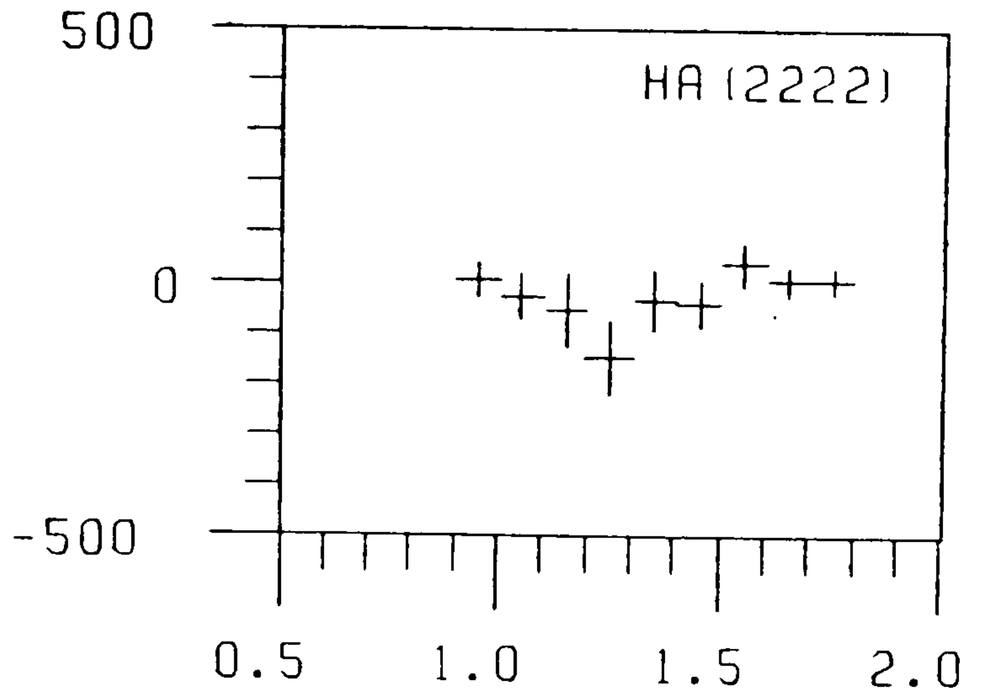
HA(2222)
500
0
-500
0.5
1.0
1.5
2.0

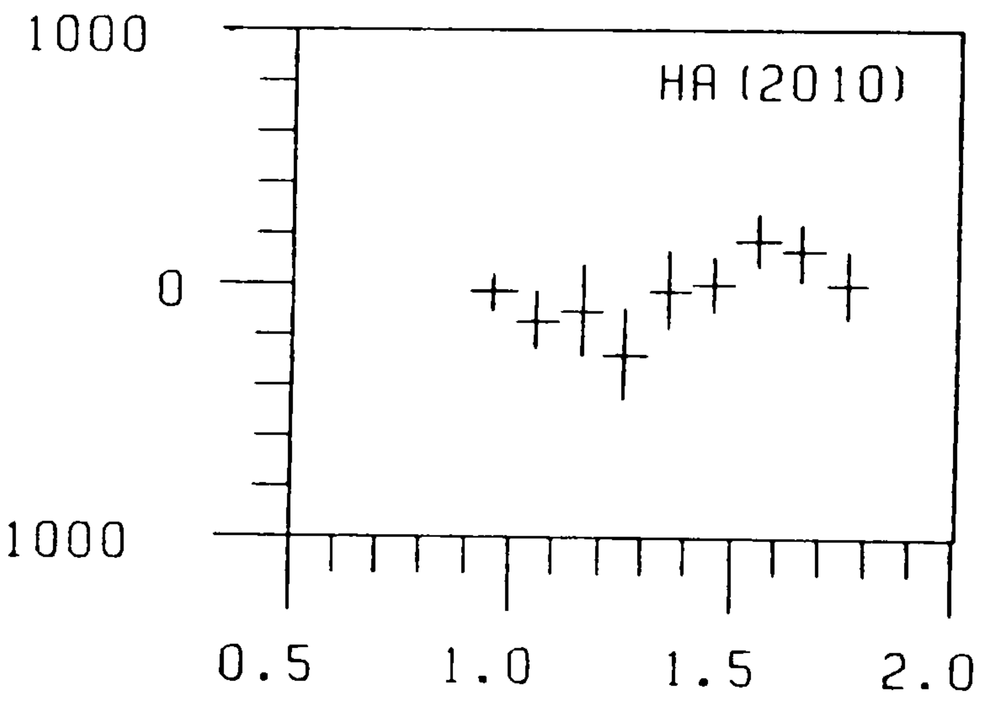
HA(2010)
1000
0
-1000
0.5
1.0
1.5
2.0

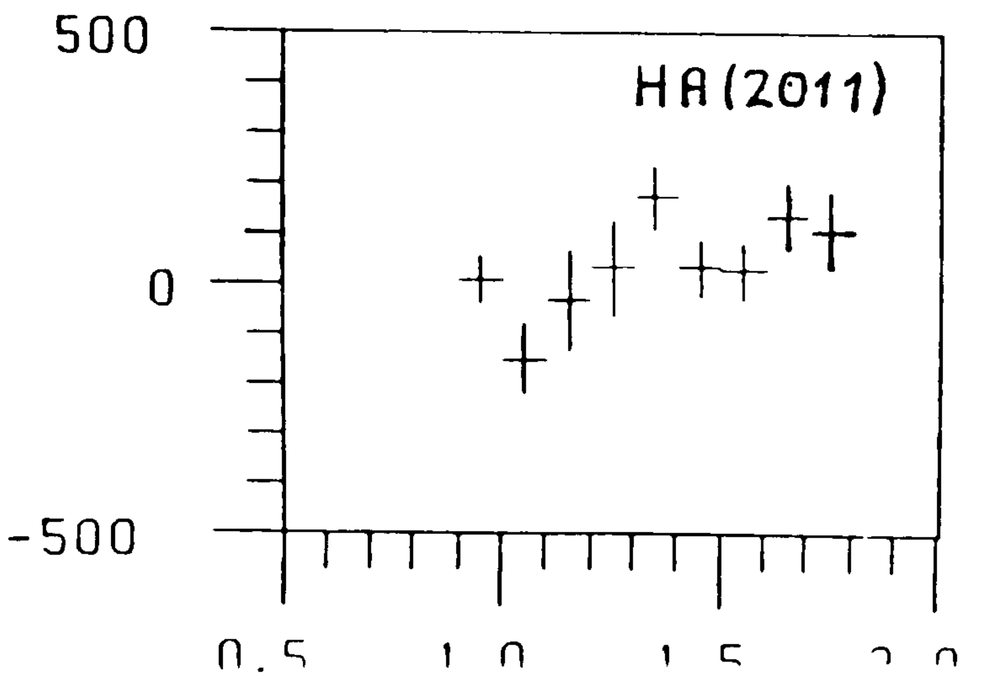
HA(2011)
500
0
-500
0.5
1.0
1.5
2.0

Figure 5.16c

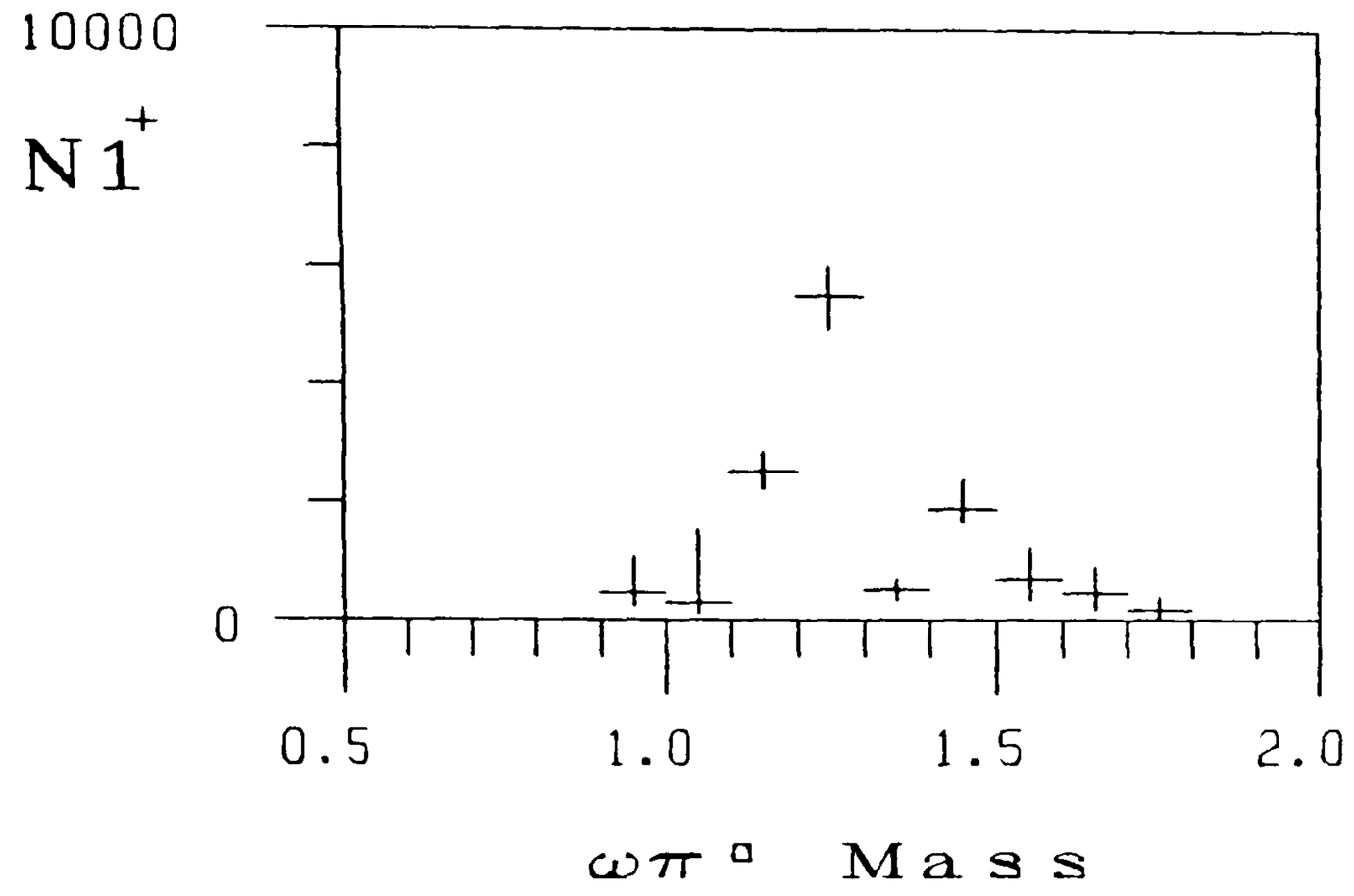
10000
$N1^+$
0
0.5
1.0
1.5
2.0
$\omega\pi^0$ Mass

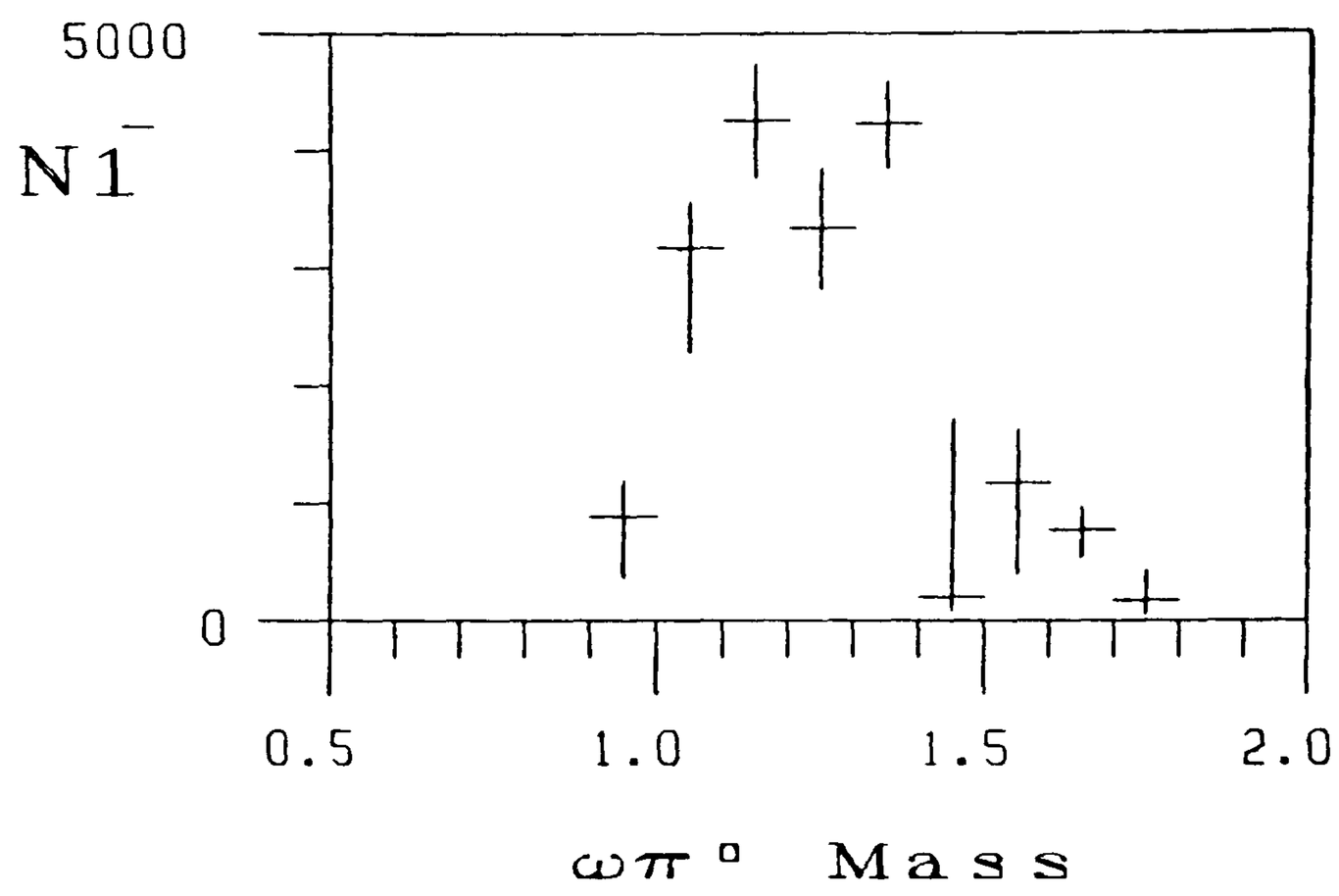
5000
$N1^-$
0
0.5
1.0
1.5
2.0
$\omega\pi^0$ Mass

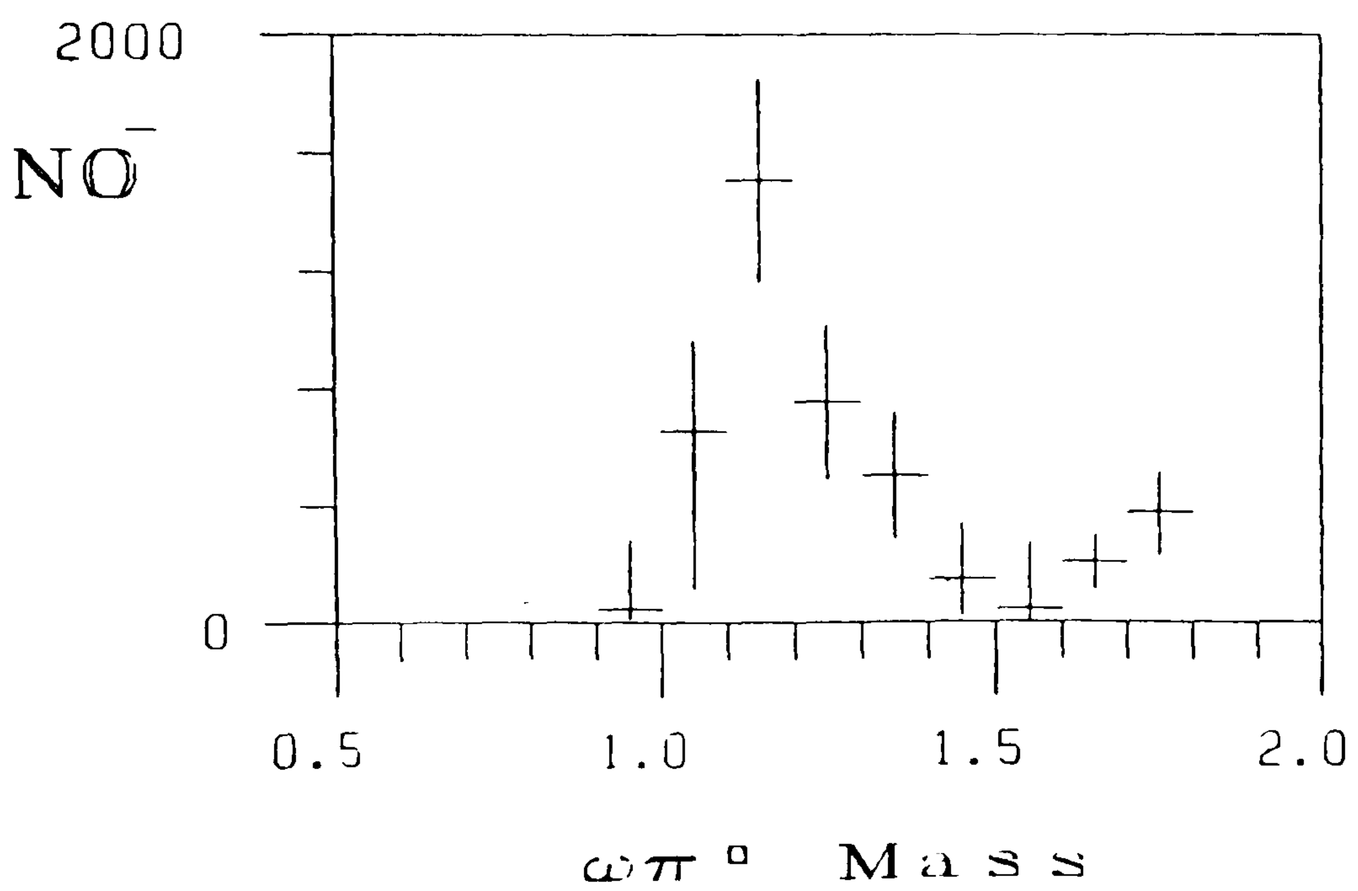
2000
NO^-
0
0.5
1.0
1.5
2.0
$\omega\pi^0$ Mass

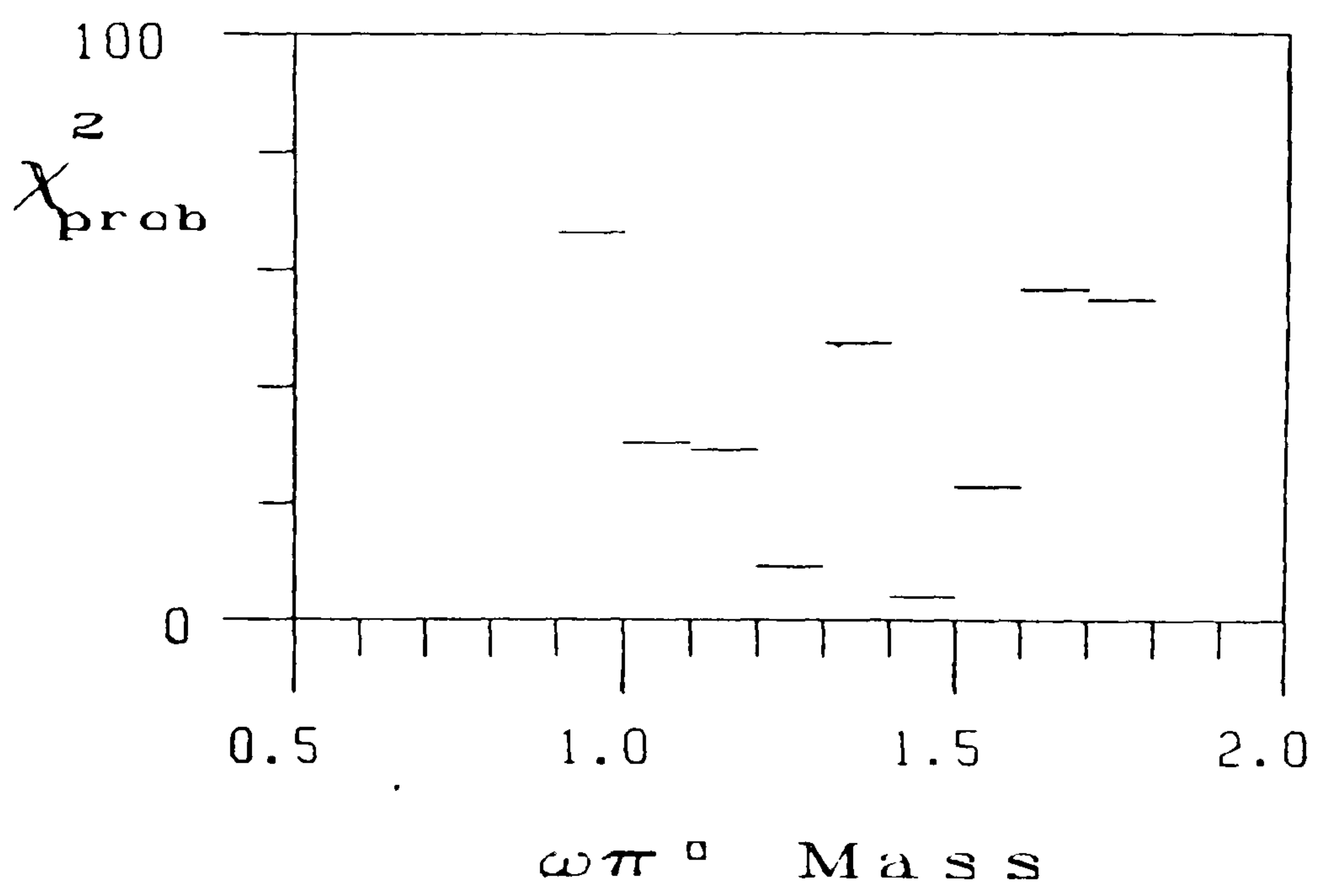
100
χ^2_{prob}
0
0.5
1.0
1.5
2.0
$\omega\pi^0$ Mass

Figure 5.19A

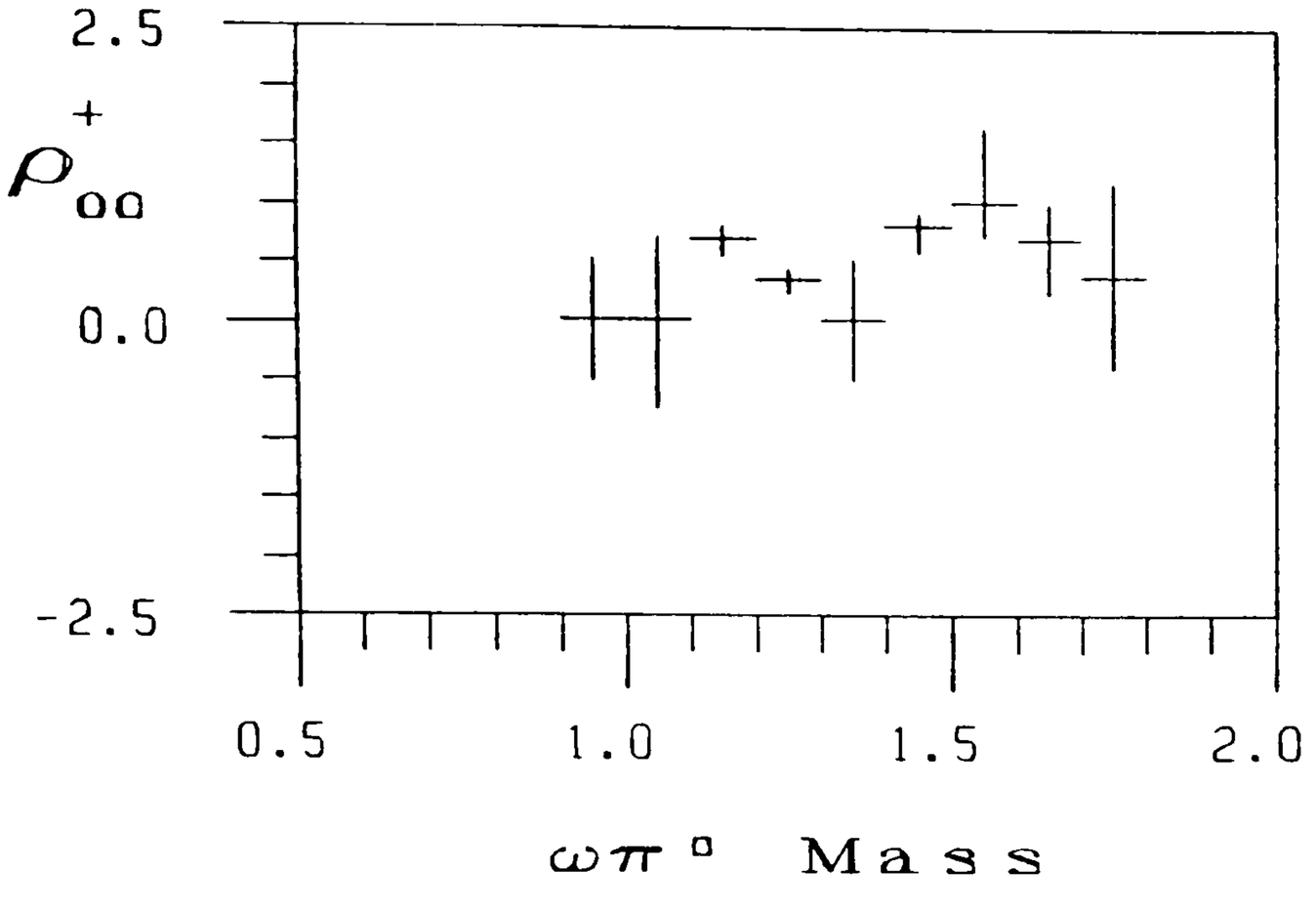
2.5
ρ^{+}_{00}
0.0
-2.5
0.5
1.0
1.5
2.0
ωπ° Mass

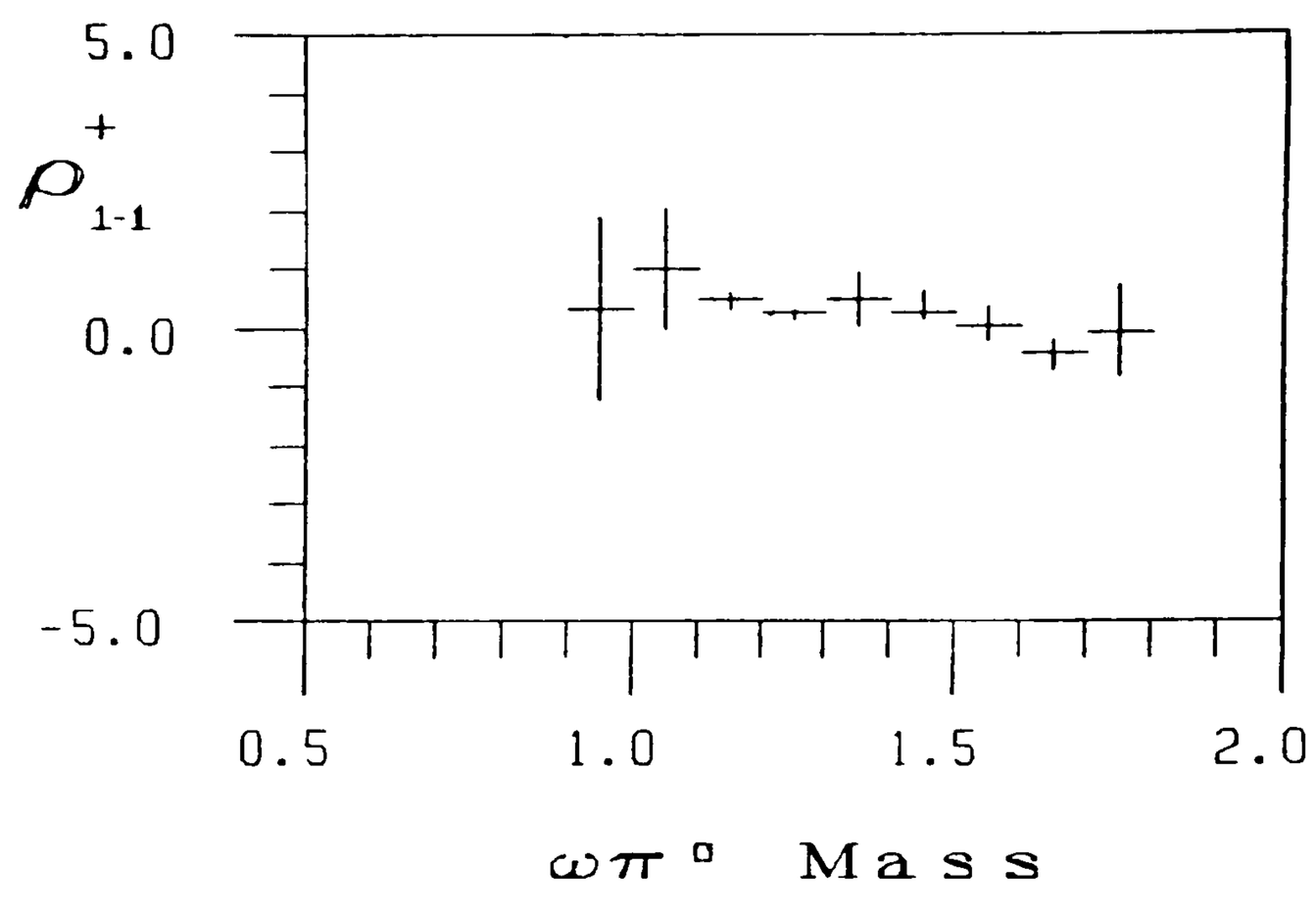
5.0
ρ^{+}_{1-1}
0.0
-5.0
0.5
1.0
1.5
2.0
ωπ° Mass

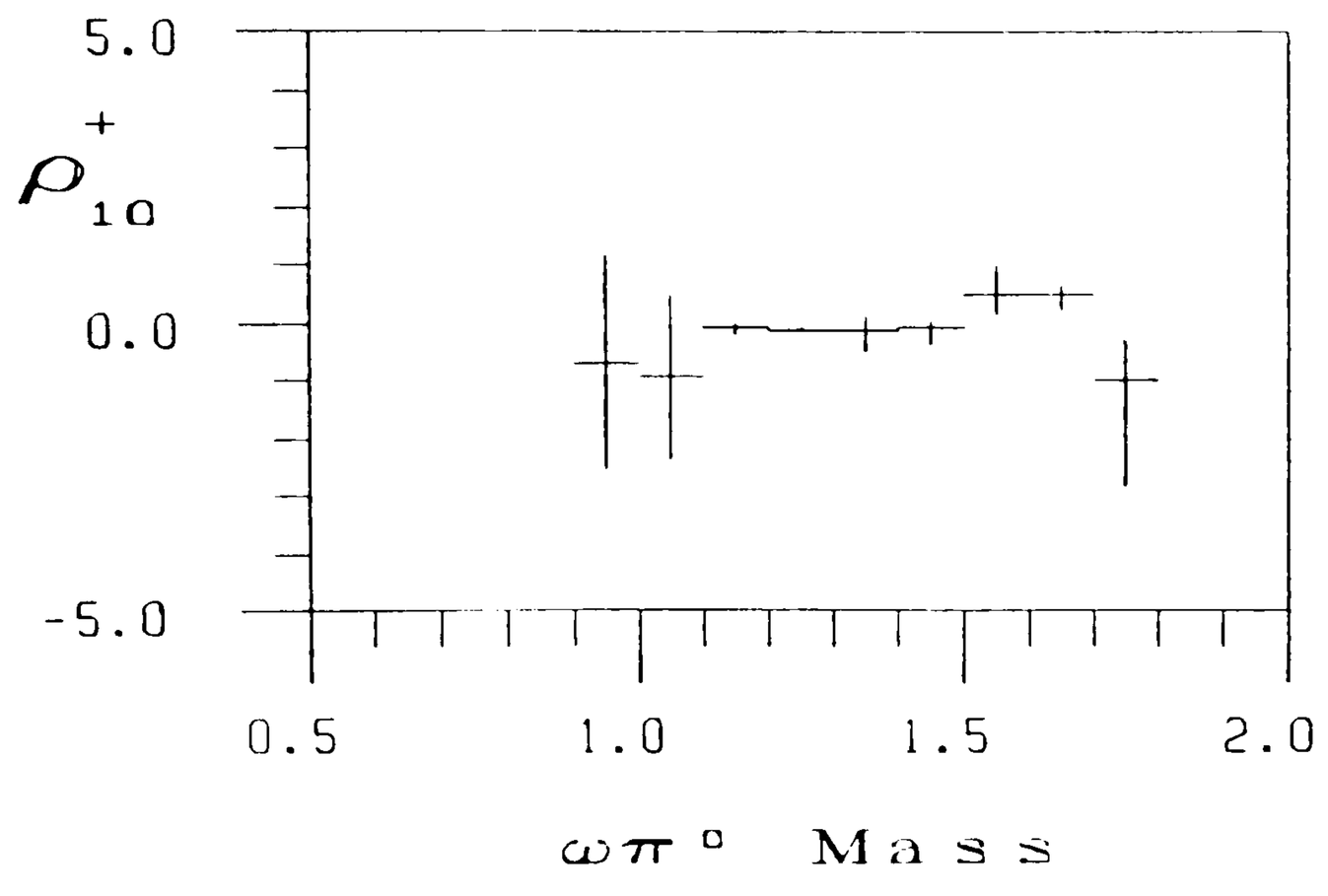
5.0
ρ^{+}_{10}
0.0
-5.0
0.5
1.0
1.5
2.0
ωπ° Mass

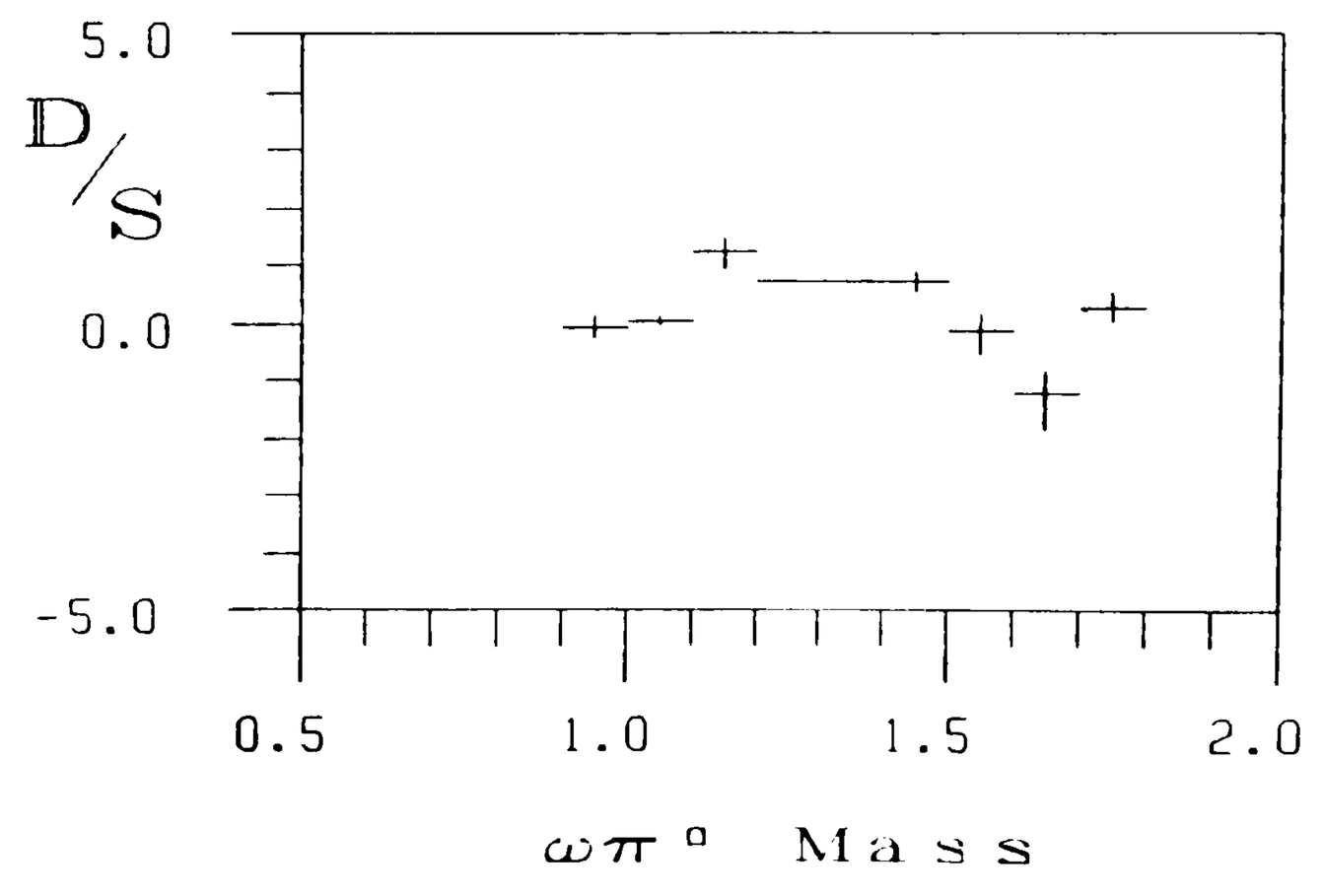
5.0
D/S
0.0
-5.0
0.5
1.0
1.5
2.0
ωπ° Mass

Figure 5.19B

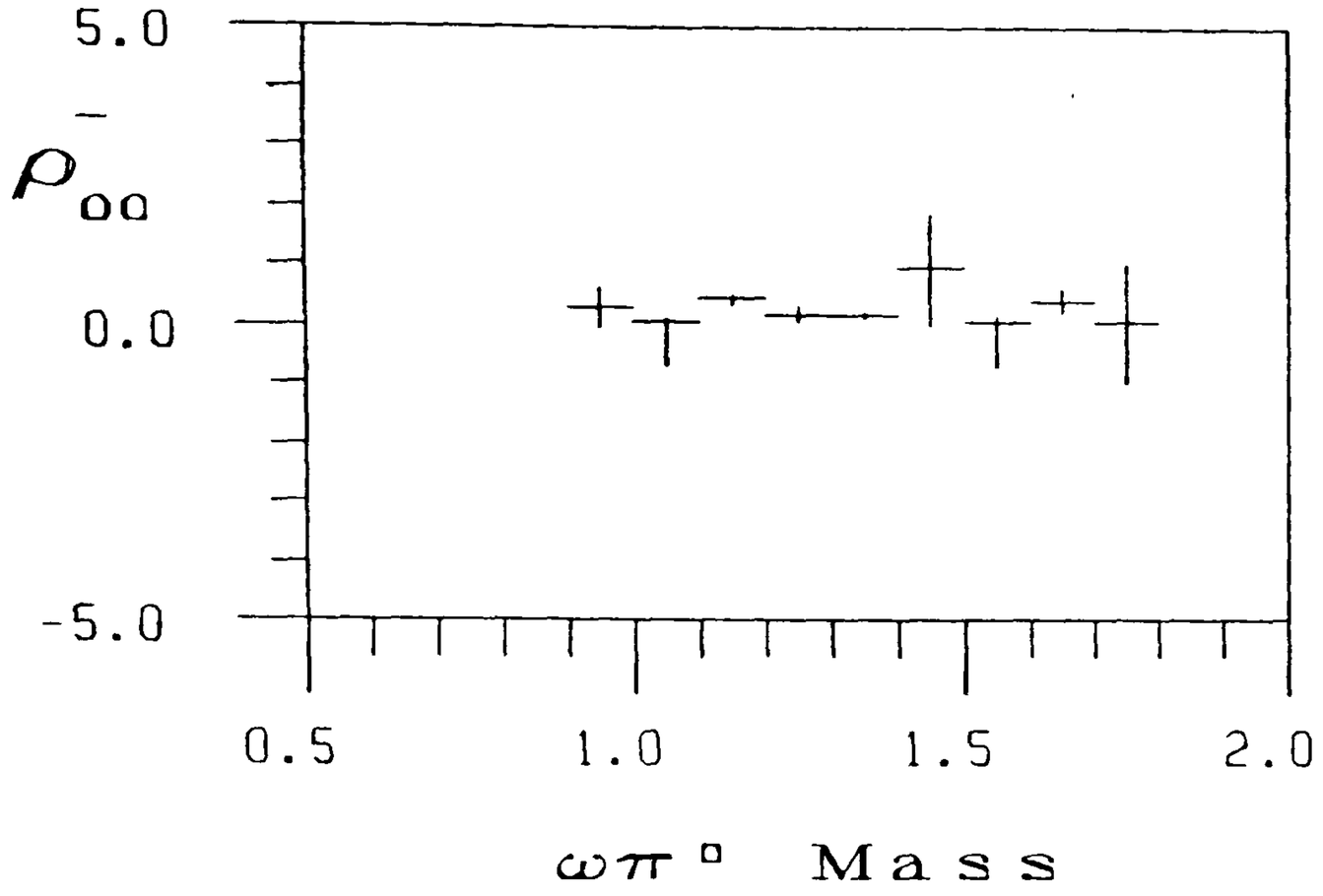
5.0
$\bar{\rho}_{00}$
0.0
-5.0
0.5
1.0
1.5
2.0
$\omega\pi^0$ Mass

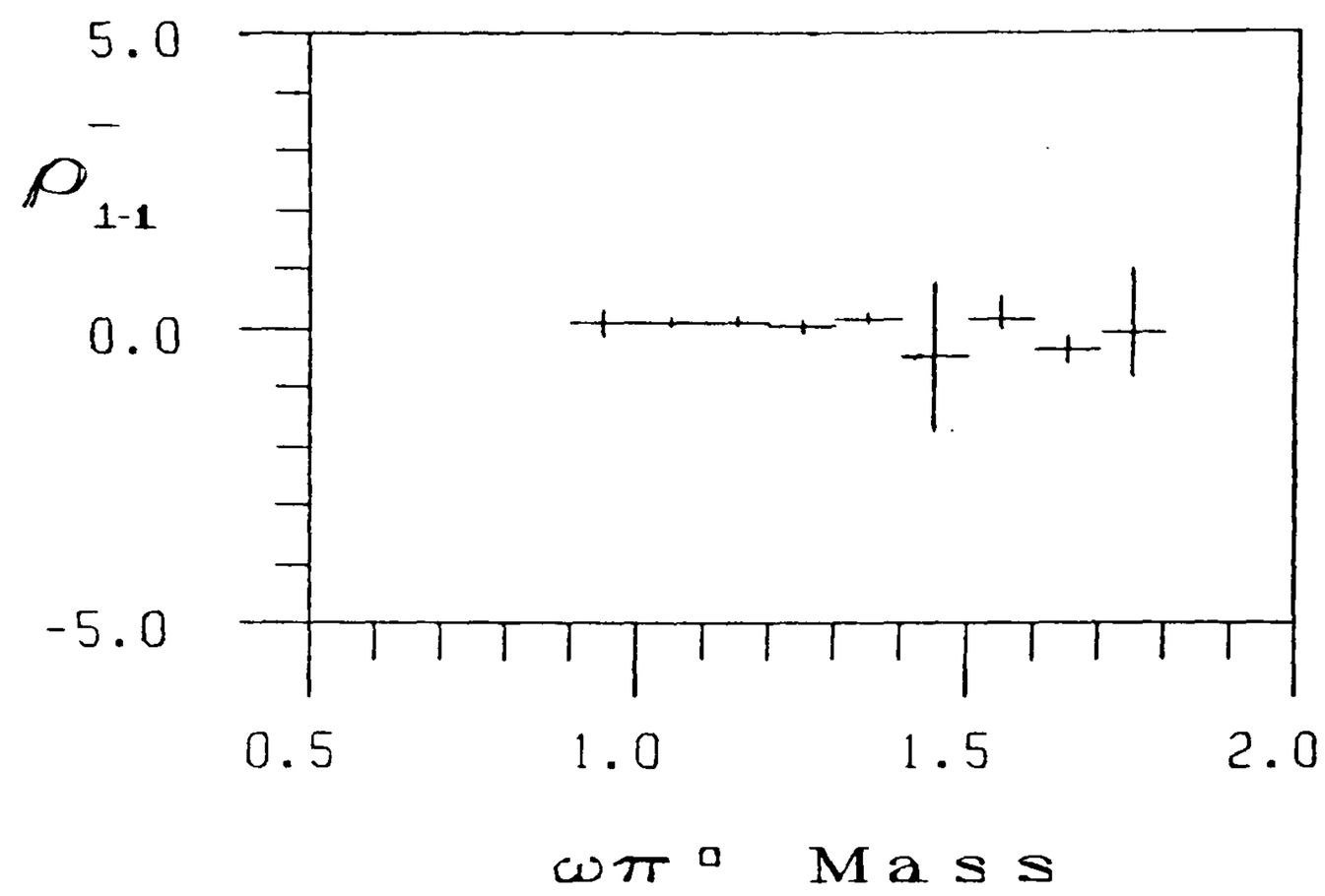
5.0
$\bar{\rho}_{1-1}$
0.0
-5.0
0.5
1.0
1.5
2.0
$\omega\pi^0$ Mass

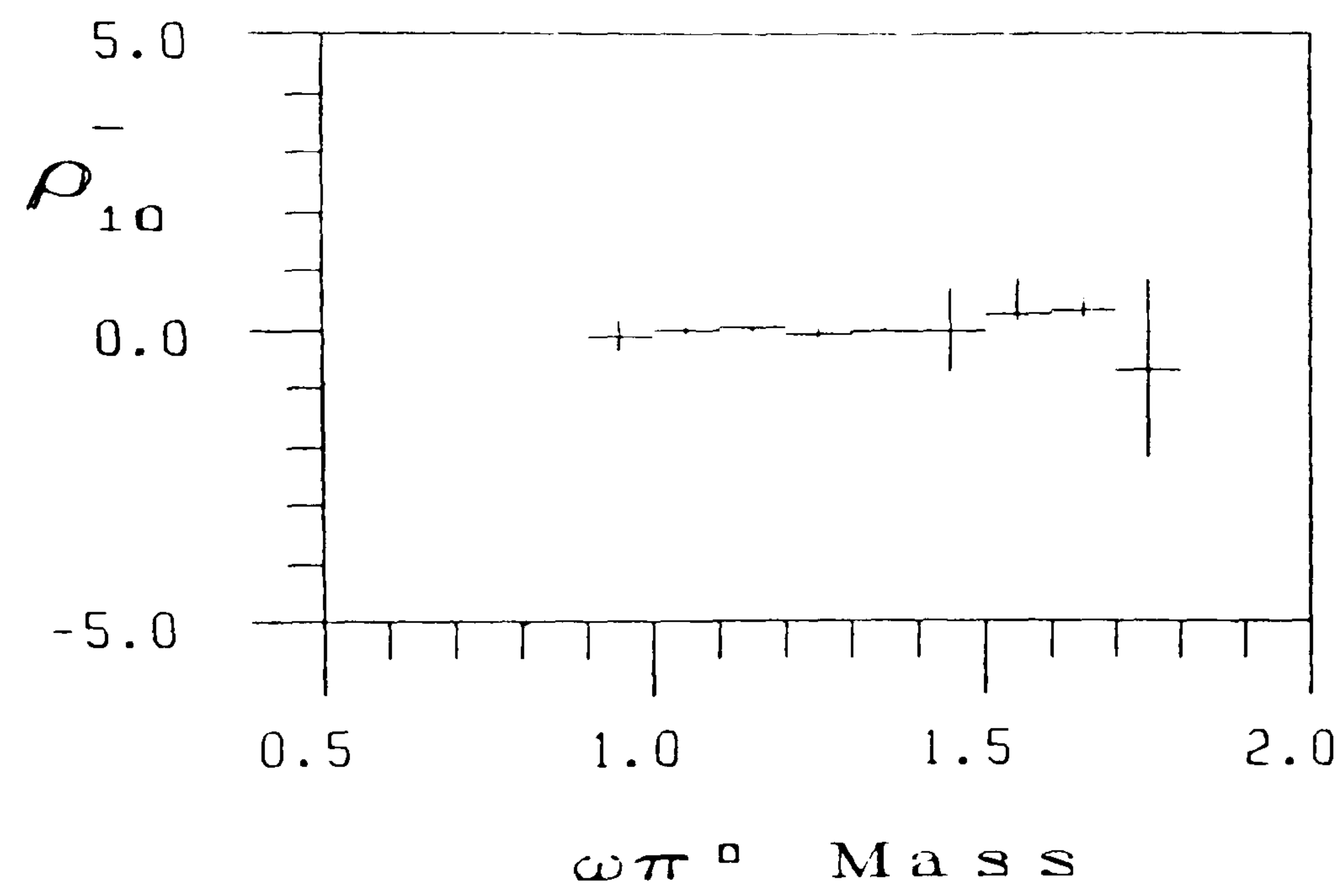
5.0
$\bar{\rho}_{10}$
0.0
-5.0
0.5
1.0
1.5
2.0
$\omega\pi^0$ Mass

Figure 5.19C

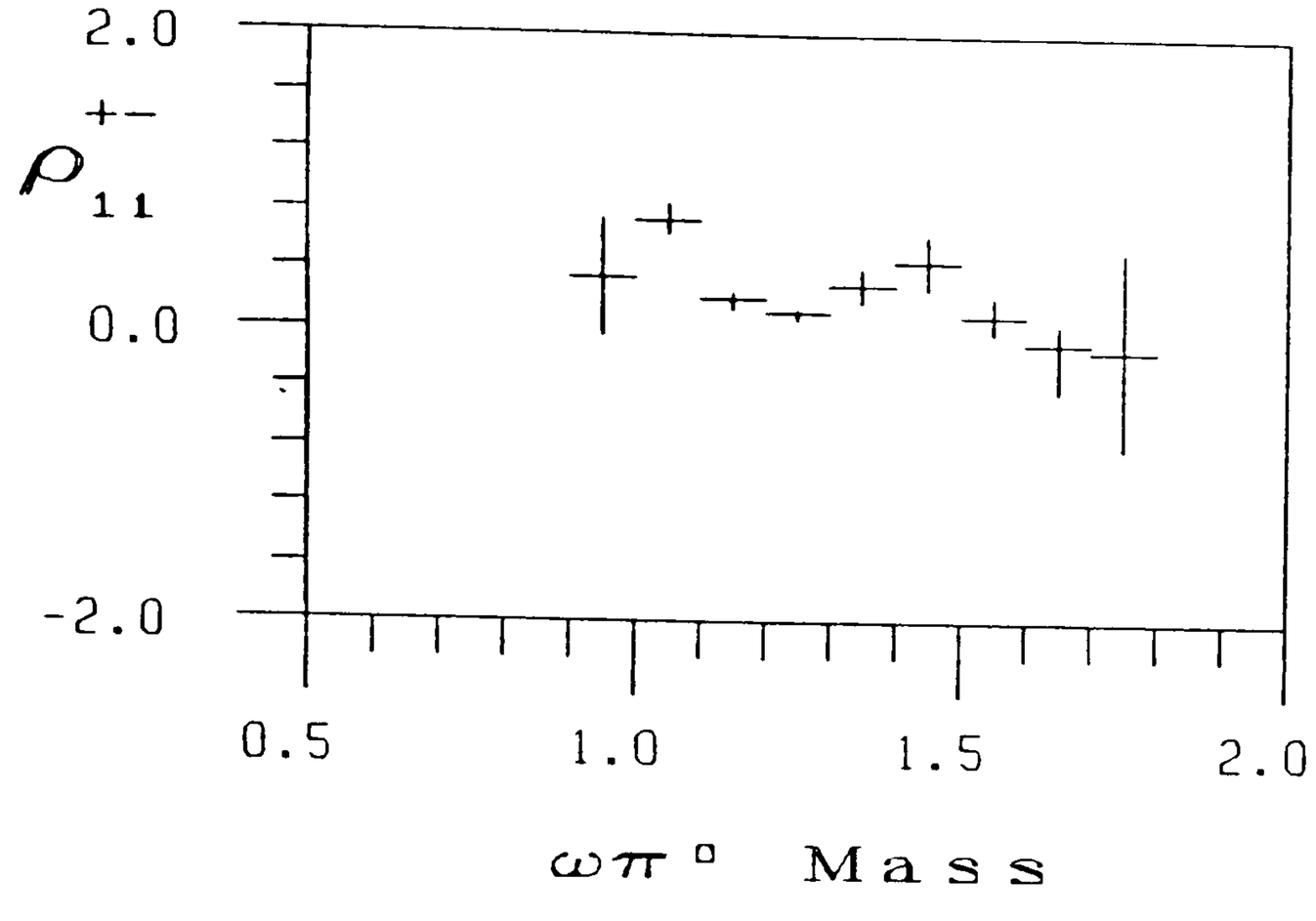
2.0
+−
ρ11
0.0
-2.0
0.5
1.0
1.5
2.0
ωπ° Mass

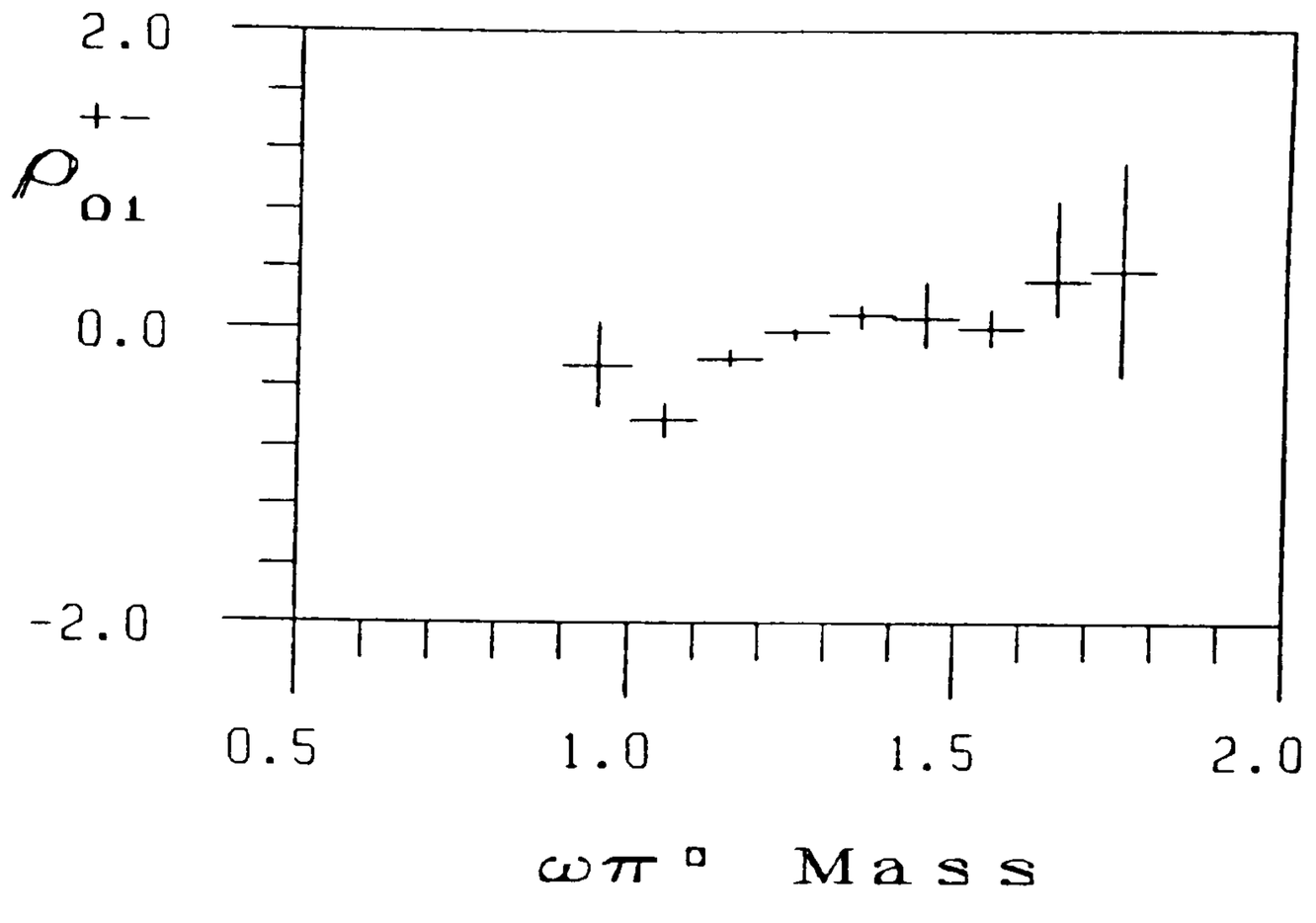
2.0
+−
ρ01
0.0
-2.0
0.5
1.0
1.5
2.0
ωπ° Mass

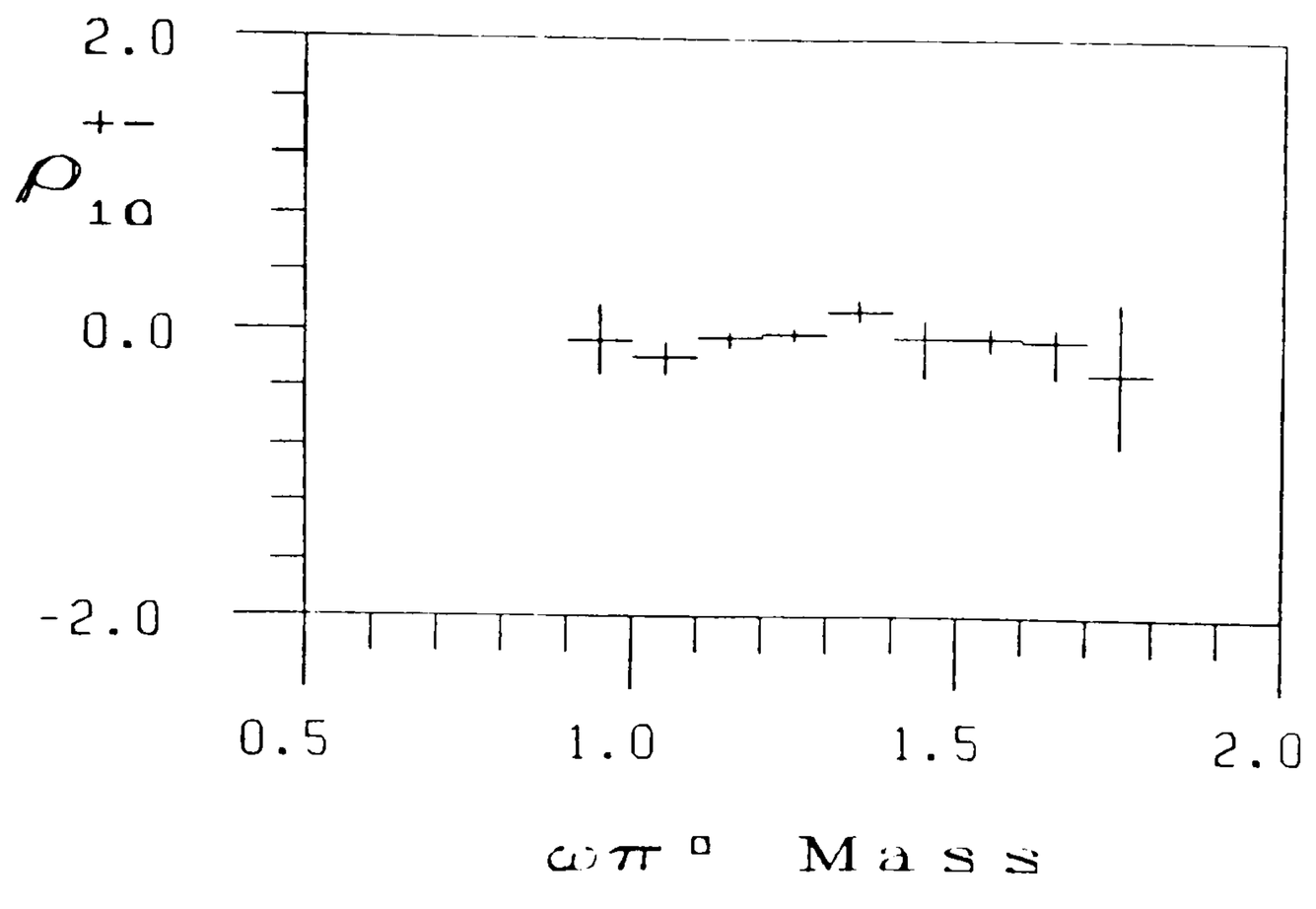
2.0
+−
ρ10
0.0
-2.0
0.5
1.0
1.5
2.0
ωπ° Mass

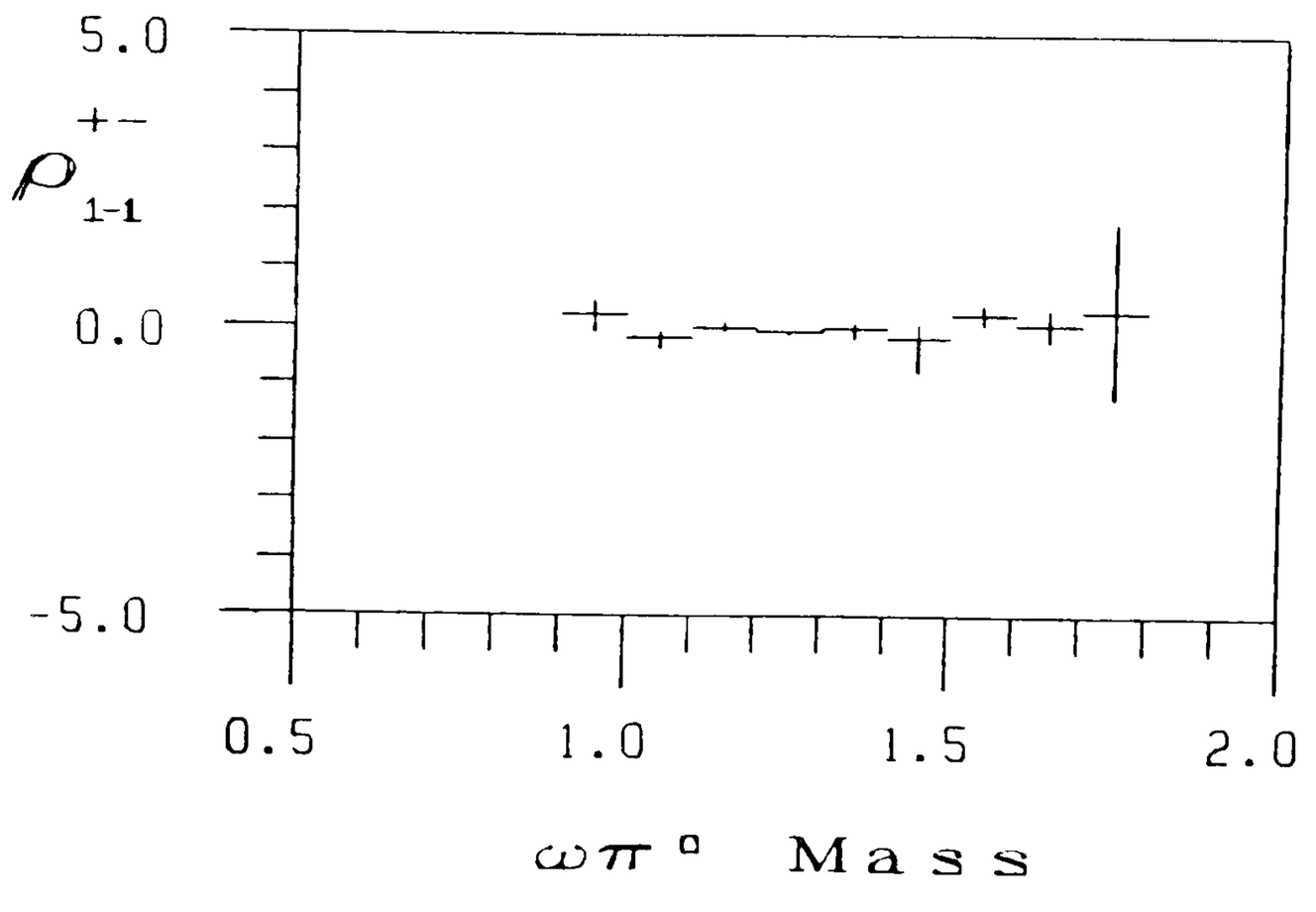
5.0
+−
ρ1-1
0.0
-5.0
0.5
1.0
1.5
2.0
ωπ° Mass

Figure 5.19D

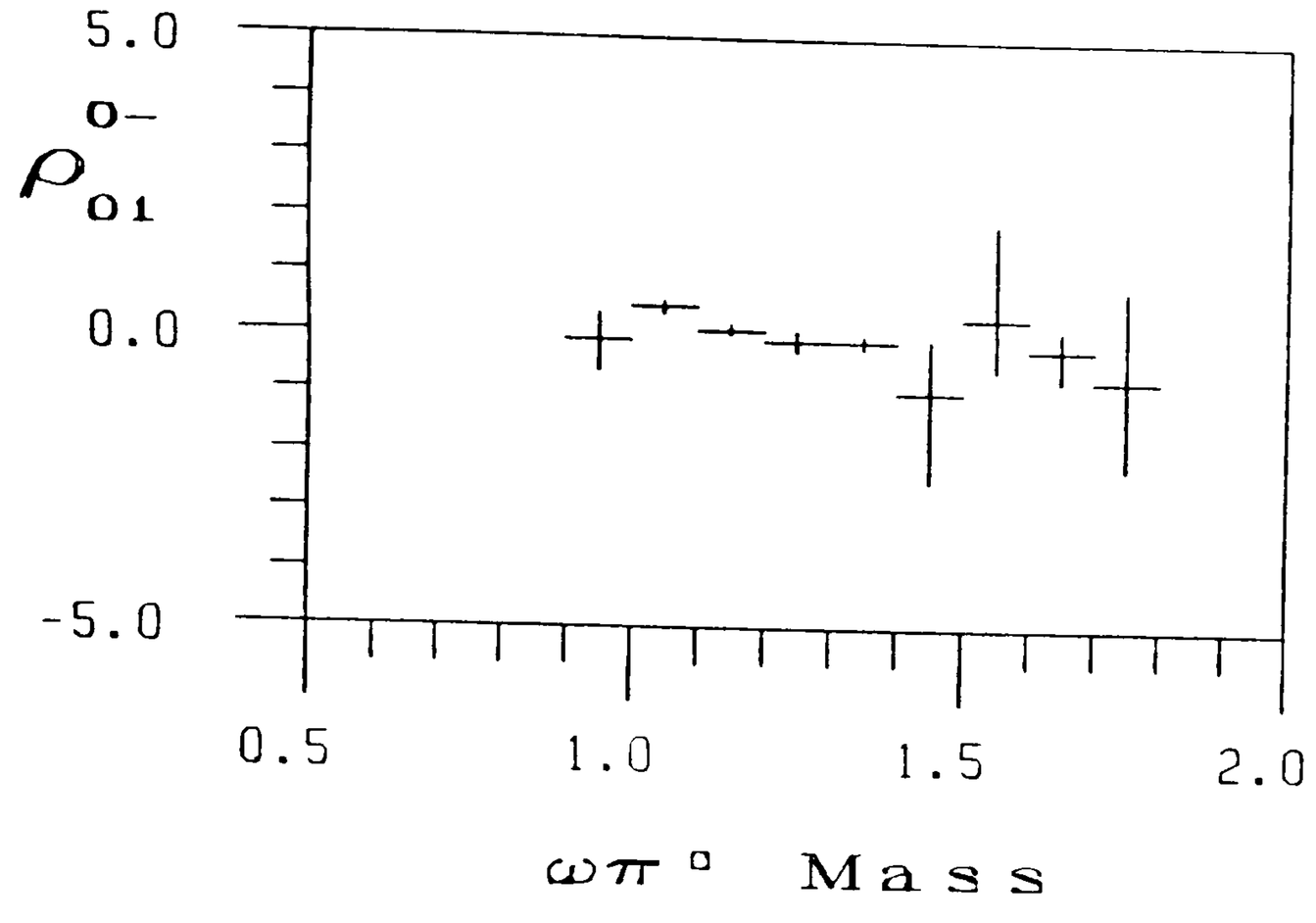
5.0
0.0
-5.0
0.5
1.0
1.5
2.0
ωπ° Mass

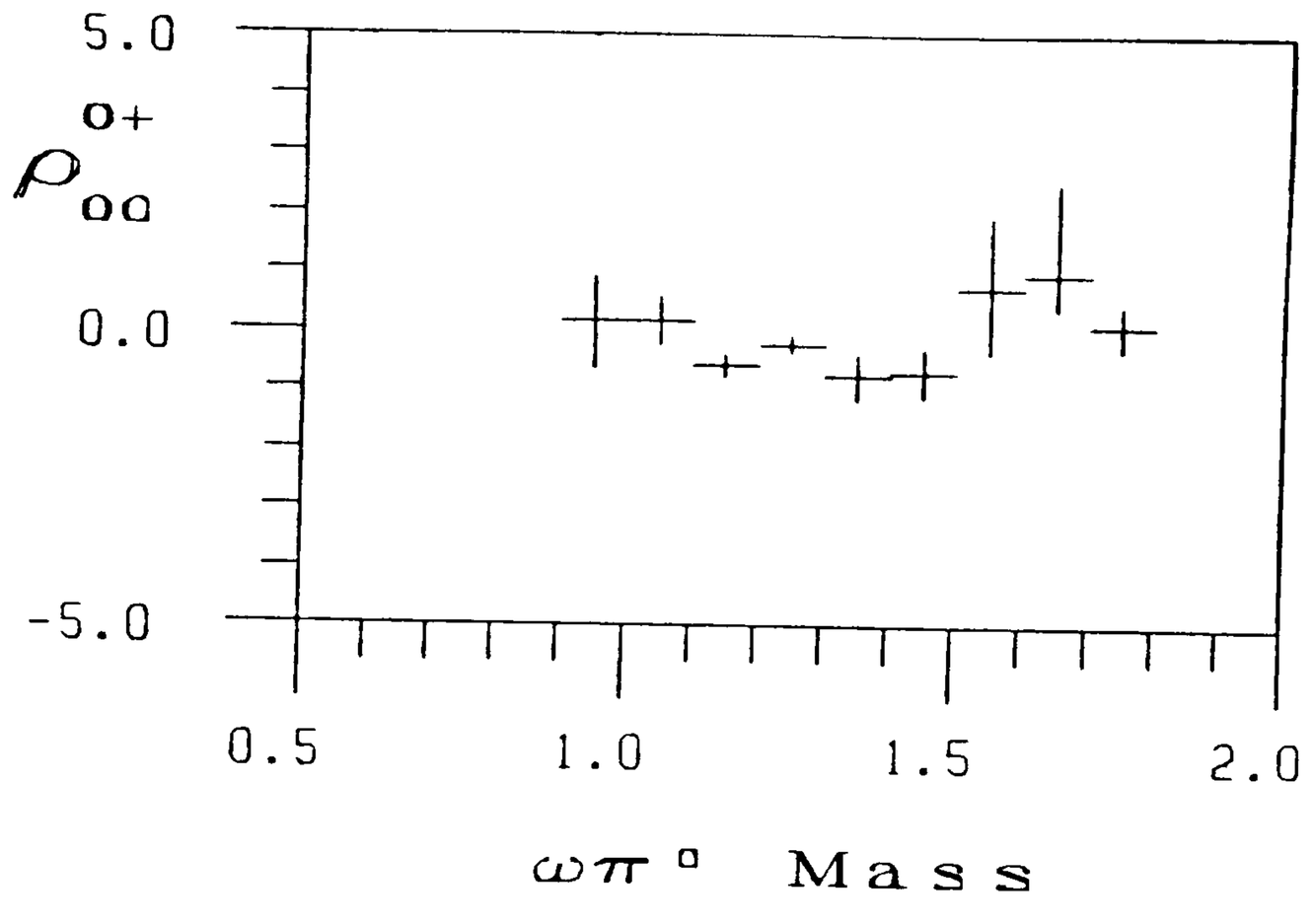
5.0
0.0
-5.0
0.5
1.0
1.5
2.0
ωπ° Mass

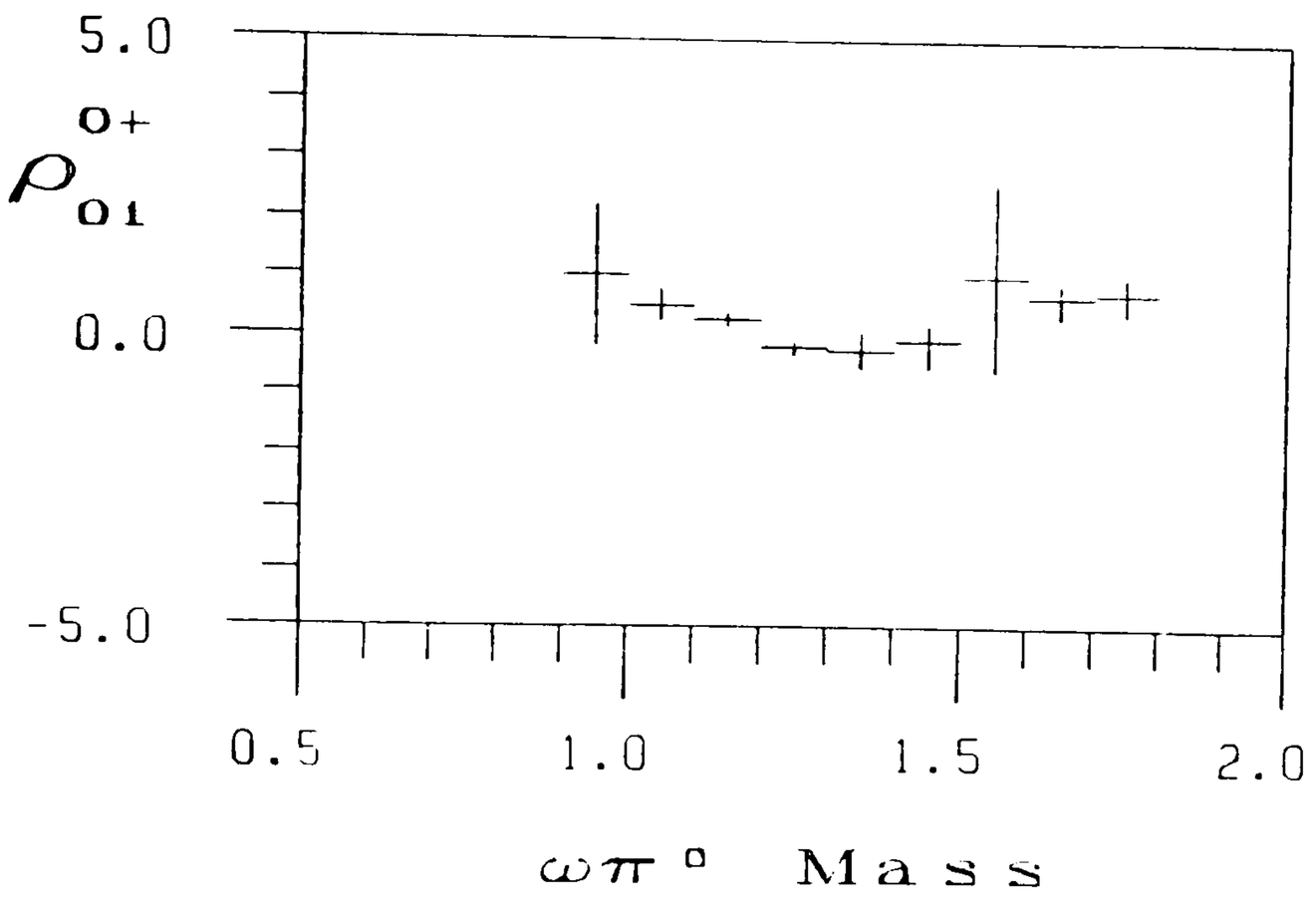
5.0
0.0
-5.0
0.5
1.0
1.5
2.0
ωπ° Mass

Figure 5.19E

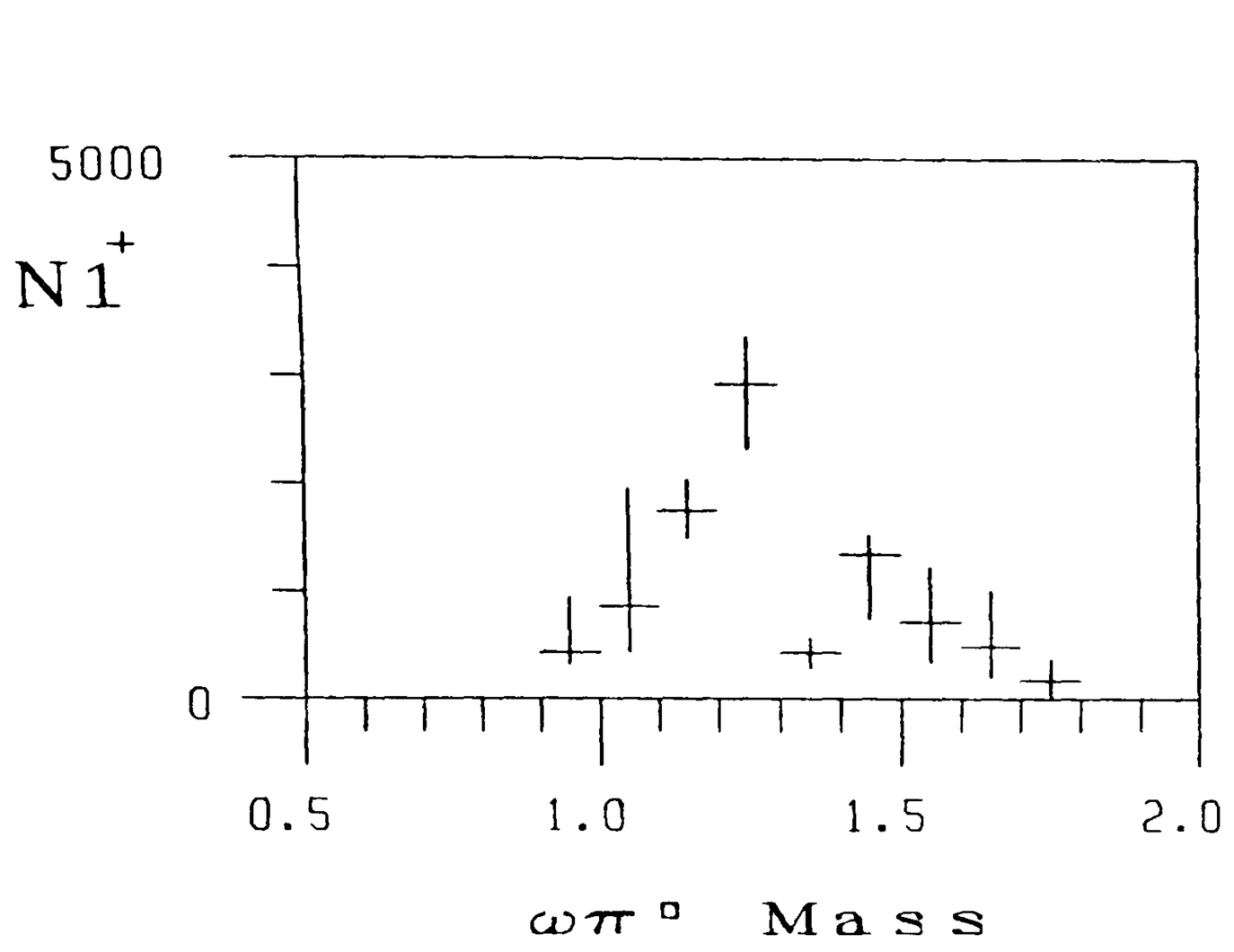
5000
N1+
0
0.5
1.0
1.5
2.0
ωπ° Mass

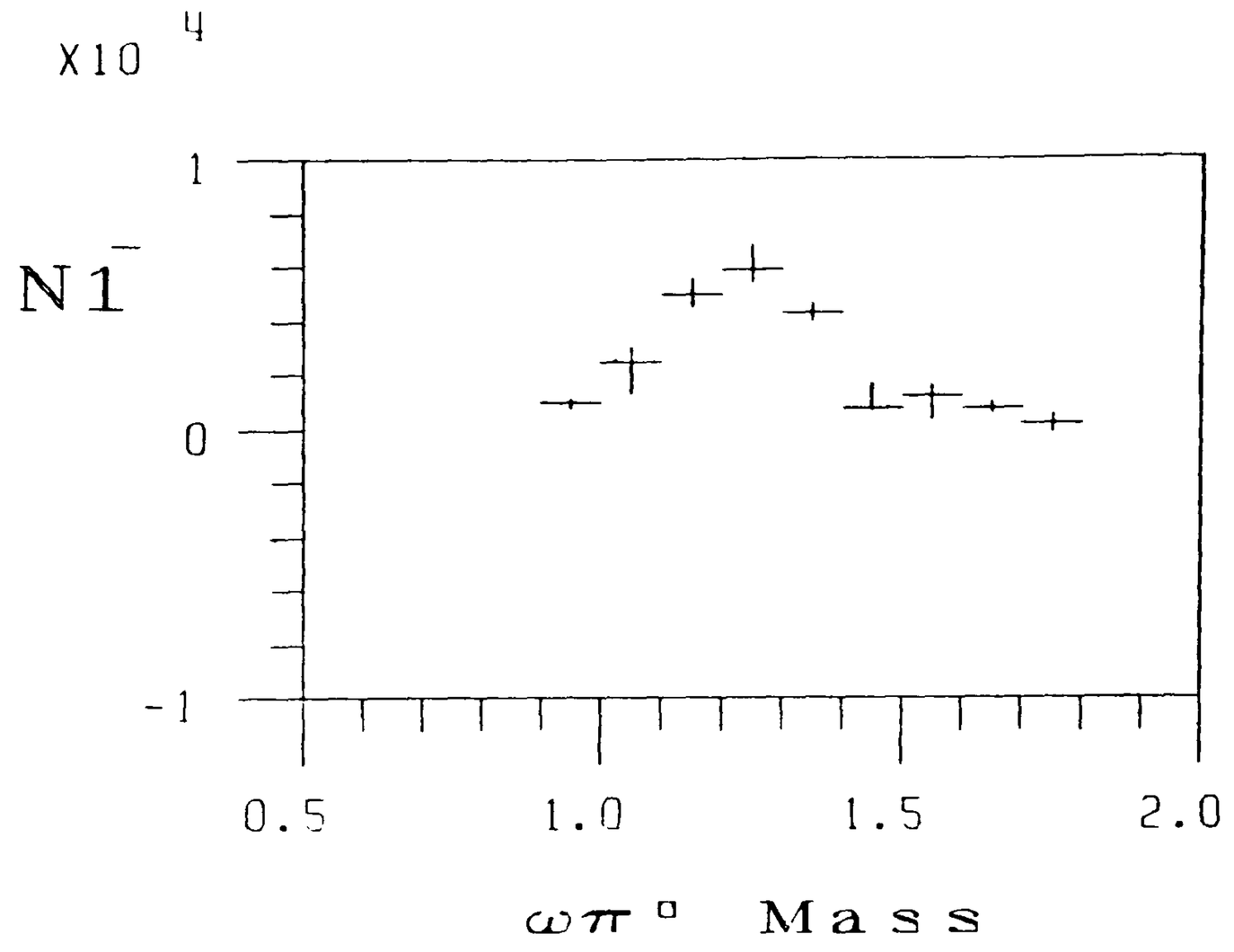
X10 4
1
N1−
0
-1
0.5
1.0
1.5
2.0
ωπ° Mass

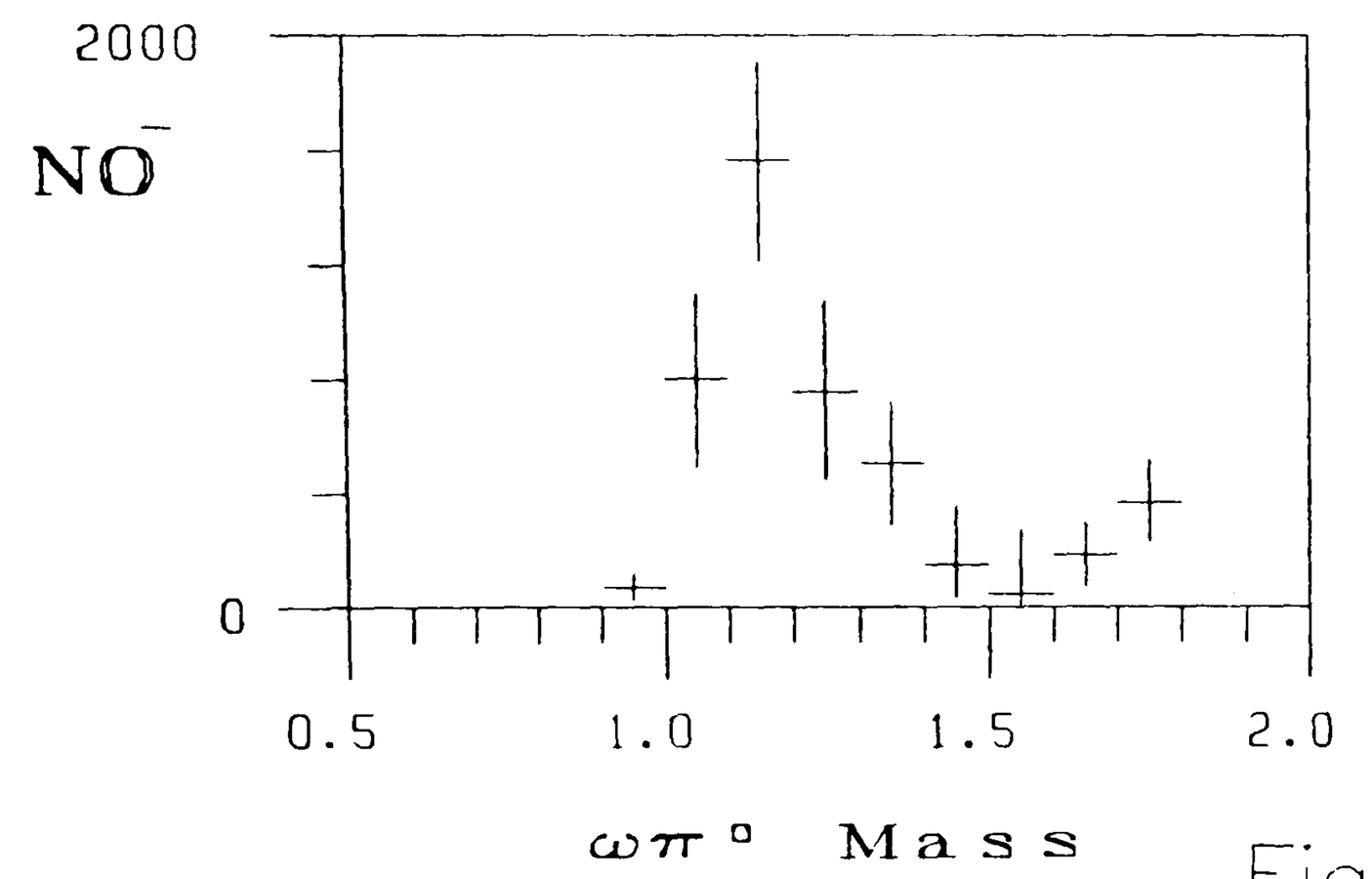
2000
NO−
0
0.5
1.0
1.5
2.0
ωπ° Mass

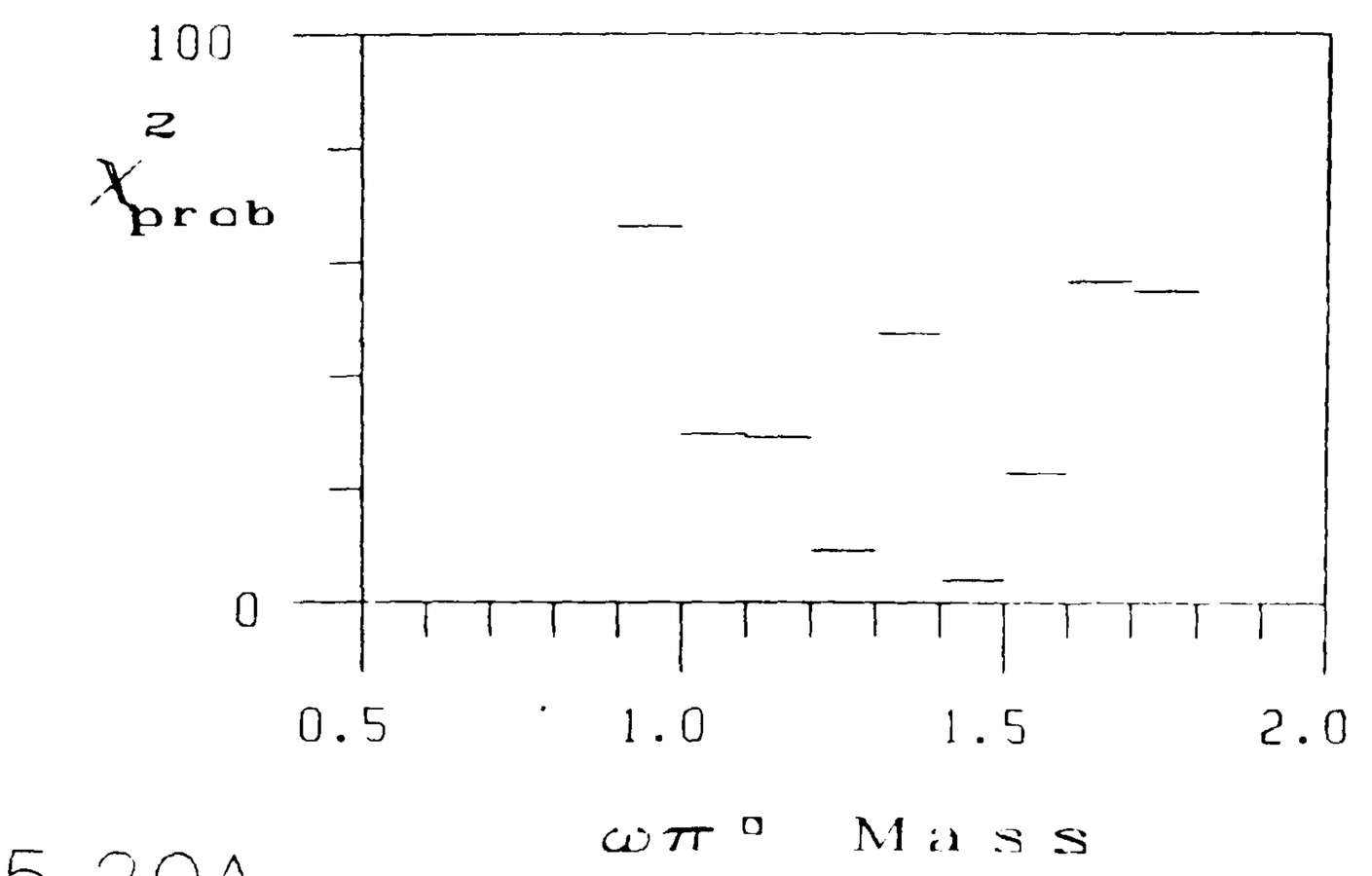
100
2
χprob
0
0.5
1.0
1.5
2.0
ωπ° Mass

Figure 5.20A

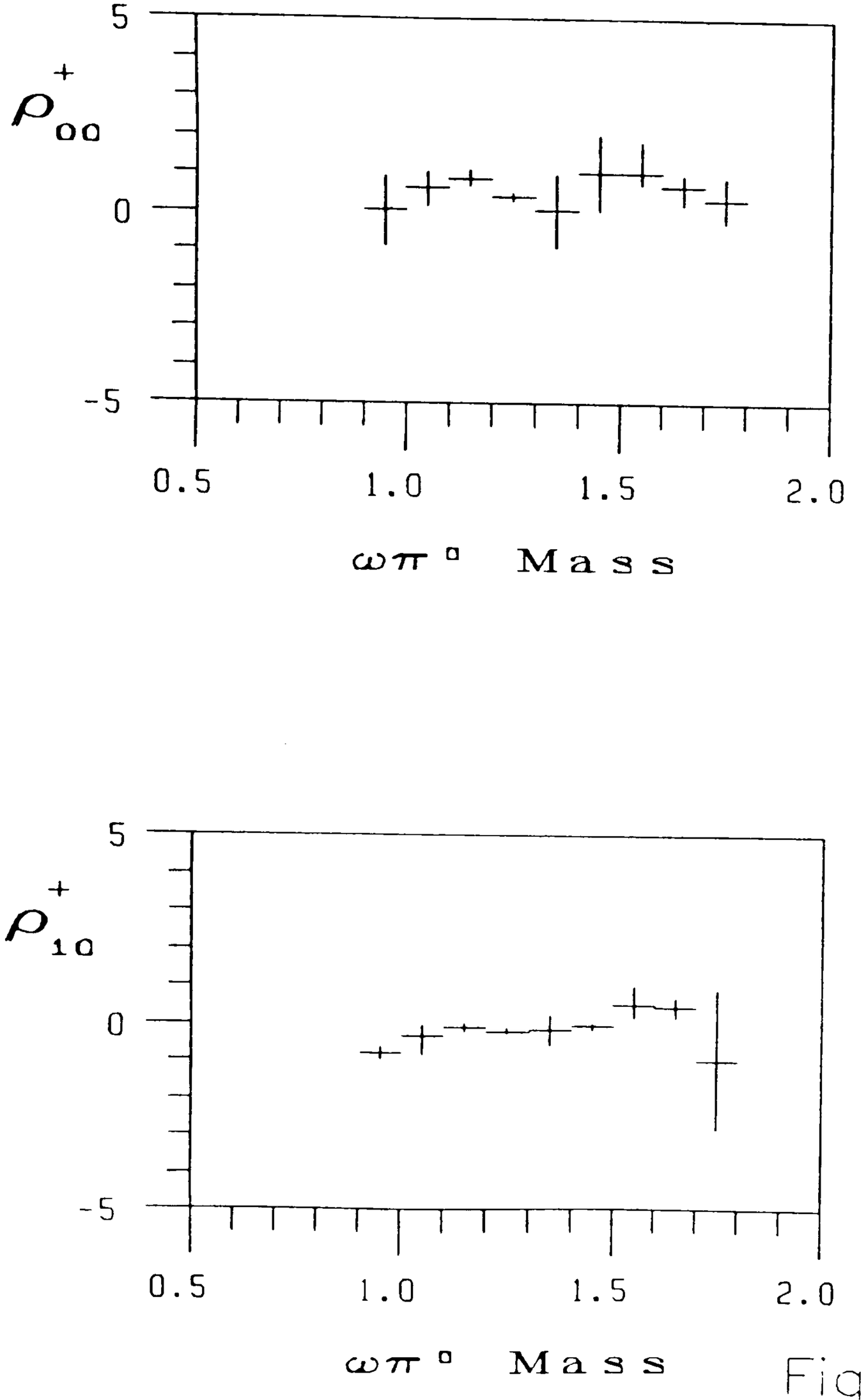
ρ^+_{00}
5
0
-5
0.5
1.0
1.5
2.0
$\omega\pi^0$ Mass

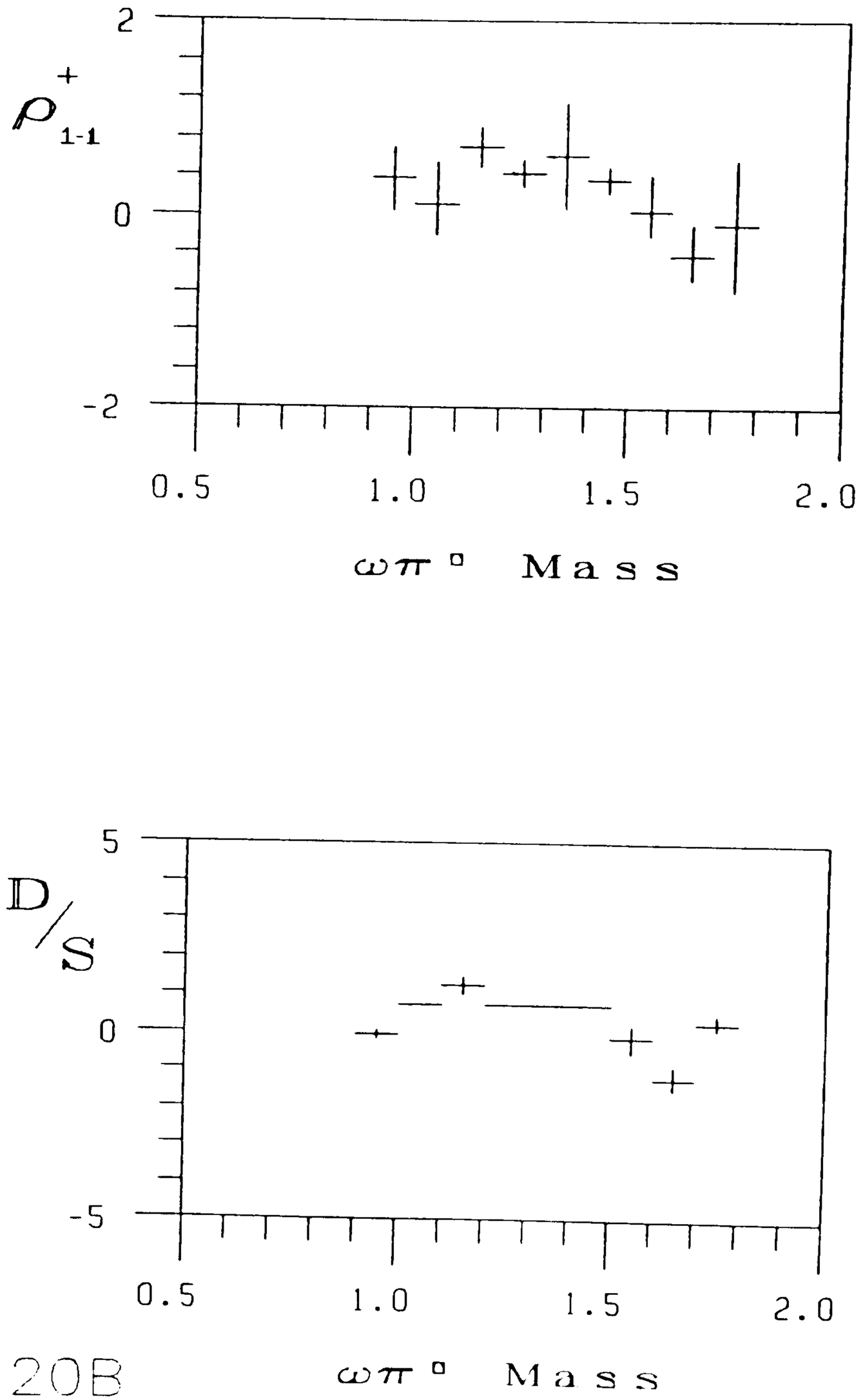
ρ^+_{1-1}
2
0
-2
0.5
1.0
1.5
2.0
$\omega\pi^0$ Mass

ρ^+_{10}
5
0
-5
0.5
1.0
1.5
2.0
$\omega\pi^0$ Mass

D/S
5
0
-5
0.5
1.0
1.5
2.0
$\omega\pi^0$ Mass

Figure 5.20B

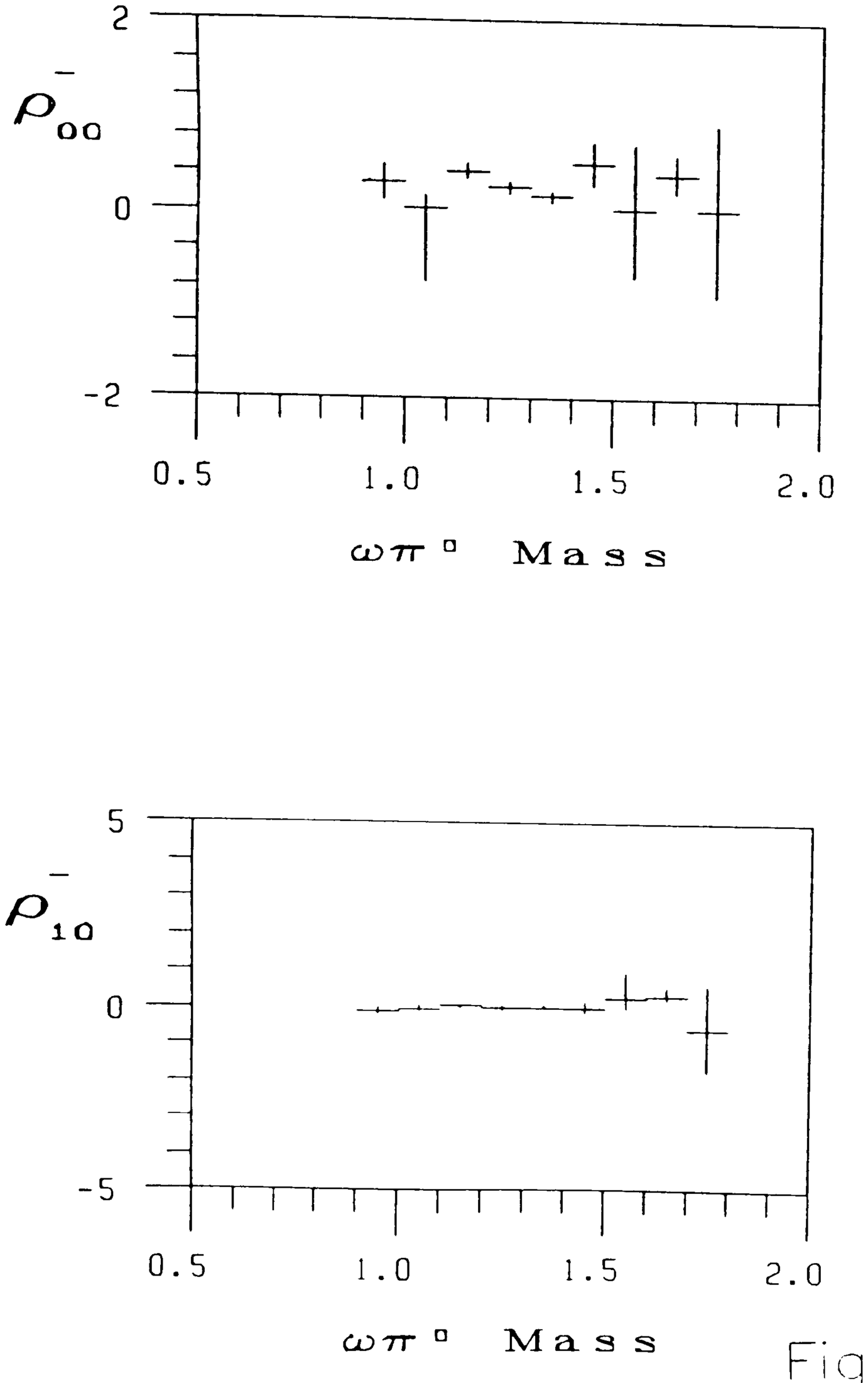
$\bar{\rho}_{00}$
2
0
-2
0.5
1.0
1.5
2.0
$\omega\pi^0$ Mass

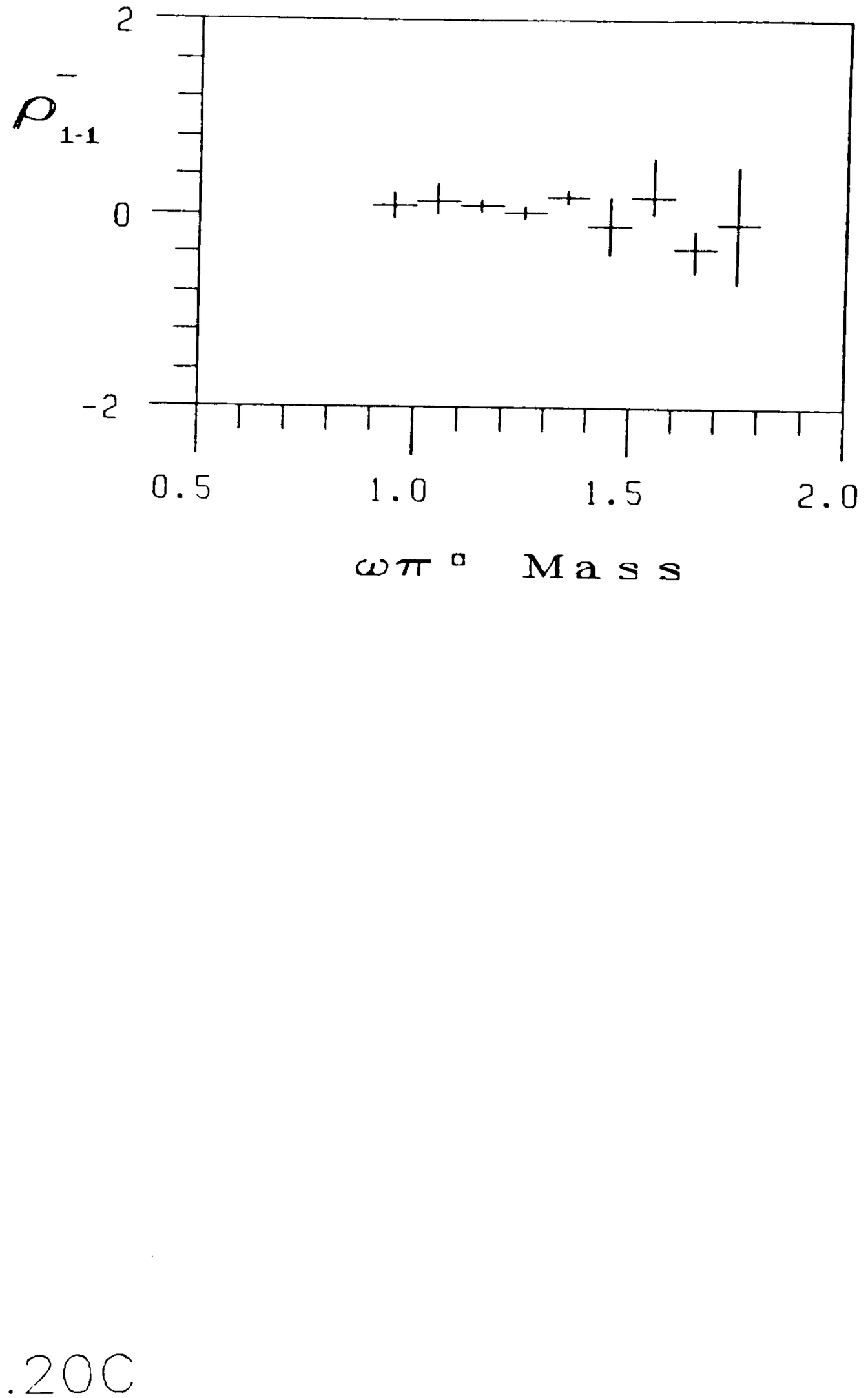
$\bar{\rho}_{1-1}$
2
0
-2
0.5
1.0
1.5
2.0
$\omega\pi^0$ Mass

$\bar{\rho}_{10}$
5
0
-5
0.5
1.0
1.5
2.0
$\omega\pi^0$ Mass

Figure 5.20C

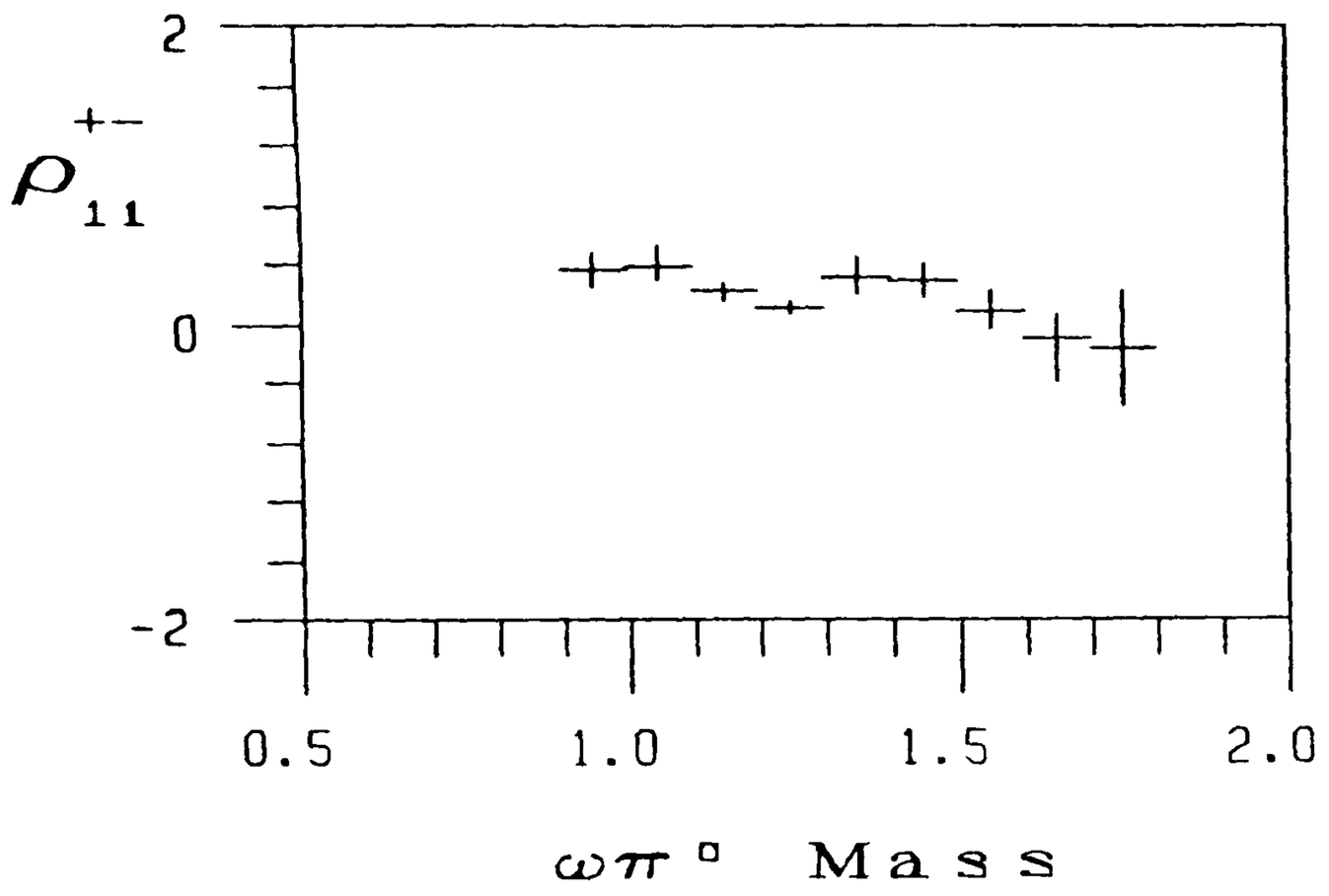
ρ_{11}^{+-}
2
0
-2
0.5
1.0
1.5
2.0
$\omega\pi^0$ Mass

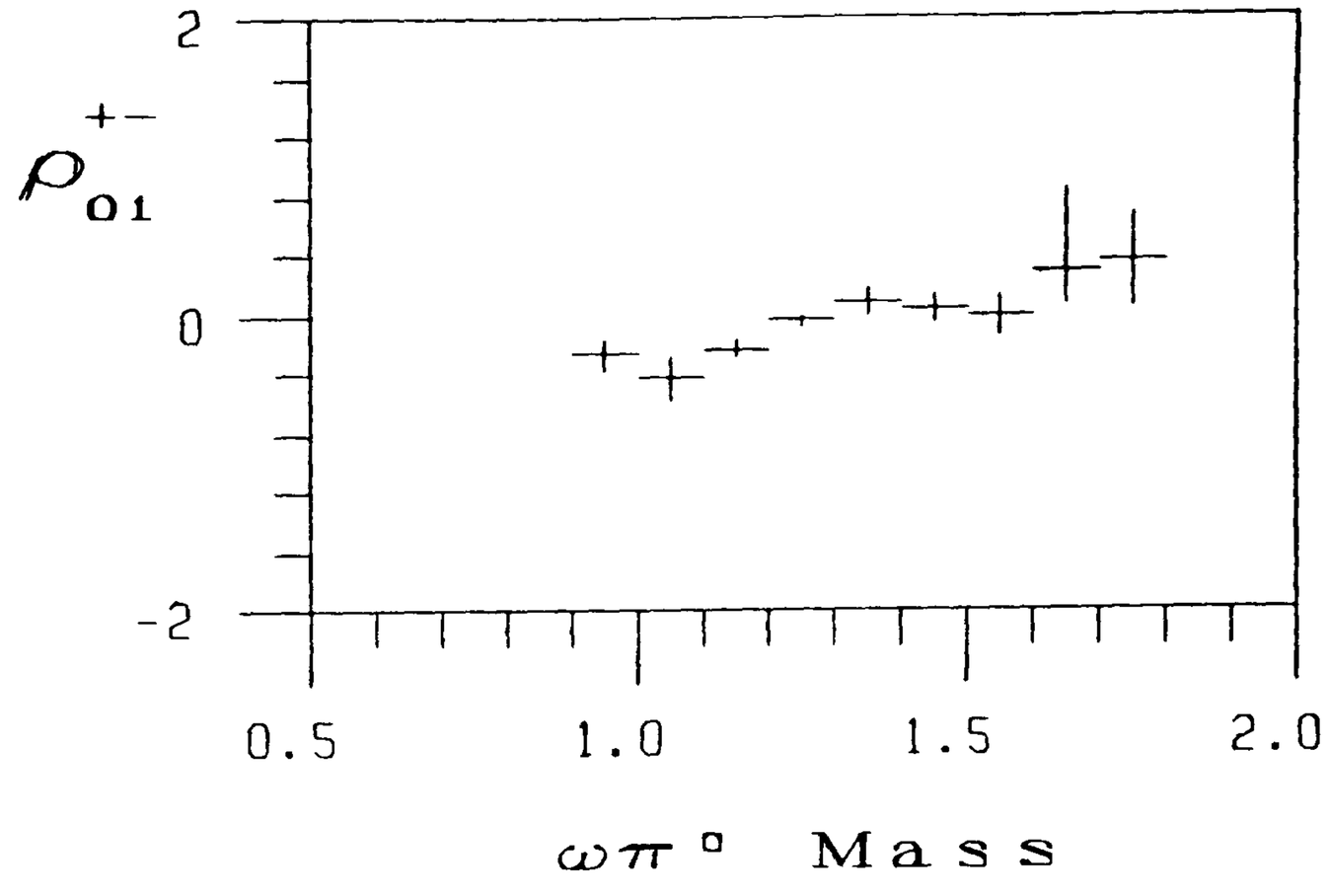
ρ_{01}^{+-}
2
0
-2
0.5
1.0
1.5
2.0
$\omega\pi^0$ Mass

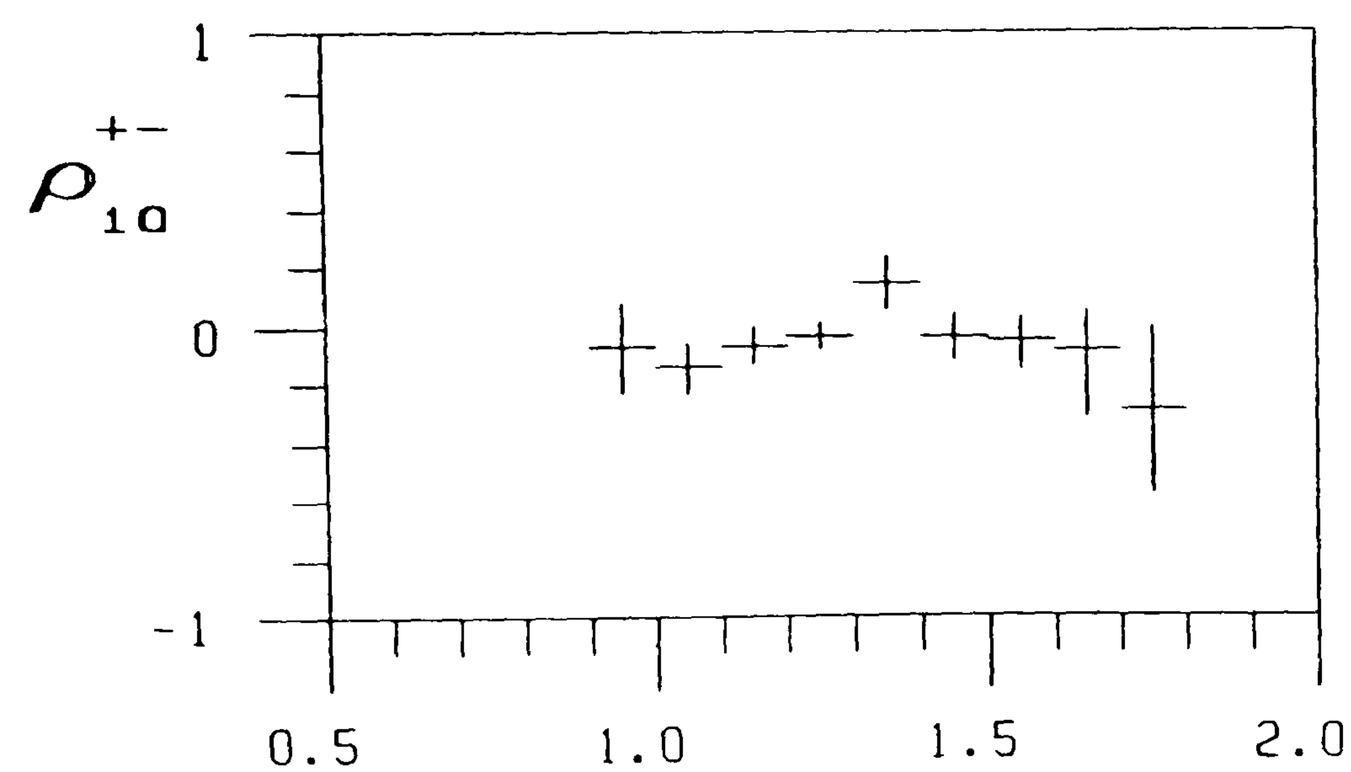
ρ_{10}^{+-}
1
0
-1
0.5
1.0
1.5
2.0
$\omega\pi^0$ Mass

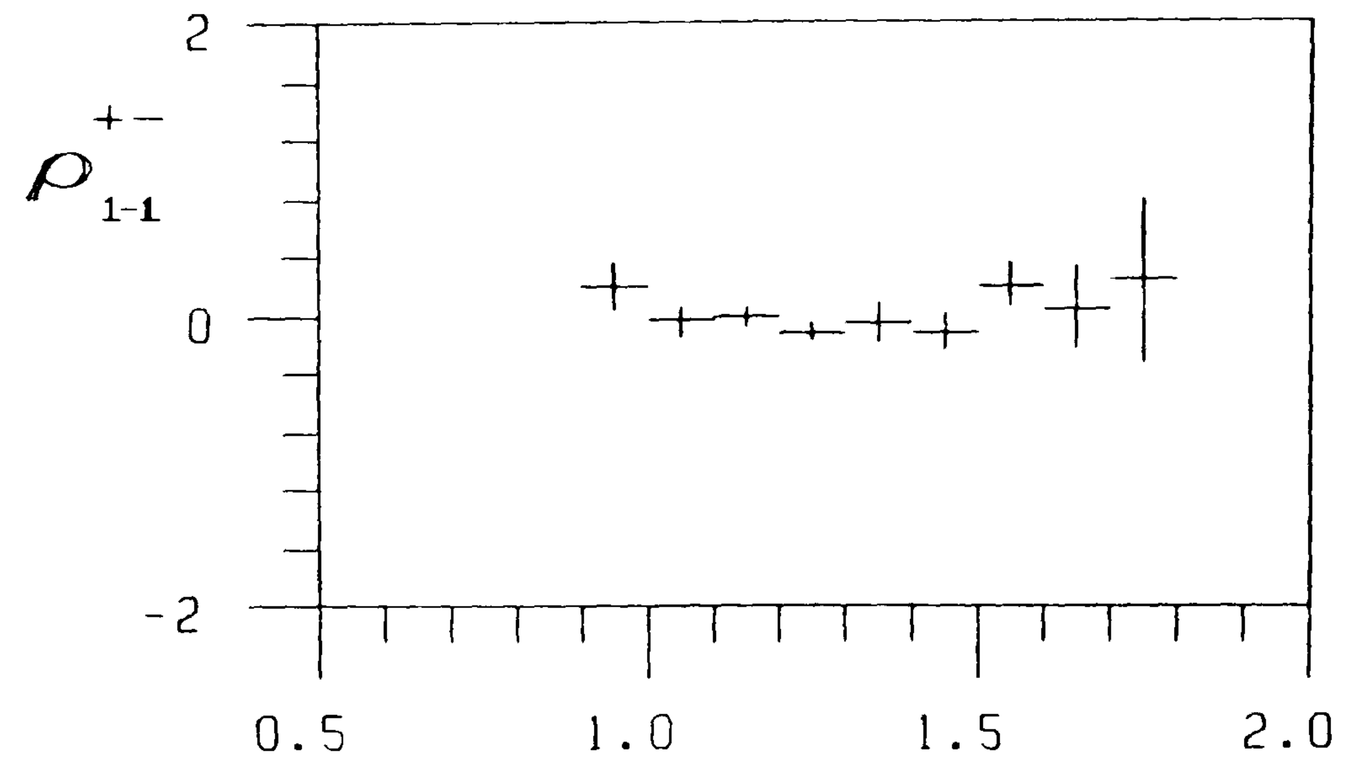
ρ_{1-1}^{+-}
2
0
-2
0.5
1.0
1.5
2.0
$\omega\pi^0$ Mass

Figure 5.20D

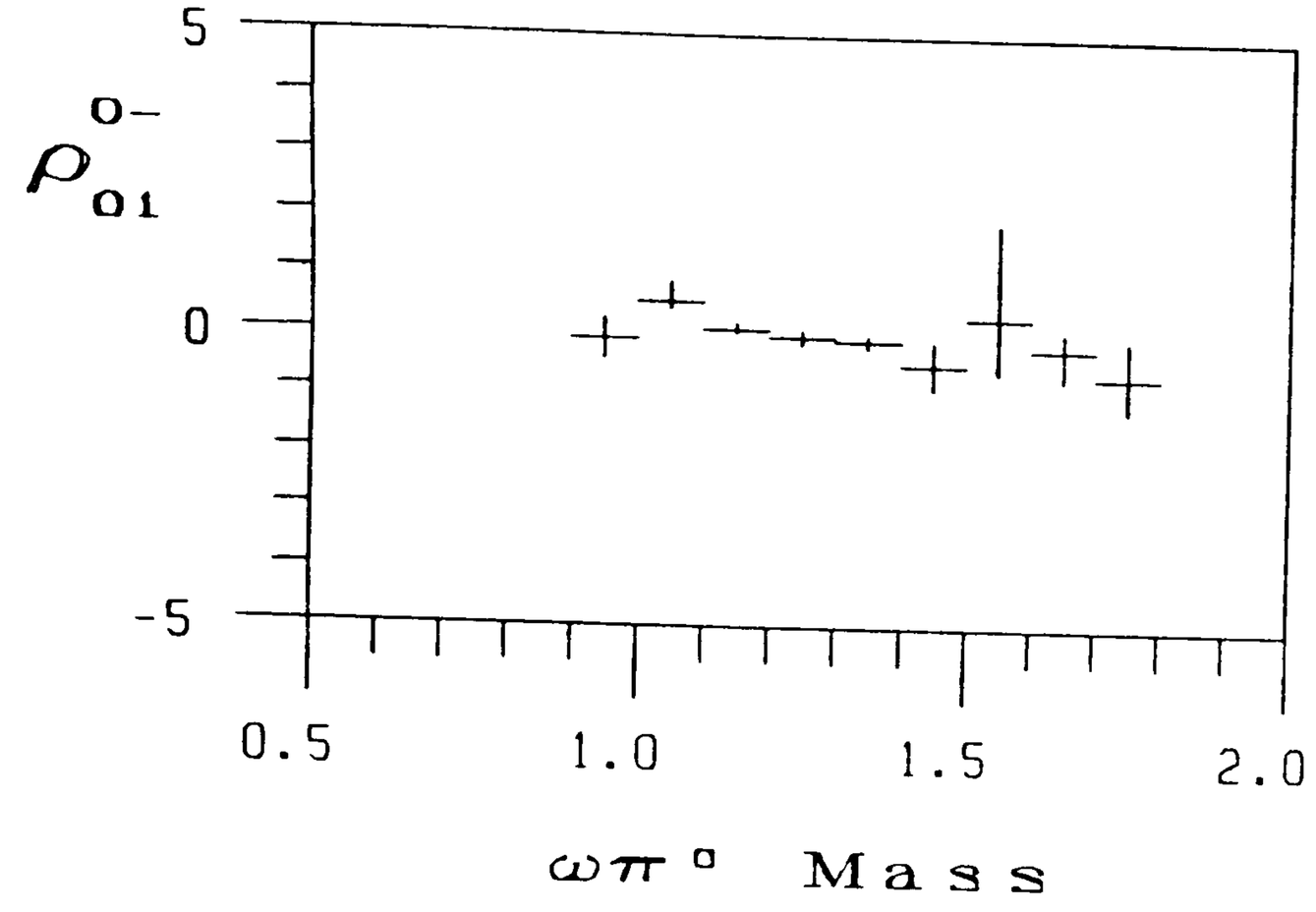
5
0
-5
0.5
1.0
1.5
2.0
ρ^{0-}_{01}
$\omega\pi^0$ Mass

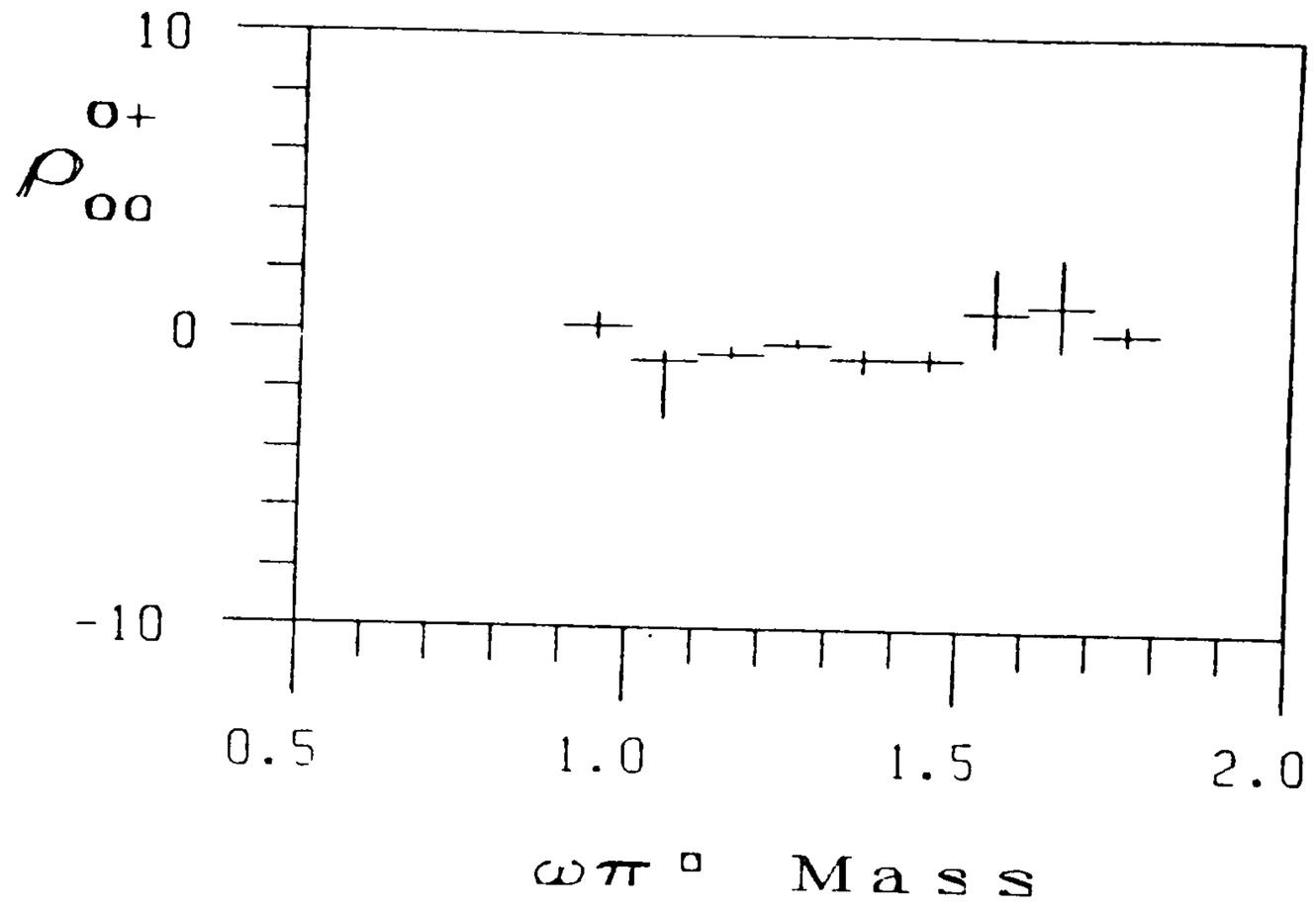
10
0
-10
0.5
1.0
1.5
2.0
ρ^{0+}_{00}
$\omega\pi^0$ Mass

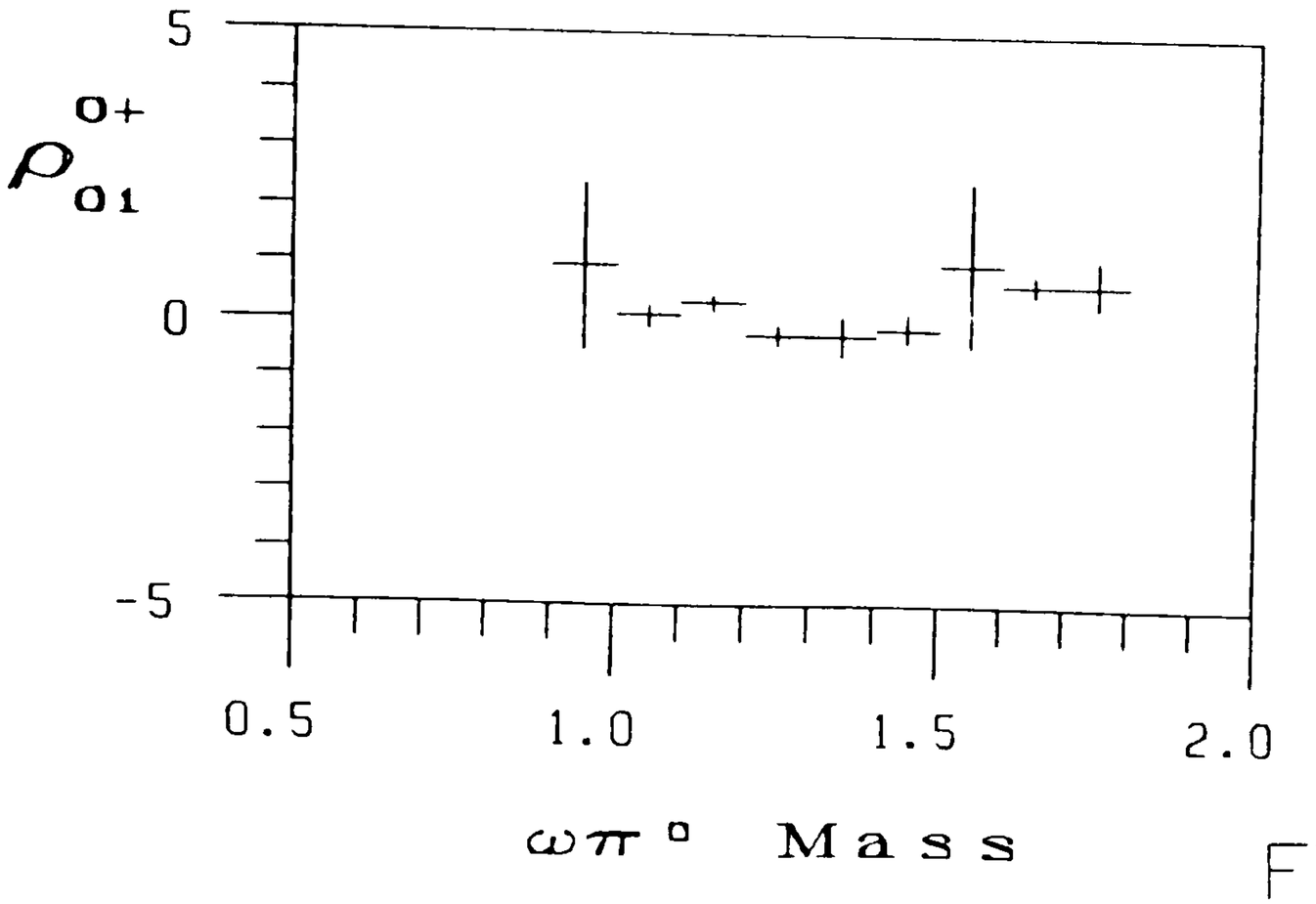
5
0
-5
0.5
1.0
1.5
2.0
ρ^{0+}_{01}
$\omega\pi^0$ Mass

Figure 5.20E

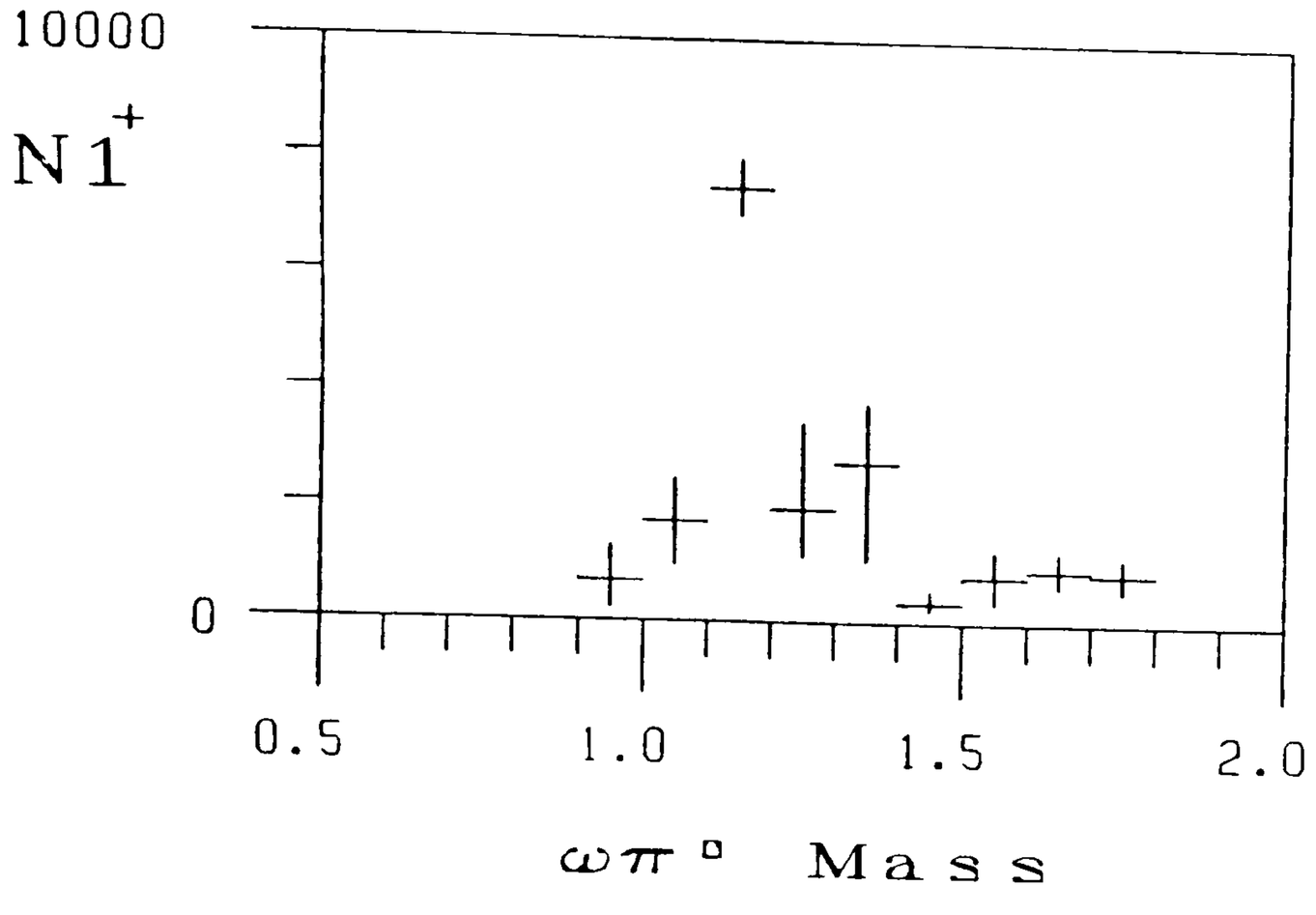
10000
N1+
0
0.5
1.0
1.5
2.0
ωπ° Mass

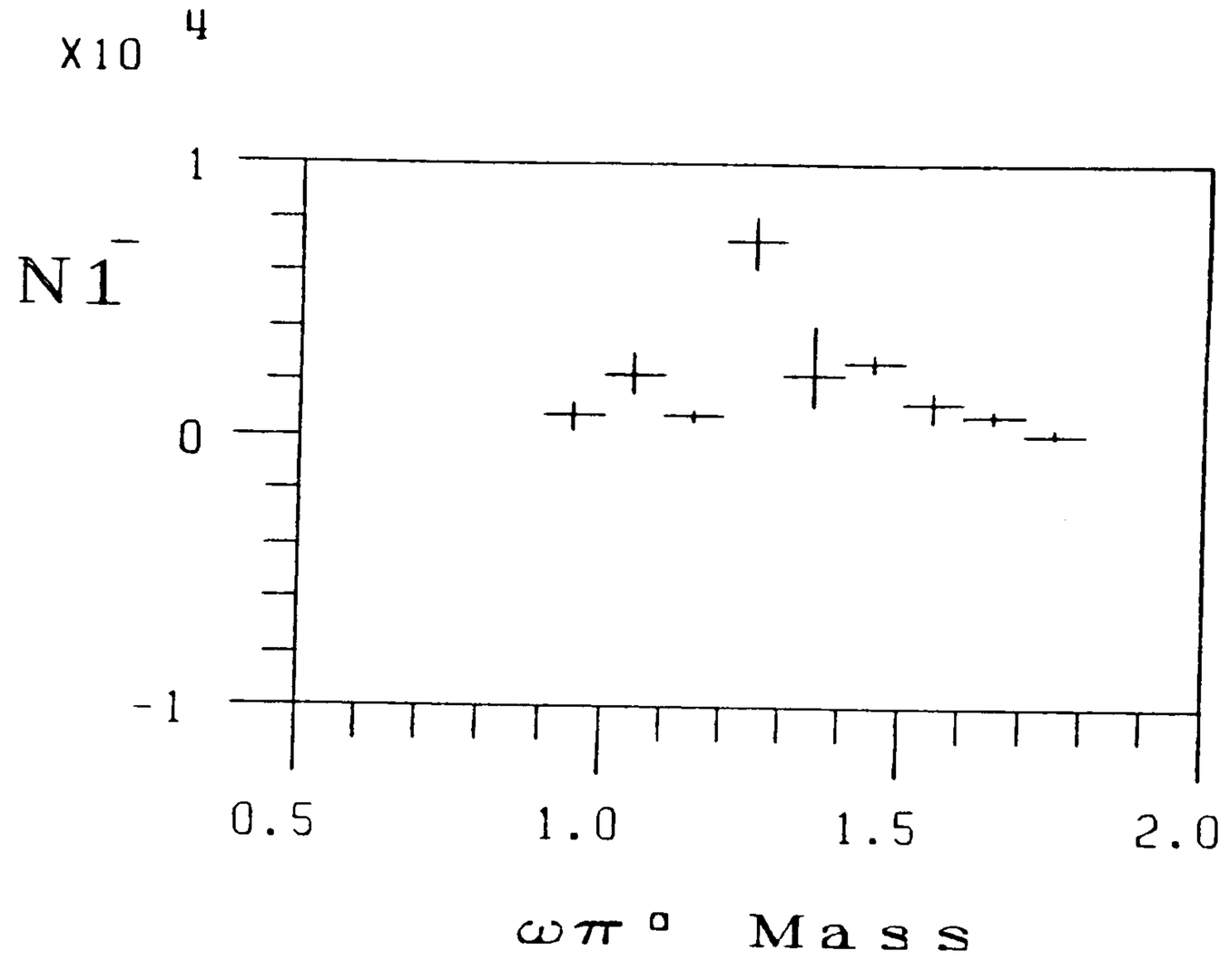
X10 4
1
N1-
0
-1
0.5
1.0
1.5
2.0
ωπ° Mass

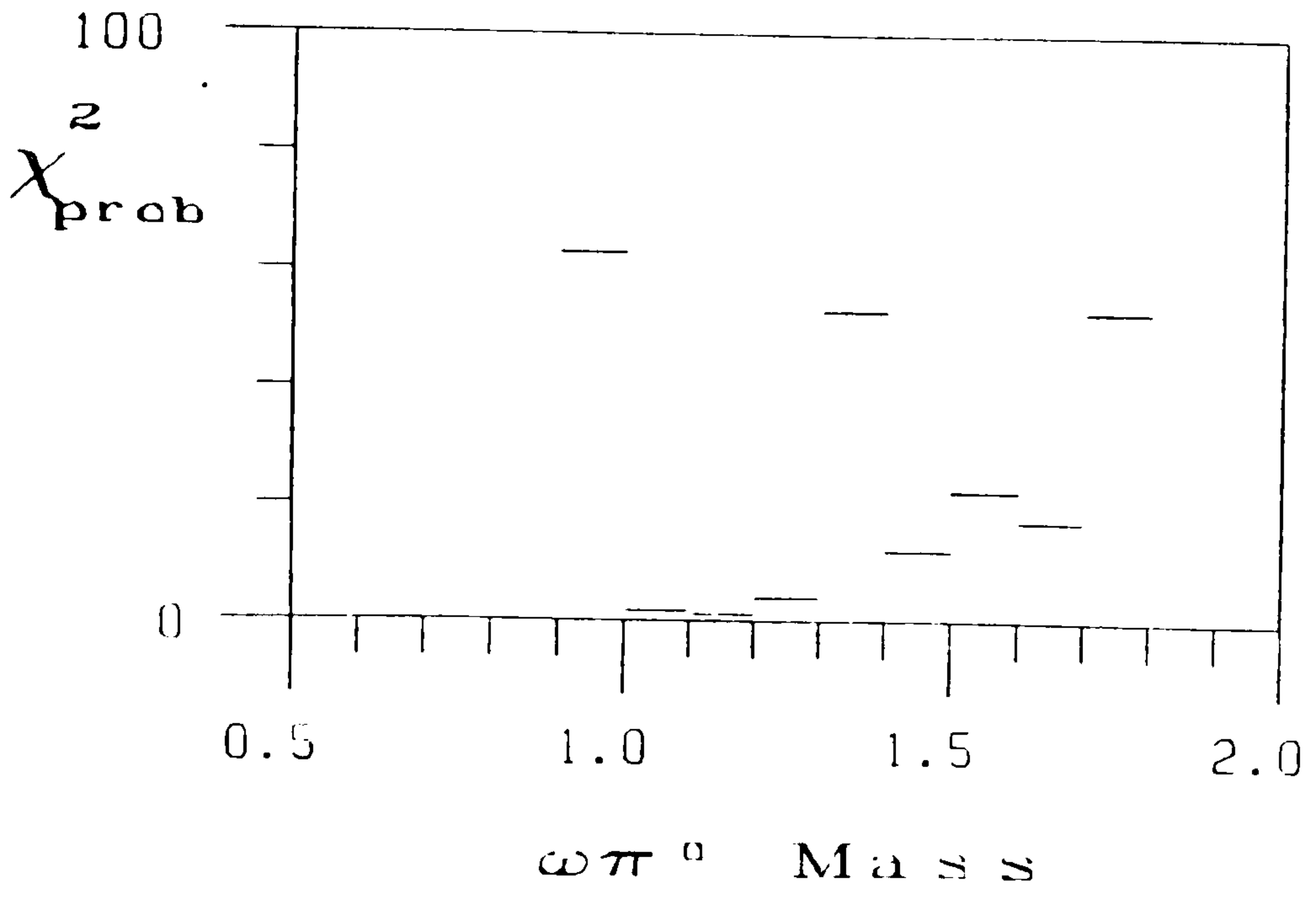
100
z
χprob
0
0.5
1.0
1.5
2.0
ωπ° Mass

Figure 5.21A

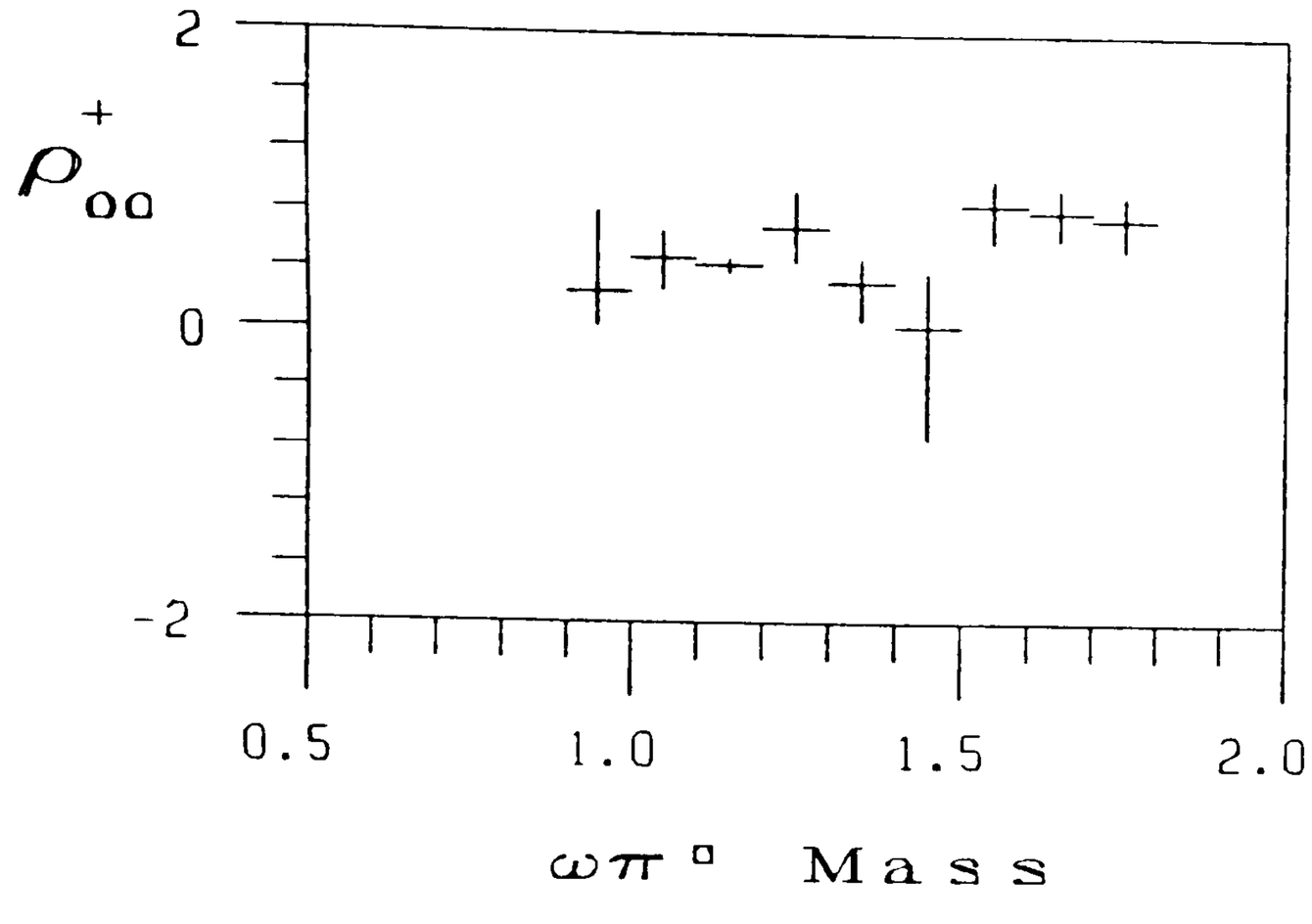
ρ^+_{00}
2
0
-2
0.5
1.0
1.5
2.0
ωπ° Mass

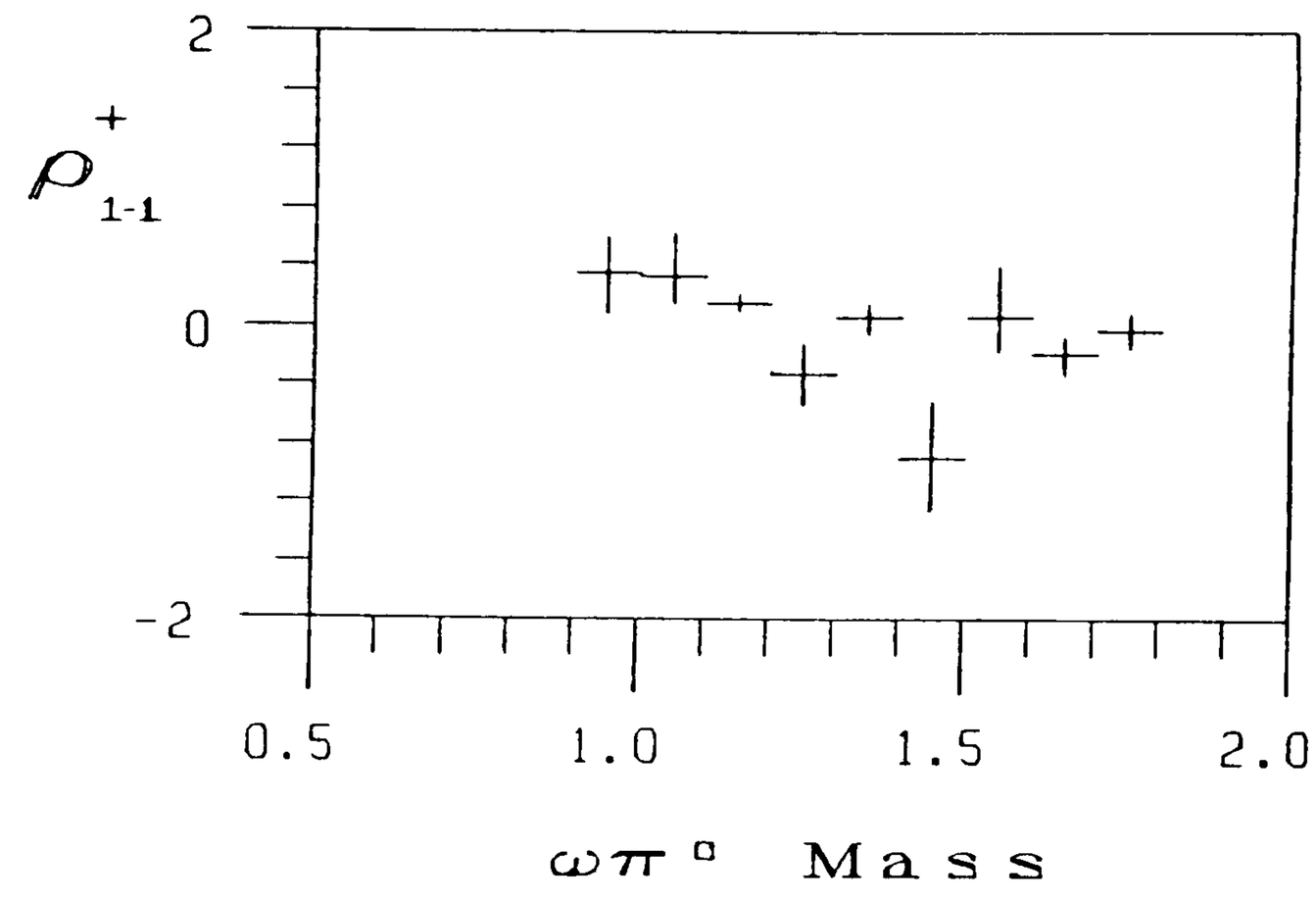
ρ^+_{1-1}
2
0
-2
0.5
1.0
1.5
2.0
ωπ° Mass

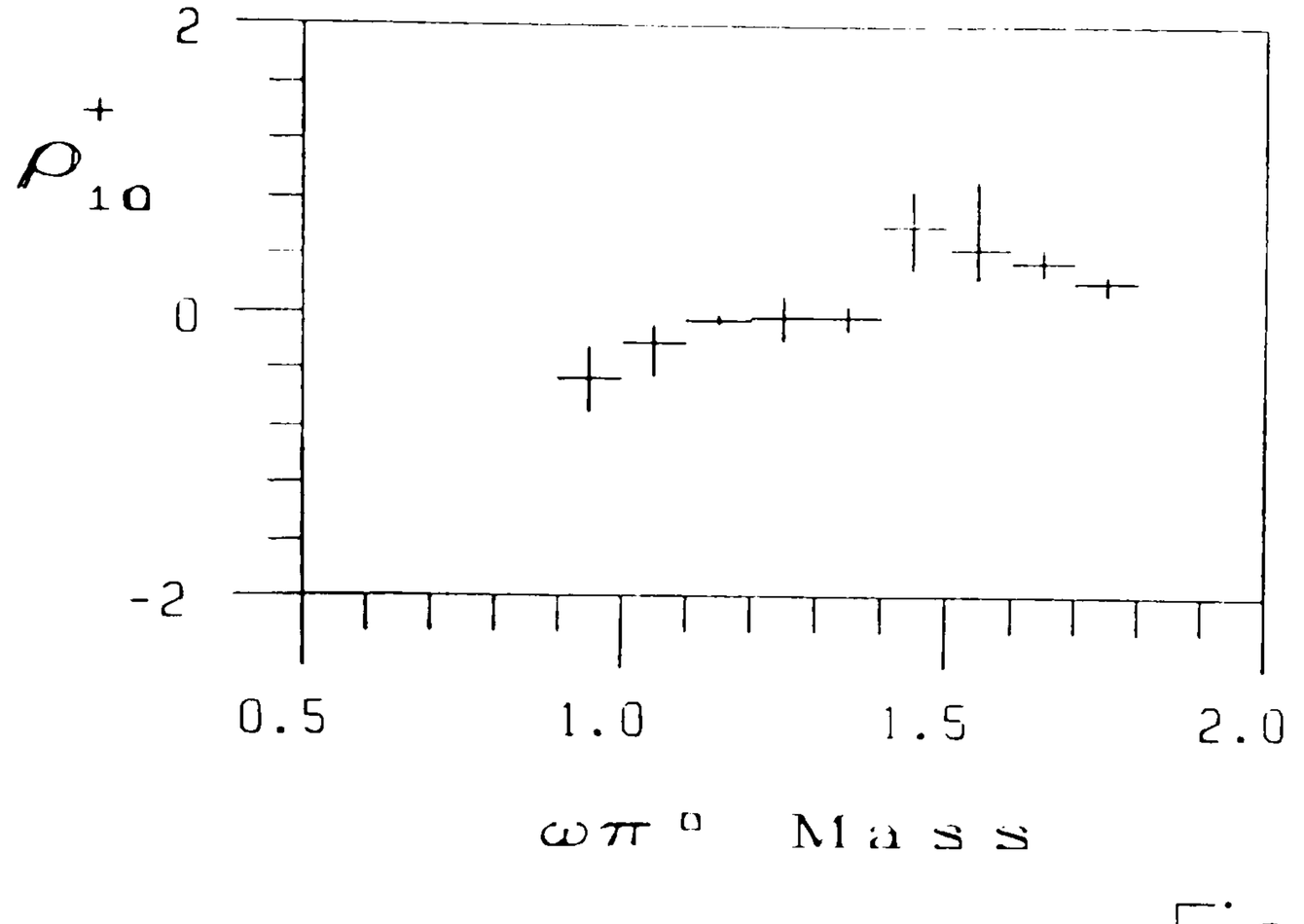
ρ^+_{10}
2
0
-2
0.5
1.0
1.5
2.0
ωπ° Mass

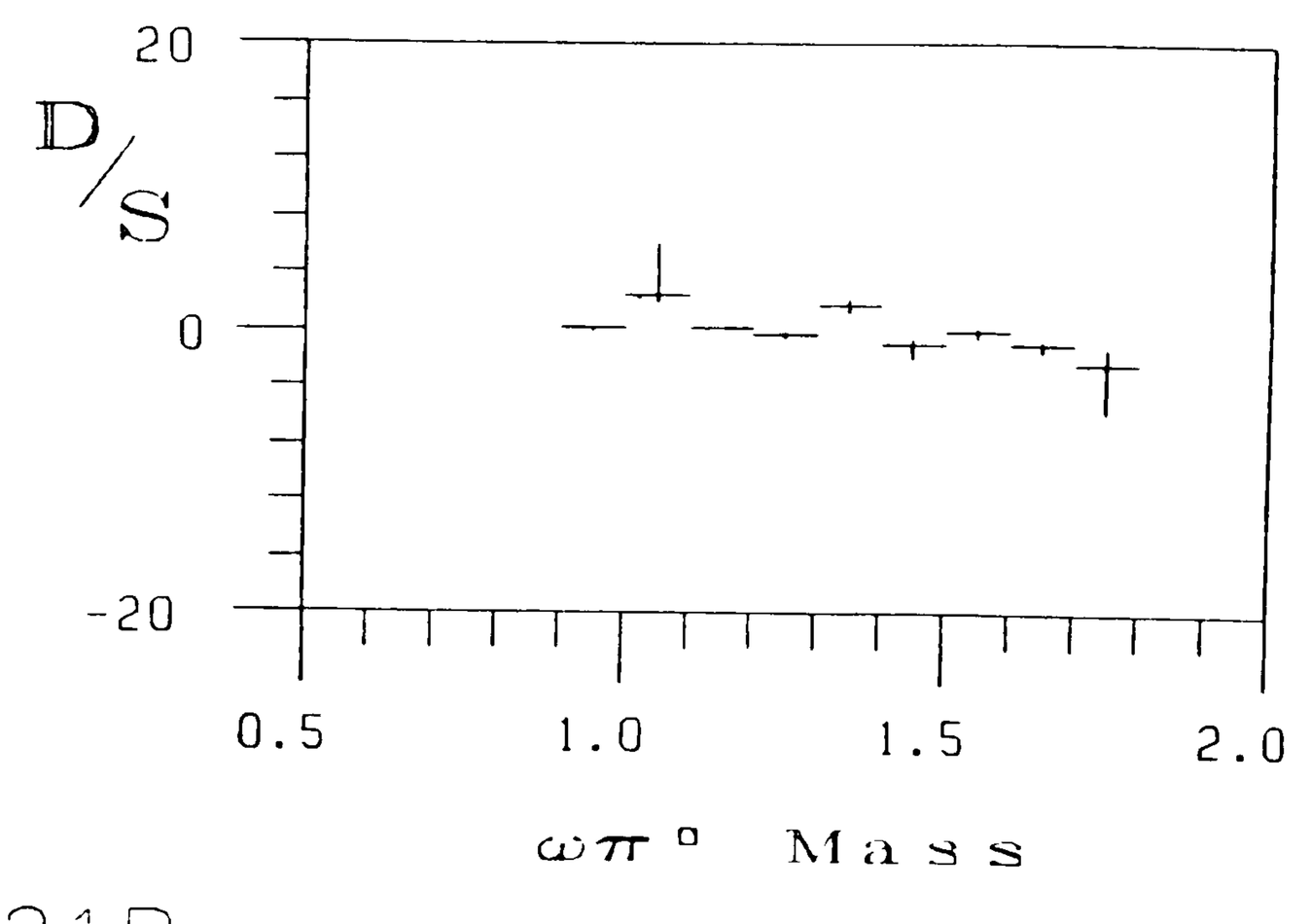
D/S
20
0
-20
0.5
1.0
1.5
2.0
ωπ° Mass

Figure 5.21B

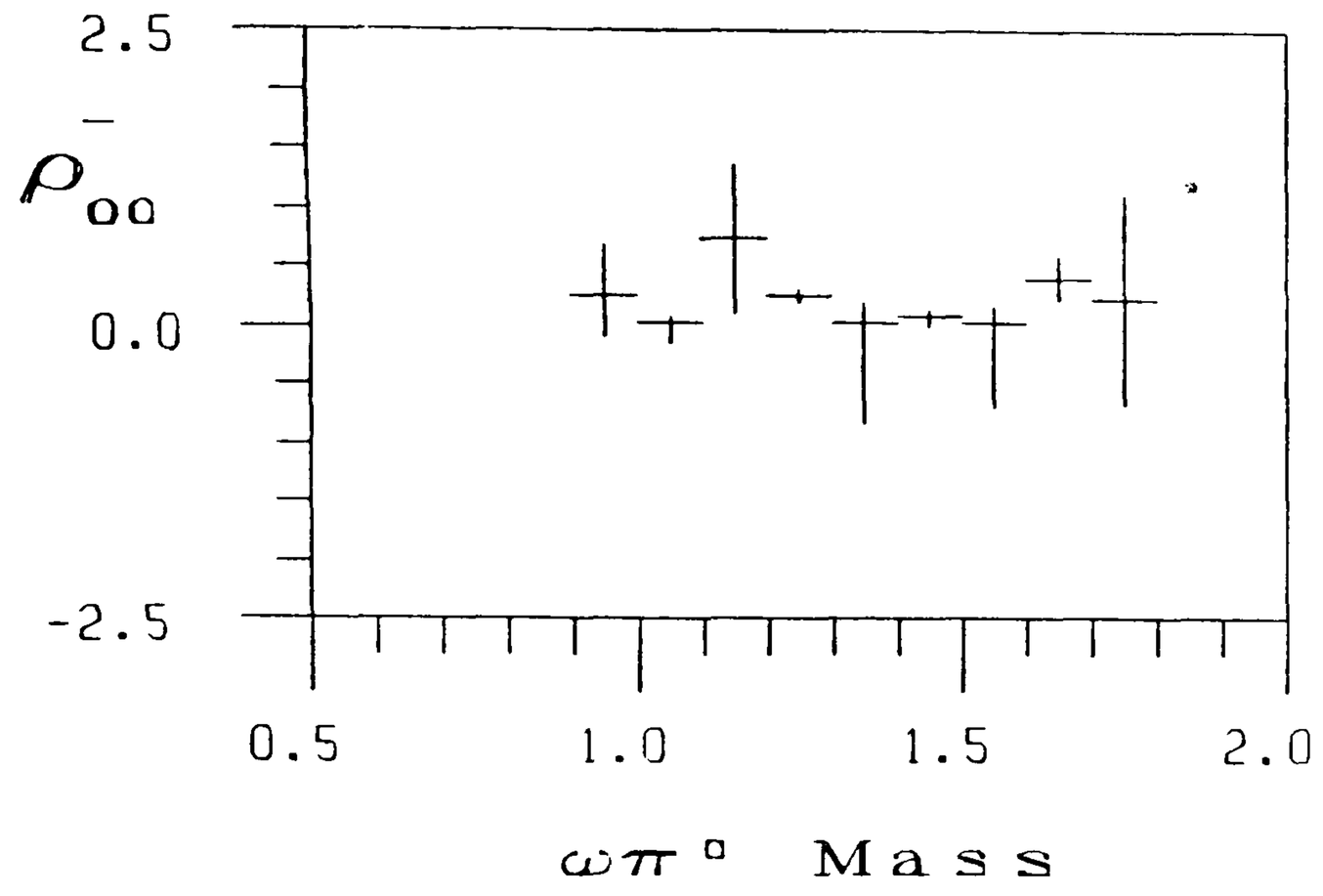
2.5
$\bar{\rho}_{00}$
0.0
-2.5
0.5
1.0
1.5
2.0
$\omega\pi^0$ Mass

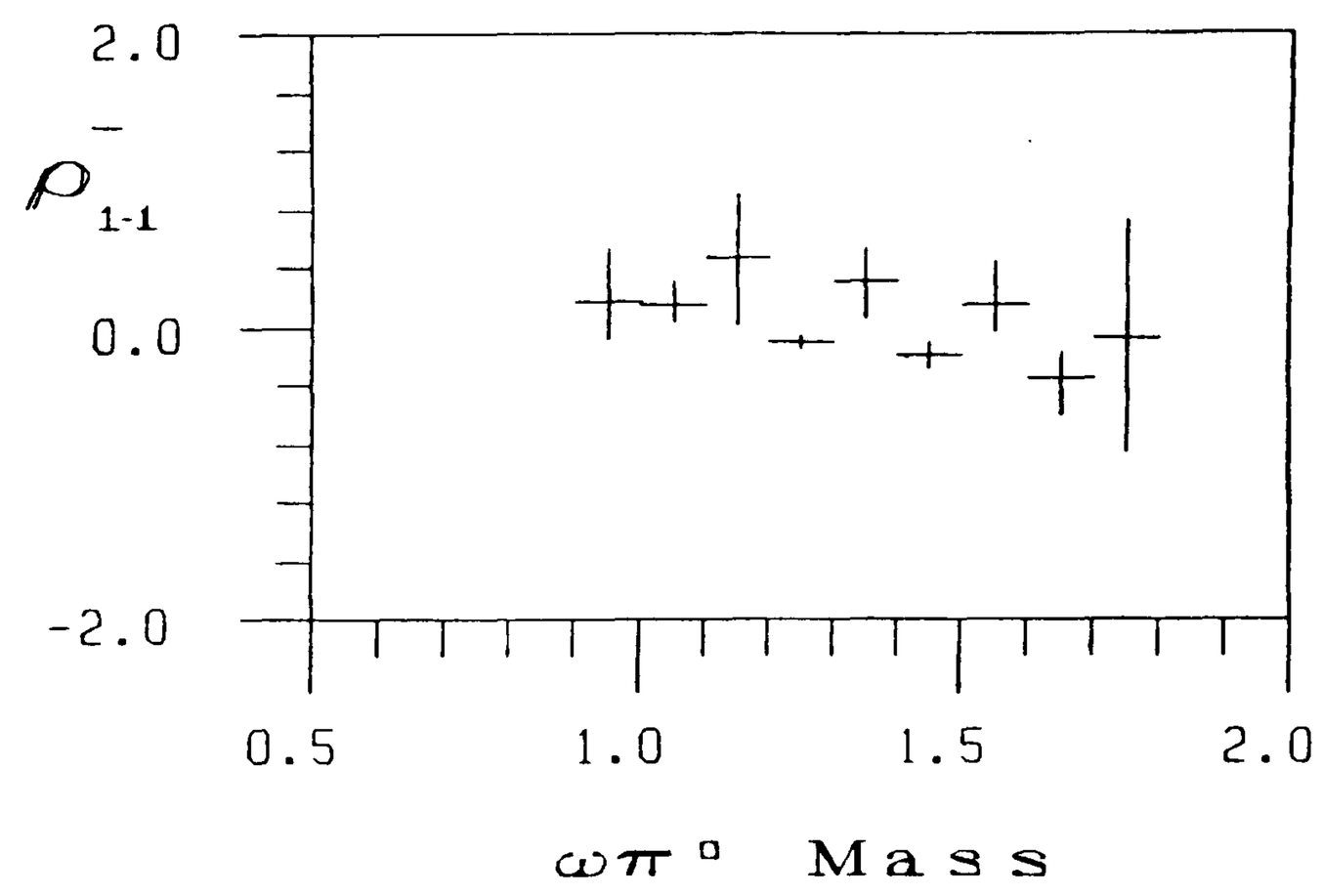
2.0
$\bar{\rho}_{1-1}$
0.0
-2.0
0.5
1.0
1.5
2.0
$\omega\pi^0$ Mass

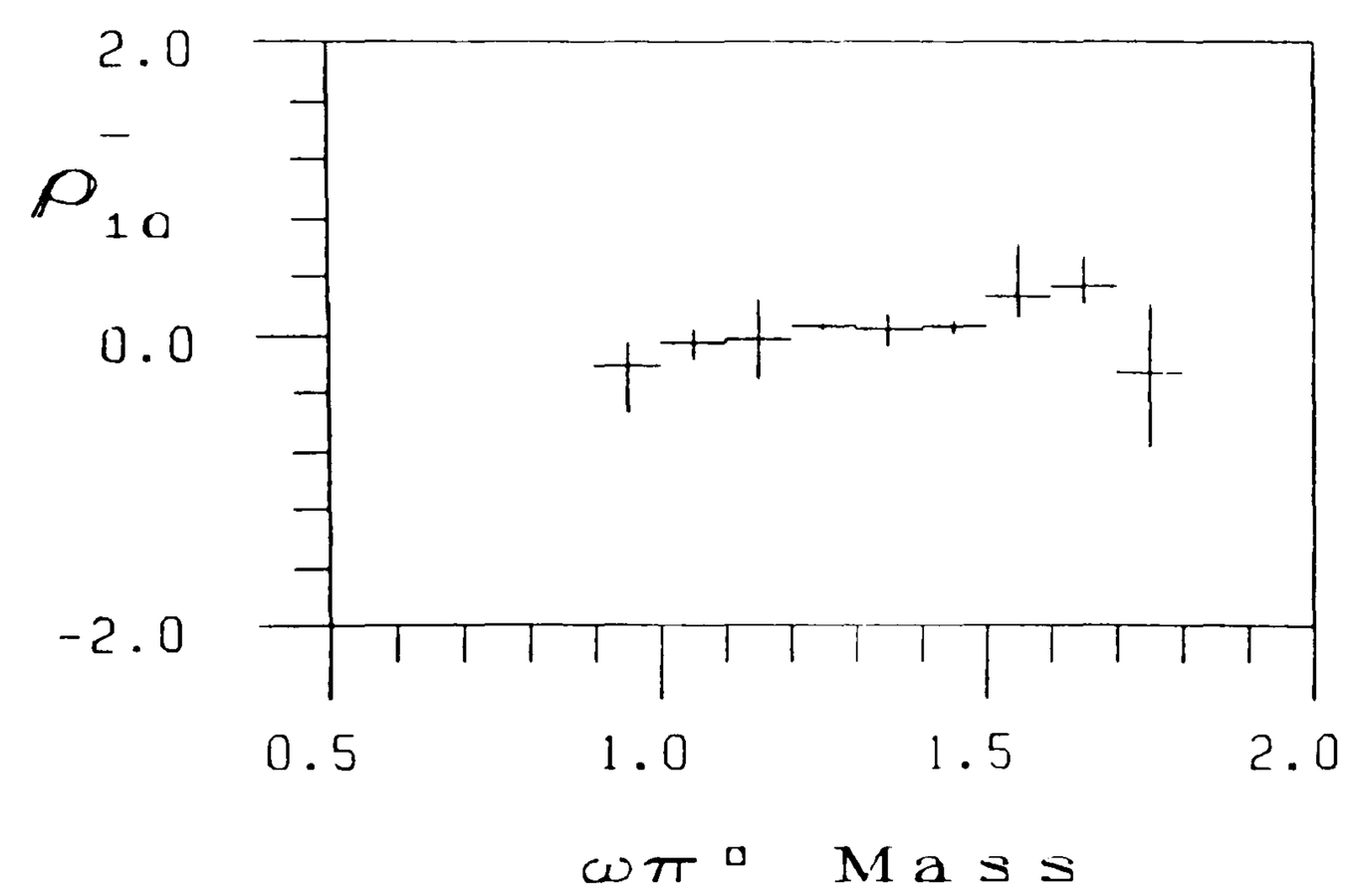
2.0
$\bar{\rho}_{10}$
0.0
-2.0
0.5
1.0
1.5
2.0
$\omega\pi^0$ Mass

Figure 5.21C

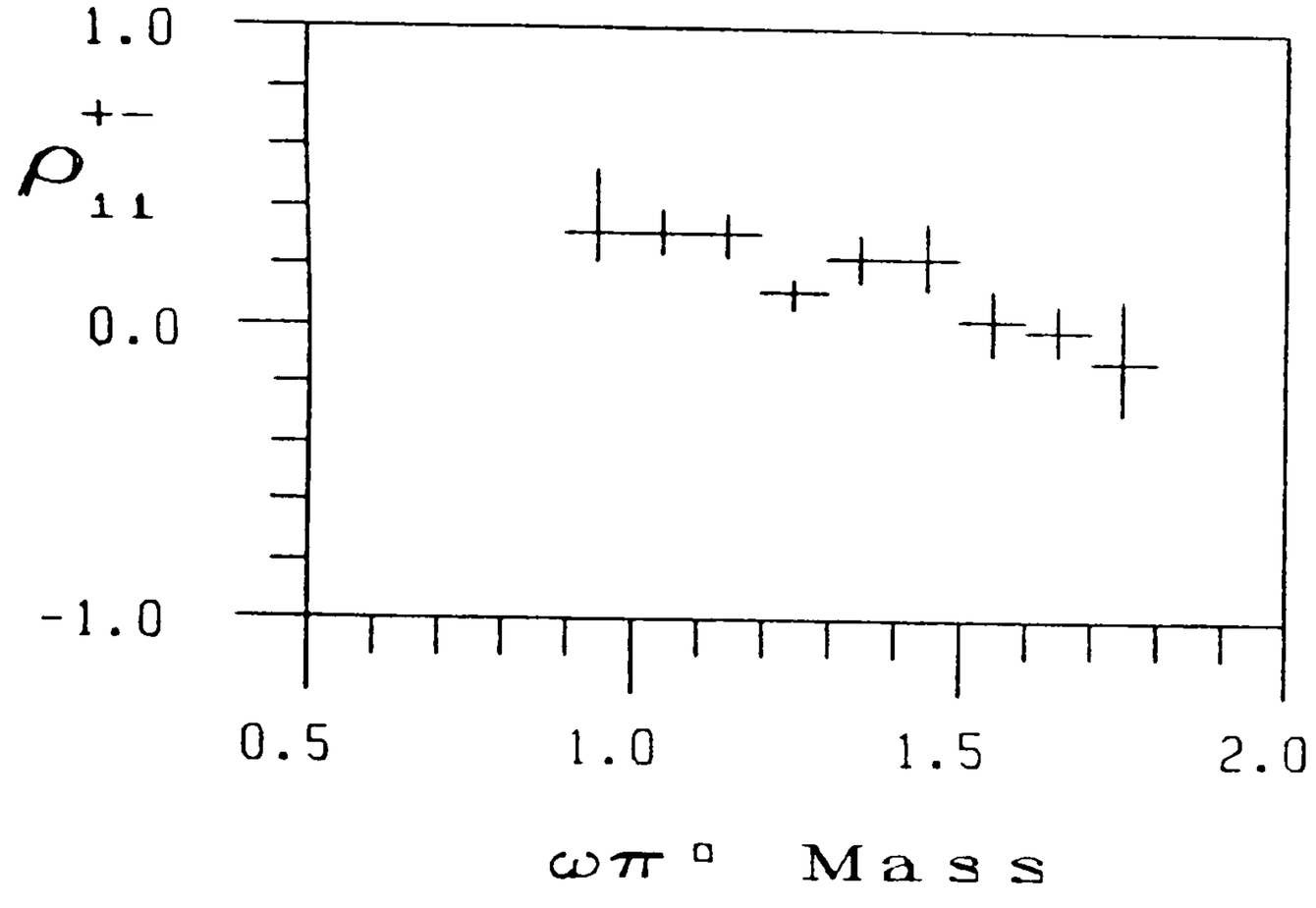
1.0
+−
ρ_{11}
0.0
-1.0
0.5
1.0
1.5
2.0
ωπ° Mass

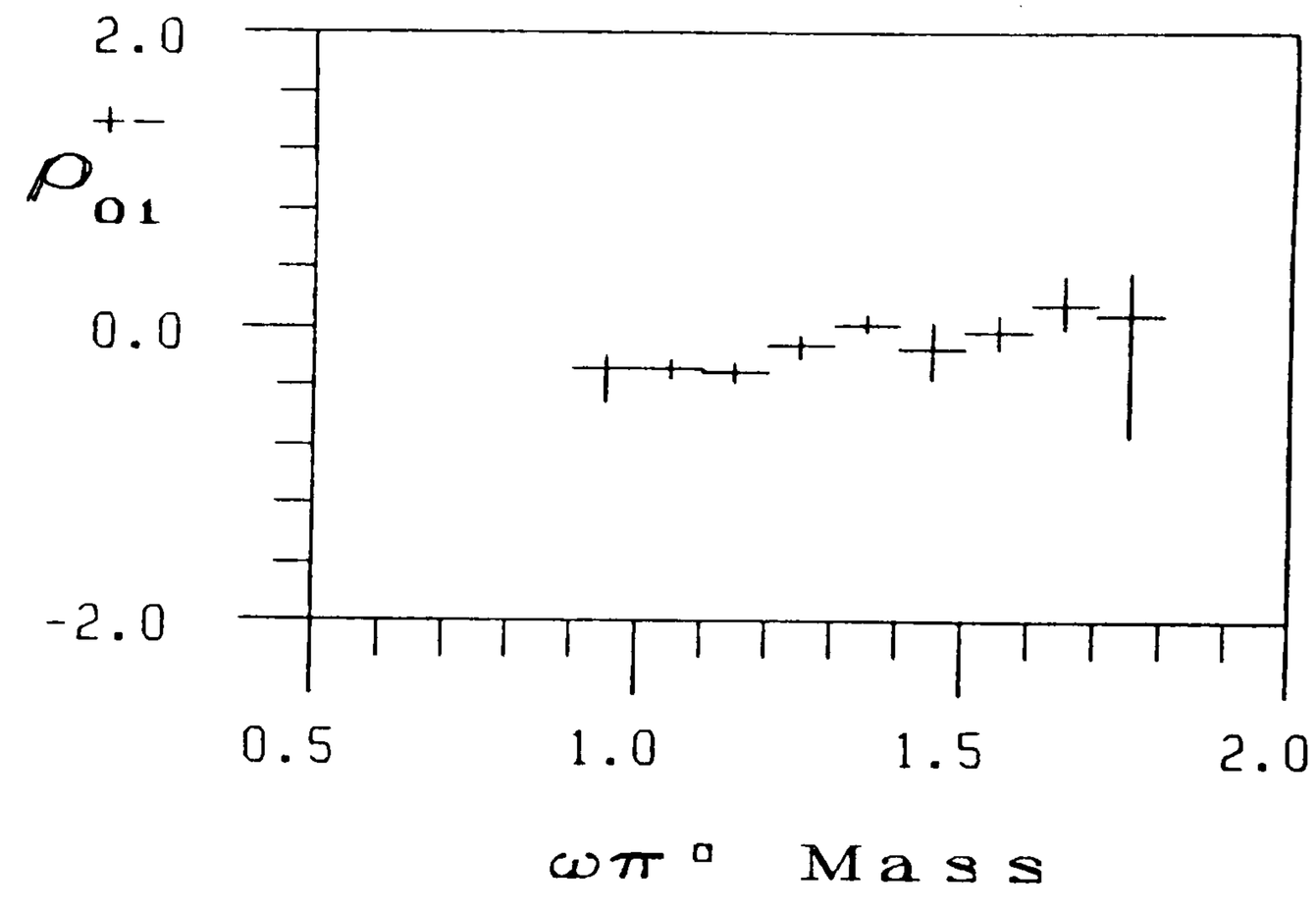
2.0
+−
ρ_{01}
0.0
-2.0
0.5
1.0
1.5
2.0
ωπ° Mass

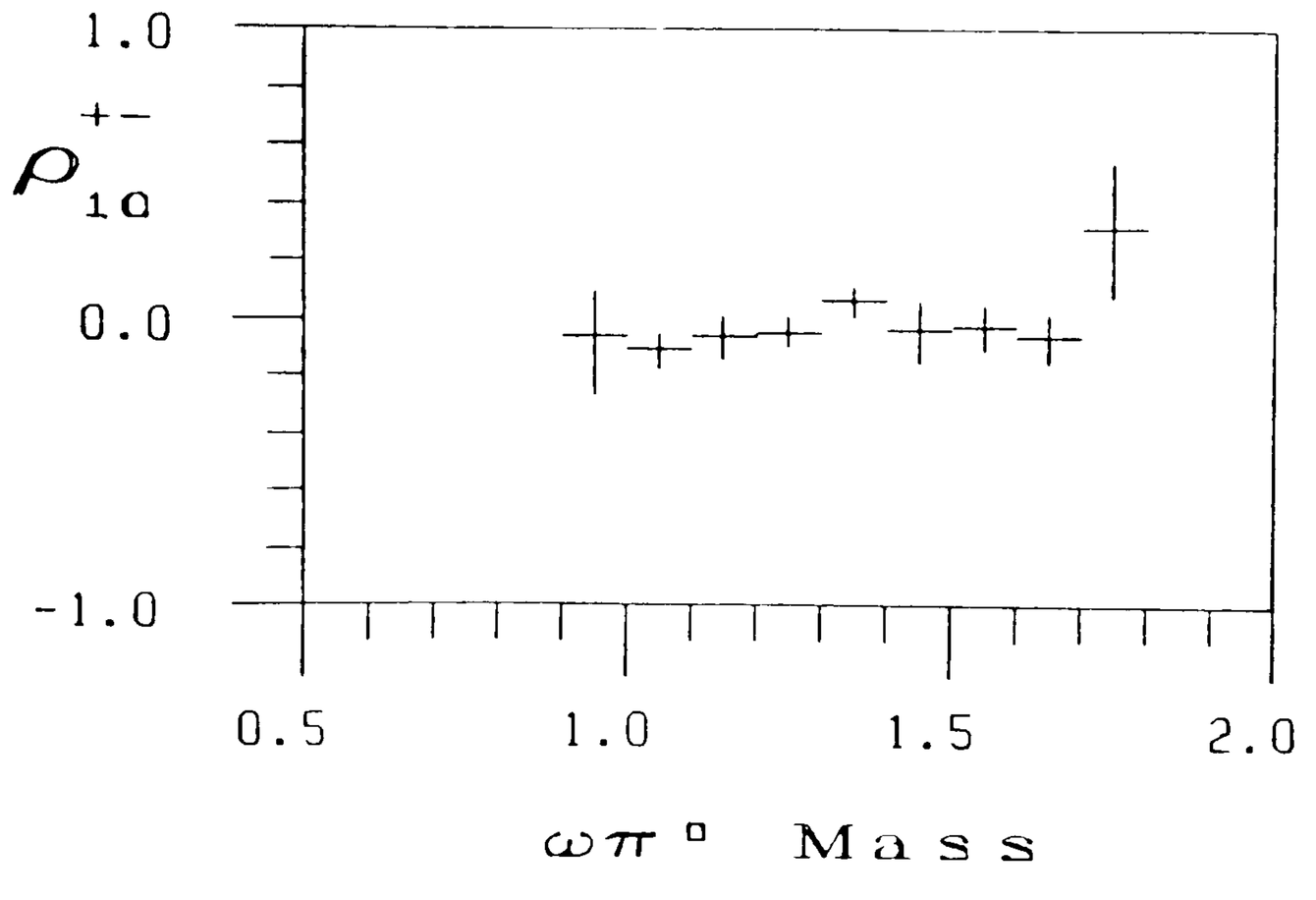
1.0
+−
ρ_{10}
0.0
-1.0
0.5
1.0
1.5
2.0
ωπ° Mass

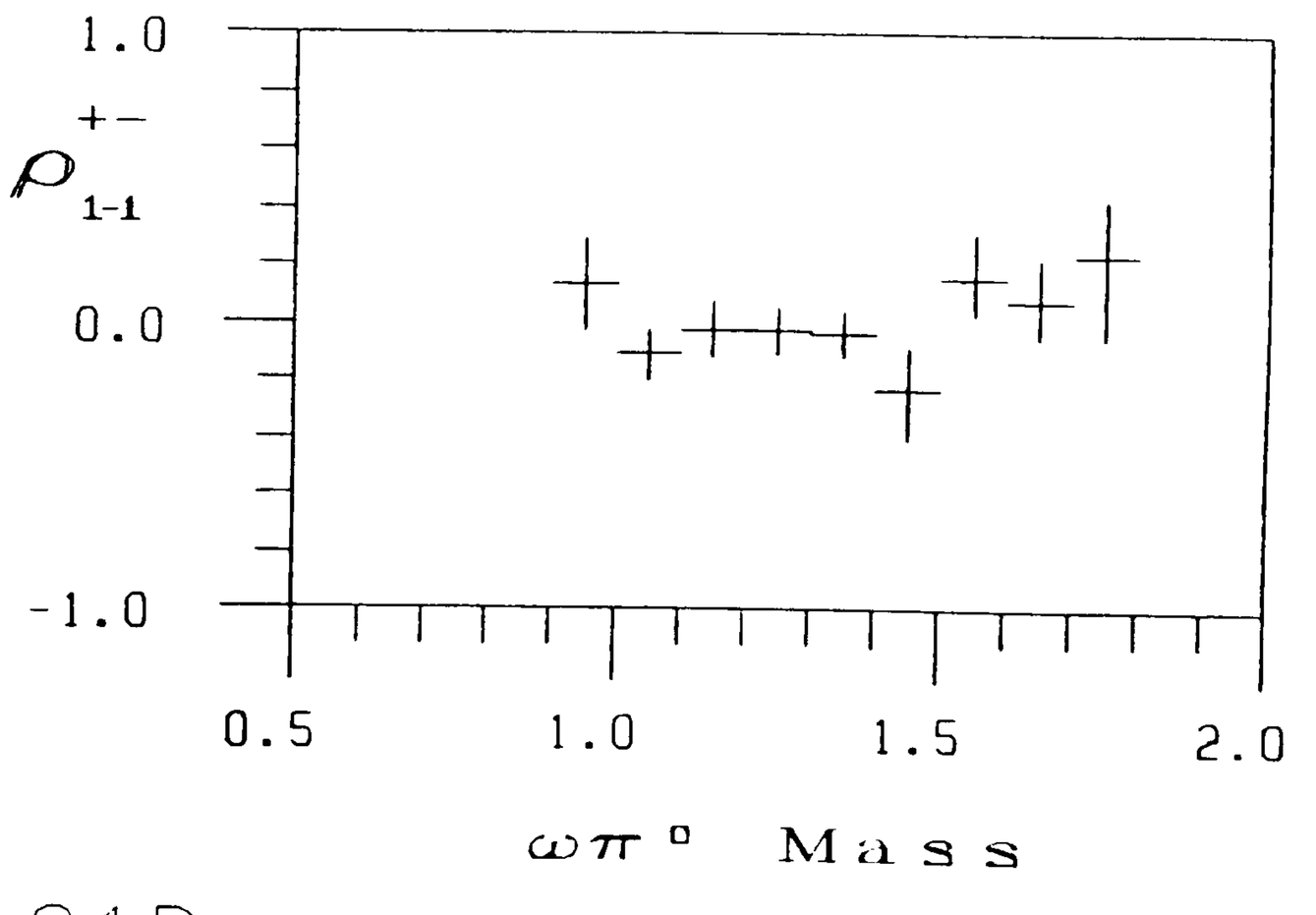
1.0
+−
ρ_{1-1}
0.0
-1.0
0.5
1.0
1.5
2.0
ωπ° Mass

Figure 5.21D

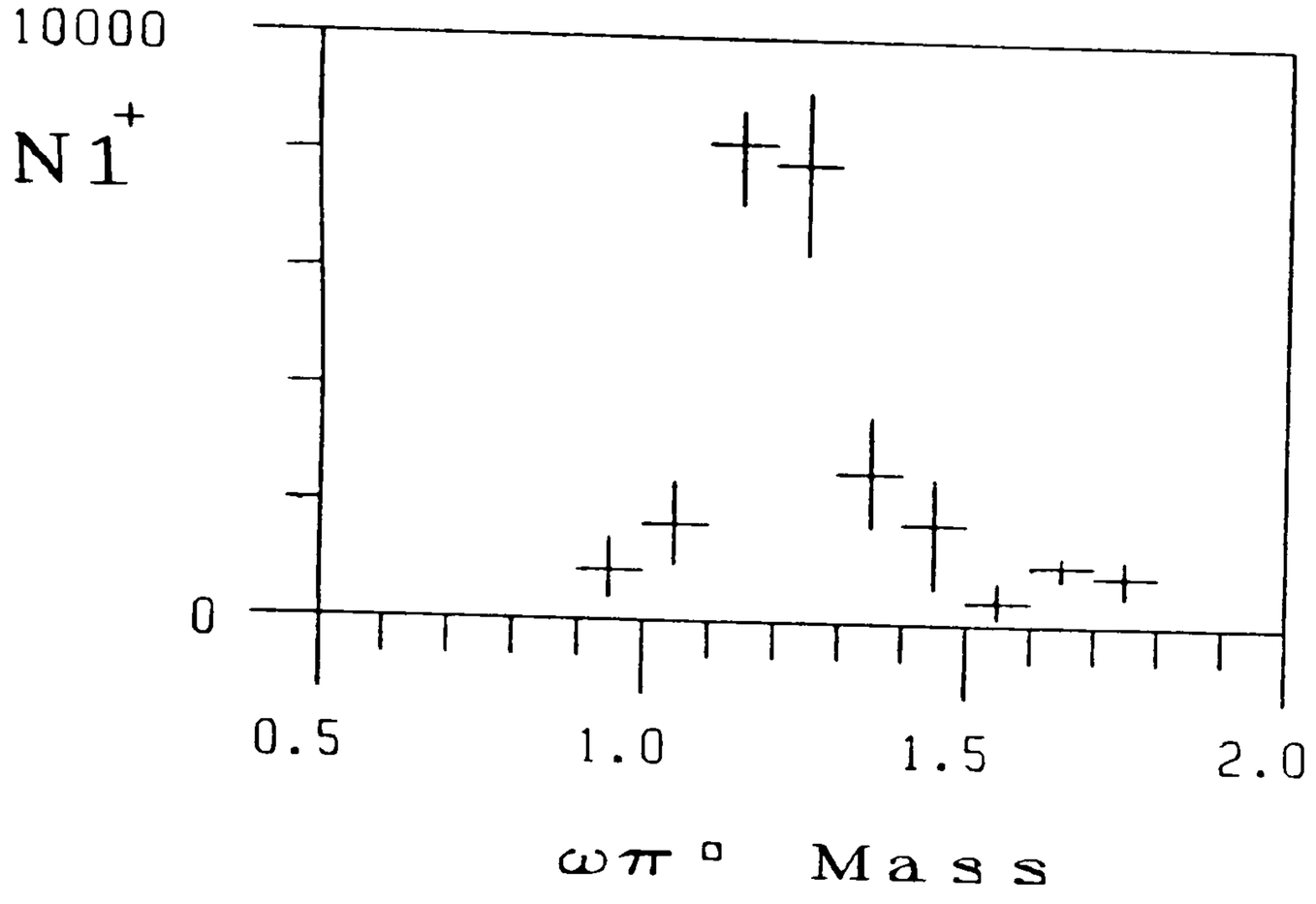
10000
N1+
0
0.5
1.0
1.5
2.0
ωπ° Mass

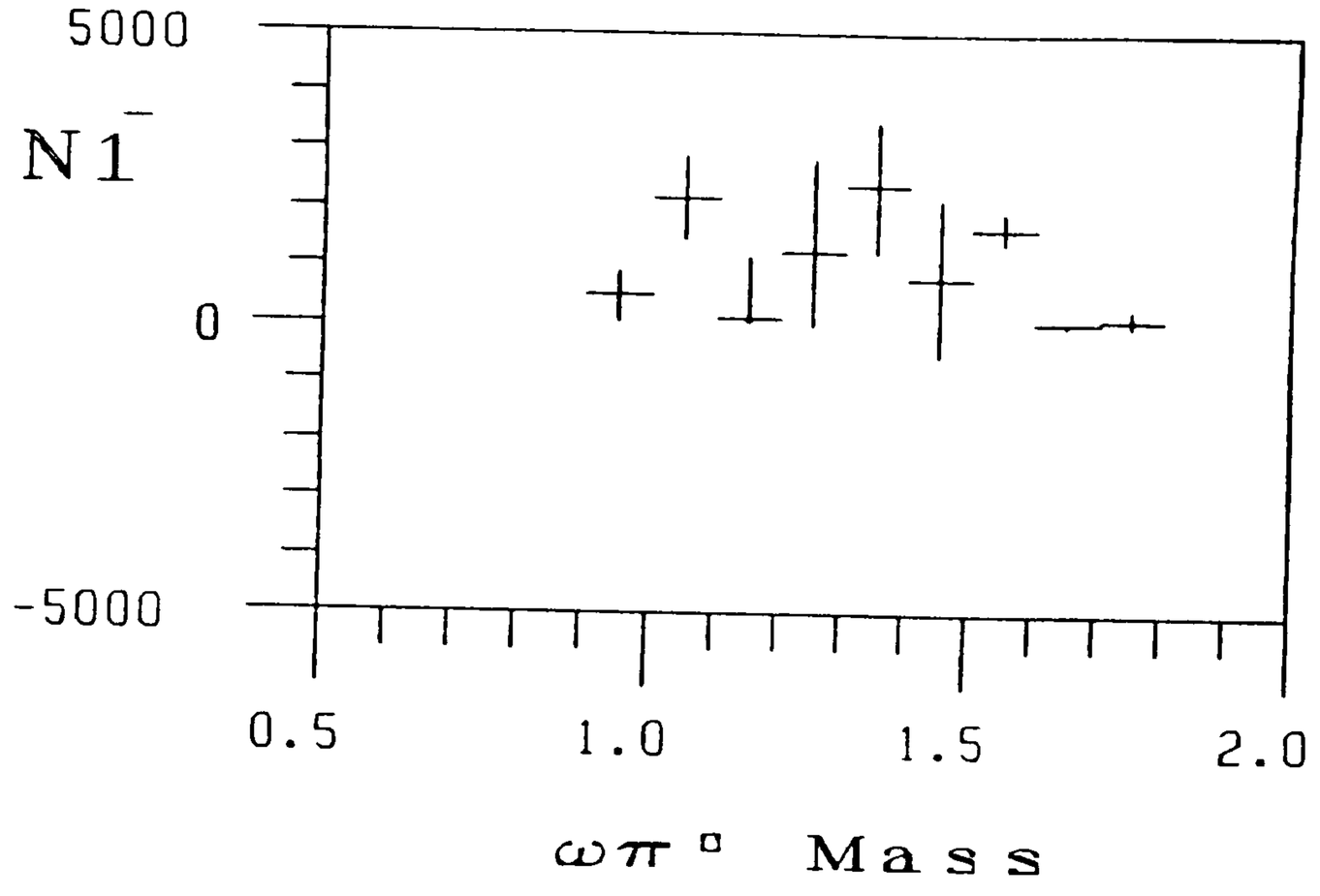
5000
N1-
0
-5000
0.5
1.0
1.5
2.0
ωπ° Mass

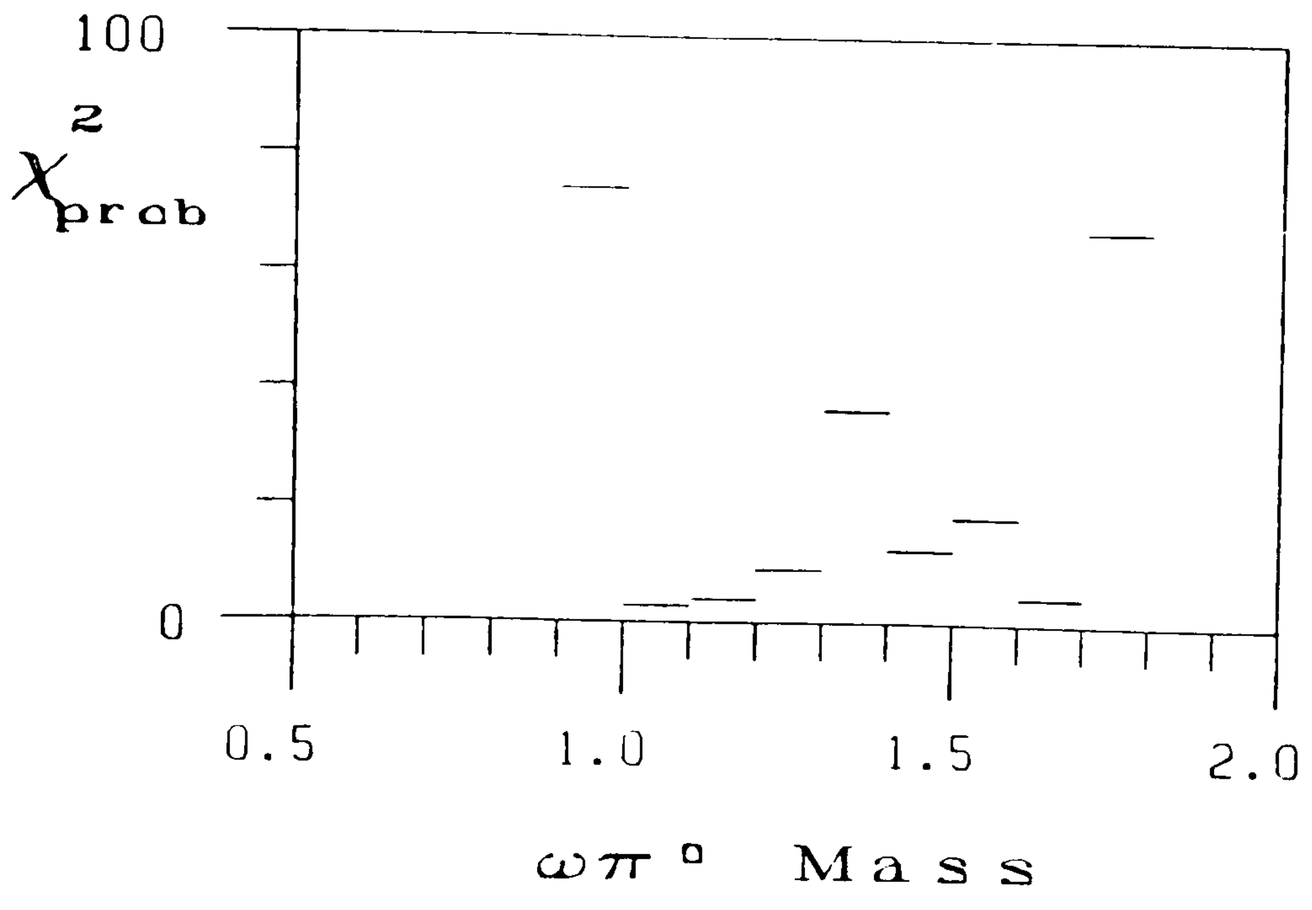
100
χ²prob
0
0.5
1.0
1.5
2.0
ωπ° Mass

Figure 5.22A

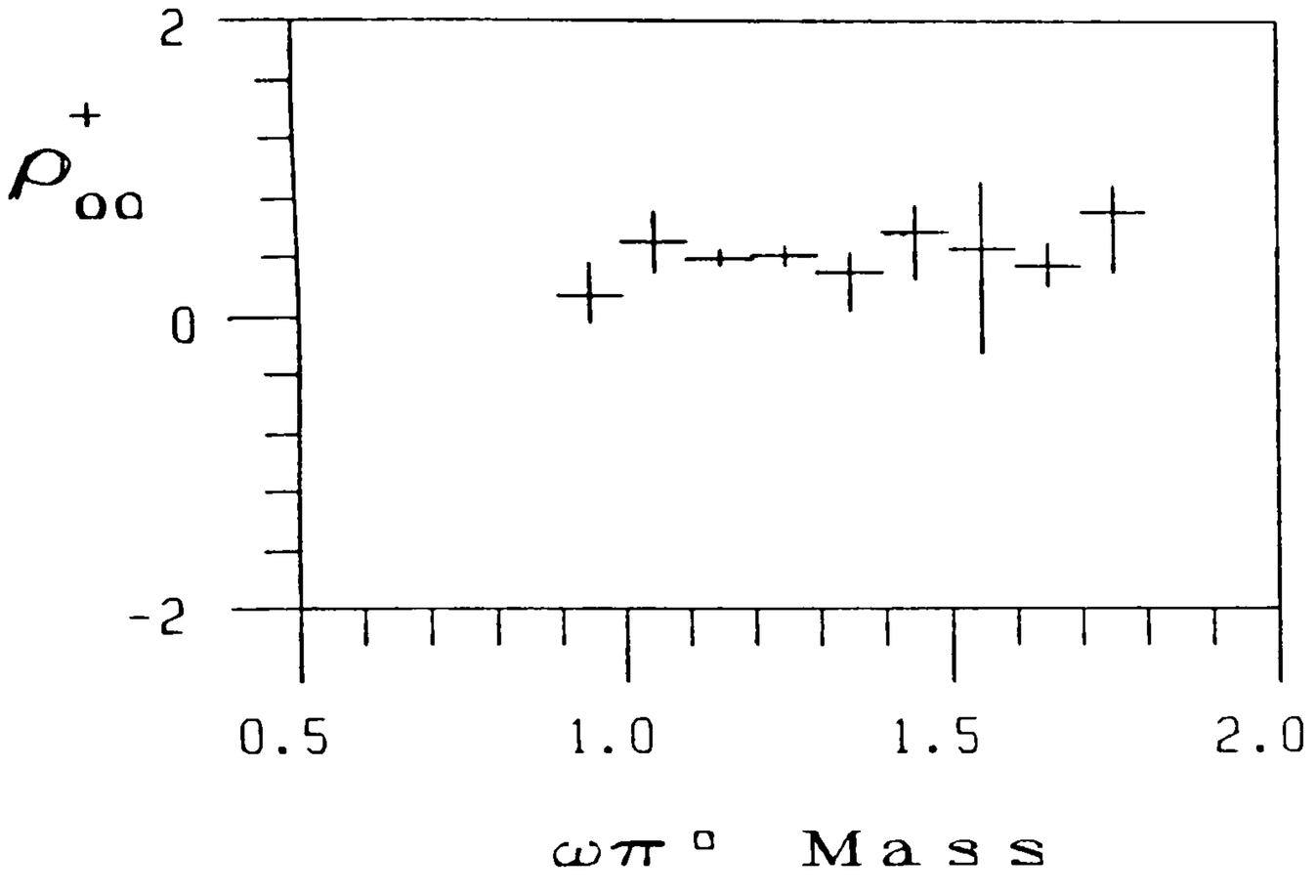
ρ^+_{00}
2
0
-2
0.5
1.0
1.5
2.0
$\omega\pi^0$ Mass

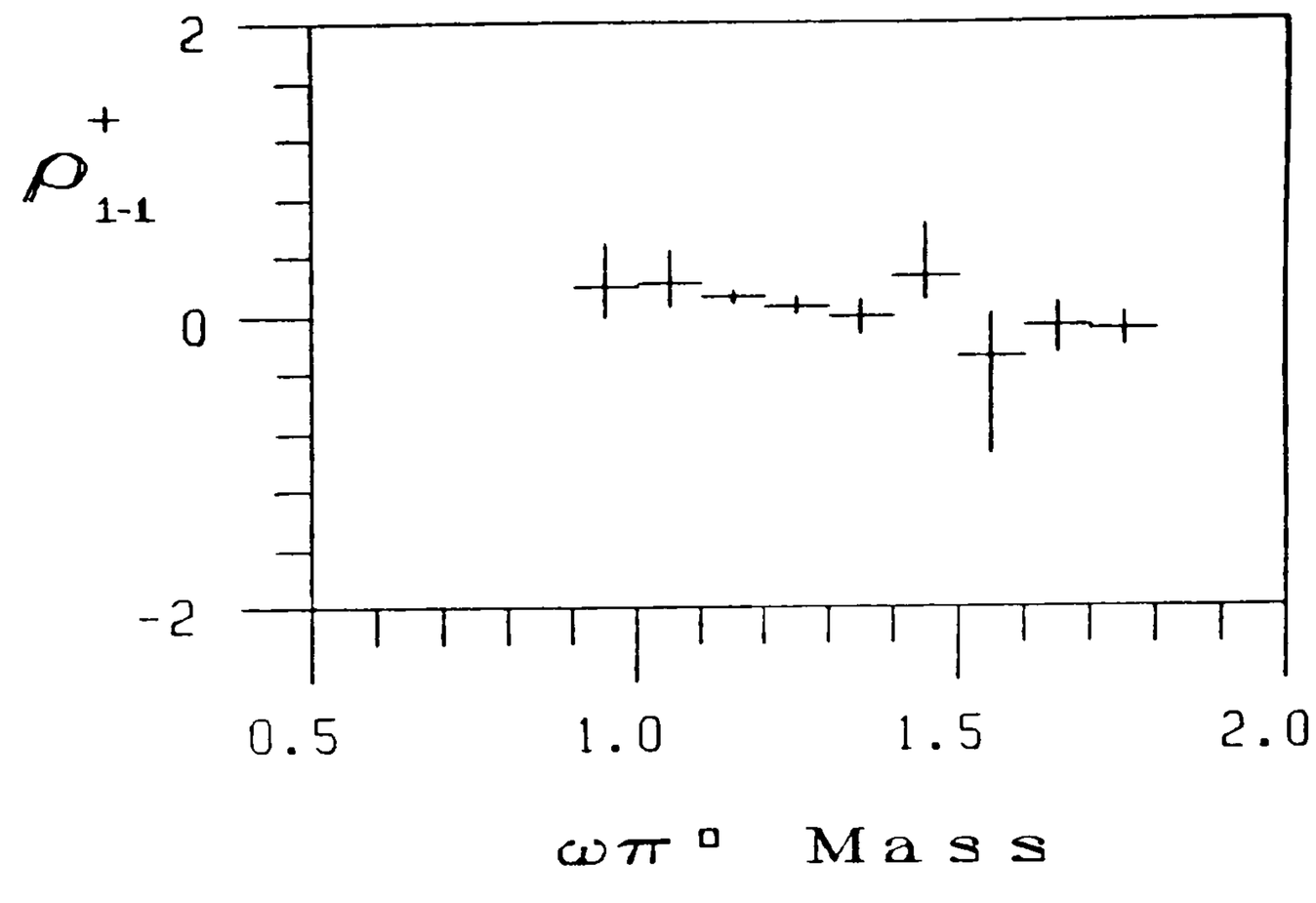
ρ^+_{1-1}
2
0
-2
0.5
1.0
1.5
2.0
$\omega\pi^0$ Mass

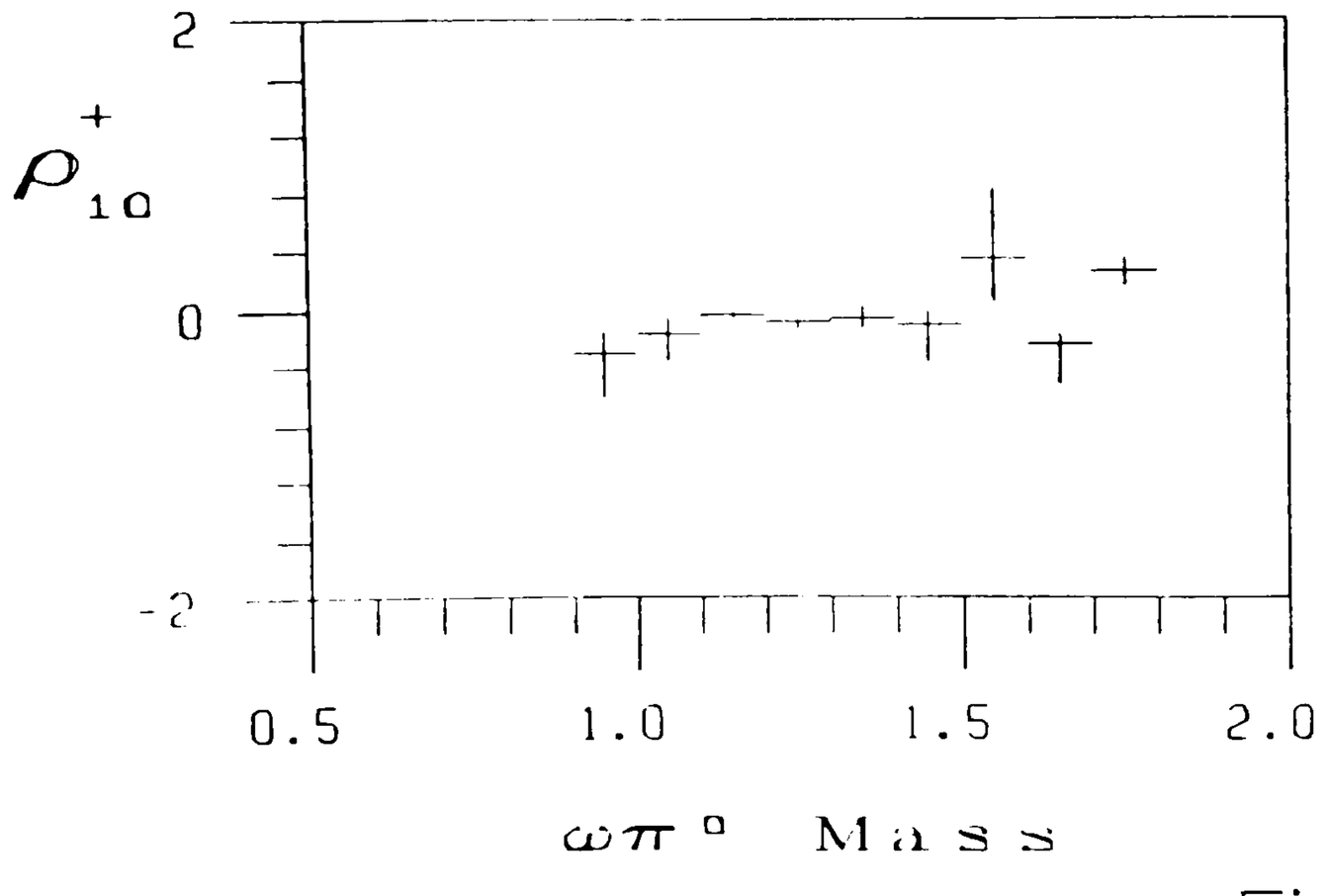
ρ^+_{10}
2
0
-2
0.5
1.0
1.5
2.0
$\omega\pi^0$ Mass

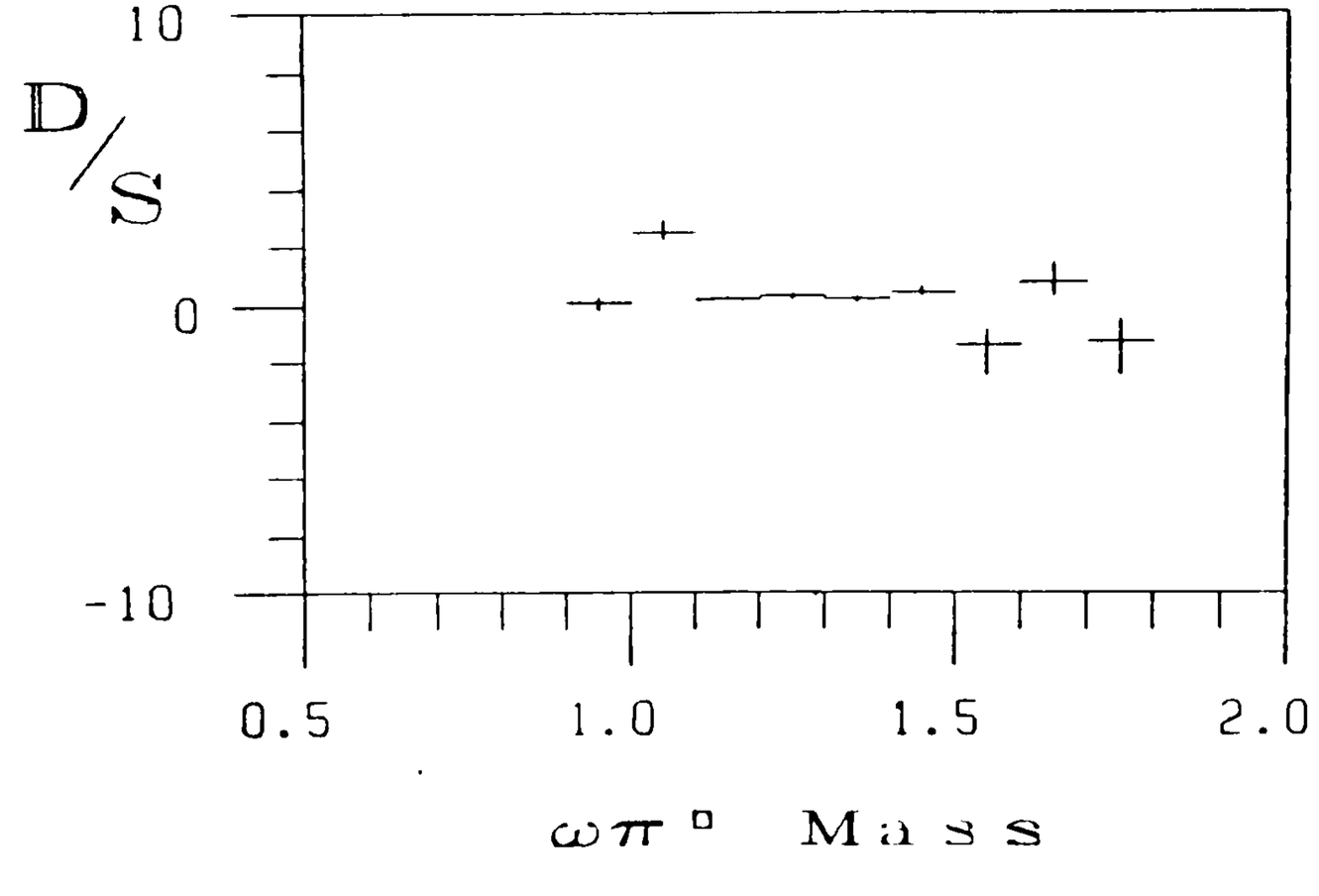
D/S
10
0
-10
0.5
1.0
1.5
2.0
$\omega\pi^0$ Mass

Figure 5.22B

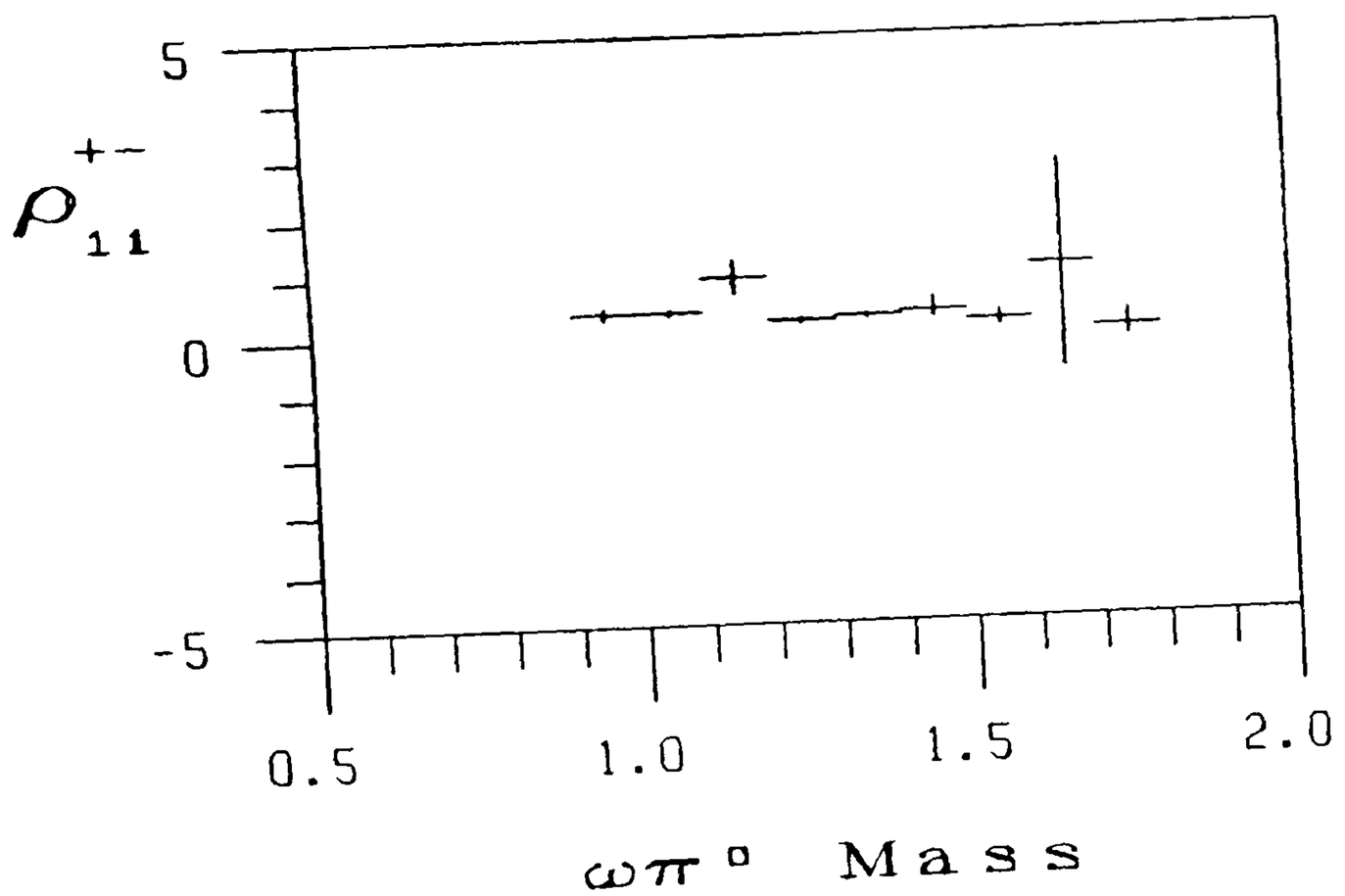
5
0
-5
0.5
1.0
1.5
2.0
ρ_{11}^{+-}
$\omega\pi^0$ Mass

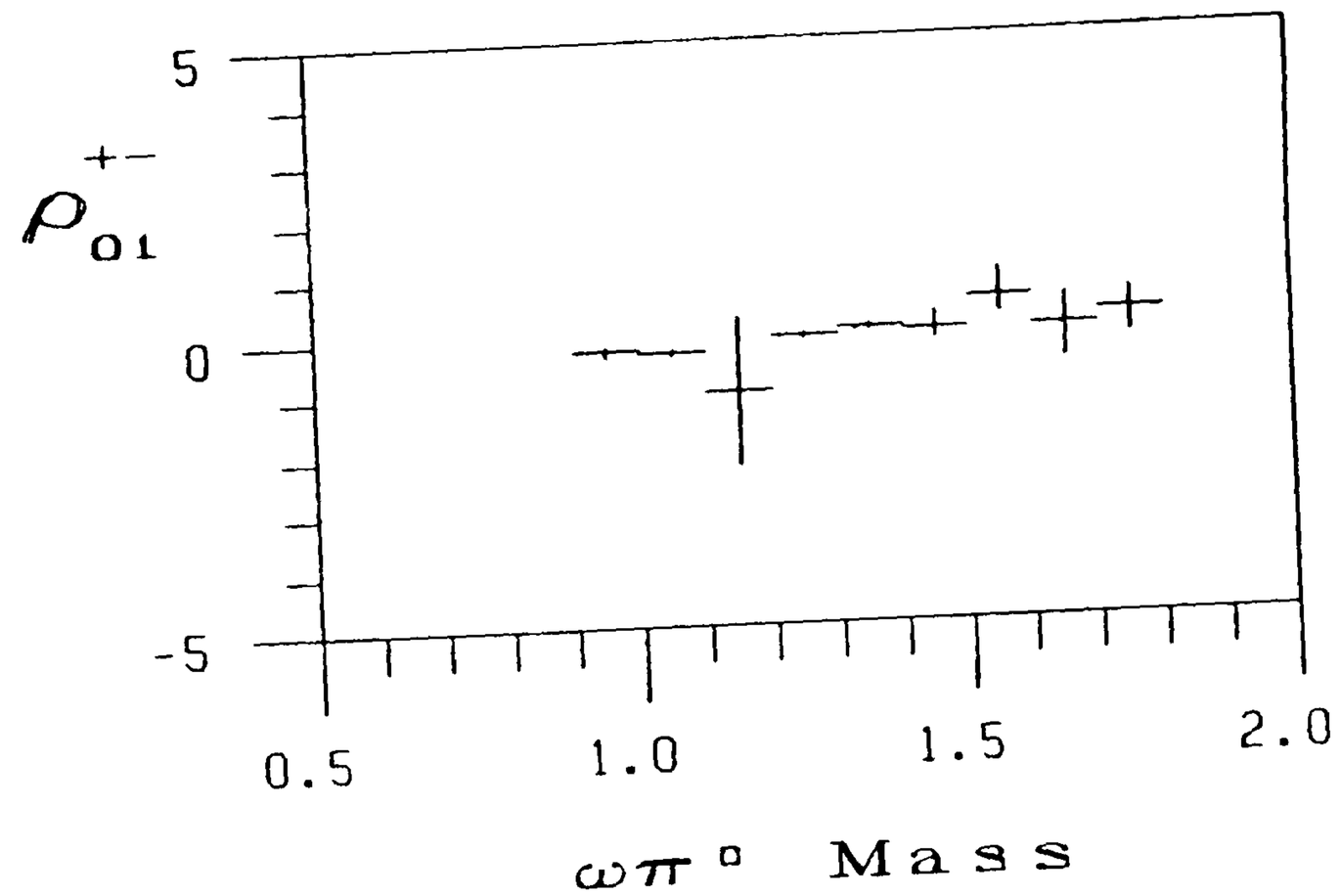
5
0
-5
0.5
1.0
1.5
2.0
ρ_{01}^{+-}
$\omega\pi^0$ Mass

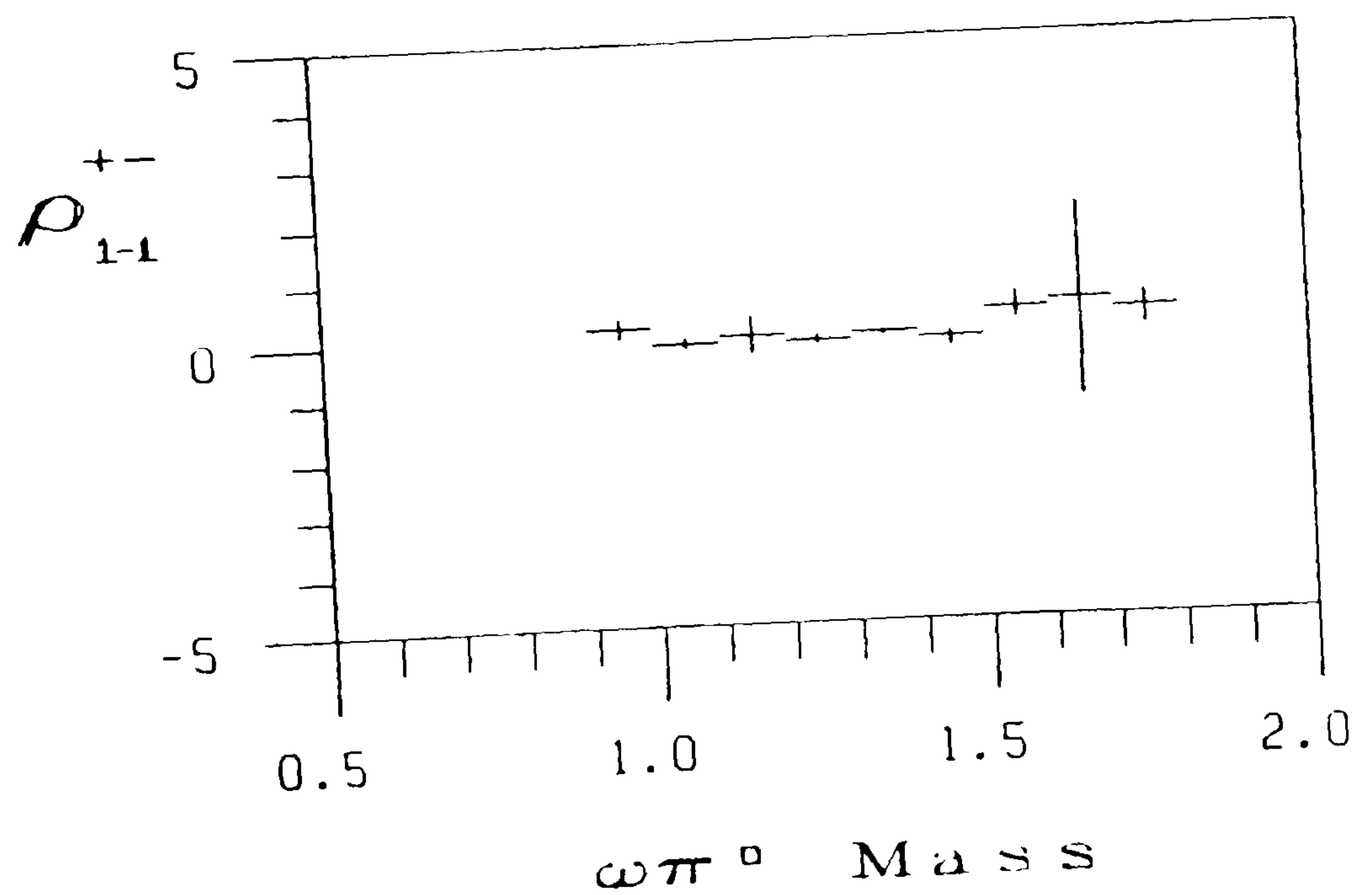
5
0
-5
0.5
1.0
1.5
2.0
ρ_{1-1}^{+-}
$\omega\pi^0$ Mass

Figure 5.22C

APPENDIX A

Double Moment Spin-Parity Analysis

The purpose of this Appendix is to describe in some detail the spin-parity analysis that was performed on the $\omega\pi^0$ data from the C.E.R.N. experiment WA57.

The method used to take account of the limited geometrical and trigger acceptance of the detector system will be described in another Appendix.

The overall transition amplitude for the reaction :---

$$\gamma p \longrightarrow X\, p \qquad \ldots\ldots (A1)$$
$$\hookrightarrow 2\pi^0$$
$$\hookrightarrow \pi^+\pi^-\pi^0$$

can be written as a product of three factors. The first of these is a production amplitude, A_p, and is used to describe the production of the $\omega\pi^0$ state with spin J and helicity Λ, from the initial photon/proton system.

This amplitude can be written as :---

$$A_p = \langle p_f \Lambda \lambda'_p \,|\, T(w_0) \,|\, p_i \lambda_\gamma \lambda_p \rangle \qquad \ldots\ldots (A2)$$

where

p_i, p_f = the initial and final c.m.s. momentum vectors

λ_p, λ'_p = the initial and final proton helicities

λ_γ = the incoming photon helicity

$T(w_0)$ = the helicity production operator which may depend

upon w_0, the overall c.m.s. energy

The second and third factors in the overall amplitude are decay amplitudes, A_{d1} and A_{d2} which describe the two steps of the sequential decay ; A_{d1} is concerned with the decay of the $\omega\pi^0$ system to $\omega\ \pi^0$ and A_{d2} describes the ω decay to three pions, $\omega \rightarrow \pi^+\pi^-\pi^0$. As shown by Chung[5-7], the amplitude describing the decay of a state with spin J and helicity Λ, to two particles with helicities λ_1 and λ_2, can be written in the rest frame of the parent state as :---

$$A_d = \left(\frac{2J+1}{4\pi}\right)^{\frac{1}{2}} \left\{ 4\pi \left(\frac{w}{|p|}\right)^{\frac{1}{2}} \langle J\Lambda\lambda_1\lambda_2 | M_J | J\Lambda \rangle D^{J*}_{\mu\Lambda}(\Omega) \right\} \quad \ldots\ (A3)$$

where

w = the effective mass of the parent particle

p = the momentum of the decay products in the parent rest frame

$\mu = \lambda_1 - \lambda_2$

Ω = the Euler angles describing the direction of p in the helicity frame of the parent state

The last factor in this expression for the amplitude is one of the "D-functions" defined by Rose[5-9], a matrix element for the rotation matrix. The case of a state decaying into three pions can be treated in an identical way, and so the amplitude A_{d2} for the ω decay can be written in the same way. In this case however, the analyser must be chosen to be the normal to the ω decay plane in the ω helicity system, rather than the direction of travel of one of the decay products. Writing :---

$$F(J, \lambda_1, \lambda_2) = 4\pi \left(\frac{w}{|p|}\right)^{\frac{1}{2}} \langle J\lambda_1\lambda_2 | M_J | J\Lambda \rangle \quad \ldots\ (A4)$$

where $F(J,\lambda_1,\lambda_2)$ is the helicity decay amplitude, the first amplitude, A_{d1}, can be written as :---

$$A_{d1} = \left(\frac{2J+1}{4\pi}\right)^{1/2} F(J,\lambda_1,\lambda_2)\, D^{J*}_{\Lambda\mu}(\Omega_1) \qquad \ldots\ldots (A5)$$

For the case in which a parent state with spin and helicity J and Λ decays into a spin 1 ω meson and a π, the amplitude A_{d1} can be written :---

$$A_{d1} = \left(\frac{2J+1}{4\pi}\right)^{1/2} F(J,\lambda,0)\, D^{J*}_{\Lambda\lambda}(\Omega_1) \qquad \ldots\ldots (A6)$$

where λ is the helicity of the ω. The ω decay into three spinless pions can be treated in the same way, with $\mu=0$, giving :---

$$A_{d2} = \left(\frac{3}{4\pi}\right)^{1/2} F(1,0,0)\, D^{1*}_{\lambda 0}(\Omega_2) \qquad \ldots\ldots (A7)$$

The overall amplitude for the process A1 can now be written as :---

$$\begin{aligned} M_{fi} &= \langle p_f \Lambda \lambda'_p | T(w_0) | p_i \lambda_\gamma \lambda_p \rangle \\ &\times \left(\frac{2J+1}{4\pi}\right)^{1/2}\left(\frac{3}{4\pi}\right)^{1/2} F(J,\lambda,0)\, F(1,0,0) \\ &\times D^{J*}_{\Lambda\lambda}(\Omega_1)\; D^{1*}_{\lambda 0}(\Omega_2) \end{aligned} \qquad \ldots\ldots (A8)$$

The joint angular decay distribution of the final state particles can be written as :---

$$\frac{d\sigma}{d\Omega_1 d\Omega_2} = \int K(w)\, dw\, d\Omega_0 \sum_{fi} |M_{fi}|^2 \qquad \ldots\ldots (A9)$$

$$I(\Omega_1,\Omega_2) = \sum_{fi} |M_{fi}|^2 \int d\Omega_0\, K(w)\, dw \qquad \ldots\ldots (A10)$$

where the summation is over all possible intermediate states. The integration in A9 is over Ω_0, the c.m.s. production angle, and w, the c.m.s. energy. The function K(w) contains all factors which might

depend upon the dynamics of the initial and intermediate states, such as phase-space factors, Breit-Wigner line shapes for resonances etc.. The summation in A9 is over all possible intermédiate spin substates and will include terms arising from the interferene between different spin parity states which might be present in the parent $\omega\pi^0$ system. The summation over intermediate states can be expressed as a summation over i,j,Λ,Λ',λ and λ', where i and j are used to label different spin-parities. Λ and Λ' label the helicity substates of the parent $\omega\pi^0$ system, and λ,λ' are the ω helicity substates. Thus the summation in A10 can be written :---

$$I_{ij}(\Omega_1,\Omega_2) = \sum_{ij\Lambda\Lambda'\lambda\lambda'} \rho^{ij}_{\Lambda\Lambda'} \left(\frac{2J_i+1}{4\pi}\right)^{\frac{1}{2}}\left(\frac{2J_j+1}{4\pi}\right)^{\frac{1}{2}} \frac{3}{4\pi}.$$

$$\times \left|F(1,0,0)\right|^2 F(J_i,\lambda,0)\, F^*(J_j,\lambda',0)$$

$$\times D^{J_i *}_{\Lambda\lambda}(\Omega_1)\, D^{J_j}_{\Lambda'\lambda'}(\Omega_1)\, D^{1*}_{\lambda 0}(\Omega_2)\, D^{1}_{\lambda' 0}(\Omega_2) \quad \ldots\ldots (A11)$$

In this expression we have introduced the interference spin-density matrix $\rho^{ij}_{\Lambda\Lambda'}$, defined by :---

$$\rho^{ij}_{\Lambda\Lambda'} = \int d\Omega_0 \langle f_f \Lambda \lambda_p' | T(W_0) | f_i \lambda_r \lambda_p \rangle \langle f_f \Lambda' \lambda_p' | T(W_0) | f_i \lambda_r \lambda_p \rangle^* \quad \ldots\ldots (A12)$$

Using the properties of the D-functions, the product of four which appears in A11 can be contracted to a summation over only two. The joint angular decay distribution can then be written :---

$$I_{ij}(\Omega_1,\Omega_2) = \sum_{lmLM} \left(\frac{2L+1}{4\pi}\right)\left(\frac{2l+1}{4\pi}\right) H_{ij}(lmLM)$$

$$\times D^{L*}_{Mm}(\Omega_1)\, D^{l*}_{m0}(\Omega_2) \quad \ldots\ldots (A13)$$

The other factors appearing in the terms of this summation are normalisation factors and the coefficients $H_{ij}(lmLM)$, which are functions

of the parameters which determine the production and subsequent decay of the $\omega\pi^0$ system. These coefficients can be written down explicitly in terms of the spin density matrix elements and helicity decay amplitudes.

$$H_{ij}(lmLM) = t^{ij*}_{LM}\, g^{ij}_{Llm} \langle 10l0|10\rangle \quad \ldots\ldots (A14)$$

where

$$t^{ij*}_{LM} = \left(\frac{2J_j+1}{2J_i+1}\right)^{1/2} \sum_{\lambda\lambda'} \rho^{ij}_{\lambda\lambda'} \langle J_j \lambda' L m | J_i \lambda\rangle \quad \ldots\ldots (A15)$$

and

$$g^{ij}_{Llm} = \int K(\omega)\, d\omega \sum_{\lambda\lambda'} F(J_i,\lambda,0)\, F^*(J_j,\lambda',0) \langle J_j \lambda' L m | J_i \lambda\rangle \langle 1\lambda' l m | 1\lambda\rangle \quad \ldots\ldots (A16)$$

and the Clebsch-Gordon coefficient comes from the decay of the ω.

The Hermitian nature of the spin-density matrix imposes certain restrictions on the matrix elements, and the symmetries which these restrictions cause propagate through to the coefficients $H_{ij}(lmLM)$. Further symmetries in the coefficients are created by the conservation of parity in the production and decay processes and the consequent symmetries between the various helicity decay amplitudes. These symmetries in the $H_{ij}(lmLM)$ can be incorporated into the expression A13 for the joint angular decay distribution, allowing the summation over l,m,L and M to be restricted to only those terms in which m and M are both ≥ 0. The resulting expression for the angular distribution is :---

$$I_{ij}(\Omega_1,\Omega_2) = \sum_{lL} \sum_{\substack{m\geq 0 \\ M\geq 0}} \left(\frac{2L+1}{4\pi}\right)\left(\frac{2l+1}{4\pi}\right)(2-\delta_{m0})(2-\delta_{M0})$$

$$\times\ 2\,\mathrm{Re}\left\{H_{ij}(lmLM)\right\} \quad \ldots\ldots (A17)$$

$$\times\ \tfrac{1}{2}\,\mathrm{Re}\left\{D^L_{Mm}(\Omega_1)\, D^L_{m0}(\Omega_2) \pm (-1)^L D^L_{M-m}(\Omega_1)\, D^L_{-m0}(\Omega_2)\right\}$$

where η_i is the parity of the state with label i. We can now define the orthogonal double moments in terms of a sum of products of D-Functions :---

$$H^{\pm}_{ij}(\Omega_1,\Omega_2) = \frac{1}{2} Re\left\{D^{L}_{M m}(\Omega_1) D^{L}_{-m 0}(\Omega_2) \pm (-1)^{L} D^{L}_{M -m}(\Omega_1) D^{L}_{-m 0}(\Omega_2)\right\} \quad \ldots\ldots (A18)$$

and write the joint angular decay distribution as :---

$$I_{ij}(\Omega_1,\Omega_2) = \sum_{lL} \sum_{\substack{m\geq 0 \\ M\geq 0}} \left(\frac{2L+1}{4\pi}\right)\left(\frac{2l+1}{4\pi}\right)(2-\delta_{m0})(2-\delta_{M0}) H^{\pm}_{ij}(\Omega_1,\Omega_2) 2.Re\left\{H_{ij}(lmLM)\right\} \ldots\ldots (A19)$$

By taking the moments of this distribution, i.e. by calculating the experimental averages of these angular terms, the coefficients, $\Re e\{H_{ij}(lmLM)\}$, can be evaluated. From the form of the double-moments, it can be seen that these expressions can be split into two groups according to whether $\eta_i\eta_j$ is odd or even : these two groups are described as odd and even moments or symmetric and anti-symmetric moments. Writing :---

$$Re\left\{H_{ij}^{\pm}(lmLM)\right\} = \frac{1}{2}\sum_{ij}\left(1 \pm \eta_i\eta_j\right) Re\left\{H_{ij}(lmLM)\right\} \quad \ldots\ldots (A20)$$

where

$$Re\left\{H_{ij}^{\pm}(lmLM)\right\} = \left\langle H_{ij}^{\pm}(\Omega_1,\Omega_2)\right\rangle \quad \ldots\ldots (A21)$$

Expressed in this way, it can be seen that the even or symmetric moments can only have contributions from pure spin parity states and from two spin parity states with the same parity. The odd or anti-symmetric moments on the other hand will contain information related to the interferences between spin parity states of opposite parity. Thus the even part of $\Re e\{H^{\pm}(lmLM)\}$ can be written :---

$$Re\left\{H^{+}(lmLM)\right\} = \sum_{i} Re\left\{H_{ii}(lmLM)\right\} + 2\sum_{\substack{i>j \\ \eta_i\eta_j=1}} Re\left\{H_{ij}(lmLM)\right\} \ldots\ldots (A22)$$

and the odd part as :---

$$Re\left\{H^{-}(lm\,LM)\right\} = 2\sum_{\substack{i\neq j \\ i,i-1}} Re\left\{H_{ij}(lm\,LM)\right\} \qquad \ldots\ldots (A23)$$

APPENDIX B

Acceptance Correction of Double Moments

The method used to correct the data for biases introduced by the limited geometrical and trigger acceptance of the detector follows the 'linear algebra' method of Grayer et al. [5-10].

For the sequential decay of (5.3) the joint angular decay distribution can be expressed as a linear sum of a set of orthogonal functions, E_i. The full set of these functions is determined by the assumed spin-parity composition of the parent state, and each E_i will have a term relating to the angles from the first step in the decay, Ω_1, and a term which is a function of the angles of the second step, Ω_2. Thus the true, produced joint angular distribution, I_t, can be expressed as : ----

$$I_t = I_t(\Omega_1, \Omega_2) = \sum_i H_i E_i(\Omega_1, \Omega_2) \quad \ldots\ldots (B1)$$

where the coefficients, the H_i, will in general depend upon the detailed characteristics of the process such as production amplitudes the spin-density matrix. The angular expressions occurring in this equation can be identified as the orthogonal double moments of Equ[n] A18.

This true joint angular decay distribution will however be modified in a complicated way by both the geometrical acceptance of the detector, and by resolution effects such as multiple Coulomb scattering of the charged tracks as they pass through the material of the detector. This complex modification can be encapsulated in the 'acceptance function', ACC, which is a function of all of the variables used to describe the event fully. Thus, the experimentally observed angular distribution, denoted by I_o, can be written as

$$I_o = ACC.\ I_t \quad \ldots\ldots (B2)$$

$$I_o = ACC. \sum_i H_i E_i(\Omega_1, \Omega_2) \quad \ldots\ldots (B3)$$

Defining the experimental moments G_i as

$$G_i = \int I_o E_i(\Omega_1, \Omega_2) d\Omega_1 d\Omega_2 \quad \ldots\ldots (B4)$$

From Equ^n B2, this can be written as

$$G_i = \sum_j H_i \int E_i(\Omega_1, \Omega_2) ACC E_j(\Omega_1, \Omega_2) d\Omega_1 d\Omega_2 \quad \ldots\ldots (B5)$$

$$= \sum_j A_{ij} H_i \quad \ldots\ldots (B6)$$

where

$$A_{ij} = \int E_i(\Omega_1, \Omega_2) ACC. E_j(\Omega_1, \Omega_2) d\Omega_1 d\Omega_2 \quad \ldots\ldots (B7)$$

This is simply a set of linear equations which can be written in matrix notation as

$$\underline{G} = \underset{\sim}{A} . \underline{H} \quad \ldots\ldots (B8)$$

This matrix equation can be solved for the vector H by inverting A, such that

$$\underline{H} = \underset{\sim}{A}^{-1} . \underline{G} \quad \ldots\ldots (B9)$$

In practice the experimental moments G_i were formed as

$$G_i = \frac{1}{N_{observed}} \cdot \sum_i w_i E_i(\Omega_1, \Omega_2) \quad \ldots\ldots (B10)$$

and the integrals in Equ^n (B7) were calculated by Monte-Carlo methods, as

$$A_{ij} = \sum_{\substack{events \\ accepted}} E_i(\Omega_1, \Omega_2) . E_j(\Omega_1, \Omega_2) \quad \ldots\ldots (B12)$$

The weighting factors w_i appearing in Equ^n (B10) include any event dependant corrections such as the background subtraction weight described in Section 5.2. This weight also included an additional term connected with the event polarisation which is explained above.

With this method of correcting the data angular distribution, the vector of true coefficients, H, of the true angular distribution could be obtained.